

**Three-dimensional scattering of time harmonic elastic waves from  
axisymmetric surface indentations in a half-space**

**by**

**Peter Heinrich Albach, Dipl.-Ing., M.Sc.**

**A thesis submitted for the degree of  
Doctor of Philosophy**

**Department of Mechanical Engineering  
University College London  
University of London**

**November 1989**

ProQuest Number: 10630796

All rights reserved

INFORMATION TO ALL USERS

The quality of this reproduction is dependent upon the quality of the copy submitted.

In the unlikely event that the author did not send a complete manuscript and there are missing pages, these will be noted. Also, if material had to be removed, a note will indicate the deletion.



ProQuest 10630796

Published by ProQuest LLC (2017). Copyright of the Dissertation is held by the Author.

All rights reserved.

This work is protected against unauthorized copying under Title 17, United States Code  
Microform Edition © ProQuest LLC.

ProQuest LLC.  
789 East Eisenhower Parkway  
P.O. Box 1346  
Ann Arbor, MI 48106 – 1346

## Abstract

This thesis reports a study with the aim of assessing the possibilities of detecting and characterising the early stages of pitting corrosion, which is located on the remote side a thick aluminium plate. The work concentrated on the use of ultrasonic techniques. An incoming ultrasound plane wave is scattered from a corrosion pit, and the scattered field can provide information about the size and the shape of the surface perturbation and therefore of the extent of corrosion present on the surface. The corrosion pit can be represented as an axisymmetric indentation in the stress free surface of an elastic half-space, and the three-dimensional nature of pits requires numerical models capable of simulating three-dimensional elastic wave scattering processes.

The numerical method used here is an indirect boundary method. The incident compressional or shear wave is expanded in into an infinite series of spherical vector functions. The scattered field can also be described as an infinite series of outgoing spherical waves with unknown coefficients. For numerical purposes both series are truncated to a finite number of terms. The boundary conditions of vanishing normal stress components along the free boundary are applied using a least squares matching method which gives the coefficients for the outward travelling waves. The axisymmetric nature of the surface obstacle allows a decomposition of the three-dimensional scattering problem to a set of two-dimensional subproblems with a given angular dependence, which can be solved separately and the solutions are then superimposed to give the full three-dimensional solution. The results obtained with the numerical model are compared with experimental data and support the findings of the theoretical predictions.

### Acknowledgement

I would like to thank my supervisor Dr. Leonard Bond for his help and support during this project. I am also grateful to Prof. Brian Davies from University College London and Dr. David Bruce from MoD Farnborough for many helpful discussions and valuable suggestions. Finally I would like to thank my colleagues Dr. Nader Saffari, Jicheng Yang and Ioannis Tsironis for their moral support.

Peter H. Albach, London, November 1989

## Contents

	Page
List of Tables	7
List of Figures	9
1. Introduction	43
1.1 Motivation, outline and contribution	43
1.1.1 Statement of the problem and outline of the thesis	43
1.1.2 Claim of contribution	47
1.2 Corrosion in NDE	50
1.3 Mathematical models for the scattering from a corroded surface	58
2. Numerical Method	65
2.1 Basic idea	65
2.2 Theory	67
2.2.1 The multipole expansion of the elastic field	67
2.2.2 Plane waves and their reflection from plane stress free surfaces	73
2.2.3 Implementation of the least squares matching method	79
2.2.4 Azimuthal decomposition of the elastic field	84
2.2.5 Non-hemispherical surface obstacles	87
3. Results	94
3.1 Numerical accuracy	94
3.2 Expansion of plane compressional and shear waves in terms of spherical vector functions	101
3.3 Comparison of results obtained by this study with published results	108

3.4	Compressional wave incident under 60 degrees and shear waves normally incident on to an axisymmetric pit at different stages of growth	127
3.5	Comparison between numerical predictions and measurements	179
4.	Discussion and conclusion	198
4.1	Discussion of the numerical and experimental results	198
4.1.1	Performance of the numerical method presented in this study	198
4.1.2	Discussion of the far-field results and measurements	200
4.1.3	Discussion of the surface displacements in the near-field	205
4.2	Suggested further improvements to the numerical simulation model	207
Appendix A		
	Displacements and stress components in spherical coordinates	211
Appendix B		
	Numerical treatment of the displacement and stress components	215
Appendix C		
	Expansion of a vector plane wave using spherical vector functions	227
Appendix D		
	Far-field approximation and differential scattering cross-section	236

<b>Appendix E</b>	
<b>Supplementary results</b>	<b>239</b>
<b>Normally incident compressional and shear waves</b>	<b>239</b>
<b>Compressional and shear waves incident at 30 degrees</b>	<b>261</b>
<b>Bibliography</b>	<b>288</b>

## List of Tables

Table		Page
1	Critical values for $kr$ for a multipole expansion of a plane compressional or shear wave	95
2	Total least squares residual as function of the number of basis functions in the multipole expansion	97
3	Comparison of the number of basis functions used here and in [9]	108
4	Figure numbers of the results for the cases (a) — (h) presented in chapter 3.4	128
5	Scaling factors of the far-field displacement plots for the cases (a) — (h) presented in chapter 3.4 and a P wave incident at 60 degrees	129
6	Scaling factors of the differential cross-section plots for the cases (a) — (h) presented in chapter 3.4 and P wave incident at 60 degrees	129
7	Scaling factors of the far-field displacement plots for the cases (a) — (h) presented in chapter 3.4 and a normally incident SV wave	130
8	Scaling factors of the differential cross-section plots for the cases (a) — (h) presented in chapter 3.4 and a normally incident SV wave	130
9	Figure numbers of the results for the cases (a) — (d) presented in Appendix E for a normally incident P and SV wave	240

10	Scaling factors of the far-field displacement plots for the cases (a) — (d) presented in Appendix E and a normally incident P wave	241
11	Scaling factors of the differential cross-section plots for the cases (a) — (d) presented in Appendix E and a normally incident P wave	241
12	Scaling factors of the far-field displacement plots for the cases (a) — (d) presented in Appendix E and a normally incident SV wave	242
13	Scaling factors of the differential cross-section plots for the cases (a) — (d) presented in Appendix E and a normally incident SV wave	242
14	Figure numbers of the results for the cases (a) — (d) presented in Appendix E for a P and SV wave incident at 30 degrees	261
15	Scaling factors of the far-field displacement plots for the cases (a) — (d) presented in Appendix E and a P wave incident at 30 degrees	262
16	Scaling factors of the differential cross-section plots for the cases (a) — (d) presented in Appendix E and a P wave incident at 30 degrees	262
17	Scaling factors of the far-field displacement plots for the cases (a) — (d) presented in Appendix E and a SV wave incident at 30 degrees	263
18	Scaling factors of the differential cross-section plots for the cases (a) — (d) presented in Appendix E and a SV wave incident at 30 degrees	263

## List of Figures

Figure		Page
1	Ultrasonic pulse-echo inspection of a corroded surface	51
2	Most common types of corrosion encountered in aircraft engineering	52
3	Pitting of stainless steel by acid-chloride solution	53
4	Chemical processes occurring during pitting corrosion	54
5	Superficial pitting and exfoliation corrosion of aluminium-copper-magnesium alloy	55
6	Crevice corrosion on a large stainless steel pipe flange	56
7	Intergranular stress-corrosion cracking of brass	57
8	Compressional plane wave incident on a plane surface with hemispherical surface disturbance representing a corrosion pit	64
9	Geometry of a cartesian and a spherical coordinate system	66
10	P wave incident on a stress free plane surface	76
11	SH wave incident on a stress free plane surface	76
12	SV wave incident on a stress free plane surface	78
13	Sampling path in the $x-z$ plane indicating the stress free surface of a half-space with hemispherical surface indentation	81
14	Unit normals and rotation angle $\alpha$ of a coordinate transformation in the $r-\theta$ plane	88
15	Surface obstacle with the shape of a section of a hemicircle	89
16	Surface obstacle with the shape of a semi-ellipse	90
17	Surface obstacle with the shape of a section of a semi-ellipse	91

18	Magnitude of normalised x-displacement, spherical vector harmonics approximation truncated to 12 terms, P wave	102
19	Phase of normalised x-displacement, spherical vector harmonics approximation truncated to 12 terms, P wave	102
20	Magnitude of normalised x-displacement, spherical vector harmonics approximation truncated to 16 terms, P wave	103
21	Phase of normalised x-displacement, spherical vector harmonics approximation truncated to 16 terms, P wave	103
22	Magnitude of normalised x-displacement, spherical vector harmonics approximation truncated to 20 terms, P wave	104
23	Phase of normalised x-displacement, spherical vector harmonics approximation truncated to 20 terms, P wave	104
24	Magnitude of normalised x-displacement, spherical vector harmonics approximation truncated to 12 terms, SV wave	105
25	Phase of normalised x-displacement, spherical vector harmonics approximation truncated to 12 terms, SV wave	105
26	Magnitude of normalised x-displacement, spherical vector harmonics approximation truncated to 16 terms, SV wave	106
27	Phase of normalised x-displacement, spherical vector harmonics approximation truncated to 16 terms, SV wave	106
28	Magnitude of normalised x-displacement, spherical vector harmonics approximation truncated to 20 terms, SV wave	107
29	Phase of normalised x-displacement, spherical vector harmonics approximation truncated to 20 terms, SV wave	107

- 30 Amplitude of the surface displacements in the  $x-z$  plane for a compressional wave normally incident on a hemispherical surface indentation with  $\frac{2a}{\lambda_p} = 0.25$  and Poisson's ratio  $\nu = 0.25$ . Top : result obtained by the present study, bottom : result published in [9]. 112
- 31 Amplitude of the surface displacements in the  $x-z$  plane for a compressional wave normally incident on a hemispherical surface indentation with  $\frac{2a}{\lambda_p} = 0.5$  and Poisson's ratio  $\nu = 0.25$ . Top : result obtained by the present study, bottom : result published in [9]. 113
- 32 Amplitude of the surface displacements in the  $x-z$  plane for a compressional wave normally incident on a hemispherical surface indentation with  $\frac{2a}{\lambda_p} = 0.75$  and Poisson's ratio  $\nu = 0.25$ . Top : result obtained by the present study, bottom : result published in [9]. 114
- 33 Amplitude of the surface displacements in the  $x-z$  plane for a compressional wave normally incident on a hemispherical surface indentation with  $\frac{2a}{\lambda_p} = 1.5$  and Poisson's ratio  $\nu = 0.25$ . Top : result obtained by the present study, bottom : result published in [9]. 115
- 34 Amplitude of the surface displacements in the  $x-z$  plane for a compressional wave incident under 60 degrees on to a hemispherical surface indentation with  $\frac{2a}{\lambda_s} = 1.0$  and Poisson's ratio  $\nu = 0.25$ . Top : result obtained by the present study, bottom : result published in [8]. 116

35	Amplitude of the surface displacements in the $y-z$ plane for a compressional wave incident under 60 degrees on to a hemispherical surface indentation with $\frac{2a}{\lambda_s} = 1.0$ and Poisson's ratio $\nu = 0.25$ . Top : result obtained by the present study, bottom : result published in [8].	117
36	Surface displacements $u_x$ for a compressional wave incident under 30 degrees on to a hemispherical surface indentation with $\frac{2a}{\lambda_s} = 0.5$ and Poisson's ratio $\nu = 0.25$ , published in [104]	118
37	Surface displacements $u_y$ for a compressional wave incident under 30 degrees on to a hemispherical surface indentation with $\frac{2a}{\lambda_s} = 0.5$ and Poisson's ratio $\nu = 0.25$ , published in [104]	118
38	Surface displacements $u_z$ for a compressional wave incident under 30 degrees on to a hemispherical surface indentation with $\frac{2a}{\lambda_s} = 0.5$ and Poisson's ratio $\nu = 0.25$ , published in [104]	119
39	Surface displacements $u_x$ for a horizontally polarised shear wave incident under 60 degrees on to a hemispherical surface indentation with $\frac{2a}{\lambda_s} = 0.5$ and Poisson's ratio $\nu = 0.25$ , published in [104]	119
40	Surface displacements $u_y$ for a horizontally polarised shear wave incident under 60 degrees on to a hemispherical surface indentation with $\frac{2a}{\lambda_s} = 0.5$ and Poisson's ratio $\nu = 0.25$ , published in [104]	120
41	Surface displacements $u_z$ for a horizontally polarised shear wave incident under 60 degrees on to a hemispherical surface indentation with $\frac{2a}{\lambda_s} = 0.5$ and Poisson's ratio $\nu = 0.25$ , published in [104]	120

42	Surface displacements in the $x-z$ plane for a compressional wave incident under 30 degrees on to a hemispherical surface indentation with $\frac{2a}{\lambda_s} = 0.5$ and Poisson's ratio $\nu = 0.25$	121
43	Surface displacements in the $y-z$ plane for a compressional wave incident under 30 degrees on to a hemispherical surface indentation with $\frac{2a}{\lambda_s} = 0.5$ and Poisson's ratio $\nu = 0.25$	121
44	Surface displacements in the $x-z$ plane for a horizontally polarised shear wave incident under 60 degrees on to a hemispherical surface indentation with $\frac{2a}{\lambda_s} = 0.5$ and Poisson's ratio $\nu = 0.25$ .	122
45	Surface displacements in the $y-z$ plane for a horizontally polarised shear wave incident under 60 degrees on to a hemispherical surface indentation with $\frac{2a}{\lambda_s} = 0.5$ and Poisson's ratio $\nu = 0.25$	122
46	Surface displacements in the $x-z$ plane for a shear wave normally incident on to a hemispherical surface indentation with $\frac{2a}{\lambda_s} = 0.5$ and Poisson's ratio $\nu = 0.25$	123
47	Surface displacements in the $y-z$ plane for a shear wave normally incident on to a hemispherical surface indentation with $\frac{2a}{\lambda_s} = 0.5$ and Poisson's ratio $\nu = 0.25$	123
48	Horizontal and vertical surface displacements for a compressional wave and a vertically polarised shear wave incident on to a semi-cylindrical canyon with $\frac{2a}{\lambda_s} = 0.5$ and Poisson's ratio $\nu = 0.33$ .	124

49	Surface displacements for a horizontally polarised shear wave normally incident on to a semi-cylindrical canyon. The diameter to shear wavelength ratio $\frac{2a}{\lambda_s} = \eta$ is varied from 0.25 to 2.0.	125
50	Surface displacements for a horizontally polarised shear wave incident under 60 degrees on to a semi-cylindrical canyon. The diameter to shear wavelength ratio $\frac{2a}{\lambda_s} = \eta$ is varied from 0.25 to 2.0.	126
51	Amplitude of the surface displacements in the x-z plane for a P wave incident under 60 degrees on to a hemispherical surface indentation with $\frac{2a}{\lambda_p} = 0.5$ and $\nu = 0.34$	131
52	Amplitude of the surface displacements in the y-z plane for a P wave incident under 60 degrees on to a hemispherical surface indentation with $\frac{2a}{\lambda_p} = 0.5$ and $\nu = 0.34$	131
53	Amplitude of the far-field displacements in the x-z plane for a P wave incident under 60 degrees on to a hemispherical surface indentation with $\frac{2a}{\lambda_p} = 0.5$ and $\nu = 0.34$	132
54	Amplitude of the far-field displacements in the y-z plane for a P wave incident under 60 degrees on to a hemispherical surface indentation with $\frac{2a}{\lambda_p} = 0.5$ and $\nu = 0.34$	132
55	Differential cross-section in the x-z plane for a P wave incident under 60 degrees on to a hemispherical surface indentation with $\frac{2a}{\lambda_p} = 0.5$ and $\nu = 0.34$	133
56	Differential cross-section in the y-z plane for a P wave incident under 60 degrees on to a hemispherical surface indentation with $\frac{2a}{\lambda_p} = 0.5$ and $\nu = 0.34$	133

- 57 Amplitude of the surface displacements in the  $x-z$  plane for a P wave incident under 60 degrees on to a surface indentation with the shape of a segment of a hemisphere, where  $\frac{2a}{\lambda_p} = 1.0$ ,  $\frac{d}{a} = 0.25$  and  $\nu = 0.34$  134
- 58 Amplitude of the surface displacements in the  $y-z$  plane for a P wave incident under 60 degrees on to a surface indentation with the shape of a segment of a hemisphere, where  $\frac{2a}{\lambda_p} = 1.0$ ,  $\frac{d}{a} = 0.25$  and  $\nu = 0.34$  134
- 59 Amplitude of the far-field displacements in the  $x-z$  plane for a P wave incident under 60 degrees on to a surface indentation with the shape of a segment of a hemisphere, where  $\frac{2a}{\lambda_p} = 1.0$ ,  $\frac{d}{a} = 0.25$  and  $\nu = 0.34$  135
- 60 Amplitude of the far-field displacements in the  $y-z$  plane for a P wave incident under 60 degrees on to a surface indentation with the shape of a segment of a hemisphere, where  $\frac{2a}{\lambda_p} = 1.0$ ,  $\frac{d}{a} = 0.25$  and  $\nu = 0.34$  135
- 61 Differential cross-section in the  $x-z$  plane for a P wave incident under 60 degrees on to a surface indentation with the shape of a segment of a hemisphere, where  $\frac{2a}{\lambda_p} = 1.0$ ,  $\frac{d}{a} = 0.25$  and  $\nu = 0.34$  136
- 62 Differential cross-section in the  $y-z$  plane for a P wave incident under 60 degrees on to a surface indentation with the shape of a segment of a hemisphere, where  $\frac{2a}{\lambda_p} = 1.0$ ,  $\frac{d}{a} = 0.25$  and  $\nu = 0.34$  136

- 63 Amplitude of the surface displacements in the  $x-z$  plane for a P wave incident under 60 degrees on to a surface indentation with the shape of a semi-ellipsoid, where  $\frac{2a}{\lambda_p} = 1.0$ ,  $\frac{d}{a} = 0.25$  and  $\nu = 0.34$  137
- 64 Amplitude of the surface displacements in the  $y-z$  plane for a P wave incident under 60 degrees on to a surface indentation with the shape of a semi-ellipsoid, where  $\frac{2a}{\lambda_p} = 1.0$ ,  $\frac{d}{a} = 0.25$  and  $\nu = 0.34$  137
- 65 Amplitude of the far-field displacements in the  $x-z$  plane for a P wave incident under 60 degrees on to a surface indentation with the shape of a semi-ellipsoid, where  $\frac{2a}{\lambda_p} = 1.0$ ,  $\frac{d}{a} = 0.25$  and  $\nu = 0.34$  138
- 66 Amplitude of the far-field displacements in the  $y-z$  plane for a P wave incident under 60 degrees on to a surface indentation with the shape of a semi-ellipsoid, where  $\frac{2a}{\lambda_p} = 1.0$ ,  $\frac{d}{a} = 0.25$  and  $\nu = 0.34$  138
- 67 Differential cross-section in the  $x-z$  plane for a P wave incident under 60 degrees on to a surface indentation with the shape of a semi-ellipsoid, where  $\frac{2a}{\lambda_p} = 1.0$ ,  $\frac{d}{a} = 0.25$  and  $\nu = 0.34$  139
- 68 Differential cross-section in the  $y-z$  plane for a P wave incident under 60 degrees on to a surface indentation with the shape of a semi-ellipsoid, where  $\frac{2a}{\lambda_p} = 1.0$ ,  $\frac{d}{a} = 0.25$  and  $\nu = 0.34$  139

- 69 Amplitude of the surface displacements in the  $x-z$  plane for a P wave incident under 60 degrees on to a surface indentation with the shape of a segment of a hemisphere, where  $\frac{2a}{\lambda_p} = 1.0$ ,  $\frac{d}{a} = 0.5$  and  $\nu = 0.34$  140
- 70 Amplitude of the surface displacements in the  $y-z$  plane for a P wave incident under 60 degrees on to a surface indentation with the shape of a segment of a hemisphere, where  $\frac{2a}{\lambda_p} = 1.0$ ,  $\frac{d}{a} = 0.5$  and  $\nu = 0.34$  140
- 71 Amplitude of the far-field displacements in the  $x-z$  plane for a P wave incident under 60 degrees on to a surface indentation with the shape of a segment of a hemisphere, where  $\frac{2a}{\lambda_p} = 1.0$ ,  $\frac{d}{a} = 0.5$  and  $\nu = 0.34$  141
- 72 Amplitude of the far-field displacements in the  $y-z$  plane for a P wave incident under 60 degrees on to a surface indentation with the shape of a segment of a hemisphere, where  $\frac{2a}{\lambda_p} = 1.0$ ,  $\frac{d}{a} = 0.5$  and  $\nu = 0.34$  141
- 73 Differential cross-section in the  $x-z$  plane for a P wave incident under 60 degrees on to a surface indentation with the shape of a segment of a hemisphere, where  $\frac{2a}{\lambda_p} = 1.0$ ,  $\frac{d}{a} = 0.5$  and  $\nu = 0.34$  142
- 74 Differential cross-section in the  $y-z$  plane for a P wave incident under 60 degrees on to a surface indentation with the shape of a segment of a hemisphere, where  $\frac{2a}{\lambda_p} = 1.0$ ,  $\frac{d}{a} = 0.5$  and  $\nu = 0.34$  142

- 75 Amplitude of the surface displacements in the  $x-z$  plane for a P wave incident under 60 degrees on to a surface indentation with the shape of a semi-ellipsoid, where  $\frac{2a}{\lambda_p} = 1.0$ ,  $\frac{d}{a} = 0.5$  and  $\nu = 0.34$  143
- 76 Amplitude of the surface displacements in the  $y-z$  plane for a P wave incident under 60 degrees on to a surface indentation with the shape of a semi-ellipsoid, where  $\frac{2a}{\lambda_p} = 1.0$ ,  $\frac{d}{a} = 0.5$  and  $\nu = 0.34$  143
- 77 Amplitude of the far-field displacements in the  $x-z$  plane for a P wave incident under 60 degrees on to a surface indentation with the shape of a semi-ellipsoid, where  $\frac{2a}{\lambda_p} = 1.0$ ,  $\frac{d}{a} = 0.5$  and  $\nu = 0.34$  144
- 78 Amplitude of the far-field displacements in the  $y-z$  plane for a P wave incident under 60 degrees on to a surface indentation with the shape of a semi-ellipsoid, where  $\frac{2a}{\lambda_p} = 1.0$ ,  $\frac{d}{a} = 0.5$  and  $\nu = 0.34$  144
- 79 Differential cross-section in the  $x-z$  plane for a P wave incident under 60 degrees on to a surface indentation with the shape of a semi-ellipsoid, where  $\frac{2a}{\lambda_p} = 1.0$ ,  $\frac{d}{a} = 0.5$  and  $\nu = 0.34$  145
- 80 Differential cross-section in the  $y-z$  plane for a P wave incident under 60 degrees on to a surface indentation with the shape of a semi-ellipsoid, where  $\frac{2a}{\lambda_p} = 1.0$ ,  $\frac{d}{a} = 0.5$  and  $\nu = 0.34$  145

- 81 Amplitude of the surface displacements in the  $x-z$  plane for a P wave incident under 60 degrees on to a surface indentation with the shape of a segment of a hemisphere, where  $\frac{2a}{\lambda_p} = 1.0$ ,  $\frac{d}{a} = 0.75$  and  $\nu = 0.34$  146
- 82 Amplitude of the surface displacements in the  $y-z$  plane for a P wave incident under 60 degrees on to a surface indentation with the shape of a segment of a hemisphere, where  $\frac{2a}{\lambda_p} = 1.0$ ,  $\frac{d}{a} = 0.75$  and  $\nu = 0.34$  146
- 83 Amplitude of the far-field displacements in the  $x-z$  plane for a P wave incident under 60 degrees on to a surface indentation with the shape of a segment of a hemisphere, where  $\frac{2a}{\lambda_p} = 1.0$ ,  $\frac{d}{a} = 0.75$  and  $\nu = 0.34$  147
- 84 Amplitude of the far-field displacements in the  $y-z$  plane for a P wave incident under 60 degrees on to a surface indentation with the shape of a segment of a hemisphere, where  $\frac{2a}{\lambda_p} = 1.0$ ,  $\frac{d}{a} = 0.75$  and  $\nu = 0.34$  147
- 85 Differential cross-section in the  $x-z$  plane for a P wave incident under 60 degrees on to a surface indentation with the shape of a segment of a hemisphere, where  $\frac{2a}{\lambda_p} = 1.0$ ,  $\frac{d}{a} = 0.75$  and  $\nu = 0.34$  148
- 86 Differential cross-section in the  $y-z$  plane for a P wave incident under 60 degrees on to a surface indentation with the shape of a segment of a hemisphere, where  $\frac{2a}{\lambda_p} = 1.0$ ,  $\frac{d}{a} = 0.75$  and  $\nu = 0.34$  148

- 87 Amplitude of the surface displacements in the  $x-z$  plane for a P wave incident under 60 degrees on to a surface indentation with the shape of a semi-ellipsoid, where  $\frac{2a}{\lambda_p} = 1.0$ ,  $\frac{d}{a} = 0.75$  and  $\nu = 0.34$  149
- 88 Amplitude of the surface displacements in the  $y-z$  plane for a P wave incident under 60 degrees on to a surface indentation with the shape of a semi-ellipsoid, where  $\frac{2a}{\lambda_p} = 1.0$ ,  $\frac{d}{a} = 0.75$  and  $\nu = 0.34$  149
- 89 Amplitude of the far-field displacements in the  $x-z$  plane for a P wave incident under 60 degrees on to a surface indentation with the shape of a semi-ellipsoid, where  $\frac{2a}{\lambda_p} = 1.0$ ,  $\frac{d}{a} = 0.75$  and  $\nu = 0.34$  150
- 90 Amplitude of the far-field displacements in the  $y-z$  plane for a P wave incident under 60 degrees on to a surface indentation with the shape of a semi-ellipsoid, where  $\frac{2a}{\lambda_p} = 1.0$ ,  $\frac{d}{a} = 0.75$  and  $\nu = 0.34$  150
- 91 Differential cross-section in the  $x-z$  plane for a P wave incident under 60 degrees on to a surface indentation with the shape of a semi-ellipsoid, where  $\frac{2a}{\lambda_p} = 1.0$ ,  $\frac{d}{a} = 0.75$  and  $\nu = 0.34$  151
- 92 Differential cross-section in the  $y-z$  plane for a P wave incident under 60 degrees on to a surface indentation with the shape of a semi-ellipsoid, where  $\frac{2a}{\lambda_p} = 1.0$ ,  $\frac{d}{a} = 0.75$  and  $\nu = 0.34$  151
- 93 Amplitude of the surface displacements in the  $x-z$  plane for a P wave incident under 60 degrees on to a hemispherical surface indentation with  $\frac{2a}{\lambda_p} = 1.0$  and  $\nu = 0.34$  152

94	Amplitude of the surface displacements in the $y-z$ plane for a P wave incident under 60 degrees on to a hemispherical surface indentation with $\frac{2a}{\lambda_p} = 1.0$ and $\nu = 0.34$	152
95	Amplitude of the far-field displacements in the $x-z$ plane for a P wave incident under 60 degrees on to a hemispherical surface indentation with $\frac{2a}{\lambda_p} = 1.0$ and $\nu = 0.34$	153
96	Amplitude of the far-field displacements in the $y-z$ plane for a P wave incident under 60 degrees on to a hemispherical surface indentation with $\frac{2a}{\lambda_p} = 1.0$ and $\nu = 0.34$	153
97	Differential cross-section in the $x-z$ plane for a P wave incident under 60 degrees on to a hemispherical surface indentation with $\frac{2a}{\lambda_p} = 1.0$ and $\nu = 0.34$	154
98	Differential cross-section in the $y-z$ plane for a P wave incident under 60 degrees on to a hemispherical surface indentation with $\frac{2a}{\lambda_p} = 1.0$ and $\nu = 0.34$	154
99	Amplitude of the surface displacements in the $x-z$ plane for a SV wave normally incident on to a hemispherical surface indentation with $\frac{2a}{\lambda_s} = 0.5$ and $\nu = 0.34$	155
100	Amplitude of the surface displacements in the $y-z$ plane for a SV wave normally incident on to a hemispherical surface indentation with $\frac{2a}{\lambda_s} = 0.5$ and $\nu = 0.34$	155
101	Amplitude of the far-field displacements in the $x-z$ plane for a SV wave normally incident on to a hemispherical surface indentation with $\frac{2a}{\lambda_s} = 0.5$ and $\nu = 0.34$	156
102	Amplitude of the far-field displacements in the $y-z$ plane for a SV wave normally incident on to a hemispherical surface indentation with $\frac{2a}{\lambda_s} = 0.5$ and $\nu = 0.34$	156

- 103 Differential cross-section in the  $x-z$  plane for a SV wave normally incident on to a hemispherical surface indentation with  $\frac{2a}{\lambda_s} = 0.5$  and  $\nu = 0.34$  157
- 104 Differential cross-section in the  $y-z$  plane for a SV wave normally incident on to a hemispherical surface indentation with  $\frac{2a}{\lambda_s} = 0.5$  and  $\nu = 0.34$  157
- 105 Amplitude of the surface displacements in the  $x-z$  plane for a SV wave normally incident on to a surface indentation with the shape of a segment of a hemisphere, where  $\frac{2a}{\lambda_s} = 1.0$ ,  $\frac{d}{a} = 0.25$  and  $\nu = 0.34$  158
- 106 Amplitude of the surface displacements in the  $y-z$  plane for a SV wave normally incident on to a surface indentation with the shape of a segment of a hemisphere, where  $\frac{2a}{\lambda_s} = 1.0$ ,  $\frac{d}{a} = 0.25$  and  $\nu = 0.34$  158
- 107 Amplitude of the far-field displacements in the  $x-z$  plane for a SV wave normally incident on to a surface indentation with the shape of a segment of a hemisphere, where  $\frac{2a}{\lambda_s} = 1.0$ ,  $\frac{d}{a} = 0.25$  and  $\nu = 0.34$  159
- 108 Amplitude of the far-field displacements in the  $y-z$  plane for a SV wave normally incident on to a surface indentation with the shape of a segment of a hemisphere, where  $\frac{2a}{\lambda_s} = 1.0$ ,  $\frac{d}{a} = 0.25$  and  $\nu = 0.34$  159
- 109 Differential cross-section in the  $x-z$  plane for a SV wave normally incident on to a surface indentation with the shape of a segment of a hemisphere, where  $\frac{2a}{\lambda_s} = 1.0$ ,  $\frac{d}{a} = 0.25$  and  $\nu = 0.34$  160

- 110 Differential cross-section in the  $y-z$  plane for a SV wave normally incident on to a surface indentation with the shape of a segment of a hemisphere, where  $\frac{2a}{\lambda_s} = 1.0$ ,  $\frac{d}{a} = 0.25$  and  $\nu = 0.34$  160
- 111 Amplitude of the surface displacements in the  $x-z$  plane for a SV wave normally incident on to a surface indentation with the shape of a semi-ellipsoid, where  $\frac{2a}{\lambda_s} = 1.0$ ,  $\frac{d}{a} = 0.25$  and  $\nu = 0.34$  161
- 112 Amplitude of the surface displacements in the  $y-z$  plane for a SV wave normally incident on to a surface indentation with the shape of a semi-ellipsoid, where  $\frac{2a}{\lambda_s} = 1.0$ ,  $\frac{d}{a} = 0.25$  and  $\nu = 0.34$  161
- 113 Amplitude of the far-field displacements in the  $x-z$  plane for a SV wave normally incident on to a surface indentation with the shape of a semi-ellipsoid, where  $\frac{2a}{\lambda_s} = 1.0$ ,  $\frac{d}{a} = 0.25$  and  $\nu = 0.34$  162
- 114 Amplitude of the far-field displacements in the  $y-z$  plane for a SV wave normally incident on to a surface indentation with the shape of a semi-ellipsoid, where  $\frac{2a}{\lambda_s} = 1.0$ ,  $\frac{d}{a} = 0.25$  and  $\nu = 0.34$  162
- 115 Differential cross-section in the  $x-z$  plane for a SV wave normally incident on to a surface indentation with the shape of a semi-ellipsoid, where  $\frac{2a}{\lambda_s} = 1.0$ ,  $\frac{d}{a} = 0.25$  and  $\nu = 0.34$  163
- 116 Differential cross-section in the  $y-z$  plane for a SV wave normally incident on to a surface indentation with the shape of a semi-ellipsoid, where  $\frac{2a}{\lambda_s} = 1.0$ ,  $\frac{d}{a} = 0.25$  and  $\nu = 0.34$  163

- 117 Amplitude of the surface displacements in the  $x-z$  plane for a SV wave normally incident on to a surface indentation with the shape of a segment of a hemisphere, where  $\frac{2a}{\lambda_s} = 1.0$ ,  $\frac{d}{a} = 0.5$  and  $\nu = 0.34$  164
- 118 Amplitude of the surface displacements in the  $y-z$  plane for a SV wave normally incident on to a surface indentation with the shape of a segment of a hemisphere, where  $\frac{2a}{\lambda_s} = 1.0$ ,  $\frac{d}{a} = 0.5$  and  $\nu = 0.34$  164
- 119 Amplitude of the far-field displacements in the  $x-z$  plane for a SV wave normally incident on to a surface indentation with the shape of a segment of a hemisphere, where  $\frac{2a}{\lambda_s} = 1.0$ ,  $\frac{d}{a} = 0.5$  and  $\nu = 0.34$  165
- 120 Amplitude of the far-field displacements in the  $y-z$  plane for a SV wave normally incident on to a surface indentation with the shape of a segment of a hemisphere, where  $\frac{2a}{\lambda_s} = 1.0$ ,  $\frac{d}{a} = 0.5$  and  $\nu = 0.34$  165
- 121 Differential cross-section in the  $x-z$  plane for a SV wave normally incident on to a surface indentation with the shape of a segment of a hemisphere, where  $\frac{2a}{\lambda_s} = 1.0$ ,  $\frac{d}{a} = 0.5$  and  $\nu = 0.34$  166
- 122 Differential cross-section in the  $y-z$  plane for a SV wave normally incident on to a surface indentation with the shape of a segment of a hemisphere, where  $\frac{2a}{\lambda_s} = 1.0$ ,  $\frac{d}{a} = 0.5$  and  $\nu = 0.34$  166

- 123 Amplitude of the surface displacements in the  $x-z$  plane for a SV wave normally incident on to a surface indentation with the shape of a semi-ellipsoid, where  $\frac{2a}{\lambda_s} = 1.0$ ,  $\frac{d}{a} = 0.5$  and  $\nu = 0.34$  167
- 124 Amplitude of the surface displacements in the  $y-z$  plane for a SV wave normally incident on to a surface indentation with the shape of a semi-ellipsoid, where  $\frac{2a}{\lambda_s} = 1.0$ ,  $\frac{d}{a} = 0.5$  and  $\nu = 0.34$  167
- 125 Amplitude of the far-field displacements in the  $x-z$  plane for a SV wave normally incident on to a surface indentation with the shape of a semi-ellipsoid, where  $\frac{2a}{\lambda_s} = 1.0$ ,  $\frac{d}{a} = 0.5$  and  $\nu = 0.34$  168
- 126 Amplitude of the far-field displacements in the  $y-z$  plane for a SV wave normally incident on to a surface indentation with the shape of a semi-ellipsoid, where  $\frac{2a}{\lambda_s} = 1.0$ ,  $\frac{d}{a} = 0.5$  and  $\nu = 0.34$  168
- 127 Differential cross-section in the  $x-z$  plane for a SV wave normally incident on to a surface indentation with the shape of a semi-ellipsoid, where  $\frac{2a}{\lambda_s} = 1.0$ ,  $\frac{d}{a} = 0.5$  and  $\nu = 0.34$  169
- 128 Differential cross-section in the  $y-z$  plane for a SV wave normally incident on to a surface indentation with the shape of a semi-ellipsoid, where  $\frac{2a}{\lambda_s} = 1.0$ ,  $\frac{d}{a} = 0.5$  and  $\nu = 0.34$  169
- 129 Amplitude of the surface displacements in the  $x-z$  plane for a SV wave normally incident on to a surface indentation with the shape of a segment of a hemisphere, where  $\frac{2a}{\lambda_s} = 1.0$ ,  $\frac{d}{a} = 0.75$  and  $\nu = 0.34$  170

- 130 Amplitude of the surface displacements in the  $y-z$  plane for a SV wave normally incident on to a surface indentation with the shape of a segment of a hemisphere, where  $\frac{2a}{\lambda_s} = 1.0$ ,  $\frac{d}{a} = 0.75$  and  $\nu = 0.34$  170
- 131 Amplitude of the far-field displacements in the  $x-z$  plane for a SV wave normally incident on to a surface indentation with the shape of a segment of a hemisphere, where  $\frac{2a}{\lambda_s} = 1.0$ ,  $\frac{d}{a} = 0.75$  and  $\nu = 0.34$  171
- 132 Amplitude of the far-field displacements in the  $y-z$  plane for a SV wave normally incident on to a surface indentation with the shape of a segment of a hemisphere, where  $\frac{2a}{\lambda_s} = 1.0$ ,  $\frac{d}{a} = 0.75$  and  $\nu = 0.34$  171
- 133 Differential cross-section in the  $x-z$  plane for a SV wave normally incident on to a surface indentation with the shape of a segment of a hemisphere, where  $\frac{2a}{\lambda_s} = 1.0$ ,  $\frac{d}{a} = 0.75$  and  $\nu = 0.34$  172
- 134 Differential cross-section in the  $y-z$  plane for a SV wave normally incident on to a surface indentation with the shape of a segment of a hemisphere, where  $\frac{2a}{\lambda_s} = 1.0$ ,  $\frac{d}{a} = 0.75$  and  $\nu = 0.34$  172
- 135 Amplitude of the surface displacements in the  $x-z$  plane for a SV wave normally incident on to a surface indentation with the shape of a semi-ellipsoid, where  $\frac{2a}{\lambda_s} = 1.0$ ,  $\frac{d}{a} = 0.75$  and  $\nu = 0.34$  173

- 136 Amplitude of the surface displacements in the  $y-z$  plane for a SV wave normally incident on to a surface indentation with the shape of a semi-ellipsoid, where  $\frac{2a}{\lambda_s} = 1.0$ ,  $\frac{d}{a} = 0.75$  and  $\nu = 0.34$  173
- 137 Amplitude of the far-field displacements in the  $x-z$  plane for a SV wave normally incident on to a surface indentation with the shape of a semi-ellipsoid, where  $\frac{2a}{\lambda_s} = 1.0$ ,  $\frac{d}{a} = 0.75$  and  $\nu = 0.34$  174
- 138 Amplitude of the far-field displacements in the  $y-z$  plane for a SV wave normally incident on to a surface indentation with the shape of a semi-ellipsoid, where  $\frac{2a}{\lambda_s} = 1.0$ ,  $\frac{d}{a} = 0.75$  and  $\nu = 0.34$  174
- 139 Differential cross-section in the  $x-z$  plane for a SV wave normally incident on to a surface indentation with the shape of a semi-ellipsoid, where  $\frac{2a}{\lambda_s} = 1.0$ ,  $\frac{d}{a} = 0.75$  and  $\nu = 0.34$  175
- 140 Differential cross-section in the  $y-z$  plane for a SV wave normally incident on to a surface indentation with the shape of a semi-ellipsoid, where  $\frac{2a}{\lambda_s} = 1.0$ ,  $\frac{d}{a} = 0.75$  and  $\nu = 0.34$  175
- 141 Amplitude of the surface displacements in the  $x-z$  plane for a SV wave normally incident on to a hemispherical surface indentation with  $\frac{2a}{\lambda_s} = 1.0$  and  $\nu = 0.34$  176
- 142 Amplitude of the surface displacements in the  $y-z$  plane for a SV wave normally incident on to a hemispherical surface indentation with  $\frac{2a}{\lambda_s} = 1.0$  and  $\nu = 0.34$  176
- 143 Amplitude of the far-field displacements in the  $x-z$  plane for a SV wave normally incident on to a hemispherical surface indentation with  $\frac{2a}{\lambda_s} = 1.0$  and  $\nu = 0.34$  177

144	Amplitude of the far-field displacements in the $y-z$ plane for a SV wave normally incident on to a hemispherical surface indentation with $\frac{2a}{\lambda_s} = 1.0$ and $\nu = 0.34$	177
145	Differential cross-section in the $x-z$ plane for a SV wave normally incident on to a hemispherical surface indentation with $\frac{2a}{\lambda_s} = 1.0$ and $\nu = 0.34$	178
146	Differential cross-section in the $y-z$ plane for a SV wave normally incident on to a hemispherical surface indentation with $\frac{2a}{\lambda_s} = 1.0$ and $\nu = 0.34$	178
147	Shape and dimensions of the aluminium test block in top view and side view	180
148	Experimental configuration for the measurement of the ultrasonic field scattered from a hemispherical surface indentation in an aluminium block	181
149	Amplitude of the far-field displacements for a P wave normally incident on to a hemispherical surface indentation in an aluminium half-space with $\frac{2a}{\lambda_p} = 0.25$ and $\nu = 0.34$	185
150	Amplitude of the far-field displacements for a P wave normally incident on to a hemispherical surface indentation in an aluminium half-space with $\frac{2a}{\lambda_p} = 0.5$ and $\nu = 0.34$	185
151	Amplitude of the far-field displacements in the $x-z$ plane for a SV wave normally incident on to a hemispherical surface indentation in an aluminium half-space with $\frac{2a}{\lambda_s} = 1.0$ and $\nu = 0.34$	186

- 152 Amplitude of the far-field displacements in the  $y-z$  plane  
for a SV wave normally incident on to a hemispherical  
surface indentation in an aluminium half-space with  
 $\frac{2a}{\lambda_s} = 1.0$  and  $\nu = 0.34$  186
- 153 Amplitude of the far-field displacements in the  $x-z$  plane  
for a SV wave normally incident on to a hemispherical  
surface indentation in an aluminium half-space with  
 $\frac{2a}{\lambda_s} = 2.0$  and  $\nu = 0.34$  187
- 154 Amplitude of the far-field displacements in the  $y-z$  plane  
for a SV wave normally incident on to a hemispherical  
surface indentation in an aluminium half-space with  
 $\frac{2a}{\lambda_s} = 2.0$  and  $\nu = 0.34$  187
- 155 Rayleigh wave amplitude as function of the azimuth angle  $\phi$   
for a compressional wave with a frequency of 1 MHz normally  
incident on to a small hemispherical surface indentation with  
a diameter of 1.6 mm. 188
- 156 Rayleigh wave amplitude as function of the azimuth angle  $\phi$   
for a compressional wave with a frequency of 1 MHz normally  
incident on to a large hemispherical surface indentation with  
a diameter of 3.2 mm. 189
- 157 Rayleigh wave amplitude as function of the azimuth angle  $\phi$   
for a shear wave with a frequency of 2 MHz normally  
incident on to a small hemispherical surface indentation  
with a diameter of 1.6 mm. 190

158	Rayleigh wave amplitude as function of the azimuth angle $\phi$ for a shear wave with a frequency of 2 MHz normally incident on to a large hemispherical surface indentation with a diameter of 3.2 mm.	191
159	Rf trace of a compressional wave pulse reflected back normally from a plane surface with a hemispherical surface indentation of 3.2 mm diameter for a normally incident compressional wave pulse with a centre frequency of 1 MHz	194
160	Frequency spectrum of a compressional wave pulse reflected back normally from a plane surface with a hemispherical surface indentation of 3.2 mm diameter for a normally incident compressional wave pulse with a centre frequency of 1 MHz	195
161	Rf trace of a shear wave pulse reflected back normally from a plane surface with a hemispherical surface indentation of 3.2 mm diameter for a normally incident shear wave pulse with a centre frequency of 2 MHz	196
162	Frequency spectrum of a shear wave pulse reflected back normally from a plane surface with a hemispherical surface indentation of 3.2 mm diameter for a normally incident shear wave pulse with a centre frequency of 2 MHz	197
163	Ultrasonic inspection of a corrosion pit using a pulse-echo configuration with an ultrasound pulse incident at $\alpha = 45^\circ$	204
164	Ultrasonic inspection of a corrosion pit using a pitch-catch tandem configuration	204

165	Amplitude of the surface displacements for a P wave normally incident on to a hemispherical surface indentation with $\frac{2a}{\lambda_P} = 0.5$ and $\nu = 0.25$	243
166	Amplitude of the surface displacements for a P wave normally incident on to a hemispherical surface indentation with $\frac{2a}{\lambda_P} = 1.0$ and $\nu = 0.25$	243
167	Amplitude of the far-field displacements for a P wave normally incident on to a hemispherical surface indentation with $\frac{2a}{\lambda_P} = 0.5$ and $\nu = 0.25$	244
168	Amplitude of the far-field displacements for a P wave normally incident on to a hemispherical surface indentation with $\frac{2a}{\lambda_P} = 1.0$ and $\nu = 0.25$	244
169	Differential cross-section for a P wave normally incident on to a hemispherical surface indentation with $\frac{2a}{\lambda_P} = 0.5$ and $\nu = 0.25$	245
170	Differential cross-section for a P wave normally incident on to a hemispherical surface indentation with $\frac{2a}{\lambda_P} = 1.0$ and $\nu = 0.25$	245
171	Amplitude of the surface displacements for a P wave normally incident on to a surface indentation with the shape of a segment of a hemisphere, where $\frac{2a}{\lambda_P} = 1.0$ , $\frac{d}{a} = 0.5$ and $\nu = 0.25$	246
172	Amplitude of the surface displacements for a P wave normally incident on to a surface indentation with the shape of a semi-ellipsoid, where $\frac{2a}{\lambda_P} = 1.0$ , $\frac{d}{a} = 0.5$ and $\nu = 0.25$	246

- 173 Amplitude of the far-field displacements for a P wave normally incident on to a surface indentation with the shape of a segment of a hemisphere, where  $\frac{2a}{\lambda_p} = 1.0$ ,  $\frac{d}{a} = 0.5$  and  $\nu = 0.25$  247
- 174 Amplitude of the far-field displacements for a P wave normally incident on to a surface indentation with the shape of a semi-ellipsoid, where  $\frac{2a}{\lambda_p} = 1.0$ ,  $\frac{d}{a} = 0.5$  and  $\nu = 0.25$  247
- 175 Differential cross-section for a P wave normally incident on to a surface indentation with the shape of a segment of a hemisphere, where  $\frac{2a}{\lambda_p} = 1.0$ ,  $\frac{d}{a} = 0.5$  and  $\nu = 0.25$  248
- 176 Differential cross-section for a P wave normally incident on to a surface indentation with the shape of a semi-ellipsoid, where  $\frac{2a}{\lambda_p} = 1.0$ ,  $\frac{d}{a} = 0.5$  and  $\nu = 0.25$  248
- 177 Amplitude of the surface displacements in the  $x-z$  plane for a SV wave normally incident on to a hemispherical surface indentation with  $\frac{2a}{\lambda_s} = 0.5$  and  $\nu = 0.25$  249
- 178 Amplitude of the surface displacements in the  $y-z$  plane for a SV wave normally incident on to a hemispherical surface indentation with  $\frac{2a}{\lambda_s} = 0.5$  and  $\nu = 0.25$  249
- 179 Amplitude of the far-field displacements in the  $x-z$  plane for a SV wave normally incident on to a hemispherical surface indentation with  $\frac{2a}{\lambda_s} = 0.5$  and  $\nu = 0.25$  250
- 180 Amplitude of the far-field displacements in the  $y-z$  plane for a SV wave normally incident on to a hemispherical surface indentation with  $\frac{2a}{\lambda_s} = 0.5$  and  $\nu = 0.25$  250

- 181 Differential cross-section in the  $x-z$  plane for a SV wave normally incident on to a hemispherical surface indentation with  $\frac{2a}{\lambda_s} = 0.5$  and  $\nu = 0.25$  251
- 182 Differential cross-section in the  $y-z$  plane for a SV wave normally incident on to a hemispherical surface indentation with  $\frac{2a}{\lambda_s} = 0.5$  and  $\nu = 0.25$  251
- 183 Amplitude of the surface displacements in the  $x-z$  plane for a SV wave normally incident on to a surface indentation with the shape of a segment of a hemisphere, where  $\frac{2a}{\lambda_s} = 1.0$ ,  $\frac{d}{a} = 0.5$  and  $\nu = 0.25$  252
- 184 Amplitude of the surface displacements in the  $y-z$  plane for a SV wave normally incident on to a surface indentation with the shape of a segment of a hemisphere, where  $\frac{2a}{\lambda_s} = 1.0$ ,  $\frac{d}{a} = 0.5$  and  $\nu = 0.25$  252
- 185 Amplitude of the far-field displacements in the  $x-z$  plane for a SV wave normally incident on to a surface indentation with the shape of a segment of a hemisphere, where  $\frac{2a}{\lambda_s} = 1.0$ ,  $\frac{d}{a} = 0.5$  and  $\nu = 0.25$  253
- 186 Amplitude of the far-field displacements in the  $y-z$  plane for a SV wave normally incident on to a surface indentation with the shape of a segment of a hemisphere, where  $\frac{2a}{\lambda_s} = 1.0$ ,  $\frac{d}{a} = 0.5$  and  $\nu = 0.25$  253
- 187 Differential cross-section in the  $x-z$  plane for a SV wave normally incident on to a surface indentation with the shape of a segment of a hemisphere, where  $\frac{2a}{\lambda_s} = 1.0$ ,  $\frac{d}{a} = 0.5$  and  $\nu = 0.25$  254

- 188 Differential cross-section in the  $y-z$  plane for a SV wave normally incident on to a surface indentation with the shape of a segment of a hemisphere, where  $\frac{2a}{\lambda_s} = 1.0$ ,  $\frac{d}{a} = 0.5$  and  $\nu = 0.25$  254
- 189 Amplitude of the surface displacements in the  $x-z$  plane for a SV wave normally incident on to a surface indentation with the shape of a semi-ellipsoid, where  $\frac{2a}{\lambda_s} = 1.0$ ,  $\frac{d}{a} = 0.5$  and  $\nu = 0.25$  255
- 190 Amplitude of the surface displacements in the  $y-z$  plane for a SV wave normally incident on to a surface indentation with the shape of a semi-ellipsoid, where  $\frac{2a}{\lambda_s} = 1.0$ ,  $\frac{d}{a} = 0.5$  and  $\nu = 0.25$  255
- 191 Amplitude of the far-field displacements in the  $x-z$  plane for a SV wave normally incident on to a surface indentation with the shape of a semi-ellipsoid, where  $\frac{2a}{\lambda_s} = 1.0$ ,  $\frac{d}{a} = 0.5$  and  $\nu = 0.25$  256
- 192 Amplitude of the far-field displacements in the  $y-z$  plane for a SV wave normally incident on to a surface indentation with the shape of a semi-ellipsoid, where  $\frac{2a}{\lambda_s} = 1.0$ ,  $\frac{d}{a} = 0.5$  and  $\nu = 0.25$  256
- 193 Differential cross-section in the  $x-z$  plane for a SV wave normally incident on to a surface indentation with the shape of a semi-ellipsoid, where  $\frac{2a}{\lambda_s} = 1.0$ ,  $\frac{d}{a} = 0.5$  and  $\nu = 0.25$  257
- 194 Differential cross-section in the  $y-z$  plane for a SV wave normally incident on to a surface indentation with the shape of a semi-ellipsoid, where  $\frac{2a}{\lambda_s} = 1.0$ ,  $\frac{d}{a} = 0.5$  and  $\nu = 0.25$  257

195	Amplitude of the surface displacements in the $x-z$ plane for a SV wave normally incident on to a hemispherical surface indentation with $\frac{2a}{\lambda_s} = 1.0$ and $\nu = 0.25$	258
196	Amplitude of the surface displacements in the $y-z$ plane for a SV wave normally incident on to a hemispherical surface indentation with $\frac{2a}{\lambda_s} = 1.0$ and $\nu = 0.25$	258
197	Amplitude of the far-field displacements in the $x-z$ plane for a SV wave normally incident on to a hemispherical surface indentation with $\frac{2a}{\lambda_s} = 1.0$ and $\nu = 0.25$	259
198	Amplitude of the far-field displacements in the $y-z$ plane for a SV wave normally incident on to a hemispherical surface indentation with $\frac{2a}{\lambda_s} = 1.0$ and $\nu = 0.25$	259
199	Differential cross-section in the $x-z$ plane for a SV wave normally incident on to a hemispherical surface indentation with $\frac{2a}{\lambda_s} = 1.0$ and $\nu = 0.25$	260
200	Differential cross-section in the $y-z$ plane for a SV wave normally incident on to a hemispherical surface indentation with $\frac{2a}{\lambda_s} = 1.0$ and $\nu = 0.25$	260
201	Amplitude of the surface displacements in the $x-z$ plane for a P wave incident under 30 degrees on to a hemispherical surface indentation with $\frac{2a}{\lambda_p} = 0.5$ and $\nu = 0.25$	264
202	Amplitude of the surface displacements in the $y-z$ plane for a P wave incident under 30 degrees on to a hemispherical surface indentation with $\frac{2a}{\lambda_p} = 0.5$ and $\nu = 0.25$	264
203	Amplitude of the far-field displacements in the $x-z$ plane for a P wave incident under 30 degrees on to a hemispherical surface indentation with $\frac{2a}{\lambda_p} = 0.5$ and $\nu = 0.25$	265

- 204 Amplitude of the far-field displacements in the  $y-z$  plane for  
a P wave incident under 30 degrees on to a hemispherical  
surface indentation with  $\frac{2a}{\lambda_p} = 0.5$  and  $\nu = 0.25$  265
- 205 Differential cross-section in the  $x-z$  plane for a P wave  
incident under 30 degrees on to a hemispherical surface  
indentation with  $\frac{2a}{\lambda_p} = 0.5$  and  $\nu = 0.25$  266
- 206 Differential cross-section in the  $y-z$  plane for a P wave  
incident under 30 degrees on to a hemispherical surface  
indentation with  $\frac{2a}{\lambda_p} = 0.5$  and  $\nu = 0.25$  266
- 207 Amplitude of the surface displacements in the  $x-z$  plane for a  
P wave incident under 30 degrees on to a surface indentation  
with the shape of a segment of a hemisphere, where  $\frac{2a}{\lambda_p} = 1.0$ ,  
 $\frac{d}{a} = 0.5$  and  $\nu = 0.25$  267
- 208 Amplitude of the surface displacements in the  $y-z$  plane for a  
P wave incident under 30 degrees on to a surface indentation  
with the shape of a segment of a hemisphere, where  $\frac{2a}{\lambda_p} = 1.0$ ,  
 $\frac{d}{a} = 0.5$  and  $\nu = 0.25$  267
- 209 Amplitude of the far-field displacements in the  $x-z$  plane for  
a P wave incident under 30 degrees on to a surface indentation  
with the shape of a segment of a hemisphere, where  $\frac{2a}{\lambda_p} = 1.0$ ,  
 $\frac{d}{a} = 0.5$  and  $\nu = 0.25$  268
- 210 Amplitude of the far-field displacements in the  $y-z$  plane for  
a P wave incident under 30 degrees on to a surface indentation  
with the shape of a segment of a hemisphere, where  $\frac{2a}{\lambda_p} = 1.0$ ,  
 $\frac{d}{a} = 0.5$  and  $\nu = 0.25$  268

- 211 Differential cross-section in the  $x-z$  plane for a P wave incident under 30 degrees on to a surface indentation with the shape of a segment of a hemisphere, where  $\frac{2a}{\lambda_p} = 1.0$ ,  $\frac{d}{a} = 0.5$  and  $\nu = 0.25$  269
- 212 Differential cross-section in the  $y-z$  plane for a P wave incident under 30 degrees on to a surface indentation with the shape of a segment of a hemisphere, where  $\frac{2a}{\lambda_p} = 1.0$ ,  $\frac{d}{a} = 0.5$  and  $\nu = 0.25$  269
- 213 Amplitude of the surface displacements in the  $x-z$  plane for a P wave incident under 30 degrees on to a surface indentation with the shape of a semi-ellipsoid, where  $\frac{2a}{\lambda_p} = 1.0$ ,  $\frac{d}{a} = 0.5$  and  $\nu = 0.25$  270
- 214 Amplitude of the surface displacements in the  $y-z$  plane for a P wave incident under 30 degrees on to a surface indentation with the shape of a semi-ellipsoid, where  $\frac{2a}{\lambda_p} = 1.0$ ,  $\frac{d}{a} = 0.5$  and  $\nu = 0.25$  270
- 215 Amplitude of the far-field displacements in the  $x-z$  plane for a P wave incident under 30 degrees on to a surface indentation with the shape of a semi-ellipsoid, where  $\frac{2a}{\lambda_p} = 1.0$ ,  $\frac{d}{a} = 0.5$  and  $\nu = 0.25$  271
- 216 Amplitude of the far-field displacements in the  $y-z$  plane for a P wave incident under 30 degrees on to a surface indentation with the shape of a semi-ellipsoid, where  $\frac{2a}{\lambda_p} = 1.0$ ,  $\frac{d}{a} = 0.5$  and  $\nu = 0.25$  271

- 217 Differential cross-section in the  $x-z$  plane for a P wave  
incident under 30 degrees on to a surface indentation with  
the shape of a semi-ellipsoid, where  $\frac{2a}{\lambda_p} = 1.0$ ,  $\frac{d}{a} = 0.5$   
and  $\nu = 0.25$  272
- 218 Differential cross-section in the  $y-z$  plane for a P wave  
incident under 30 degrees on to a surface indentation with  
the shape of a semi-ellipsoid, where  $\frac{2a}{\lambda_p} = 1.0$ ,  $\frac{d}{a} = 0.5$   
and  $\nu = 0.25$  272
- 219 Amplitude of the surface displacements in the  $x-z$  plane for  
a P wave incident under 30 degrees on to a hemispherical  
surface indentation with  $\frac{2a}{\lambda_p} = 1.0$  and  $\nu = 0.25$  273
- 220 Amplitude of the surface displacements in the  $y-z$  plane for  
a P wave incident under 30 degrees on to a hemispherical  
surface indentation with  $\frac{2a}{\lambda_p} = 1.0$  and  $\nu = 0.25$  273
- 221 Amplitude of the far-field displacements in the  $x-z$  plane for  
a P wave incident under 30 degrees on to a hemispherical  
surface indentation with  $\frac{2a}{\lambda_p} = 1.0$  and  $\nu = 0.25$  274
- 222 Amplitude of the far-field displacements in the  $y-z$  plane for  
a P wave incident under 30 degrees on to a hemispherical  
surface indentation with  $\frac{2a}{\lambda_p} = 1.0$  and  $\nu = 0.25$  274
- 223 Differential cross-section in the  $x-z$  plane for a P wave  
incident under 30 degrees on to a hemispherical surface  
indentation with  $\frac{2a}{\lambda_p} = 1.0$  and  $\nu = 0.25$  275
- 224 Differential cross-section in the  $y-z$  plane for a P wave  
incident under 30 degrees on to a hemispherical surface  
indentation with  $\frac{2a}{\lambda_p} = 1.0$  and  $\nu = 0.25$  275

- 225 Amplitude of the surface displacements in the  $x-z$  plane for a SV wave incident under 30 degrees on to a hemispherical surface indentation with  $\frac{2a}{\lambda_s} = 0.5$  and  $\nu = 0.25$  276
- 226 Amplitude of the surface displacements in the  $y-z$  plane for a SV wave incident under 30 degrees on to a hemispherical surface indentation with  $\frac{2a}{\lambda_s} = 0.5$  and  $\nu = 0.25$  276
- 227 Amplitude of the far-field displacements in the  $x-z$  plane for a SV wave incident under 30 degrees on to a hemispherical surface indentation with  $\frac{2a}{\lambda_s} = 0.5$  and  $\nu = 0.25$  277
- 228 Amplitude of the far-field displacements in the  $y-z$  plane for a SV wave incident under 30 degrees on to a hemispherical surface indentation with  $\frac{2a}{\lambda_s} = 0.5$  and  $\nu = 0.25$  277
- 229 Differential cross-section in the  $x-z$  plane for a SV wave incident under 30 degrees on to a hemispherical surface indentation with  $\frac{2a}{\lambda_s} = 0.5$  and  $\nu = 0.25$  278
- 230 Differential cross-section in the  $y-z$  plane for a SV wave incident under 30 degrees on to a hemispherical surface indentation with  $\frac{2a}{\lambda_s} = 0.5$  and  $\nu = 0.25$  278
- 231 Amplitude of the surface displacements in the  $x-z$  plane for a SV wave incident under 30 degrees on to a surface indentation with the shape of a segment of a hemisphere, where  $\frac{2a}{\lambda_s} = 1.0$ ,  $\frac{d}{a} = 0.5$  and  $\nu = 0.25$  279
- 232 Amplitude of the surface displacements in the  $y-z$  plane for a SV wave incident under 30 degrees on to a surface indentation with the shape of a segment of a hemisphere, where  $\frac{2a}{\lambda_s} = 1.0$ ,  $\frac{d}{a} = 0.5$  and  $\nu = 0.25$  279

- 233 Amplitude of the far-field displacements in the  $x-z$  plane for  
a SV wave incident under 30 degrees on to a surface indentation  
with the shape of a segment of a hemisphere, where  $\frac{2a}{\lambda_s} = 1.0$ ,  
 $\frac{d}{a} = 0.5$  and  $\nu = 0.25$  280
- 234 Amplitude of the far-field displacements in the  $y-z$  plane for  
a SV wave incident under 30 degrees on to a surface indentation  
with the shape of a segment of a hemisphere, where  $\frac{2a}{\lambda_s} = 1.0$ ,  
 $\frac{d}{a} = 0.5$  and  $\nu = 0.25$  280
- 235 Differential cross-section in the  $x-z$  plane for a SV wave  
incident under 30 degrees on to a surface indentation with  
the shape of a segment of a hemisphere, where  $\frac{2a}{\lambda_s} = 1.0$ ,  
 $\frac{d}{a} = 0.5$  and  $\nu = 0.25$  281
- 236 Differential cross-section in the  $y-z$  plane for a SV wave  
incident under 30 degrees on to a surface indentation with  
the shape of a segment of a hemisphere, where  $\frac{2a}{\lambda_s} = 1.0$ ,  
 $\frac{d}{a} = 0.5$  and  $\nu = 0.25$  281
- 237 Amplitude of the surface displacements in the  $x-z$  plane for a  
SV wave incident under 30 degrees on to a surface indentation  
with the shape of a semi-ellipsoid, where  $\frac{2a}{\lambda_s} = 1.0$ ,  $\frac{d}{a} = 0.5$   
and  $\nu = 0.25$  282
- 238 Amplitude of the surface displacements in the  $y-z$  plane for a  
SV wave incident under 30 degrees on to a surface indentation  
with the shape of a semi-ellipsoid, where  $\frac{2a}{\lambda_s} = 1.0$ ,  $\frac{d}{a} = 0.5$   
and  $\nu = 0.25$  282

- 239 Amplitude of the far-field displacements in the  $x-z$  plane for  
a SV wave incident under 30 degrees on to a surface indentation  
with the shape of a semi-ellipsoid, where  $\frac{2a}{\lambda_s} = 1.0$ ,  $\frac{d}{a} = 0.5$   
and  $\nu = 0.25$  283
- 240 Amplitude of the far-field displacements in the  $y-z$  plane for  
a SV wave incident under 30 degrees on to a surface indentation  
with the shape of a semi-ellipsoid, where  $\frac{2a}{\lambda_s} = 1.0$ ,  $\frac{d}{a} = 0.5$   
and  $\nu = 0.25$  283
- 241 Differential cross-section in the  $x-z$  plane for a SV wave  
incident under 30 degrees on to a surface indentation with  
the shape of a semi-ellipsoid, where  $\frac{2a}{\lambda_s} = 1.0$ ,  $\frac{d}{a} = 0.5$   
and  $\nu = 0.25$  284
- 242 Differential cross-section in the  $y-z$  plane for a SV wave  
incident under 30 degrees on to a surface indentation with  
the shape of a semi-ellipsoid, where  $\frac{2a}{\lambda_s} = 1.0$ ,  $\frac{d}{a} = 0.5$   
and  $\nu = 0.25$  284
- 243 Amplitude of the surface displacements in the  $x-z$  plane for  
a SV wave incident under 30 degrees on to a hemispherical  
surface indentation with  $\frac{2a}{\lambda_s} = 1.0$  and  $\nu = 0.25$  285
- 244 Amplitude of the surface displacements in the  $y-z$  plane for  
a SV wave incident under 30 degrees on to a hemispherical  
surface indentation with  $\frac{2a}{\lambda_s} = 1.0$  and  $\nu = 0.25$  285
- 245 Amplitude of the far-field displacements in the  $x-z$  plane for  
a SV wave incident under 30 degrees on to a hemispherical  
surface indentation with  $\frac{2a}{\lambda_s} = 1.0$  and  $\nu = 0.25$  286

- 246 Amplitude of the far-field displacements in the  $y-z$  plane for  
a SV wave incident under 30 degrees on to a hemispherical  
surface indentation with  $\frac{2a}{\lambda_s} = 1.0$  and  $\nu = 0.25$  286
- 247 Differential cross-section in the  $x-z$  plane for a SV wave  
incident under 30 degrees on to a hemispherical surface  
indentation with  $\frac{2a}{\lambda_s} = 1.0$  and  $\nu = 0.25$  287
- 248 Differential cross-section in the  $y-z$  plane for a SV wave  
incident under 30 degrees on to a hemispherical surface  
indentation with  $\frac{2a}{\lambda_s} = 1.0$  and  $\nu = 0.25$  287

## 1. Introduction

### 1.1 Motivation, outline and contribution

This section gives a brief summary of the motivation for this study, an outline of the presented thesis and a statement of the claims for original contributions of this research.

#### 1.1.1 Statement of the problem and outline of the thesis

The development of methods for the detection and characterisation of corrosion with the aid of ultrasound has for a long time been in the shadow of efforts concentrated on the detection of cracks and inclusions in solid materials [1 – 3]. A crack usually starts on (or close to) the surface of a material and grows inwards. It can be detected due to strong scattering signals emanating from the crack [2]. Inclusions are wholly immersed in a matrix material and the ultrasonic field scattered from such inclusions will normally consist of compressional and shear waves radiated into various directions, which can be detected with pulse-echo or pitch-catch tandem configurations [2].

Corrosion is a surface feature, and its detection in the early stages of its growth from a remote surface is difficult. In its advanced stages it can be detected by a loss-of-back-wall-reflection if the corrosion creates a rough surface [4] or by pulse-echo methods using thickness gauges when the overall thickness of the material has been reduced [5]. Methods used for the detection of corrosion are largely empirical [6], and there is an increasing need for theoretical investigations into the ultrasonic scattering from

corroded surfaces in order to devise methods that can detect and size small amounts of corrosion.

This study was initiated in order to look for possibilities of detecting the early stages of pitting corrosion in aluminium aircraft structures using ultrasound. The corrosion pits appear as small isolated surface features located on the remote side of a thick aluminium plate and the work looks at the scattering of ultrasonic compressional and shear waves from one single isolated pit. The pit is represented by a three-dimensional hemispherical or shallow surface indentation in a plane half-space. The surface diameter of the pit is assumed to be between about 1 mm and 6 mm, and the frequency of the incident plane wave is in the range from 1 MHz — 5 MHz, thereby giving a diameter to incident wavelength ratio of the order of one.

In order to investigate the scattering of compressional or shear waves from a corrosion pit with a surface diameter of the order of one incident wavelength a numerical simulation method is employed. The three-dimensional nature of pits requires methods capable of simulating elastic wave scattering in three dimensions. The most powerful methods for the simulation of scattering from three-dimensional geometries in the mid-frequency regime are boundary methods [7]. They are widely used in geophysics, where the surface movements of valleys and ridges under the influence of earthquake waves are calculated [8].

A conceptually simple indirect boundary method simulating the scattering of elastic waves from three-dimensional hemispherical surface indentations was published in [9, 10]. This method was adapted and extended for the present study in order to obtain information on the scattered far-

field from axisymmetric surface indentations that can help to design new methods for the detection of corrosion in the early stages.

This thesis gives a detailed account of the used numerical method and presents a range of numerical results for the near and far-field scattered from various axisymmetric surface indentations together with some experimental support. These results are then interpreted in order to give some suggestions for the development of new methods to detect pitting corrosion in its early stages. The thesis is divided into the following sections :

Chapter one is designed to give an insight into the nature of corrosion and investigates the applicability of different mathematical and numerical methods to the given problem. Emphasis is placed on the fact that corrosion is a genuinely three-dimensional phenomenon, and the advantages of the chosen chosen numerical method are explained.

Chapter two deals with the mathematical description of the indirect boundary method. It exploits the multipole expansion of the solution to the elastic wave equation together with a least squares point matching method. The method has the advantage that for axisymmetric surface indentations it is possible to break the three-dimensional scattering problem down into two-dimensional sub-problems, which in turn can be modelled very efficiently with moderate computer facilities rather than supercomputers.

Chapter three investigates the accuracy of the numerical method and presents results calculated with the method described in chapter two. The shape of the surface feature is varied, and the incident wave can be of compressional or shear wave type under normal or non-normal incidence.

Three types of results can be obtained from the numerical simulations :

- a) The displacements along the surface in the vicinity of the indentation
- b) Far-field displacement radiation plots
- c) Far-field differential scattering cross-section radiation plots

In addition measurements are presented and compared with calculated results.

Chapter four discusses the numerical and experimental results presented in chapter three and gives suggestions for new methods for the detection of pitting corrosion in early stages. Some suggestions for further improvements and extensions of the present work conclude the main part of the thesis.

Appendices A — D contain detailed derivations of the employed numerical expressions and these sections are included for the benefit of further workers along the lines of this work.

Appendix E contains further numerical results and is added for the sake of completeness.

### 1.1.2 Claim of contribution

The numerical method presented in this study is based on work carried out in the field of geophysics. Seismologists and earthquake engineers are interested in the surface movements of canyons and valleys under the influence of compressional, shear or Rayleigh waves incident at various angles [8 – 10]. The diameter of such a surface indentation is usually of the order of an incident wavelength, and therefore methods developed in seismology can often also be transferred to ultrasonic testing. However, in the area of ultrasonic nondestructive testing the interest is focussed mainly on displacements and energy distribution at some distance from the scatterer rather than in the vicinity of it. This means that the methods developed in seismology have to be extended in order to provide information on the far-field displacements and the far-field scattered energy.

Claim of contribution 1 : The present work applies and extends a numerical method presented in [8 – 10] to the area of nondestructive testing. The extension of this method consists of calculating the displacements and stresses in the near as well as in the far-field, thereby providing important information that can be applied to the area of nondestructive testing.

Claim of contribution 2 : The method has been extended to cover hemispherical as well as non-hemispherical shallow axisymmetric surface indentations for normal and non-normal incidence. To the authors knowledge there are only two case reported in the literature dealing with near-field results for non-normal incidence of a compressional wave on to three-dimensional surface features with dimensions of the order of one incident wavelength. The first case is concerned with the scattering from a hemispherical indentation, the second case deals with the scattering from an

axisymmetric ridge [8]. The present work proceeded independently from these results, and a comparison of calculated results with published results shows very good agreement. A range of novel results are presented for the near-field displacements as well as for the far-field displacements and the differential cross-section in the far-field for compressional and shear plane waves incident under normal and non-normal incidence on to various surface features.

Claim of contribution 3 : An investigation into the stability and accuracy of the numerical method has been carried out. It was found that the method is sensitive to the number of basis functions used to describe the scattered field. This was not reported in [8 – 10], and some of the results presented in [9] do not seem to employ the optimum number of basis function, thereby allowing for improvements. The choice of an optimum number for the basis functions is also critical for the far-field computations, since the far-field calculations lead to incorrect results when carried out outside the stable region. This phenomenon is due to the finite accuracy and word length of computers used for computations rather than an intrinsic error of the numerical method.

Claim of contribution 4 : Measurements have been carried out and are presented to support the findings of the numerical simulations. The experiments were carried out in order to measure the far-field quantities scattered from a hemispherical surface indentation with a diameter of the order of an incident wavelength, where the incident wave was a compressional or shear wave under normal incidence. To the authors knowledge, these measurements have not been reported in the literature before.

Claim of contribution 5 : The interpretation of the numerical simulations and the experiments give a novel insight into the difficulties of detecting pitting

corrosion in early stages and may help to devise new methods in the area of the detection and characterisation of pitting corrosion. Suggestions emerging from this work are :

- The frequency of the incident wave should be chosen so that the wavelength is smaller than the depth of the expected corrosion pits.
- Shear wave transducers should be used rather than compressional wave transducers.
- The ultrasonic beam should be non-normally incident on to the corroded surface, and the use of pitch-catch tandem configurations will be of advantage.

This work was presented at two conferences in summer 1989 and the contributions are published in the corresponding conference proceedings :

1) Peter H. Albach and Leonard J. Bond : Numerical Simulation of Elastic Wave Scattering from Three-Dimensional Axisymmetric Surface Features, Review of Progress in Quantitative Nondestructive Evaluation, 23rd July — 28th July 1989, Bowdoin College, Brunswick, Maine, USA, Conference Proceedings to be published by Plenum Press

2) Peter H. Albach and Leonard J. Bond : Three-Dimensional Numerical Simulation of Elastic Body Wave Scattering from a Half-Space with Hemispherical or Shallow Surface Indentations, IUTAM Symposium on Elastic Wave Propagation and Ultrasonic Nondestructive Evaluation, 30th July — 3rd August 1989, Boulder, University of Colorado, USA, Conference Proceedings to be published by Elsevier Science Publishers

## 1.2 Corrosion in NDE

Although recent years have shown a great deal of progress in the development of new NDE techniques for detecting cracks and inclusions in metals [1 – 3, 11], there is now also an increasing need for the development of new methods for the detection and characterisation of corrosion in its early stages [5, 6, 12, 13]. Often corrosion is located on the remote and inaccessible side of metal structures (e.g. inside aluminium aircraft fuel tanks), and visual inspection is not possible.

Radiography and thermal neutron radiography can be used to inspect complex structures, but a main drawback of these techniques is the size of the technical equipment which makes in-service inspection very difficult or impossible. Also both sides of the object under inspection have to be accessible [6].

Acoustic emission testing requires heating of the surface of the tested object and is therefore also unsuitable for in-service inspection [5, 6].

Eddy current techniques are mainly used to detect thickness changes of thin aluminium alloy layers with a thickness of up to 7.6 mm. They can also be used in multiple layered structures [14, 15]. The eddy current instrument is calibrated using taper gauges. The loci of lift-off, corrosion and cracks can then be distinguished on the impedance plane display of the test instrument [16, 17].

Ultrasonic techniques are mainly used for monitoring relatively thick single layered objects. The basic method commonly employed is the pulse-echo inspection, see Fig. 1. Two variants of this method are possible, their

use depends on the roughness of the corroded area [4 – 6, 18] :

- Material thinning due to corrosion creates a new interface. The pulses reflected from this new interface arrive in a much shorter time period at the ultrasonic receiver than the pulses reflected from the original back surface of the material. The recording of the reflected pulses on an A-scan display calibrated to the original thickness of the material then allows the estimation of the remaining thickness of the material. By using a focussed transducer it is possible to focus the incident beam below the surface at the depth of the expected corrosion and thereby minimising the scattering noise.
- Corrosion generally results in a rough surface. An ultrasonic beam incident on a very rough surface is scattered in a wide range of directions, thus allowing only very little of the incident energy to reach the receiver — a reflected pulse can only be observed in a highly attenuated form (or not at all). This is commonly called the "pulse-echo loss-of-back-wall-reflection technique". A C-scan recording then leads to a map of the corroded areas. The loss-of-back-wall-reflection method can give ambiguous results, since other effects (like excess paint on the front surface) can also be the cause of strong attenuation [4].

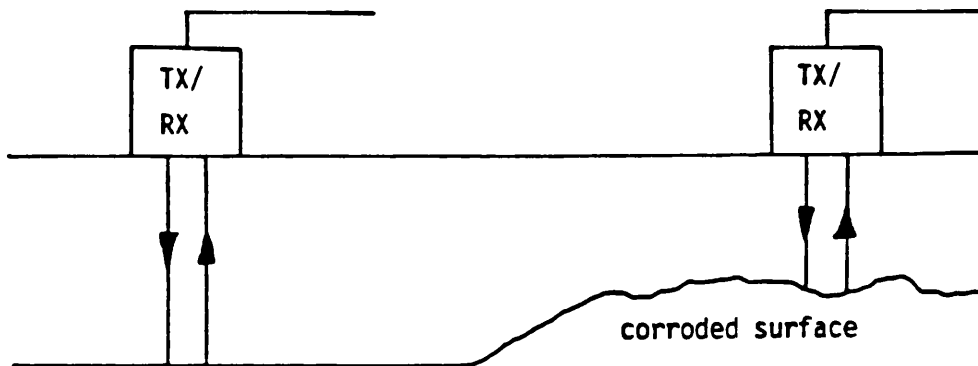


Fig. 1 : Ultrasonic pulse-echo inspection of a corroded surface.

The detection and characterisation of corrosion is of particular importance in aircraft inspection and maintenance. An aircraft is a highly complex structure. Heavy demands are made on the airframe where at the same time the weight of the frame has to be kept at a minimum. Often areas that are exposed to a corrosive environment are not easily accessed, like fuel tanks and the inside of the passenger cabin (which is covered with panels) including the vicinity of lavatory systems. Many areas under severe load consist of several different metals bonded together and are therefore susceptible to certain kinds of corrosion [6, 18].

Six common types of corrosion are encountered in aircraft engineering [6, 18] and are shown in Fig. 2 :

## TYPES OF CORROSION

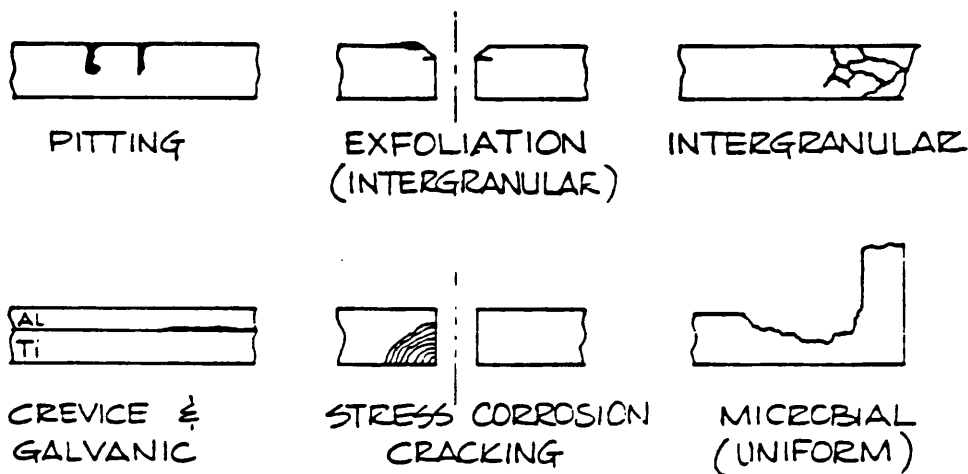


Fig. 2 : Most common types of corrosion encountered in aircraft engineering,  
 diagram taken from [18]

— Pitting corrosion

Pitting corrosion is an electrochemical reaction which causes the occurrence of holes in metals. The holes may be small or large in diameter. They can undercut the surface, and subsurface damage is sometimes much more severe than indicated by the surface appearance, see Figs. 3 and 4.



Fig. 3 : Pitting of stainless steel by acid-chloride solution, taken from [19]

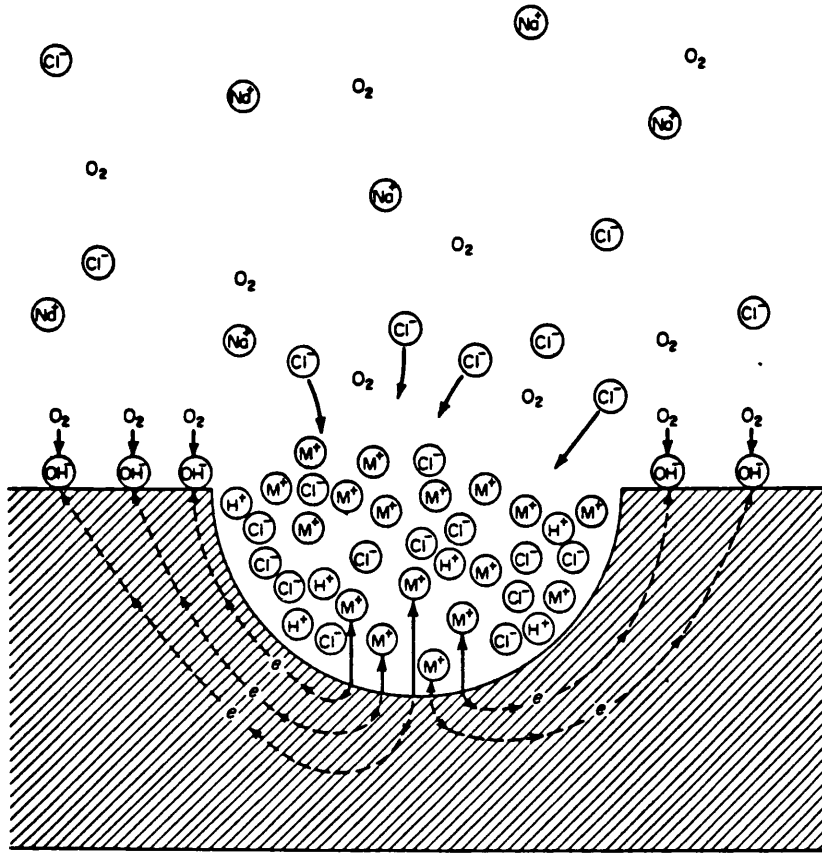


Fig. 4 : Chemical processes occurring during pitting corrosion. The metal (M) is attacked by an aerated sodium chloride solution. The diagram was taken from [19]

— Intergranular corrosion

This form of corrosion attacks the grain boundaries of a material. In its advanced stage it becomes

— Exfoliation corrosion

A large amount of grain boundaries have been attacked. This results in the delamination of thin layers of the affected material and causes a considerable loss of strength due to material thinning, see Fig. 5.

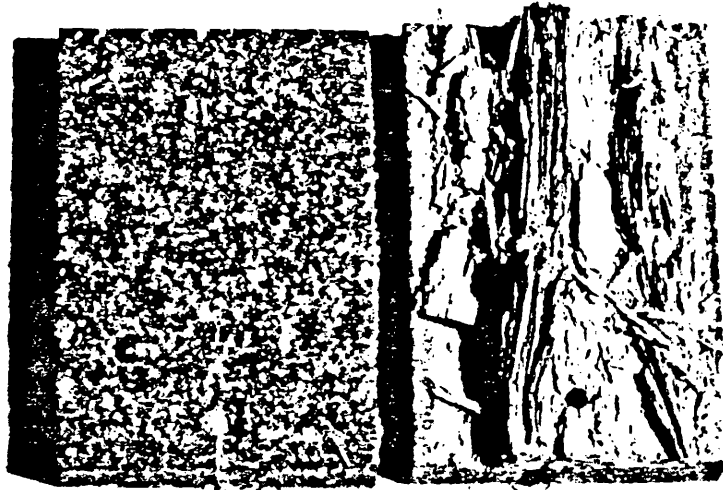


Fig. 5 : Superficial pitting (left) and exfoliation corrosion (right) of aluminium-copper-magnesium alloy, taken from [20]

— Crevice and galvanic corrosion

Both crevice and galvanic corrosion occur when metal is in direct contact with a second material. If this second material is a metal different from the first one and both materials are exposed to an electrolyte, galvanic corrosion takes place, i.e. electrolytic dissolution of the less corrosion resistant material [19]. If metal is in direct contact with any material (e.g. sealing compound) but the contact is such that crevices between the two materials occur, then a basis for crevice corrosion is given. Any chemically active material which gets into the crevice between the two materials will dissolve them, as can be seen in Fig. 6.

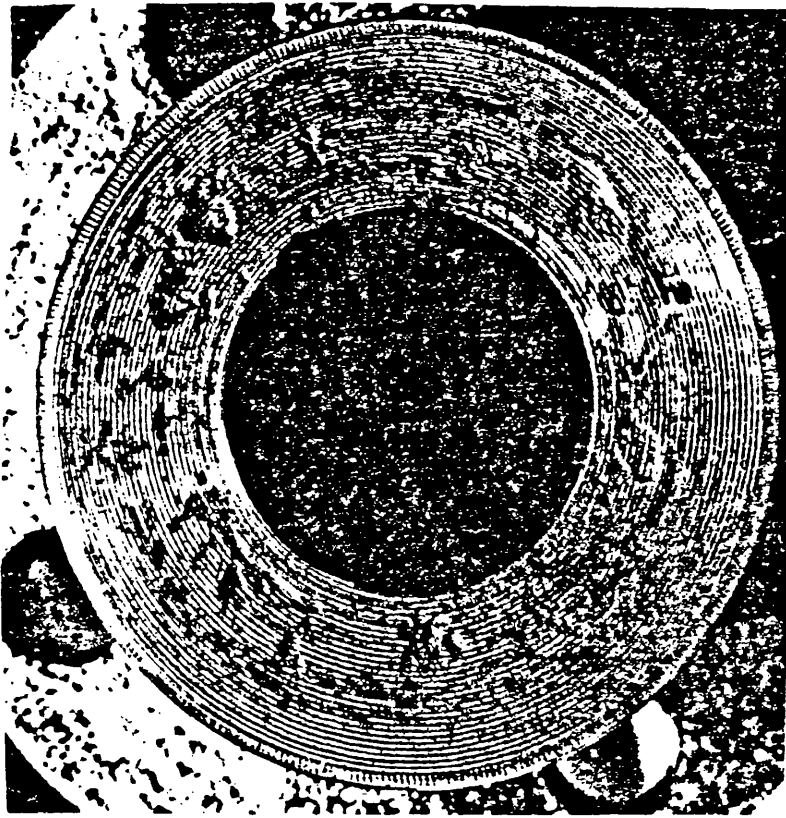


Fig. 6 : Crevice corrosion on a large stainless steel pipe flange, taken from [19]

— Stress-corrosion cracking

Stress-corrosion cracking occurs when at the same time a metal is under tensile stress and a corrosive medium is present. The surface of the metal exposed to the corrosive medium remains virtually unattacked while fine cracks progress through the material. The cracks can occur along grain boundaries when intergranular attack is present, as shown in Fig. 7, but they can also advance without any reference to grain boundaries [19].



Fig. 7 : Intergranular stress-corrosion cracking of brass, taken from [19]

— Microbiological corrosion

Microbiological corrosion occurs when material is exposed to a biologically active environment. In aircraft engineering these situations arise for example inside aluminium aircraft fuel tanks which contained contaminated fuel. The growth of fungi inside the tanks leads to corrosion of the fuel tank walls, where pitting corrosion is usually predominant [20].

### 1.3 Mathematical models for the scattering from a corroded surface

The aim of this study is to assess the possibilities of detection and characterisation of pitting corrosion located on the remote side of thick aluminium plates using ultrasound. Initially the question of how to represent a corroded surface had to be addressed. It was found that two approaches are possible :

#### 1) The corroded surface is represented as a randomly rough surface.

The shape of the surface can be considered as being generated by a random process. The parameters of that statistical process (like mean value, standard deviation and autocorrelation function) determine the roughness of the surface and therefore the properties of the corrosion. An ultrasonic beam scattered from such a randomly rough surface can be split into two parts — the coherently scattered field (or mean field) and the diffuse (or fluctuating) field<sup>1</sup>. Either part can serve as an indication of the roughness of the surface. Two theoretical approaches to the scattering of elastic waves from randomly rough surfaces can be found :

- Perturbation theory [22 – 24], whereby the roughness of the surface is expressed in terms of equivalent stresses on the mean, flat surface. The deviations of the actual surface from the mean surface have to be small compared to the wavelength (i.e. it is a low frequency approximation). Also the gradient (slope) of the rough surface has to be much smaller than one, so that multiple scattering can be neglected. These limitations impose

---

<sup>1</sup> A comprehensive literature review on acoustic and elastic wave scattering from rough surfaces including detailed explanations of theories and approaches can be found in [21]

severe restrictions on the number of permissible surface shapes, and the approach seems to lead to results similar to the scattering from smooth surfaces [25].

- Kirchhoff theory [26, 27], whereby the radius of curvature of the surface is assumed as smaller than the wavelength of the incident wave. The surface then behaves as if it was locally flat and reflects the incident wave at any point in the specular direction. Restrictions due to the Kirchhoff approximation are that the scale of roughness has to be much larger than the wavelength (i.e. it is a high frequency approximation) and that multiple scattering is not taken into account.

Both of the above mentioned approaches allow surfaces with roughness in one or two dimensions.

Experimental investigations into the scattering from rough surfaces have only been carried out for the acoustic (scalar) case. An object with a randomly rough surface was immersed in a water tank together with an ultrasound transducer. The signal backscattered from the surface was analysed using scalar Kirchhoff theory [28 – 33].

It seems that some types of corrosion (like exfoliation corrosion) can be represented very effectively as a random surface, whereas other types (like pitting corrosion) have to be assumed as deterministic surface features :

II) The corroded surface is represented as a flat surface with deterministic perturbations

Many theoretical studies deal with elastic scattering from obstacles [34 – 37]. In the area of NDE they are mostly concerned with scattering from either surface-breaking and subsurface cracks (e.g. [38 – 40]) or elastic inclusions

and defects in bulk material (e.g. [41 — 49]). The scattering from extended surface disturbances of an elastic half-space has attracted some attention in the field of geophysics and earthquake research. Of prime interest is here the examination of the ground motion of valleys, alluvial deposits and ridges under the influence of body waves and Rayleigh waves originating from earthquakes or explosions. Work carried out in this area include :

- The solution of two-dimensional time dependent scattering problems using finite difference methods [50 — 54]. Here the second order partial differential equation governing the propagation of elastic waves is approximated by a finite difference scheme. This allows the solution of scattering problems with incident pulses rather than time harmonic plane waves. The number of possible boundary shapes, normally restricted due to the finite difference grid, can be extended by using a combined finite difference — finite element method for the spatial discretisations and a finite difference scheme for the temporal discretisation [55, 56]. These methods are very effective for incident shear and compressional wave pulses as well as for incident Rayleigh wave pulses. Unfortunately, the extension of finite difference and mixed finite element — finite difference schemes to three spatial dimensions requires supercomputers (at least at this moment in time) due to massively increased computation time and storage requirements. Recently reported three-dimensional finite difference models can include material anisotropy and inhomogenities within the bulk material [57, 58]. For axisymmetric geometries with axisymmetric excitation a reduction of the three-dimensional problem down to two dimensions is possible by choosing appropriate boundary conditions for the reduced problem (this is sometimes referred to as  $2 \frac{1}{2}$  dimensional geometries), see [59].

- The solution of two-dimensional elastic scattering problems from periodic interfaces using a boundary integral equation method [60]. This topic is also of special interest to microwave engineers, since delay lines and signal-processing devices used in microwave systems employ surface-acoustic-wave (SAW) devices. These SAW devices convert microwave signals into Rayleigh waves by means of a corrugated surface. The Rayleigh wave undergoes a time delay and is then converted back into microwave signals [61 — 63].

Experimental data for incident ultrasonic pulses is compared with the theoretical model, taking account of finite beamwidth and time dependence via spatial and temporal Fourier analysis. The agreement between theory and experimental data was shown to be very good [64 — 68]. A different method, known as Rayleigh method (where the scattered field is expanded into outgoing plane waves), has also been applied successfully to compute the scattering from periodic surface profiles [69, 70].

- The solution of two-dimensional and three-dimensional scattering from surface obstacles using perturbation theory [61 — 63, 71 — 73]. Here, as for the case of a randomly rough surface, the dimensions of the surface perturbation have to be small compared to the wavelength and the slope of the obstacle has to be smaller than one. It is then possible to replace the irregularity by a stress distribution on the plane, undisturbed surface. The problem is now reduced to Lamb's problem for distributed surface sources, which can be solved. Comparisons with experimental data show good agreement as long as the assumptions are met (e.g. slopes below 25°), see [74, 75].
- The solution of two-dimensional and three-dimensional scattering from surface and subsurface obstacles using boundary methods. The term

boundary methods encompasses a variety of mathematical approaches. In contrast to finite difference and finite element methods, where the wave equation is satisfied approximately inside the computational domain and accurately at the boundaries (except for the radiation condition at infinity), boundary methods satisfy the wave equation and the radiation condition exactly, while approximating the boundary conditions [76]. This can be done in various ways. One common approach is to write the solution to the wave equation as an integral equation, which is then solved by numerical means [77]. Another, conceptually simpler method, is to expand the elastic stresses and displacements inside the computational domain into a (possibly infinite) set of trial functions with unknown coefficients. The trial functions (which are also called basis functions) are exact solutions of the elastic wave equation, and the unknown coefficients are chosen such that the boundary conditions of the problem are satisfied approximately. This method avoids the cumbersome numerical treatment of integral equations, which are often singular. A suitable set of trial functions for the two-dimensional case of a half-space with a surface disturbance can, for example, be constructed from Lamb's solutions for buried compressional and shear line sources. These solutions implicitly satisfy the boundary conditions on a stress free plane surface and the Sommerfeld-Kupradze elastic radiation condition at infinity. Several of these solutions with the line sources placed above the disturbance are superimposed. The appropriate choice of coefficients to these solutions guarantees that the boundary conditions along the surface perturbation are satisfied in the least squares sense [78, 79]. An alternative to the trial functions described above was given in [80]. Here the set of basis functions is taken as the multipole expansion of the solution of the elastic wave

equation in full space. This choice has the disadvantage that the treatment of the boundaries has to be extended to the stress-free surface of the half-space since none of the elements in the expansion satisfies the condition of zero normal stress along a plane free surface on its own. On the other hand it turns out that these elements are numerically much simpler to construct, and that an extension from two-dimensional to three-dimensional geometries is straight forward [8 — 10]. This is not the case for the solutions of Lamb's problem, where the solutions for point sources (i.e. the three-dimensional solutions) are much more involved than the solutions for line sources [81, 82]. For the two-dimensional case finite element methods have been incorporated into the boundary method in order to account for multiple scattering effects near the surface disturbance. This also speeds up the numerical calculations [83 — 91].

The three-dimensional deterministic nature of corrosion pits and their similarities to hemispherical valleys suggests the use of boundary methods for simulating the scattering from a metal plate attacked by pitting corrosion. It is assumed that the metal plate can be described by a half-space with a hemispherical surface disturbance representing an isolated pit. The elastic field generated by the ultrasound transducer is approximated by an infinite plane compressional or shear wave incident on the corroded surface, see Fig. 8.

The scattering of elastic waves from a layered half-space with irregular interfaces using the Rayleigh method is investigated in [116, 117]. The geometry is assumed to be two-dimensional, periodic in space, and the field scattered from the irregular interface is expanded into a finite series of outward propagating homogeneous and inhomogeneous plane waves. This results in a set of coupled integral equations, which are solved in the (spatial) Fourier domain. The period of the geometry has to be sufficiently large in order to avoid aliasing effects in the Fourier domain. The incident wave field can be a plane wave [116] or a cylindrical wave generated by a line source [117]. The main drawback of this method is that it does not completely describe the scattered wave field near the corrugated surface, since near the surface the existence of inward travelling waves is possible. The errors due to the incomplete description of the scattered field can be kept small if the slope of the corrugated surface is small and the wavelength of the incident wave does not exceed the dimensions of the irregular surface.

The scattering of pulsed P, SV and SH waves from two-dimensional surface discontinuities using finite element analysis is examined in [118]. The geometries under investigation (triangular ridge, semi-cylindrical alluvial valley and a deep earthquake zone) are modelled with quadrilateral finite elements and the wavefields are propagated in the time domain by a fourth order Runge-Kutta algorithm. An extension of this method to three dimensions is theoretically possible, but will result in a massive increase in computer memory and cpu time.

The high frequency seismic wave resonances in a three-dimensional semi-elliptical sedimentary basin are calculated in [119]. The scalar wave equation is solved in triaxial ellipsoidal coordinates using high frequency asymptotics and the WKB approach. A uniform elastic and isotropic sediment of semi-elliptical shape is located on the surface of a half-space, and high seismic contrast between the sediment and the half-space is assumed. This creates the conditions for resonant wave modes trapped in the basin for near normal incidence of compressional or shear waves. The modes can be visualized through ray tracing. Since this method is based on a high frequency scalar wave approximation, mode conversion and low frequency phenomena can not be studied.

The wave expansion method described in [9] and employed in this study is also used in [120] in order to investigate the diffraction of shear waves from a three-dimensional hemispherical alluvial valley located on the surface of a half-space. The incoming plane shear wave and the reflected components due to the stress free surface of the half space are expanded in spherical coordinates. The scattered and refracted field components due to the alluvial valley are given as finite series of spherical vector functions with unknown coefficients, which are determined by fulfilling the boundary and interface conditions in a least squares sense. In order to obtain results in the time domain a range of calculations in the frequency domain for different diameter to wavelength ratios are carried out. A fast Fourier transform then provides time domain traces for a given incident wave pulse.

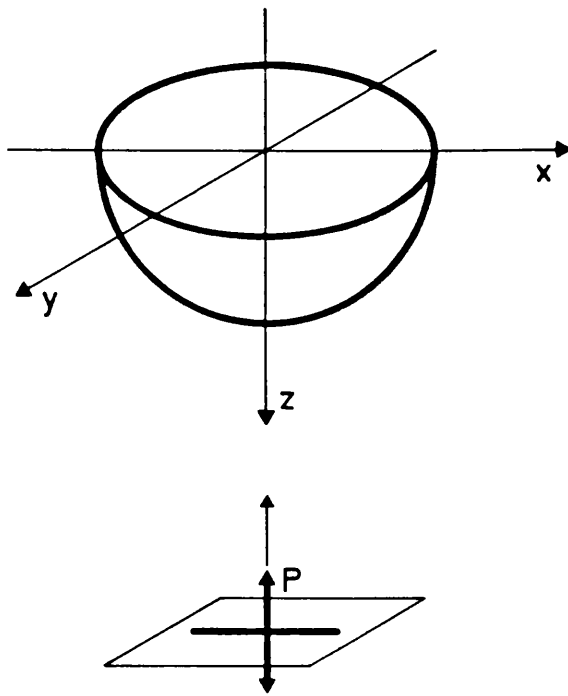


**Fig. 8 : Compressional plane wave incident on a plane surface with hemispherical surface disturbance representing a corrosion pit, taken from [9]**

## 2. Numerical method

### 2.1 Basic idea

The most appropriate choice for the modelling of scattering from spherical and hemispherical objects is a spherical coordinate system :

- The elastic wave equation is separable in spherical coordinates
- The elastic displacement can be expressed in terms of three scalar potentials, each of them obeying the scalar wave equation in spherical coordinates
- all boundaries are along coordinate surfaces and therefore the boundary conditions take a simple form
- The functions describing the coordinate dependences of the three scalar potentials are spherical Bessel functions, Legendre polynomials and trigonometric functions, all obeying certain recurrence relations. These recurrence relations can be employed to eliminate any derivatives of these functions and therefore simplify numerical computations considerably (e.g. stress components are easily calculated).

In order to compute the interaction of time harmonic elastic plane waves with a hemispherical pit with a radius of the order of  $\lambda_p$  (at 2 MHz this is equivalent to a radius of 3 mm in aluminium) the following method is employed :

- a) The reflection of elastic plane waves along a plane stress free boundary is described analytically, and the results are easily expressed in spherical coordinates.
- b) The shape of the plane boundary is now deformed by a hemispherical indentation. The elastic field scattered from this indentation can be

represented as the analytical solution valid for the plane boundary plus a distortion due to the hemispherical pit. The disturbance can be represented as an infinite series of scalar potential solutions with unknown coefficients. For numerical computations the series has to be truncated, thus causing an error. The coefficients of the series can be determined in such a way as to minimise the error of the stress components along the stress free boundary (including the hemisphere) with a least squares point matching method.

- c) Having obtained the coefficients of the series it is now possible to calculate the displacement in an area surrounding the hemisphere very accurately. It is also possible to evaluate the far-field radiation patterns generated by the surface disturbance if asymptotic formulae for the spherical Bessel functions are used. This gives insight into how pits reflect and scatter elastic waves generated by an ultrasonic transducer.

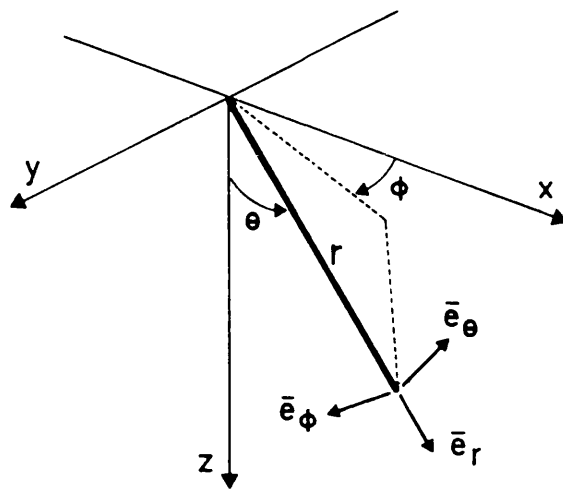


Fig. 9 : Geometry of a cartesian and a spherical coordinate system,  
taken from [9]

## 2.2 Theory

### 2.2.1 The multipole expansion of the elastic field

The elastic wave equation can be written as (see e.g. 36, 90, 91)

$$(\lambda + 2\mu) \text{grad div } \vec{u} - \mu \text{curl curl } \vec{u} - \rho \ddot{\vec{u}} = 0 \quad (2.1)$$

where  $\vec{u}$  is the elastic displacement. Any vector field can be expressed as the sum of the gradient of a scalar potential  $\varphi$  and the curl of a vector potential  $\vec{A}$ , where the divergence of  $\vec{A}$  is taken as zero. This is known as the Helmholtz theorem [41, 92]

$$\vec{u} = \text{grad } \varphi + \text{curl } \vec{A} \quad (2.2a)$$

$$\text{div } \vec{A} = 0 \quad (2.2b)$$

The substitution of (2.2a) and (2.2b) into (2.1) leads to a scalar and a vector wave equation for the two potentials

$$c_p^2 \nabla^2 \varphi - \ddot{\varphi} = 0 \quad (2.3a)$$

$$c_p^2 = \frac{(\lambda + 2\mu)}{\rho} \quad (2.3b)$$

$$c_s^2 \nabla^2 \vec{A} - \ddot{\vec{A}} = 0 \quad (2.4a)$$

$$c_s^2 = \frac{\mu}{\rho} \quad (2.4b)$$

$\rho$  designates the density, and the material constants  $\lambda$  and  $\mu$  are always positive (except for nonviscous fluids, where  $\mu$  is zero [92, 93]) and therefore

$$c_p^2 > c_s^2 \quad (2.5)$$

For time harmonic wave propagation all field quantities are proportional to

$e^{-j\omega t}$  and equations (2.3) and (2.4) simplify to<sup>2</sup>

$$\nabla^2 \varphi + k_p^2 \varphi = 0 \quad (2.6a)$$

$$k_p^2 = \frac{\omega^2}{c_p^2} = \frac{\omega^2 \rho}{\lambda + 2\mu} \quad (2.6b)$$

$$\nabla^2 \vec{A} + k_s^2 \vec{A} = 0 \quad (2.7a)$$

$$k_s^2 = \frac{\omega^2}{c_s^2} = \frac{\omega^2 \rho}{\mu} \quad (2.7b)$$

Equations (2.3) and (2.6) represent compressional wave motion with  $k_p$  as the compressional wave number, whereas equations (2.4) and (2.7) represent shear wave motion with  $k_s$  as the shear wave number

Any shear plane wave can be decomposed into two shear plane waves with orthogonal polarisation. This raises the question whether it is possible to split the shear vector potential into two independent parts, each part describing one polarisation. An analysis of (2.2a) and (2.2b) in orthogonal curvilinear coordinates shows that for six coordinate systems (including spherical coordinates) it is indeed possible to replace the vector potential  $\vec{A}$  by two scalar potentials  $\psi$  and  $\chi$ , each being the solution to the scalar wave equation in the corresponding coordinate system [41, 94, 95].

There are now three contributions to the displacement  $\vec{u}$  derived from the three scalar potentials. In spherical coordinates (where  $(r, \theta, \phi)$  denote the coordinate components) they are defined as follows :

---

<sup>2</sup> Time harmonic dependence of all field quantities is assumed from now on, and the factor  $e^{-j\omega t}$  will be omitted

$$\vec{u} = \vec{L}(k_p, r, \theta, \phi) + \vec{M}(k_s, r, \theta, \phi) + \vec{N}(k_s, r, \theta, \phi) \quad (2.8)$$

where

$$\vec{L}(k_p, r, \theta, \phi) = \text{grad } \varphi(k_p, r, \theta, \phi) \quad (2.9a)$$

$$\nabla^2 \varphi + k_p^2 \varphi = 0 \quad (2.9b)$$

$$\vec{M}(k_s, r, \theta, \phi) = \text{curl}(r \psi(k_s, r, \theta, \phi) \vec{e}_r) \quad (2.10a)$$

$$= \text{grad}(r \psi) \times \vec{e}_r \quad (2.10b)$$

$$\nabla^2 \psi + k_s^2 \psi = 0 \quad (2.10c)$$

$$\vec{N}(k_s, r, \theta, \phi) = \frac{1}{k_s} \text{curl curl}(r \chi(k_s, r, \theta, \phi) \vec{e}_r) \quad (2.11a)$$

$$= \frac{1}{k_s} \text{grad} \frac{\partial(r\chi)}{\partial r} + k_s r \chi \vec{e}_r \quad (2.11b)$$

$$\nabla^2 \chi + k_s^2 \chi = 0 \quad (2.11c)$$

with

$\vec{e}_r$  : unit vector in radial direction

$k_p$  : compressional wave number

$k_s$  : shear wave number

The elements of the stress tensors are derivatives of the displacement components. In spherical coordinates they can be written as [92]

$$\sigma_{rr} = \lambda \text{div } \vec{u} + 2\mu \frac{\partial u_r}{\partial r} \quad (2.12a)$$

$$\sigma_{\theta\theta} = \lambda \text{div } \vec{u} + 2\mu \left[ \frac{1}{r} \frac{\partial u_\theta}{\partial \theta} + \frac{u_r}{r} \right] \quad (2.12b)$$

$$\sigma_{\phi\phi} = \lambda \text{div } \vec{u} + \frac{2\mu}{r \sin \theta} \left[ \frac{\partial u_\phi}{\partial \phi} + u_r \sin \theta + u_\theta \cos \theta \right] \quad (2.12c)$$

$$\sigma_{r\theta} = \sigma_{\theta r} = \mu \left[ \frac{\partial u_\theta}{\partial r} + \frac{1}{r} \left( \frac{\partial u_r}{\partial \theta} - u_\theta \right) \right] \quad (2.12d)$$

$$\sigma_{r\phi} = \sigma_{\phi r} = \mu \left[ \frac{\partial u_\phi}{\partial r} + \frac{1}{r \sin \theta} \left( \frac{\partial u_r}{\partial \phi} - u_\phi \sin \theta \right) \right] \quad (2.12e)$$

$$\sigma_{\theta\phi} = \sigma_{\phi\theta} = \mu \left[ \frac{1}{r} \frac{\partial u_\phi}{\partial \theta} + \frac{1}{r \sin \theta} \left( \frac{\partial u_\theta}{\partial \phi} - u_\phi \cos \theta \right) \right] \quad (2.12f)$$

with

$$\text{div } \vec{u} = \frac{\partial u_r}{\partial r} + \frac{1}{r} \frac{\partial u_\theta}{\partial \theta} + \frac{u_r}{r} + \frac{1}{r \sin \theta} \left( \frac{\partial u_\phi}{\partial \phi} + u_r \sin \theta + u_\theta \cos \theta \right) \quad (2.12g)$$

The stress – potential relationships are easily derived if equations (2.8) – (2.11) are substituted into the set (2.12). Detailed expressions for the displacement and stress components in terms of the three scalar potentials can be found in Appendix A.

The general solution of the scalar wave equation in spherical coordinates is well known and can be found, for example, in [41, 94, 96]. For a scalar potential  $\varphi(k, r, \theta, \phi)$  the solution can be written as an infinite series of the form

$$\varphi(k, r, \theta, \phi) = \sum_{n=0}^{\infty} \sum_{m=0}^n \sum_{\sigma=e}^o a_{\sigma,m,n} \varphi_{\sigma,m,n}(k, r, \theta, \phi) \quad (2.13a)$$

$$\varphi_{e,m,n}(k, r, \theta, \phi) = z_n(kr) P_n^m(\cos \theta) \cos(m\phi) \quad (2.13b)$$

$$\varphi_{o,m,n}(k, r, \theta, \phi) = z_n(kr) P_n^m(\cos \theta) \sin(m\phi) \quad (2.13c)$$

with the following meaning for the subscripts

' $\sigma$ ' : index for the azimuth dependence

'e' : even azimuth dependence

'o' : odd azimuth dependence

'm' : order of solution in the azimuth direction

'n' : order of solution in the colatitude direction

$z_n$  is a spherical Bessel function of the first, second or third kind  
and of order  $n$

$P_n^m$  is the associated Legendre Polynomial of order  $(n, m)$ .

Equations (2.13) combined with (2.8) — (2.11) and the equivalent set for the stress components (see Appendix A, equations (A.10)) make it possible to write down explicit expressions for the displacement and stress components. The occurring derivatives can be eliminated using recurrence relations, so that numerical computations can be carried out easily. Such expressions can be found in [41, 94 — 96] and are derived in Appendix B.

Any time harmonic wave motion in unbounded space can now be described as an infinite series, provided that the correct choice for the radial dependence has been made (i.e. Bessel functions of the first kind for geometries including the origin and Bessel functions of the third kind for geometries extending to infinity)

$$\begin{aligned} \vec{u}(r, \theta, \phi) = & \sum_{n=0}^{\infty} \sum_{m=0}^n \sum_{\sigma=e}^o a_{\sigma,m,n} \vec{L}_{\sigma,m,n}(k_p, r, \theta, \phi) + \\ & \sum_{n=0}^{\infty} \sum_{m=0}^n \sum_{\sigma=e}^o b_{\sigma,m,n} \vec{M}_{\sigma,m,n}(k_s, r, \theta, \phi) + \\ & \sum_{n=0}^{\infty} \sum_{m=0}^n \sum_{\sigma=e}^o c_{\sigma,m,n} \vec{N}_{\sigma,m,n}(k_s, r, \theta, \phi) \end{aligned} \quad (2.14)$$

The  $a_{\sigma,m,n}$ ,  $b_{\sigma,m,n}$  and  $c_{\sigma,m,n}$  are unknown and have to be determined for any given problem. For numerical calculations the infinite series have to be

truncated and therefore constitute an approximation to the physical problem. An example of the series expansion of a particular type of wave motion, a vectorial plane wave, is given in Appendix C and will also be considered in the next chapter.

### 2.2.2 Plane waves and their reflection from plane stress free surfaces

In unbounded space, two different types of plane elastic waves can be distinguished, according to their propagation velocity :

- Compressional waves propagate with wave speed  $c_p$ , and the displacement associated with this wave type is oriented in the direction of propagation. Compressional waves (commonly also called P waves) are marked with the subscript 'p'.

$$\vec{u}_p = \vec{e}_p e^{i\vec{k}_p \vec{r}} \quad (2.15a)$$

$$\vec{e}_p \parallel \vec{k}_p \quad (2.15b)$$

- Shear waves propagate with wave speed  $c_s$  and the displacement associated with this wave type is oriented normal to the direction of propagation. Two different polarisations are possible. Shear waves with anti-plane motion, i.e. with horizontal displacement are called horizontally polarised shear waves (or short SH waves) and are characterized by the subscript 'sh'. Shear waves with in-plane motion, i.e. with vertical displacement are called vertically polarised shear waves (or short SV waves) and are marked with the subscript 'sv'.

$$\vec{u}_{sh} = \vec{e}_{sh} e^{i\vec{k}_s \vec{r}} \quad (2.16a)$$

$$\vec{e}_{sh} \perp \vec{k}_s \quad (2.16b)$$

$$\vec{u}_{sv} = \vec{e}_{sv} e^{i\vec{k}_s \vec{r}} \quad (2.17a)$$

$$\vec{e}_{sv} \perp \vec{k}_s \quad (2.17b)$$

$$\vec{e}_{sv} \perp \vec{e}_{sh} \quad (2.17c)$$

Without loss of generality the wave propagation vector  $\vec{k}$  can be assumed to lie in the  $x-z$  plane (due to the axisymmetry of the problem). The P and SV wave displacements are then also in the  $x-z$  plane, and the SH wave displacement is in the  $y$  direction. The P and SV waves are said to be decoupled from the SH wave.

The decomposition of a vectorial plane wave of arbitrary polarisation in terms of the spherical vector wave functions  $\vec{L}$ ,  $\vec{M}$  and  $\vec{N}$  is given in [94]

$$\begin{aligned} \vec{e} e^{i\vec{k}\vec{r}} = & \sum_{n=0}^{\infty} \sum_{m=0}^n \sum_{\sigma=\pm e} \epsilon_m i^n (2n+1) \frac{(n-m)!}{(n+m)!} \\ & \times \left\{ -\frac{i}{k_p} \left[ \vec{e} \cdot \vec{P}_{\sigma,m,n}(\alpha, \beta) \right] \vec{L}_{\sigma,m,n}(k_p, \theta, \phi) + \right. \\ & \frac{1}{\sqrt{n(n+1)}} \left[ \left[ \vec{e} \cdot \vec{C}_{\sigma,m,n}(\alpha, \beta) \right] \vec{M}_{\sigma,m,n}(k_s, \theta, \phi) \right. \\ & \left. \left. - i \left[ \vec{e} \cdot \vec{B}_{\sigma,m,n}(\alpha, \beta) \right] \vec{N}_{\sigma,m,n}(k_s, \theta, \phi) \right] \right\} \end{aligned} \quad (2.18)$$

where  $\vec{e}$  is the polarisation of the plane wave and  $\vec{k}$  is either the compressional or the shear wave vector. The spherical vector harmonics  $\vec{P}$ ,  $\vec{B}$  and  $\vec{C}$  together with the polarisation vector  $\vec{e}$  constitute the expansion coefficients. A detailed discussion of equation (2.18) may be found in Appendix C.

Equation (2.18) can be simplified considerably if the propagation vector is located in the  $x-z$  plane. The azimuth ( $\phi$ ) dependence of the spherical vector wave functions reduces to either  $\sin(m\phi)$  or  $\cos(m\phi)$  terms and summation over the parity is no longer necessary. Also the series expansion for a compressional wave will consist only of  $\vec{L}_{\sigma,m,n}$ , whereas the

decomposition of any shear wave will employ only  $\vec{M}_{\sigma,m,n}$  and  $\vec{N}_{\sigma,m,n}$  (see Appendix C).

A compressional plane wave incident at an angle  $\theta_i$  on to a stress free plane surface will generally result in two different reflected waves [92, 93], see Fig. 10 :

- A compressional plane wave reflected at  $\theta_p$
- A shear plane wave with vertical polarisation reflected at  $\theta_{sv}$

where

$$\theta_p = \theta_i \quad (2.19a)$$

$$\theta_{sv} = \arcsin \left( \frac{\sin \theta_i}{\kappa} \right) \quad (2.20a)$$

$$\kappa = \frac{k_s}{k_p} = \sqrt{\frac{\lambda + 2\mu}{\mu}} \quad (2.20b)$$

If  $A_i$  denotes the amplitude of the incident wave, then the amplitudes of the reflected waves are given by

$$A_p = A_i \frac{\sin 2\theta_{sv} \sin 2\theta_i - \kappa^2 \cos^2 2\theta_{sv}}{\sin 2\theta_{sv} \sin 2\theta_i + \kappa^2 \cos^2 2\theta_{sv}} \quad (2.19b)$$

for the reflected compressional wave and

$$A_{sv} = A_i \frac{-2 \kappa \sin 2\theta_i \cos 2\theta_{sv}}{\sin 2\theta_{sv} \sin 2\theta_i + \kappa^2 \cos^2 2\theta_{sv}} \quad (2.20c)$$

for the reflected shear vertical wave.

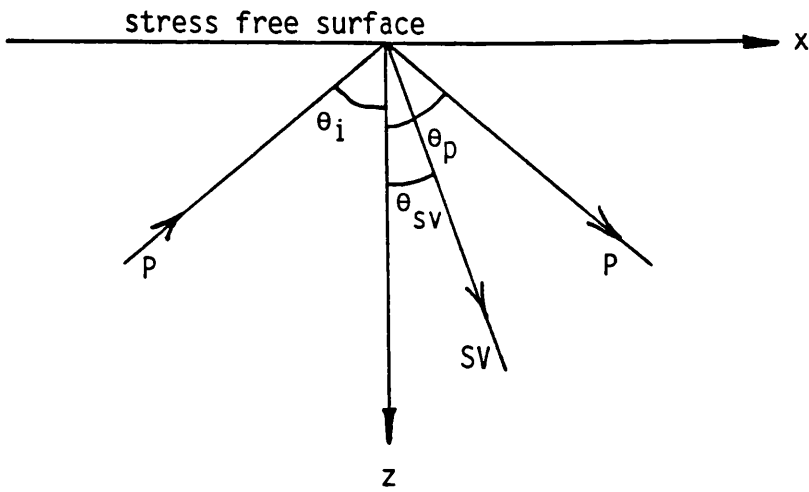


Fig. 10 : P wave incident on a stress free plane surface

Similarly, a shear plane wave incident at  $\theta_i$  on a stress free plane surface generally gives rise to a reflected shear and a compressional plane wave. The decomposition of shear waves into plane waves with horizontal and vertical polarisation requires the investigation of two cases :

An incident shear plane wave with horizontal polarisation results in a reflected shear plane wave only, the angle and amplitude of this reflected wave being (see also Fig. 11)

$$\theta_{sh} = \theta_i \quad (2.21)$$

$$A_{sh} = A_i \quad (2.22)$$

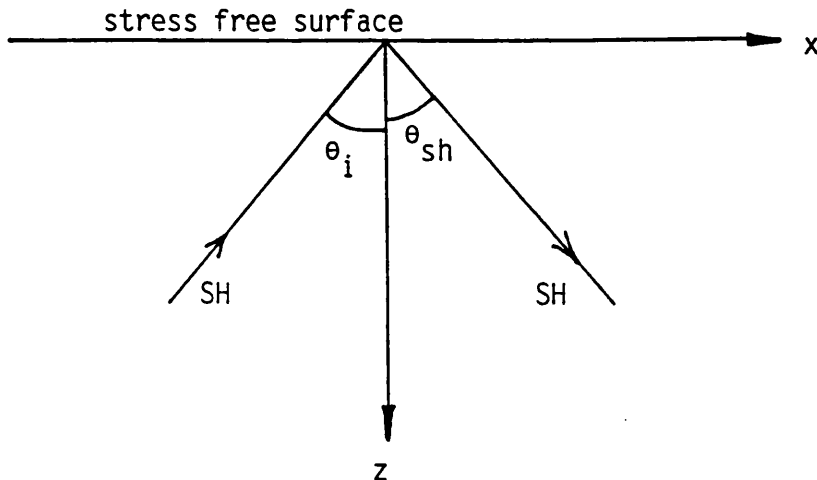


Fig. 11 : SH wave incident on a stress free plane surface

An incident shear plane wave with vertical polarisation, however, generates both a reflected shear vertical wave and a compressional wave, see Fig. 12 :

– The shear vertical wave reflects at  $\theta_{sv}$  with amplitude  $A_{sv}$

– The compressional wave reflects at  $\theta_p$  with amplitude  $A_p$

$$\theta_{sv} = \theta_i \quad (2.23a)$$

$$\theta_p = \arcsin (\kappa \sin \theta_i) \quad (2.24a)$$

$$A_{sv} = A_i \frac{\sin 2\theta_p \sin 2\theta_i - \kappa^2 \cos^2 2\theta_i}{\sin 2\theta_p \sin 2\theta_i + \kappa^2 \cos^2 2\theta_i} \quad (2.23b)$$

$$A_p = A_i \frac{\kappa \sin 4\theta_i}{\sin 2\theta_p \sin 2\theta_i + \kappa^2 \cos^2 2\theta_i} \quad (2.24b)$$

As equation (2.20b) indicates,  $\kappa$  is always greater than one. This means that there is a critical angle  $\theta_{cr}$  for the incident shear vertical wave, above which the product of  $\kappa$  and  $\sin \theta_i$  is greater than one

$$\theta_{cr} = \arcsin \left( \frac{1}{\kappa} \right) \quad (2.25)$$

Mathematical analysis shows that above the critical angle the reflected compressional wave changes its character from a propagating plane wave to a wavetype decaying exponentially with depth and propagating along the stress free surface, a so-called surface wave (or inhomogeneous plane wave). For this wave type the decomposition (2.18) is no longer valid. A shear vertical plane wave incident beyond the critical angle will therefore in this study be excluded. Expanding the incident and reflected stress and displacement components in the unperturbed half-space in cylindrical coordinates with a subsequent coordinate transformation allows the incorporation of surface waves (reflected inhomogeneous P waves as well as incident Rayleigh waves) into the model [9]. This improvement is planned as the next step in the further development of this work.

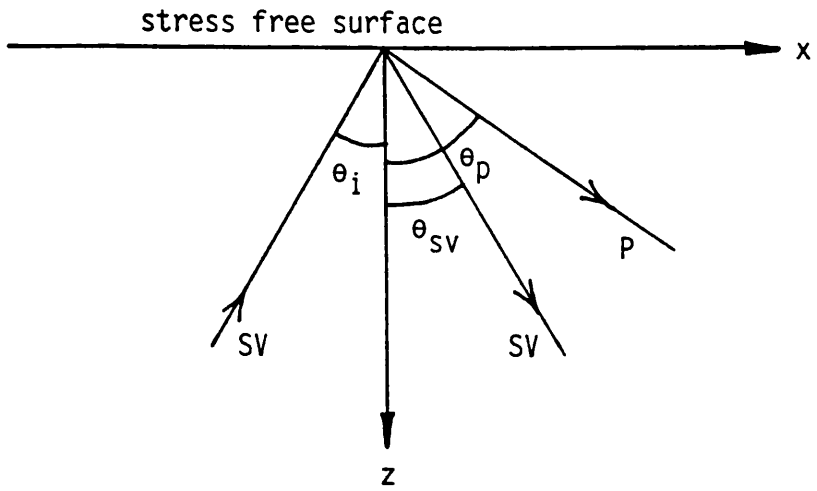


Fig. 12 : SV wave incident on a stress free plane surface

Surface waves can also occur as an independent solution to the elastic wave equation when a stress free surface is present. This wave type is called a Rayleigh wave and consists of the superposition of an inhomogeneous compressional wave and an inhomogeneous shear wave, both travelling with Rayleigh wave velocity  $c_r$  along the stress free surface [97]. If the surface is plane, then

$$c_r < c_s < c_p \tag{2.26}$$

As in the case of inhomogeneous compressional waves, the series expansion (2.18) can not be applied to Rayleigh waves. It is, however, plausible to assume that such a decomposition is possible for both types of surface waves (i.e. that the expansion (2.14) is complete in a half-space).

### 2.2.3 Implementation of the least squares matching method

For an incident plane wave the deformed surface of a stress free elastic half-space gives rise to scattered waves that are no longer simple plane waves. These waves can be described as a superposition of the plane waves reflected from the ideal half-space plus a perturbation term. The perturbation term is given as a (for numerical reasons) finite series of spherical vector functions with unknown coefficients. The coefficients are determined in such a way that the normal stress components are approximately zero along the ideally stress free surface. This can be achieved in the following way :

- For a hemispherical surface indentation in a half-space the boundary conditions can be written as

$$\sigma_{\theta\theta}(r, \theta, \phi) = 0 \quad (2.27a)$$

$$\sigma_{r\theta}(r, \theta, \phi) = 0 \quad (2.27b)$$

$$\sigma_{\theta\phi}(r, \theta, \phi) = 0 \quad (2.27c)$$

for

$$a < r < \infty \quad (2.27d)$$

$$\theta = \pi/2 \quad (2.27e)$$

$$0 \leq \phi \leq 2\pi \quad (2.27f)$$

and

$$\sigma_{rr}(r, \theta, \phi) = 0 \quad (2.28a)$$

$$\sigma_{r\theta}(r, \theta, \phi) = 0 \quad (2.28b)$$

$$\sigma_{r\phi}(r, \theta, \phi) = 0 \quad (2.28c)$$

for

$$r = a \quad (2.28d)$$

$$0 \leq \theta \leq \frac{\pi}{2} \quad (2.28e)$$

$$0 \leq \phi \leq 2\pi \quad (2.28f)$$

where  $a$  is the radius of the hemispherical surface obstacle.

- The stress components due to the half-space are sampled along the distorted surface in an area of, say,  $-3a \leq r \leq 3a$ . The number of sampling points employed is  $n_1$  along the hemisphere and  $n_2$  along the plane part of the surface, the numbers are chosen so that the distribution of points along the entire surface is equidistant (see Fig. 13). The half-space satisfies equations (2.27) by definition, and therefore the sampled normal stress components along the plane part of the surface vanish. This will, however, not be the case for the normal stresses on the surface of the hemisphere.

The normal stress components at the sampling points along the hemisphere are

$$\vec{e}_n \vec{\sigma}_{hs} \Big|_{\vec{r}_i} = \vec{t}_{hs} \Big|_{\vec{r}_i} \quad (2.29a)$$

$$1 \leq i \leq n_1 \quad (2.29b)$$

and sampling along the plane surface yields

$$\vec{e}_n \vec{\sigma}_{hs} \Big|_{\vec{r}_i} = \vec{t}_{hs} \Big|_{\vec{r}_i} = 0 \quad (2.29c)$$

$$n_1 + 1 \leq i \leq n_1 + n_2 \quad (2.29d)$$

Here  $\vec{e}_n$  indicates the normal to the surface and the subscript 'hs' refers to the half-space. The three normal stress components are, as is commonly done, combined in vector form to give the so-called traction vector  $\vec{t}$ .

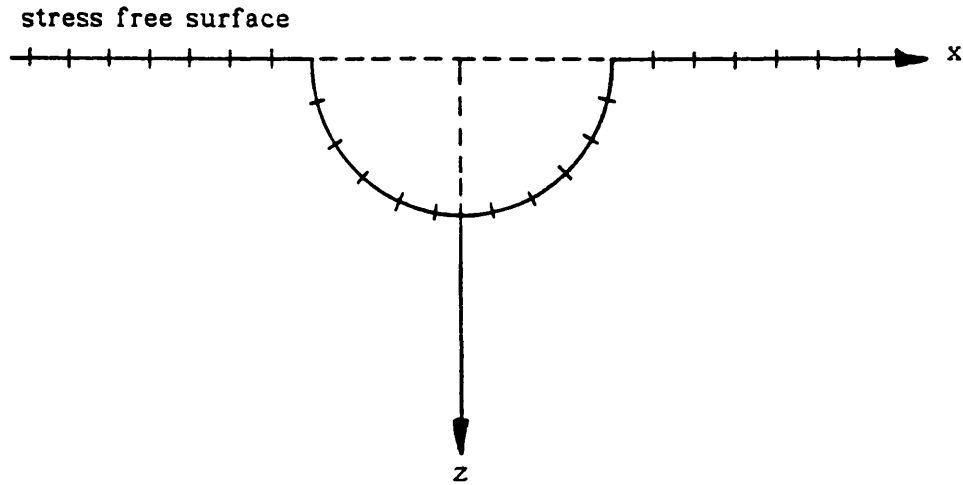


Fig. 13 : Sampling path in the  $x-z$  plane indicating the stress free surface of a half-space with hemispherical surface indentation

— Now the stress components due to the spherical vector functions (see Appendix B, equations (B10) – (B.15)) are evaluated

$$\vec{e}_n \vec{\sigma}_{\varphi,m,n} \Big|_{\vec{r}_i} = \vec{t}_{\varphi,m,n} \Big|_{\vec{r}_i} \quad (2.30a)$$

$$\vec{e}_n \vec{\sigma}_{\psi,m,n} \Big|_{\vec{r}_i} = \vec{t}_{\psi,m,n} \Big|_{\vec{r}_i} \quad (2.30b)$$

$$\vec{e}_n \vec{\sigma}_{\chi,m,n} \Big|_{\vec{r}_i} = \vec{t}_{\chi,m,n} \Big|_{\vec{r}_i} \quad (2.30c)$$

at the sampling points along the hemisphere

$$1 \leq i \leq n_1 \quad (2.30d)$$

and at the sampling points along the plane surface

$$n_1 + 1 \leq i \leq n_1 + n_2 \quad (2.30e)$$

Spherical Bessel functions of the third kind (i.e. spherical Hankel functions of the first kind) were chosen for the radial dependence of the spherical vector functions and hence the stress components in order to guarantee outgoing spherical waves at infinity.

- Observing the boundary conditions along the sampling points leads to a set of linear equations

$$\sum_{n=0}^{n_m-1} \sum_{m=0}^n \left( a_{m,n} \vec{t}_{\varphi,m,n} \Big|_{\vec{r}_i} + b_{m,n} \vec{t}_{\psi,m,n} \Big|_{\vec{r}_i} + c_{m,n} \vec{t}_{\chi,m,n} \Big|_{\vec{r}_i} \right) + \vec{t}_{hs} \Big|_{\vec{r}_i} = 0 \quad (2.31a)$$

for the sampling points along the hemisphere

$$1 \leq i \leq n_1 \quad (2.31b)$$

and for the sampling points along the plane surface

$$n_1 + 1 \leq i \leq n_1 + n_2 \quad (2.31c)$$

where  $n_m$  is the number of terms employed for the series expansion. A summation over the parity in equation (2.31a) is not necessary for reasons that will become clear in chapter 2.2.4.

The system (2.31) consists of  $3 \times (n_1 + n_2)$  complex equations with  $3 \times \frac{n_m(n_m + 1)}{2}$  complex unknowns. If the total number of sampling points is chosen so that the number of equations is equal to the number of unknowns, then (2.31) is a (hopefully) determined system of equations with a unique solution for the unknown coefficients  $a_{m,n}$ ,  $b_{m,n}$  and  $c_{m,n}$ . This solution enforces the boundary conditions at the sampling points, but allows for non-zero normal stress components in the intervall between them.

- The total number of sampling points can also be chosen to be much greater than the number of unknowns. The system (2.31) is then overdetermined and can be solved in a least squares sense [98 — 100]. This means that the normal stress components are no longer forced to vanish at certain points but that their deviations from zero along the sampling points (the so-called residuals) are minimised, thus ensuring small but

slowly varying errors everywhere along the boundary. Equation (2.31a) can now be written as

$$\sum_{n=0}^{n_m-1} \sum_{m=0}^n \left( a_{m,n} \vec{t}_{\varphi,m,n} \Big|_{\vec{r}_i} + b_{m,n} \vec{t}_{\psi,m,n} \Big|_{\vec{r}_i} + c_{m,n} \vec{t}_{\chi,m,n} \Big|_{\vec{r}_i} \right) \simeq - \vec{t}_{hs} \Big|_{\vec{r}_i} \quad (2.32a)$$

$$1 \leq i \leq n_1 + n_2 \quad (2.32b)$$

or in matrix form<sup>3</sup>

$$\underline{\underline{A}} \vec{x} \simeq \vec{t} \quad (2.33)$$

The vector  $\vec{x}$  contains the unknown coefficients  $a_{m,n}$ ,  $b_{m,n}$  and  $c_{m,n}$ , the vector  $\vec{t}$  contains the traction components at the sampling points and the matrix  $\underline{\underline{A}}$  (called the design matrix) consists of the normal stress components due to the potentials  $\varphi$ ,  $\psi$  and  $\chi$  at the sampling points. The overdetermined system of linear equations (2.33) is solved in the least squares sense by QR factorisation or by singular value decomposition of the matrix  $\underline{\underline{A}}$ , details can be found in [98 – 100].

In the limit for  $n_m \rightarrow \infty$  and under the assumption that the spherical vector functions form a complete set in the elastic half-space it can be shown that the error residuals along the boundary will vanish everywhere on the surface, thus giving an exact solution to the scattering problem.

---

<sup>3</sup> The matrix character of a quantity is indicated by underlining

#### 2.2.4 Azimuthal decomposition of the elastic field

The shape of the surface perturbation is axisymmetric with respect to the  $z$  axis and is therefore independent of the azimuth coordinate  $\phi$ . This allows a decomposition of the three-dimensional scattering problem into several two-dimensional sub-problems with given  $\phi$  dependence :

The azimuth dependence of the displacement and stress components of the incident and scattered wave field are described as a superposition of trigonometric functions

$$f(\phi) = \sum_{m=0}^{\infty} A_m \cos(m\phi) + B_m \sin(m\phi) \quad (2.34)$$

where  $f(\phi)$  can be a stress or displacement component.

This is a Fourier expansion of the function  $f(\phi)$  with respect to the (spatial) variable  $\phi$  in the interval  $[0, 2\pi]$ . The shape of the scatterer is independent of  $\phi$  and therefore does not alter the azimuth dependence of the the individual Fourier components of the elastic field, hence it is possible to regard each component separately.

Equation (2.34) simplifies if the wave vector of the incident wave is located in the  $x-z$  plane. This amounts to a rotation of the coordinate system around the  $z$  axis so that either  $A_m \equiv 0$  or  $B_m \equiv 0$  for all  $m$ . The angular dependence of the displacement components then reduce to (see Appendix C) :

a) incident P or SV wave

$u_r, u_\theta, \sigma_{rr}, \sigma_{\theta\theta}, \sigma_{\phi\phi}$  and  $\sigma_{r\theta}$  are proportional to  $\cos(m\phi)$

$u_\phi, \sigma_{r\phi}$  and  $\sigma_{\theta\phi}$  are proportional to  $-\sin(m\phi)$

and

b) incident SH wave

$u_r, u_\theta, \sigma_{rr}, \sigma_{\theta\theta}, \sigma_{\phi\phi}$  and  $\sigma_{r\theta}$  are proportional to  $\sin(m\phi)$

$u_\phi, \sigma_{r\phi}$  and  $\sigma_{\theta\phi}$  are proportional to  $\cos(m\phi)$

In the case of normally incident compressional or shear waves (i.e. plane waves with a wave vector parallel to the z axis) the angular dependence simplifies even more. For normally incident compressional waves the displacement varies in the z direction, and there is no azimuth variation of the displacement or stress components :

$u_r, u_\theta, \sigma_{rr}, \sigma_{\theta\theta}, \sigma_{\phi\phi}$  and  $\sigma_{r\theta}$  are non-zero, but without any  $\phi$  dependence and  $u_\phi, \sigma_{r\phi}$  and  $\sigma_{\theta\phi}$  are zero.

For normally incident shear vertically polarised waves the displacement varies in the x-direction :

$u_r, u_\theta, \sigma_{rr}, \sigma_{\theta\theta}, \sigma_{\phi\phi}$  and  $\sigma_{r\theta}$  are proportional  $\cos \phi$ ,

$u_\phi, \sigma_{r\phi}$  and  $\sigma_{\theta\phi}$  are proportional to  $-\sin \phi$ .

Normally incident shear horizontally polarised waves consist of a displacement component in the y direction only :

$u_r, u_\theta, \sigma_{rr}, \sigma_{\theta\theta}, \sigma_{\phi\phi}$  and  $\sigma_{r\theta}$  are proportional to  $\sin \phi$ ,

$u_\phi, \sigma_{r\phi}$  and  $\sigma_{\theta\phi}$  are proportional to  $\cos \phi$ .

The general case of compressional or shear waves incident onto a stress free surface with the wave vector located in the x-z plane can be split into  $n_m$  sub-problems. These can be regarded as two-dimensional with a fixed azimuth dependence ( $0 \leq m \leq n_m - 1$ ) factorised out of the problem (see Appendix C, equations (C.16) and (C.18)). The scattering problem can now be solved for each of the sub-problems separately, whereby equations (2.32) are rewritten as

$$\sum_{n=m}^{n_m-1} \left( a_{m,n} \vec{t}_{\varphi,m,n} \Big|_{\vec{r}_i} + b_{m,n} \vec{t}_{\psi,m,n} \Big|_{\vec{r}_i} + c_{m,n} \vec{t}_{\chi,m,n} \Big|_{\vec{r}_i} \right) \simeq - \vec{t}_{hs,0} \Big|_{\vec{r}_i} \quad (2.35a)$$

$$1 \leq i \leq n_1 + n_2 \quad (2.35b)$$

$$0 \leq m \leq n_m - 1, m \text{ fixed} \quad (2.35c)$$

due to the requirement<sup>4</sup> that  $n \geq |m|$ .

Then the azimuth dependence is taken into account and the problems are superimposed to give the full three-dimensional solution. For normally incident plane waves there is only one sub-problem,  $m = 0$  for compressional waves and  $m = 1$  for shear waves.

---

<sup>4</sup> There will be no contribution to the displacement and stress components for  $|m| > n$  since then the Legendre polynomials  $P_n^m$  are identically zero

### 2.2.5 Non-hemispherical surface obstacles

It is possible to apply the least squares matching method described in chapter 2.2.3 to axisymmetric surface obstacles with a cross-sectional shape other than that of a semi-circle. This requires a modification of the boundary conditions (2.28). The normal  $\vec{e}_n$  and the tangential  $\vec{e}_t$  to the surface of the disturbance are no longer equivalent to  $\vec{e}_r$  and  $\vec{e}_\theta$ , respectively. The vanishing normal stress components along the surface of the indentation are now linear combinations of the different components of the stress tensor in spherical coordinates. They can be obtained by a coordinate transformation, see [101] :

$$\sigma_{nn} = \sigma_{rr} \cos^2 \alpha + \sigma_{\theta\theta} \sin^2 \alpha - 2 \sigma_{r\theta} \cos \alpha \sin \alpha \quad (2.36a)$$

$$\sigma_{nt} = \sigma_{rr} \cos \alpha \sin \alpha - \sigma_{\theta\theta} \cos \alpha \sin \alpha + \sigma_{r\theta} \cos 2\alpha \quad (2.36b)$$

$$\sigma_{n\phi} = \sigma_{r\phi} \cos \alpha - \sigma_{\theta\phi} \sin \alpha \quad (2.36c)$$

The tangential stress components can be expressed as

$$\sigma_{tt} = \sigma_{rr} \sin^2 \alpha + \sigma_{\theta\theta} \cos^2 \alpha + 2 \sigma_{r\theta} \cos \alpha \sin \alpha \quad (2.36d)$$

$$\sigma_{\phi\phi} = \sigma_{\phi\phi} \quad (2.36e)$$

$$\sigma_{t\phi} = \sigma_{r\phi} \sin \alpha + \sigma_{\theta\phi} \cos \alpha \quad (2.36f)$$

and the displacement are now

$$u_n = u_r \cos \alpha - u_\theta \sin \alpha \quad (3.37a)$$

$$u_t = u_r \sin \alpha + u_\theta \cos \alpha \quad (2.37b)$$

$$u_\phi = u_\phi \quad (2.37c)$$

where  $\alpha$  is the rotation angle in the  $r - \theta$  plane, see Fig. 14. Due to the axisymmetry of the geometry the  $\phi$  component is not affected by the rotation and is therefore not shown in the diagram.

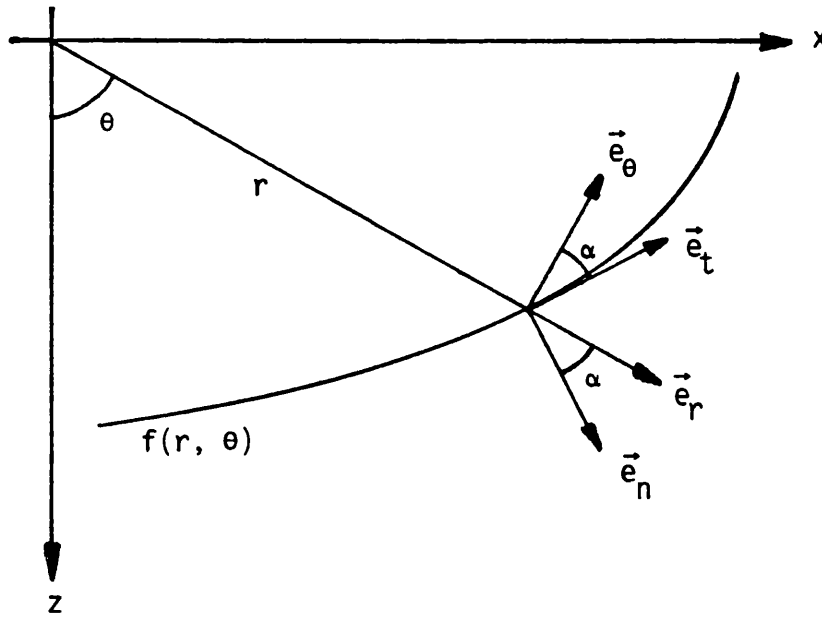


Fig. 14 : Unit normals and rotation angle  $\alpha$  of a coordinate transformation in the  $r - \theta$  plane

The angle  $\alpha$  depends on the form of the surface and is a function of the coordinates  $r$  and  $\theta$ . Four cross-sectional shapes were considered and their shape is given in spherical coordinates in a parametric form together with the rotation angle and the angle  $\alpha_0$  with the normal to the plane free surface at the intersection :

a) Hemicircle of given radius  $a$

This case is trivial :

$$r(t) = a \quad (2.38a)$$

$$\theta(t) = t \quad (2.38b)$$

$$\alpha(t) = 0 \quad (2.38c)$$

$$0 \leq t \leq \frac{\pi}{2} \quad (2.38d)$$

$$\alpha_0 = 0 \quad (2.38e)$$

b) Section of a hemicircle with given surface diameter  $2a$  and depth  $d$ , see Fig. 15. This case includes the hemicircle as special case ( $d = a$ ) :

$$r(t) = \sqrt{R^2 - 2 R h \cos t + h^2} \quad (2.39a)$$

$$\theta(t) = \arctan \left( \frac{R \sin t}{R \cos t - h} \right) \quad (2.39b)$$

$$\alpha(t) = \arctan \left( \frac{h \sin t}{R - h \cos t} \right) \quad (2.39c)$$

$$0 \leq t \leq 2 \arctan \frac{d}{a} \quad (2.39d)$$

$$R = \frac{d^2 + a^2}{2d} \quad (2.39e)$$

$$h = R - d \quad (2.39f)$$

$$\alpha_0 = \arctan \frac{h}{\sqrt{R^2 - h^2}} \quad (2.39g)$$

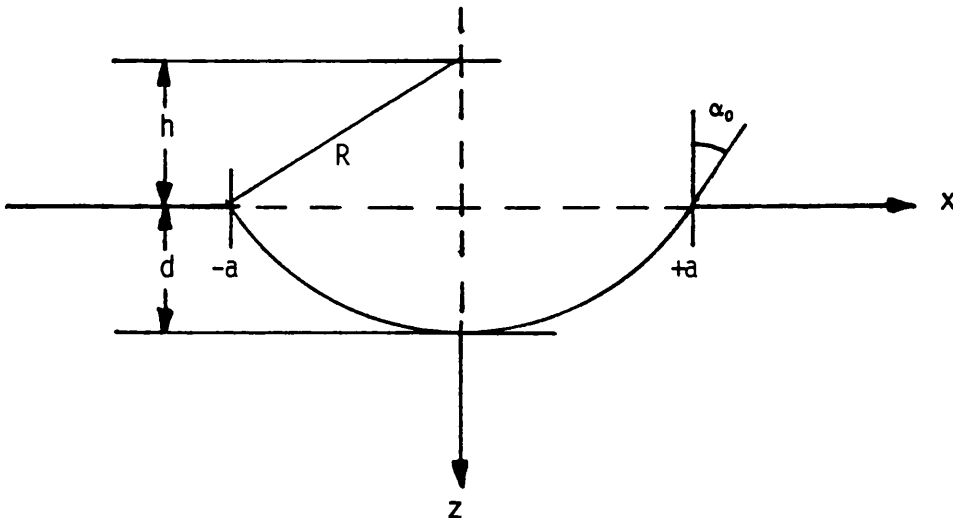


Fig. 15 : Surface obstacle with the shape of a section of a hemicircle

c) Semi-ellipse with given surface diameter  $2a$  and depth  $d$ , see Fig. 16.

This case includes the hemicircle as special case ( $d = a$ ) :

$$r(t) = \sqrt{a^2 \sin^2 t + d^2 \cos^2 t} \quad (2.40a)$$

$$\theta(t) = \arctan \left( \frac{a}{d} \tan t \right) \quad (2.40b)$$

$$\alpha(t) = \arctan \left( \frac{(a^2 - d^2) \cos t \sin t}{a d} \right) \quad (2.40c)$$

$$0 \leq t \leq \frac{\pi}{2} \quad (2.40d)$$

$$\alpha_0 = 0 \quad (2.40e)$$

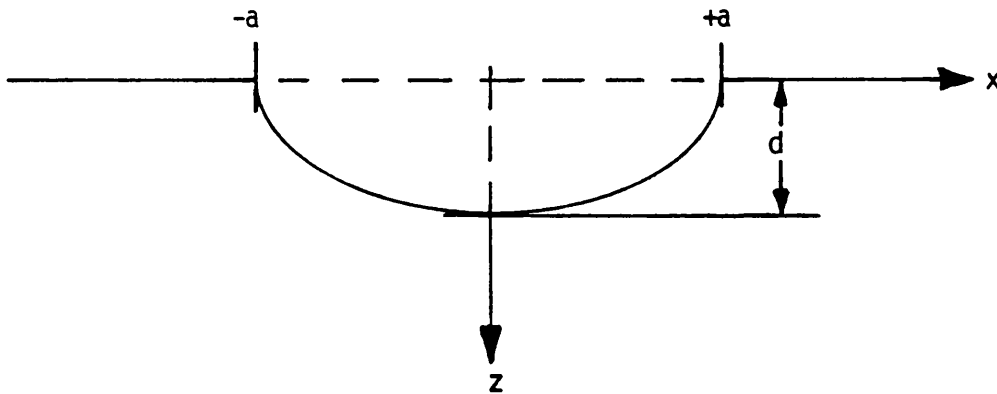


Fig. 16 : Surface obstacle with the shape of a semi-ellipse

d) Section of a semi-ellipse with given surface diameter  $2a$ , depth  $d$  and angle  $\alpha_0$ , see Fig. 17. Cases a — c are included for special values of  $a$ ,  $d$  and  $\alpha_0$  :

$$r(t) = \sqrt{b_2^2 \sin^2 t + b_1^2 \cos^2 t - 2 b_1 h \cos t + h^2} \quad (2.41a)$$

$$\theta(t) = \arctan \left( \frac{b_2 \sin t}{b_1 \cos t - h} \right) \quad (2.41b)$$

$$\alpha(t) = \arctan \left( \frac{(b_2^2 - b_1^2) \sin t \cos t + b_1 h \sin t}{b_1 b_2 - b_2 h \cos t} \right) \quad (2.41c)$$

$$0 \leq t \leq \arccos \frac{h}{d+h} \quad (2.41d)$$

$$h = \frac{d^2 \tan \alpha_0}{a - 2 d \tan \alpha_0} \quad (2.41e)$$

$$b_1 = d + h \quad (2.41f)$$

$$b_2 = \frac{(d+h)a}{\sqrt{d^2 + 2dh}} \quad (2.41g)$$

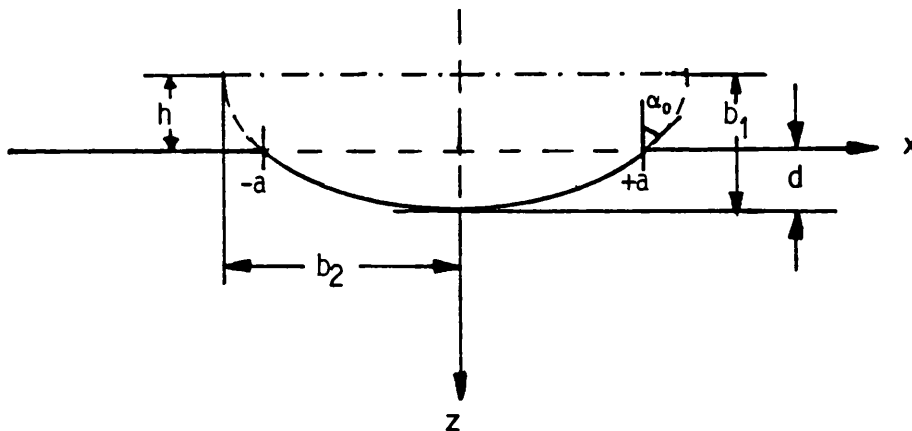


Fig. 17 : Surface obstacle with the shape of a section of a semi-ellipse

The modified boundary conditions along the stress-free surface can now be written as

$$\sigma_{\theta\theta}(r, \theta, \phi) = 0 \quad (2.42a)$$

$$\sigma_{r\theta}(r, \theta, \phi) = 0 \quad (2.42b)$$

$$\sigma_{\theta\phi}(r, \theta, \phi) = 0 \quad (2.42c)$$

for

$$a < r < \infty \quad (2.42d)$$

$$\theta = \pi/2 \quad (2.42e)$$

$$0 \leq \phi \leq 2\pi \quad (2.42f)$$

and

$$\sigma_{nn}(r, \theta, \phi, \alpha) = 0 \quad (2.43a)$$

$$\sigma_{nt}(r, \theta, \phi, \alpha) = 0 \quad (2.43b)$$

$$\sigma_{n\phi}(r, \theta, \phi, \alpha) = 0 \quad (2.43c)$$

$$r = r(t) \quad (2.43d)$$

$$\theta = \theta(t) \quad (2.43e)$$

$$\alpha = \alpha(t) \quad (2.43f)$$

for

$$0 \leq t \leq t_{max} \quad (2.43g)$$

$$0 \leq \phi \leq 2\pi \quad (2.43h)$$

where the sampling path along the surface of the indentation is determined by its shape, and the sampling points are given by discrete values of the parameter  $t$  within the limits

$$\begin{array}{llll} t = 0 & r = d & \theta = 0 & \alpha = 0 \\ t = t_{max} & r = a & \theta = \frac{\pi}{2} & \alpha = \alpha_0 \end{array}$$

The unknown coefficients in the expansion of the scattered field can now be calculated in exactly the same manner as previously described. The

only alteration to chapter 2.2.3 is that now the normal stress components consist of a linear combination of stress components in spherical coordinates rather than one single stress component. However, since the stress components (2.36a) — (2.36f) emerge from the same potential, the expansion coefficient will be the same for all six components.

By modelling the scattering from surface indentations other than hemispheres some consideration has to be given to the representation of the scattered field. The expansion (2.14) employs only outgoing spherical wave functions. For many types of surface shapes (e.g. surface obstacles that undercut the surface) such an expansion does not represent all occurring wavetypes, since incoming waves due to multiple scattering have been neglected. This problem has received widespread attention in form of the so-called Rayleigh hypothesis in the area of electromagnetic wave scattering [102, 103]. The surface shapes that are considered in this study were originally chosen so that the scattered field could safely be represented in terms of solely outward propagating elastic waves : hemispheres and segments of hemispheres will not give rise to multiple scattering, independent of the angle of incidence of the incoming plane wave. Some investigations were then made into the scattering from semi-ellipsoids. A representation of the scattered field by only outgoing waves gives physically meaningful results, and therefore seems to be correct, see chapter 3. The scattering from the generalised surface feature of a section of an ellipsoid (shape d) has not been investigated so far (although implemented in the computer simulation program), and a further study might reveal interesting results for this case.

## Chapter 3 : Results

### 3.1 Numerical accuracy

In order to test the accuracy of the multipole expansion of the elastic field it is most useful to compare the computed values of a truncated expansion of a known harmonic wave motion with the values derived from the analytic expression of that wave motion. This has been done using expansion (2.18) for compressional and shear plane waves propagating at arbitrary angles through an unbounded elastic medium. The maximum number of terms in (2.18)  $n_{max}$  was chosen to be 12, 16 and 20, and the computed displacement components were divided by the values obtained from the analytic expression for plane waves. The normalised magnitude and phase of the  $u_x$  displacement component of P and SV waves plotted against the normalised distance from the origin  $kr$  are shown in section 3.2. The results for SH waves are identical to the results for SV waves, also the graphs of the normalised displacement components  $u_y$  and  $u_z$  are identical to the ones of  $u_x$ , and so plots for these cases were omitted. Figures 18 — 29 show clearly that the accuracy of the expansion improves with increasing number of terms. Both magnitude and phase are stable up to a critical point  $(kr)_{crit}$ , then the approximation breaks down. The value of this critical point increases with increasing number of terms. From this it is reasonable to conclude that the accuracy is mainly determined by the spherical Bessel functions  $z_n(kr)$ . The relation between the number of terms and the critical values for  $kr$  is tabulated below, where the critical point is defined as :

$$kr = (kr)_{crit} \quad \text{when normalised magnitude} < 0.99$$
$$\quad \quad \quad \text{or normalised magnitude} > 1.01$$

number of terms	compressional wave	shear wave
	$(kr)_{crit}$	$(kr)_{crit}$
8	3.0	5.2
12	6.7	7.5
16	10.5	12.0
20	13.5	14.2

Table 1 : Critical values of  $kr$  for a multipole expansion of a plane compressional or shear wave

This table shows that it is possible to represent a plane compressional or shear wave by a multipole expansion using 20 terms with 1% accuracy in a domain of  $kr \leq 13.0$  or  $r \leq 2\lambda$ . This result will equally apply to any kind of wave motion, provided that the expansion coefficients are properly chosen.

An investigation of the accuracy of the stress components generated by a plane compressional or shear wave shows that the value of the critical point there is somewhat lower than that for the critical point for the displacements (using the same number of terms). This is to be expected since the stress components are derivatives of the displacements and will therefore be less accurate.

A further point that needs investigation is the handling and accuracy of the least squares point matching procedure. Ideally an increase in the number of basis functions leads to an increase in accuracy. However, this also lowers the condition number of the design matrix  $\underline{A}$  due to spherical Hankel functions of high order evaluated near the origin. The high order basis functions become linearly dependent within the numerical accuracy of

the computer program and the least squares method generates inaccurate results. The coefficients obtained for a set containing degenerated basis functions still produce a least squares approximation to the scattering problem in the near-field, but they do not reflect any longer the true physical contribution of each basis function to the scattered field (since the degeneracy is only numerical, not actual). As a consequence the far-field results will be incorrect when obtained from a set of basis functions that are degenerate in the numerical sense. Also the near-field results will become increasingly inaccurate with an increasing number of degenerate basis functions. There will be an optimal value for the number of basis functions just before degeneracy occurs. This optimal value can be found by increasing the number of basis functions until the singular value decomposition indicates the break down in accuracy via the spread of singular values with respect to a tolerance parameter [98 — 100]. The example given below looks at the rank of the design matrix and the total least squares residual (i.e. the sum of all the residual normal stress components along the sampling points) as the number of basis functions increases. The chosen scattering problem was also calculated in [9], it consists of a compressional wave normally incident on to a hemispherical surface indentation in a half-space. The ratio of diameter of the surface obstacle to incident wavelength is 0.5, i.e. the radius of the hemispherical indentation is a quarter of an incident wavelength. It can clearly be seen that with increasing number of basis functions the least squares residual decreases, thereby giving improved solutions. As soon as the set of basis functions contains linearly dependent elements the matrix becomes degenerate and the accuracy degrades. The observation of this is independent of the incident wave type, angle of incidence and material properties. All the examples presented in this thesis were calculated using

the optimum value for the number of basis functions, which for the example below is 13 basis functions. The result given in [9] employs 15 basis functions and it can be seen that the least squares residual for this case is higher than the residual of the result presented here (see section 3.3). The residual normal stress components normally have their largest values near the rim of the indentation.

Number of basis functions $n_{max}$	rank of design matrix $\underline{A}$	total least squares residual
10	38	2.7916
11	42	2.5166
12	46	2.1026
13	50	1.6635
14	52 (degenerate)	2.5926
15	50 (degenerate)	4.6154
16	42 (degenerate)	29.649

Table 2 : Total least squares residual as function of the number of basis functions in the multipole expansion

It was found that the least squares matching method is not very sensitive to the number of points along the sampling path as long as the total number is much greater than the number of basis functions used in the expansion of the scattered field. Due to the axisymmetry of the surface perturbation it is possible to perform the least squares matching procedure along the positive x axis only for a given azimuth dependence (see chapters 2.2.4 and 2.2.5). The number of sampling points used to obtain the results

shown in this chapter were :

$n_{s1} = 35$  along the surface indentation

$n_{s2} = 45$  along the plane surface,  $a < x < 3a$

So far, there have been very few publications on elastic wave scattering from three-dimensional surface features [8], all of which deal with the surface amplitudes near the indentation. The number of cases available for a comparison of results is therefore limited and has to be confined to a discussion of the near-field results. The method presented here follows the approach of [9], where the surface motion of a three-dimensional hemispherical surface indentation under the influence of normally incident compressional waves was investigated. The results obtained by [9] for this case are shown in section 3.3, where they are compared with results calculated here. They compare very well, and the minor discrepancies can be explained by the difference in the number of employed basis functions and possibly by a different treatment of the corners between the surface disturbance and the plane surface. No information on the treatment of these corners is given in [9], but it is assumed that the edges were rounded. This can be concluded from the horizontal surface movements, which are shown as smooth curves in [9]. The present study assumes sharp corners throughout, which are 90 degrees for a hemispherical surface indentation. This results in a less smooth behaviour of the horizontal surface movements near the corner and in slightly larger surface movements along the plane surface.

Cases of non-normal incidence of elastic waves on to a hemispherical surface indentation were published in [8] and [104]. These cases were also compared to calculated results in section 3.3. The results presented in [8] (Figs. 34 and 35) were calculated by the same method that was used here and

show very good agreement. The surface movements of the x displacement component shows a slightly larger amplitude in the y-z plane near the rim of the indentation for the case calculated for this study. This could be due to a rounded corner in [8] or due to a different arrangement of the sampling points near the corner. The number of basis functions used was chosen to be 13 for the result obtained by the present study, and is not known for the result given in [8]. A difference in the number of basis functions could also contribute to the slightly stronger surface motion in Fig 35. The results presented in [104] were calculated with a wave expansion method employing the orthogonality and the power series representation in r, the radial distance, of the spherical wave functions. The surface displacements in [104] are only given outside the indentation, and due to their presentation it is difficult to compare the shape of the surface displacements with results calculated here. A detailed discussion can be found in section 3.3.

A great number of studies have been carried out in order to calculate the near-field displacements of compressional and shear waves scattered from two-dimensional canyons [78, 80, 83, 105 — 107]. Results for these cases are considered as limiting cases and are compared with three-dimensional results in section 3.3.

Section 3.4 presents the surface displacements and far-field plots for compressional wave incident under 60 degrees and a shear waves normally incident on to a on to a growing pit in an aluminium plate with Poisson's ratio  $\nu = 0.34$ . The various stages of the growing pit are represented by hemispherical and shallow surface indentations of various shapes and dimensions.

Section 3.5 compares numerical (single frequency) results with measurements for a compressional or shear wave pulse normally incident on to a hemispherical surface indentation in an aluminium block. Two different surface features were considered : the first was 1.6 mm in diameter, the second was 3.2 mm in diameter. The centre frequency of the incident compressional wave pulse was 1MHz (with a compressional wavelength of 6.4 mm in aluminium), and the centre frequency of the incident shear wave pulse was 2 MHz (with a shear wavelength of 1.6 mm in aluminium), thereby giving the following diameter to incident wavelength ratios at the centre frequency :

— incident compressional wave :  $\frac{2a}{\lambda_{inc}} = 0.25$  and  $0.5$

— incident shear wave :  $\frac{2a}{\lambda_{inc}} = 1.0$  and  $2.0$

3.2 Expansion of plane compressional and shear waves in terms of spherical vector functions

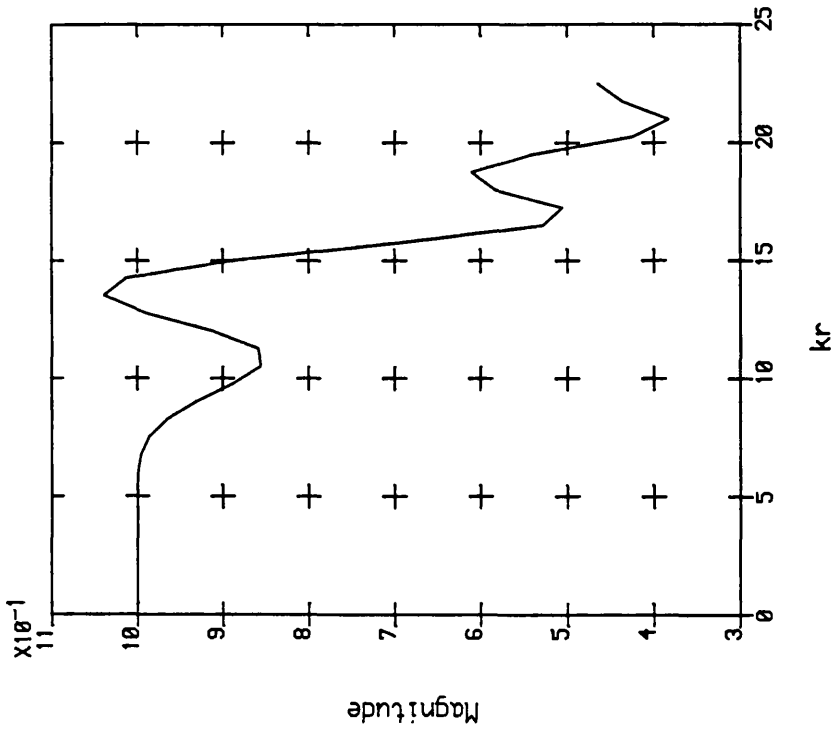


Fig. 18 : Normalised x - displacement, spherical vector harmonics approximation, truncated to 12 terms, P - Wave

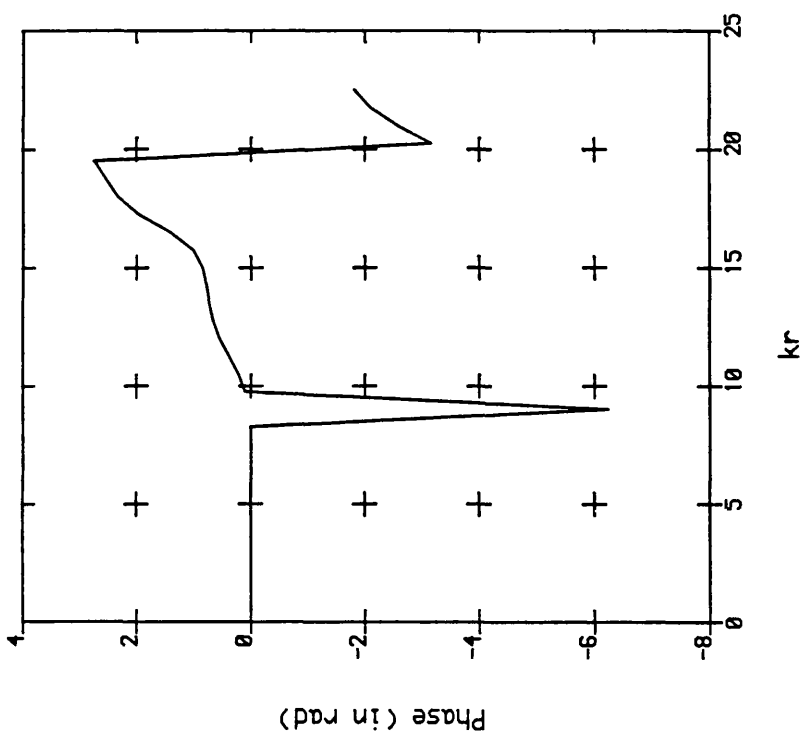


Fig. 19 : Normalised x - displacement, spherical vector harmonics approximation, truncated to 12 terms, P - Wave

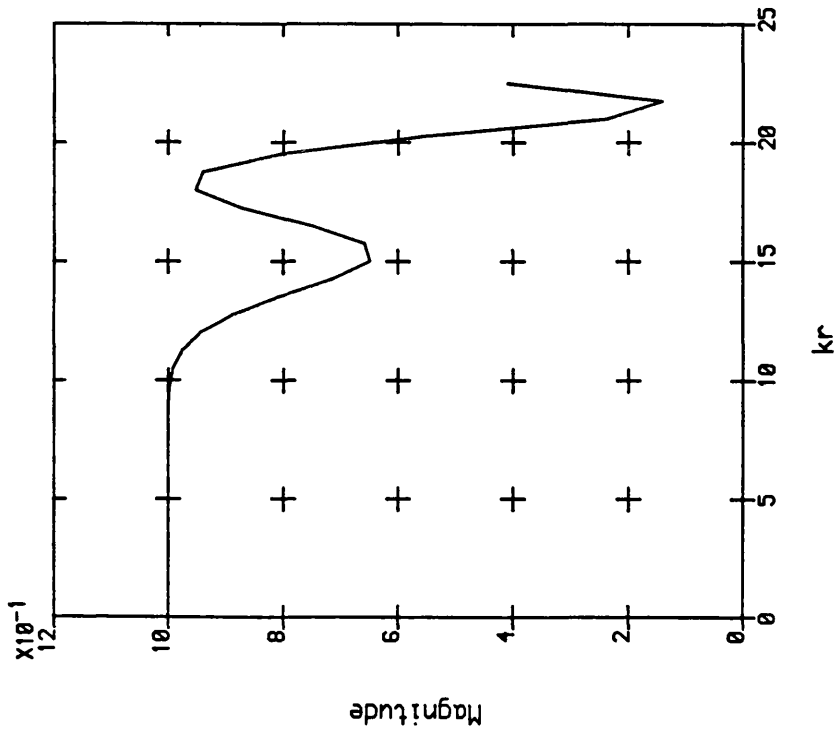


Fig. 20 : Normalised x - displacement, spherical vector harmonics approximation, truncated to 16 terms, P - Wave

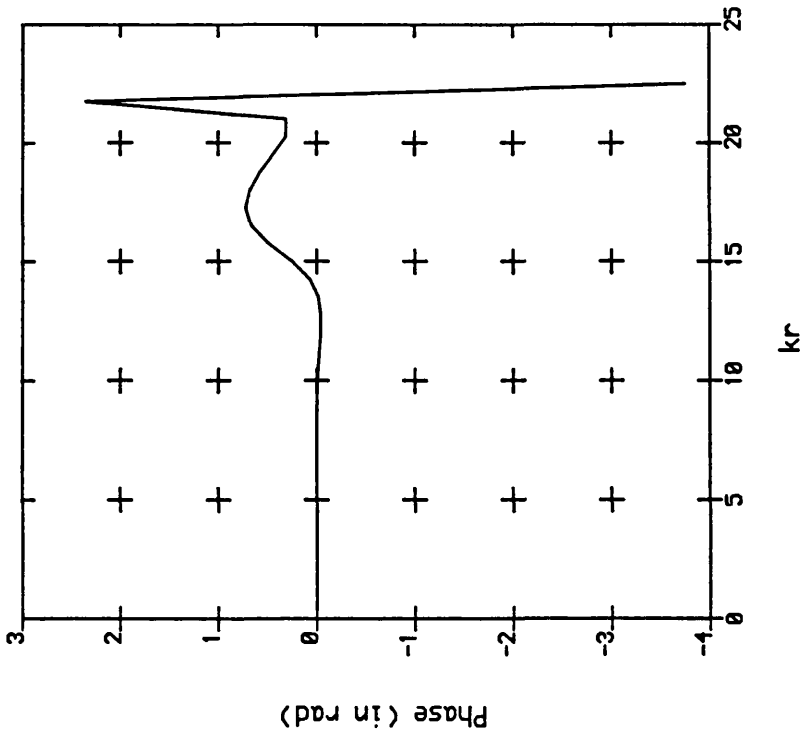


Fig. 21 : Normalised x - displacement, spherical vector harmonics approximation, truncated to 16 terms, P - Wave

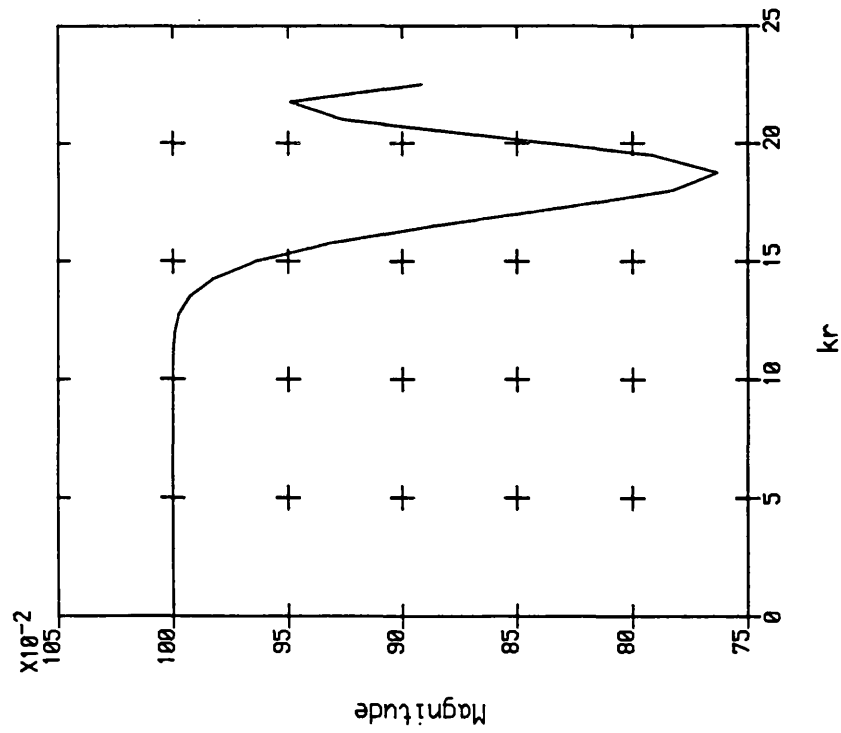


Fig. 22 : Normalised x - displacement, spherical vector harmonics approximation, truncated to 20 terms, P - Wave

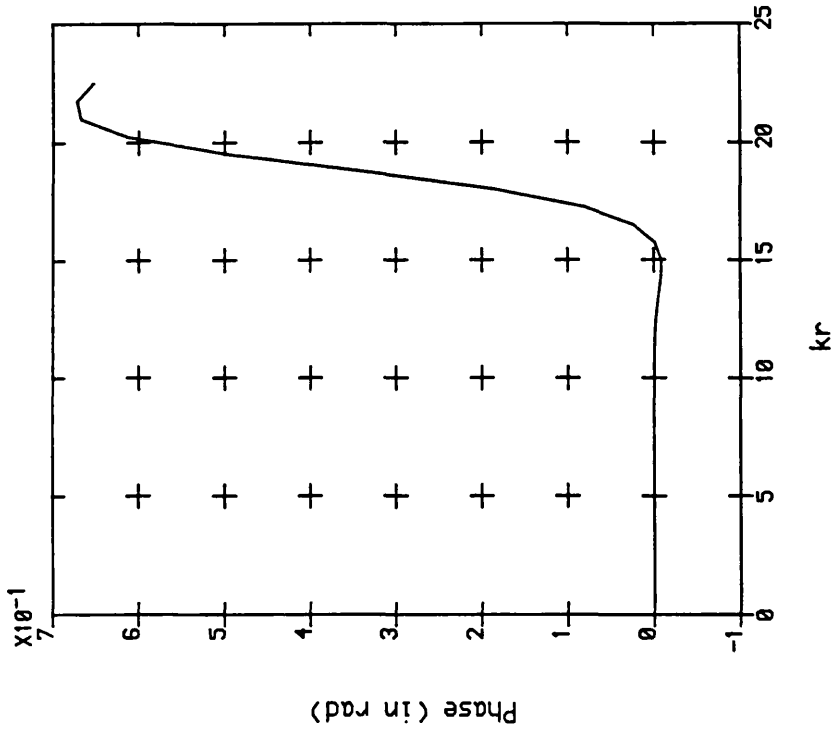


Fig. 23 : Normalised x - displacement, spherical vector harmonics approximation, truncated to 20 terms, P - Wave

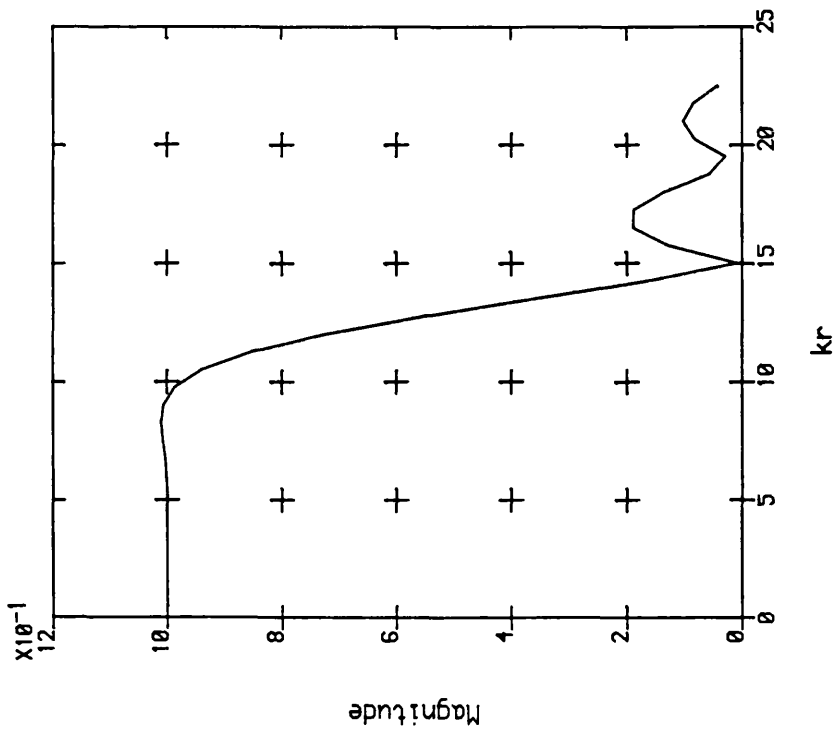


Fig. 24 : Normalised x - displacement, spherical vector harmonics approximation, truncated to 12 terms, SV - Wave

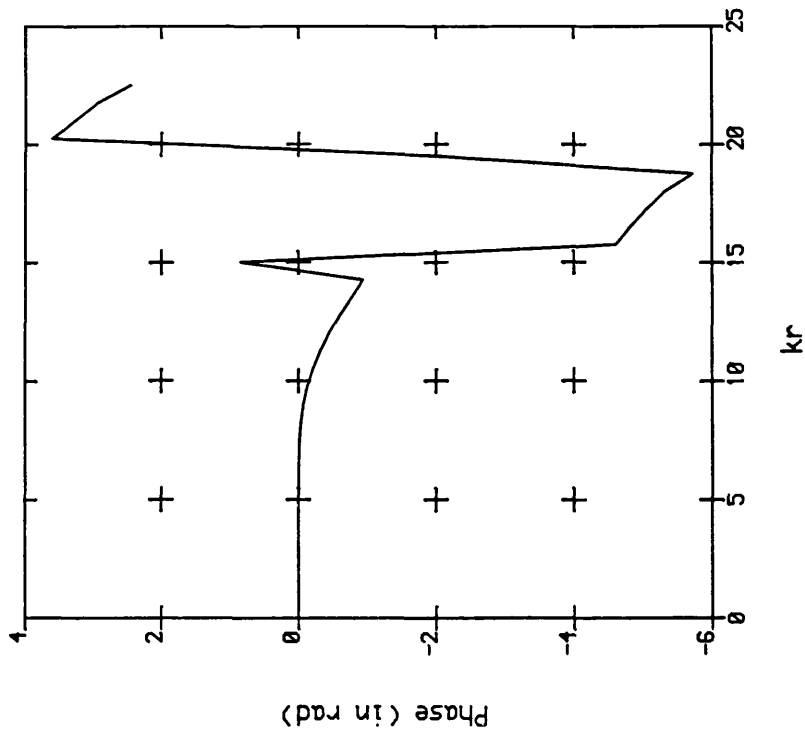


Fig. 25 : Normalised x - displacement, spherical vector harmonics approximation, truncated to 12 terms, SV - Wave

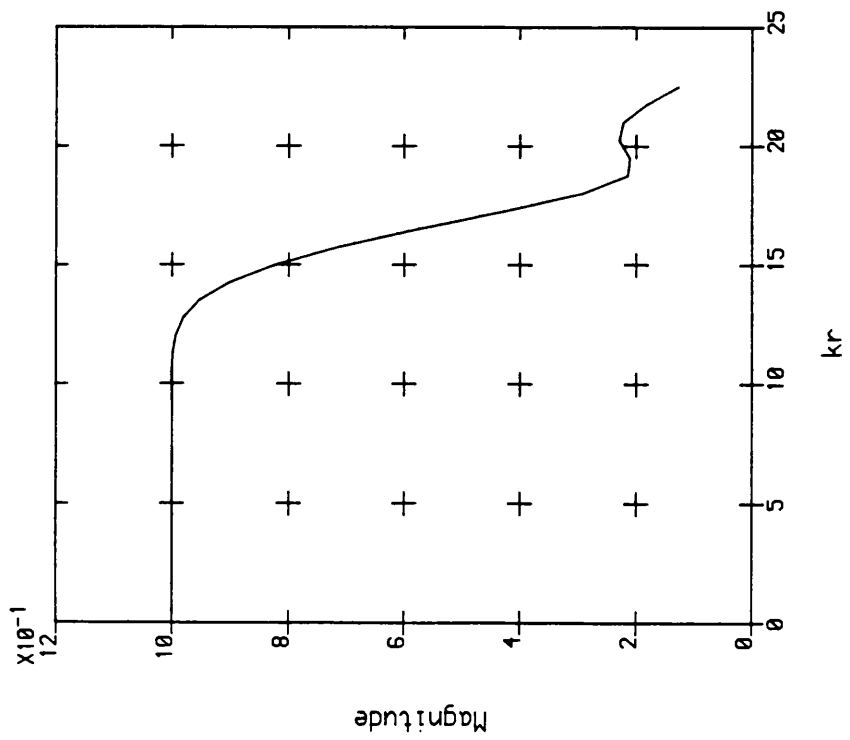


Fig. 26 : Normalised x - displacement, spherical vector harmonics approximation, truncated to 16 terms, SV - Wave

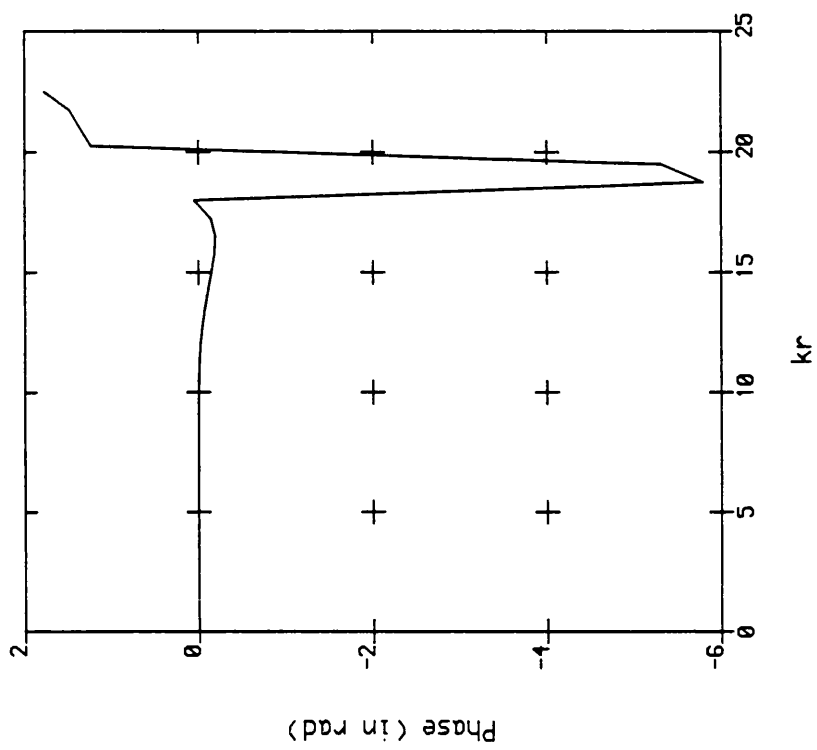


Fig. 27 : Normalised x - displacement, spherical vector harmonics approximation, truncated to 16 terms, SV - Wave

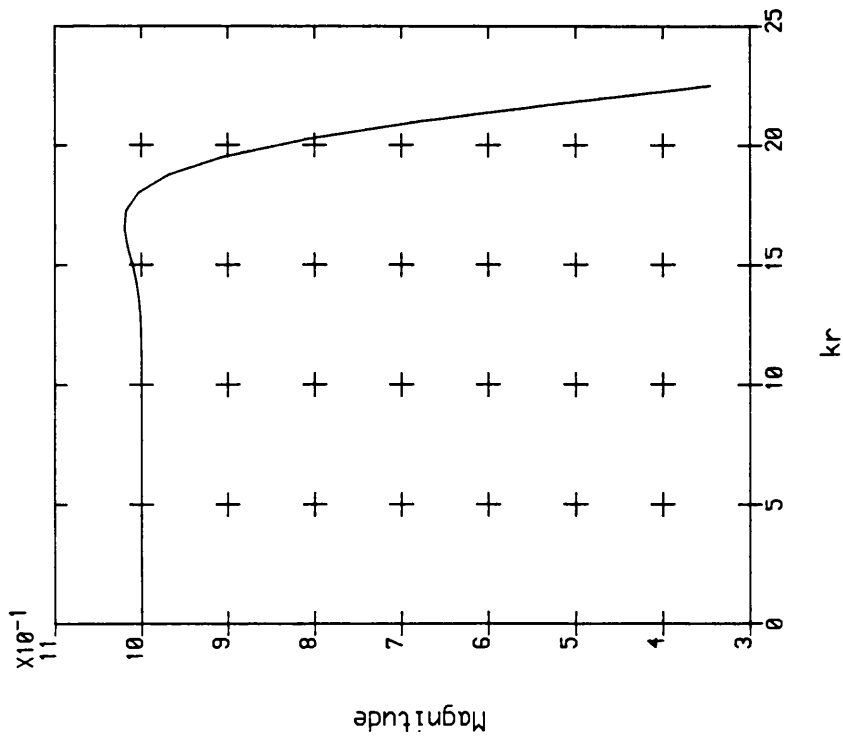


Fig. 28 : Normalised x - displacement, spherical vector harmonics approximation, truncated to 20 terms, SV - Wave

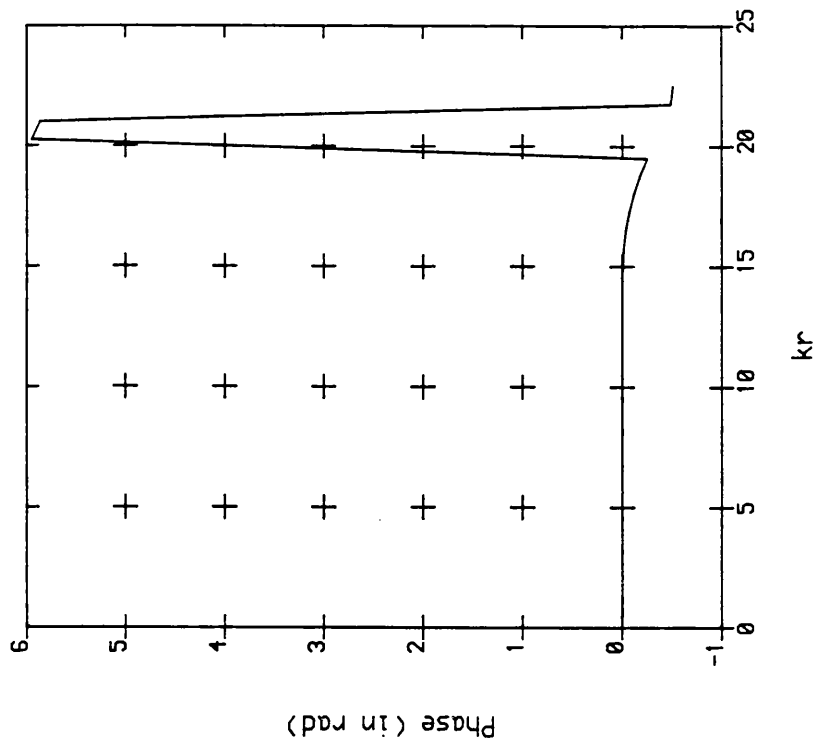


Fig. 29 : Normalised x - displacement, spherical vector harmonics approximation, truncated to 20 terms, SV - Wave

### 3.3 Comparison of results obtained by this study with published results

This section presents a comparison of the three-dimensional near-field results calculated in this study with two-dimensional and three-dimensional near-field results published in the literature. In Figs. 30 — 33 the surface movements of a hemispherical surface indentation generated by a normally incident compressional plane wave are compared with results published in [9]. The diameter to compressional wavelength ratio is varied between 0.25 and 1.5. The number of basis functions chosen for the different cases are given below and differ from [9] due to reasons given in section 3.1. Poisson's ratio is  $\nu = 0.25$  for all cases.

$\frac{2a}{\lambda_p}$	basis functions used here	basis functions used in [9]
0.25	11	10
0.5	13	15
0.75	15	15
1.5	18	15

Table 3 : Comparison of the number of basis functions used here and in [9]

Figs. 34 and 35 compare the surface displacements of a compressional plane wave incident under 60 degrees on to a hemispherical surface indentation with a diameter of one shear wavelength. The plots at the top of the page were calculated here, the plots at the bottom of the page were published in [8]. The number of basis functions for the expansion of the scattered field in [8] is not known and was chosen to be 13 for the present study. Poisson's ratio is  $\nu = 0.25$  as before. A discussion of these results can

be found in section 3.1.

Figs. 36 — 41 show the surface displacements of a compressional wave incident under 30 degrees and a horizontally polarised shear wave incident under 60 degrees on to a hemispherical surface indentation with a diameter to shear wavelength ratio of 0.5 and Poisson's ratio  $\nu = 0.25$ . The results were computed by a wave expansion method described in [104], which employs the orthogonality of the spherical wave functions and their power series representation in  $r$ , the radial distance. Figs. 42 — 45 show the displacements for the same cases calculated with the method presented here. Due to the presentation of the results in [104] it is difficult to compare the amplitude of the displacements. It can be seen that the displacement components computed at some distance from the indentation have the same values, whereas the displacement components close to the rim of the indentation are different. This could be due to the fact that the two methods satisfy the boundary conditions along the stress free surface in different ways, which can result in different emphasis of the corners between the indentation and the half-space and therefore different displacements near the indentation. The shape of the displacement components along the  $x$  and  $y$  axes is similar for the results calculated here and in [104], except that the  $x$  displacement component shown in [104] oscillates along the  $y$  axis for both the P and the SH case (Figs. 36 and 39), whereas it decays without oscillation in Figs. 43 and 45. The case of an incident SV wave presented in [104] can not be calculated here, since the angle of incidence is 45 degrees and therefore beyond the critical angle of the reflected P wave (see chapter 2.2.2).

The calculation of surface displacements for incident compressional and shear waves on to semi-cylindrical canyons has been the subject of

investigations for some time. This scattering geometry is two-dimensional, and the comparison of surface displacements with the results from three-dimensional cases provides some information on the limitations of two-dimensional approximations to three-dimensional scattering problems. Three cases are considered here.

The first case looks at the in-plane displacements for a compressional wave incident under 30 degrees on to a semi-cylindrical canyon (Fig. 48) in comparison to the in-plane displacements generated by a compressional wave incident under 30 degrees on to a hemispherical indentation (Fig. 42). The diameter to incident shear wavelength is  $\frac{2a}{\lambda_s} = 0.5$  for both cases. The two-dimensional results were calculated with the same boundary method that is used here (see [80]), and the Poisson's ratio for this case is  $\nu = 0.33$  compared to the Poisson's ratio for the three-dimensional case, which is  $\nu = 0.25$ . It can be seen that curves for both the horizontal and vertical displacements have the same shape for the two-dimensional and the three-dimensional case, but the amplitudes are slightly larger for the displacements calculated for the two-dimensional geometry.

The second case looks at the anti-plane displacements for a horizontally polarised shear wave incident under 60 degrees on to a semi-cylindrical canyon and a hemisphere with  $\frac{2a}{\lambda_s} = 0.5$  for both cases. The two-dimensional results were calculated with a wave expansion method presented in [105] and are shown in Fig. 50. The three-dimensional results are shown in Fig. 44. As for the case of the incident compressional wave, the shape of the curve for the horizontal displacement is almost the same in two and in three dimensions, whereas the amplitudes are larger for the two-dimensional geometry. This might be expected, since the two-dimensional geometry does

not take any account of displacements in the plane perpendicular to the incident wave vector (y-z) plane, which are significant in three dimensions.

The last case looks at the in-plane and the anti-plane displacements for a normally incident shear wave on to a hemisphere with  $\frac{2a}{\lambda_s} = 0.5$ . The in-plane displacements for the two-dimensional case were calculated in [80] and are shown in Fig. 48, the anti-plane displacements were calculated in [105] and are shown in Fig. 49. The three-dimensional results are shown in Fig. 46 for the in-plane components and in Fig. 47 for the anti-plane components and the shape of the curves for the in-plane and the anti-plane displacement components compare quite well with the two-dimensional results. It can therefore be concluded that two-dimensional approximations to three-dimensional geometries give a qualitative analysis of surface movements in the plane of observation, while neglecting surface movements occurring in the plane perpendicular to the two-dimensional approximation.

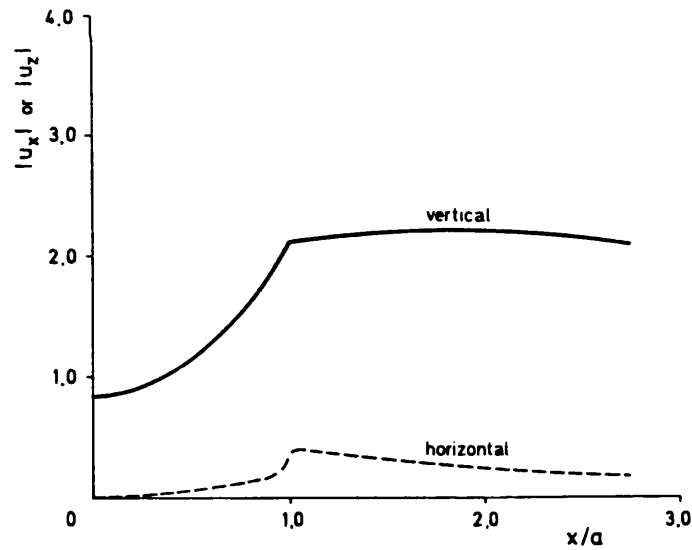
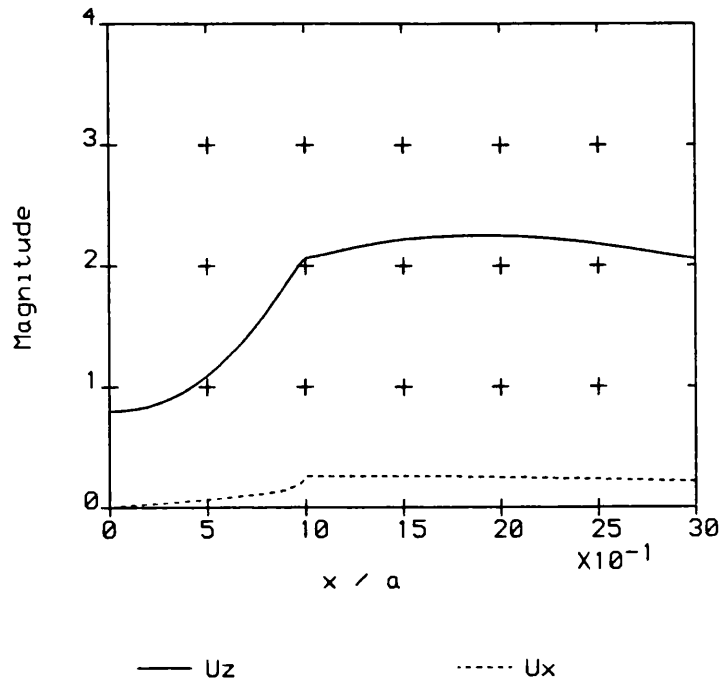


Fig. 30 : Amplitude of the surface displacements in the  $x-z$  plane for a compressional wave normally incident on a hemispherical surface indentation with  $\frac{2a}{\lambda_p} = 0.25$  and Poisson's ratio  $\nu = 0.25$ . Top : result obtained by the present study, bottom : result published in [9].

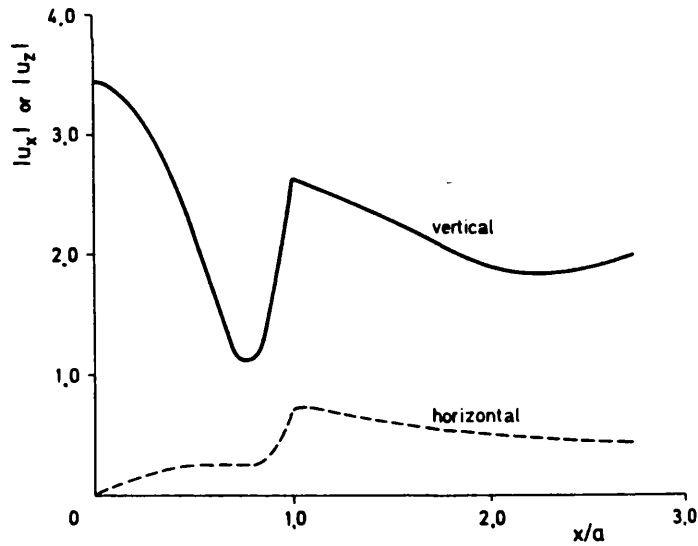
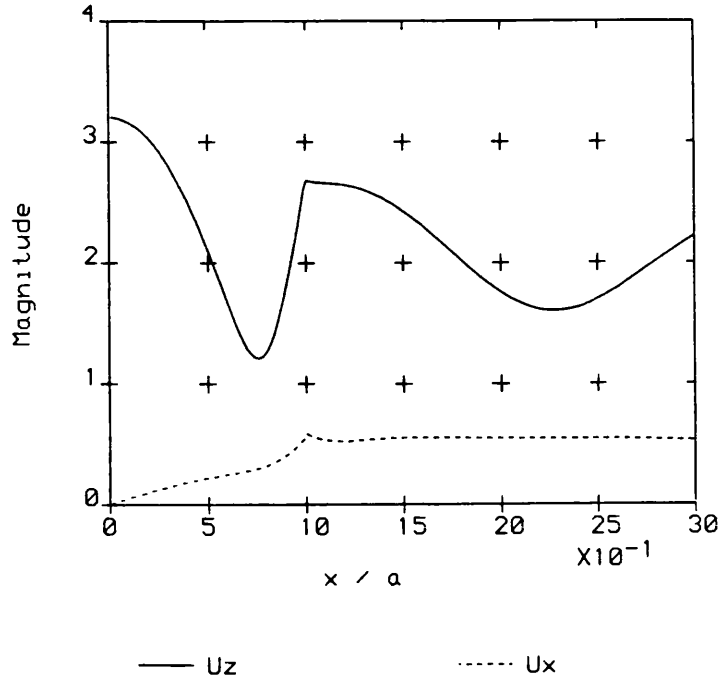


Fig. 31 : Amplitude of the surface displacements in the  $x-z$  plane for a compressional wave normally incident on a hemispherical surface indentation with  $\frac{2a}{\lambda_p} = 0.5$  and Poisson's ratio  $\nu = 0.25$ . Top : result obtained by the present study, bottom : result published in [9].

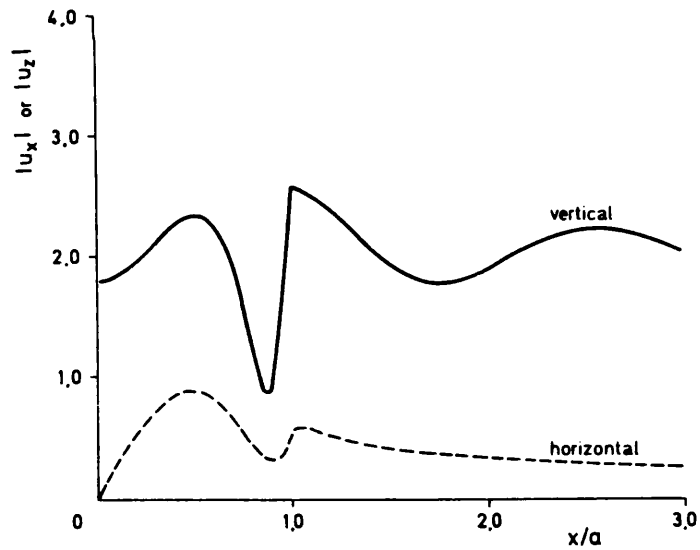
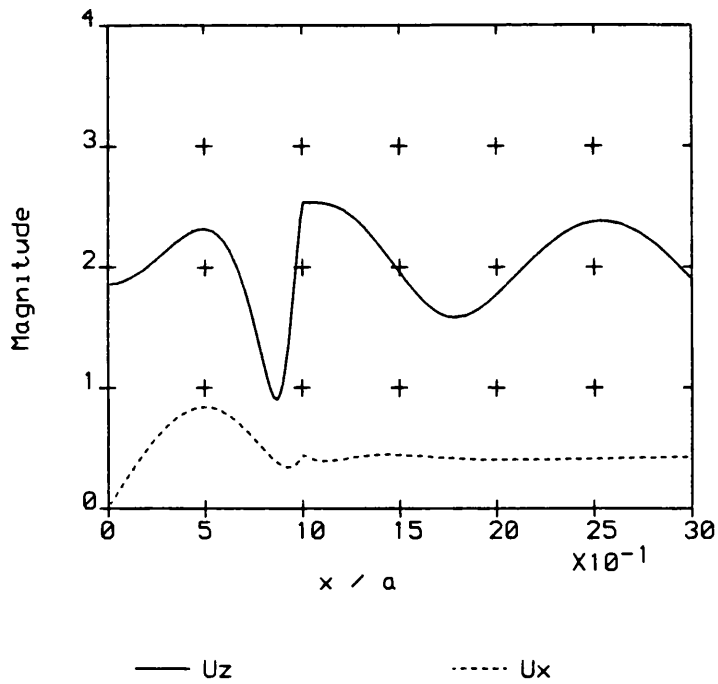


Fig. 32 : Amplitude of the surface displacements in the  $x-z$  plane for a compressional wave normally incident on a hemispherical surface indentation with  $\frac{2a}{\lambda_p} = 0.75$  and Poisson's ratio  $\nu = 0.25$ . Top : result obtained by the present study, bottom : result published in [9].

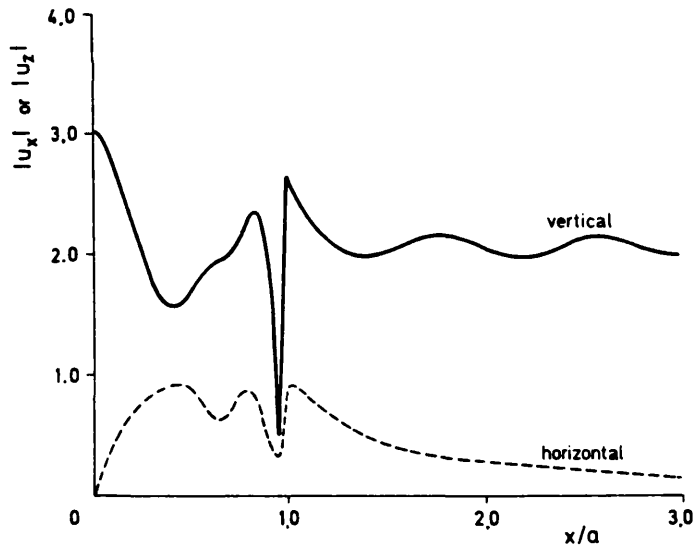
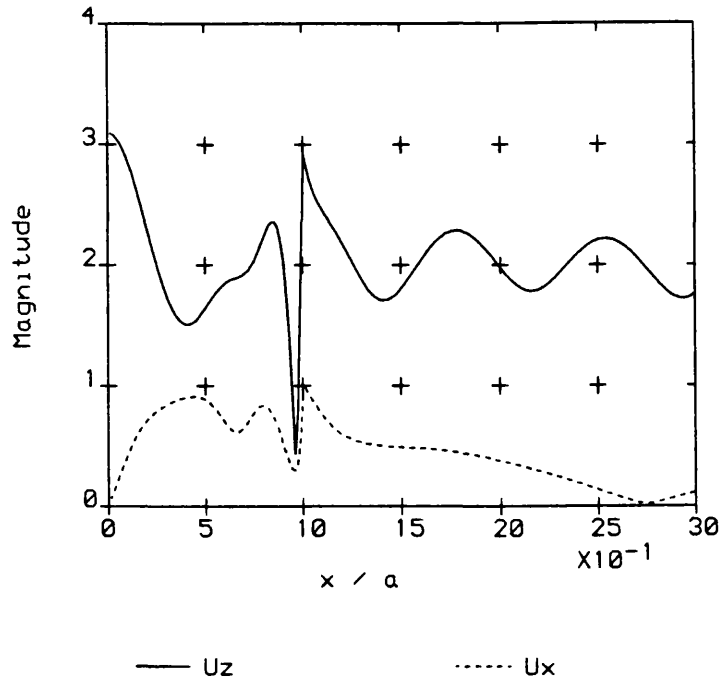


Fig. 33 : Amplitude of the surface displacements in the  $x-z$  plane for a compressional wave normally incident on a hemispherical surface indentation with  $\frac{2a}{\lambda_p} = 1.5$  and Poisson's ratio  $\nu = 0.25$ . Top : result obtained by the present study, bottom : result published in [9].

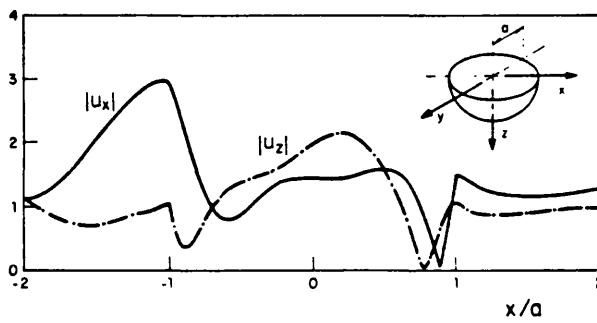
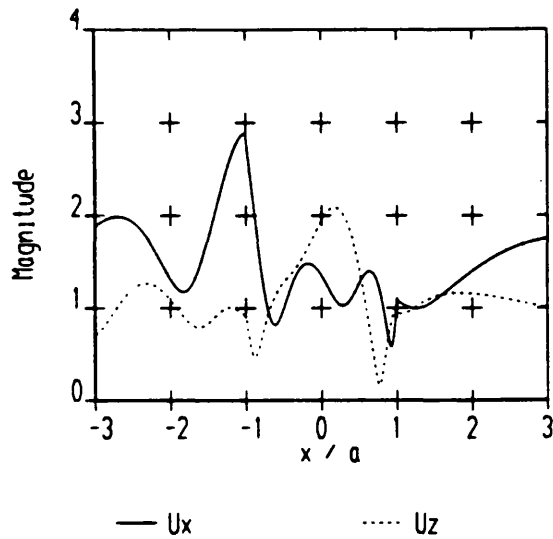


Fig. 34 : Amplitude of the surface displacements in the  $x-z$  plane (plane of the incident wave vector) for a compressional wave incident under 60 degrees on to a hemispherical surface indentation with  $\frac{2a}{\lambda_s} = 1.0$  and Poisson's ratio  $\nu = 0.25$ . Top : result obtained by the present study, bottom : result published in [8].

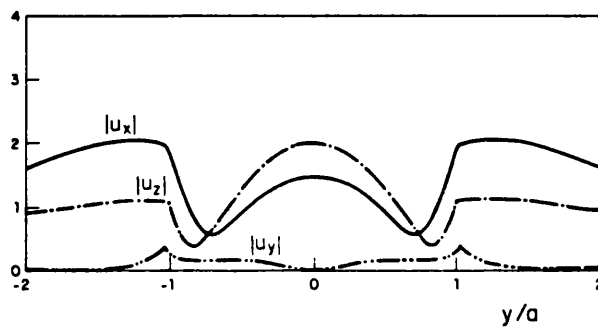
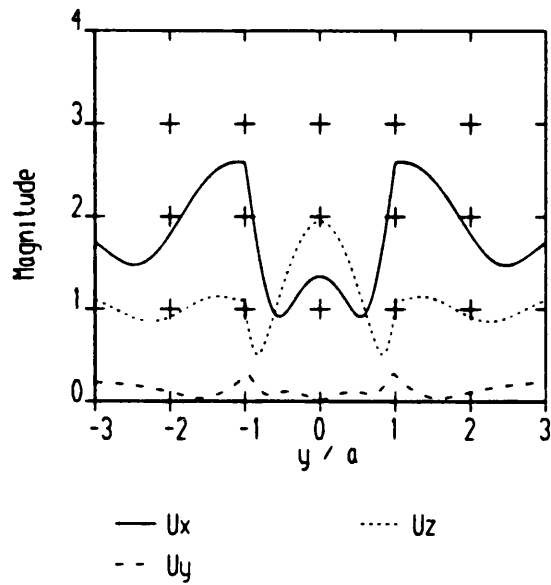


Fig. 35 : Amplitude of the surface displacements in the  $y-z$  plane (plane perpendicular to the incident wave vector) for a compressional wave incident under 60 degrees on to a hemispherical surface indentation with  $\frac{2a}{\lambda_s} = 1.0$  and Poisson's ratio  $\nu = 0.25$ . Top : result obtained by the present study, bottom : result published in [8].

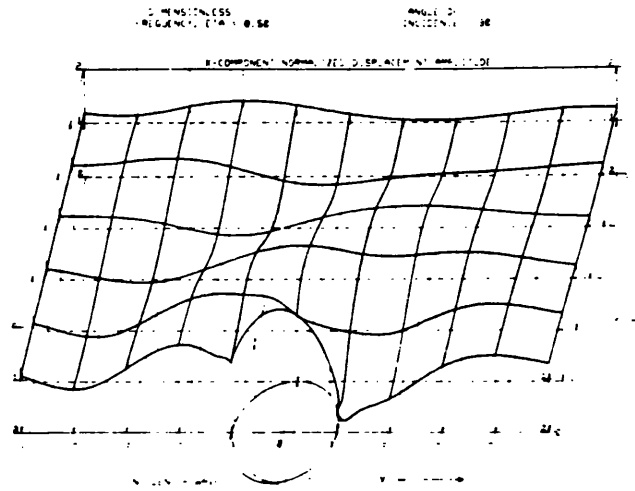


Fig. 36 : Surface displacements  $u_x$  for a compressional wave incident under 30 degrees on to a hemispherical surface indentation with  $\frac{2a}{\lambda_s} = 0.5$  and Poisson's ratio  $\nu = 0.25$ , published in [104].

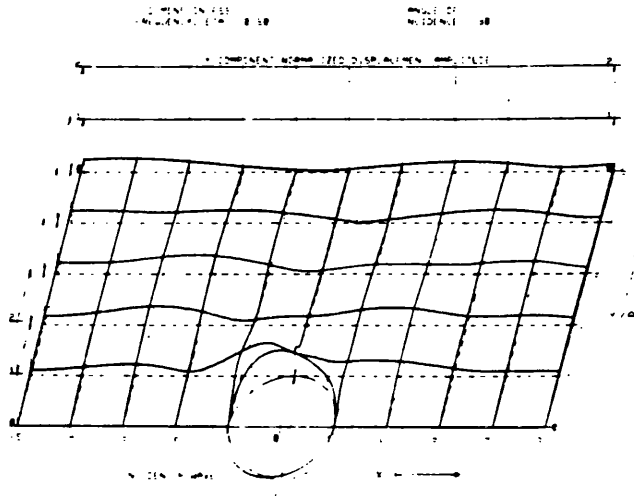


Fig. 37 : Surface displacements  $u_y$  for a compressional wave incident under 30 degrees on to a hemispherical surface indentation with  $\frac{2a}{\lambda_s} = 0.5$  and Poisson's ratio  $\nu = 0.25$ , published in [104].

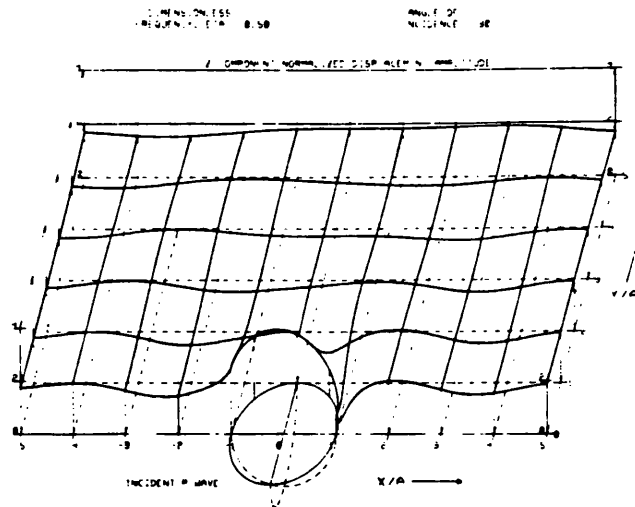


Fig. 38 : Surface displacements  $u_z$  for a compressional wave incident under 30 degrees on to a hemispherical surface indentation with  $\frac{2a}{\lambda_s} = 0.5$  and Poisson's ratio  $\nu = 0.25$ , published in [104].

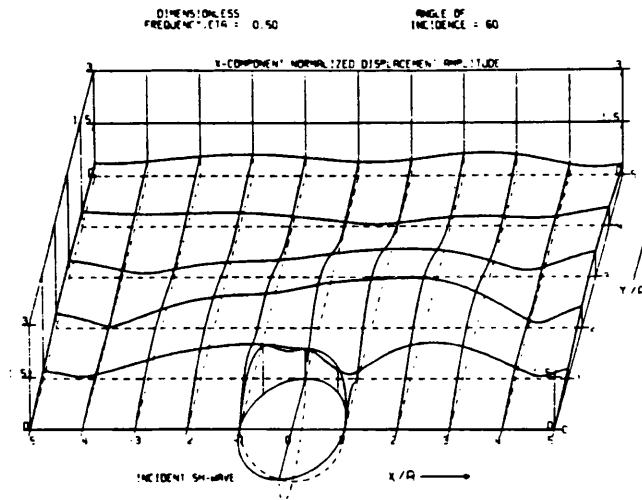


Fig. 39 : Surface displacements  $u_x$  for a horizontally polarised shear wave incident under 60 degrees on to a hemispherical surface indentation with  $\frac{2a}{\lambda_s} = 0.5$  and Poisson's ratio  $\nu = 0.25$ , published in [104].

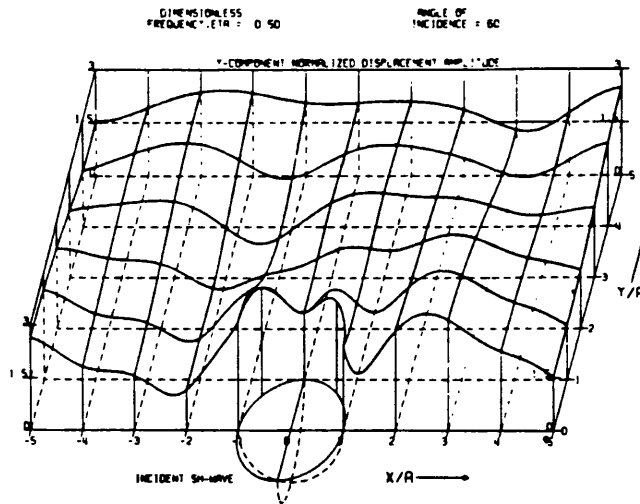


Fig. 40 : Surface displacements  $u_y$  for a horizontally polarised shear wave incident under 60 degrees on to a hemispherical surface indentation with  $\frac{2a}{\lambda_s} = 0.5$  and Poisson's ratio  $\nu = 0.25$ , published in [104].

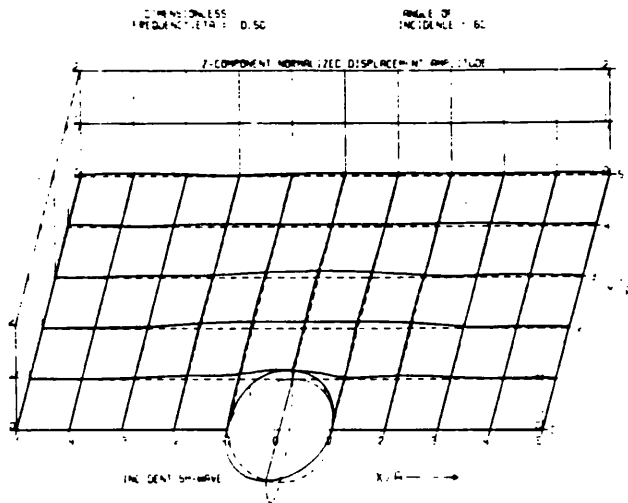


Fig. 41 : Surface displacements  $u_z$  for a horizontally polarised shear wave incident under 60 degrees on to a hemispherical surface indentation with  $\frac{2a}{\lambda_s} = 0.5$  and Poisson's ratio  $\nu = 0.25$ , published in [104].

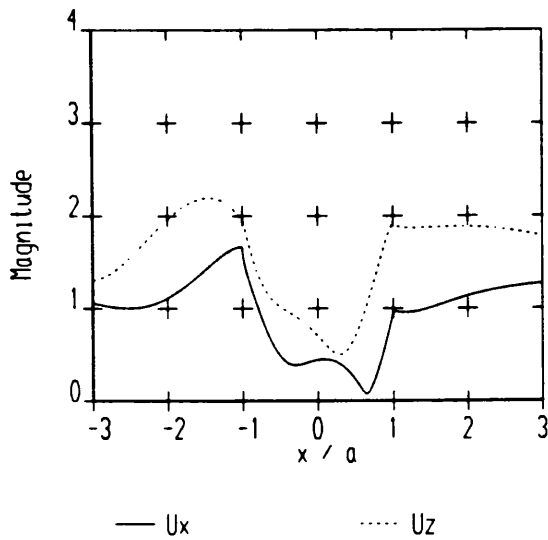


Fig. 42 : Surface displacements in the  $x-z$  plane for a compressional wave incident under 30 degrees on to a hemispherical surface indentation with  $\frac{2a}{\lambda_s} = 0.5$  and Poisson's ratio  $\nu = 0.25$ . Eleven basis functions were used in the expansion.

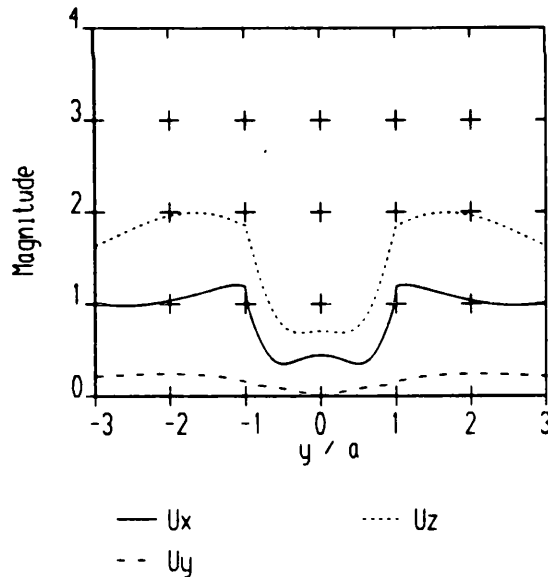


Fig. 43 : Surface displacements in the  $y-z$  plane for a compressional wave incident under 30 degrees on to a hemispherical surface indentation with  $\frac{2a}{\lambda_s} = 0.5$  and Poisson's ratio  $\nu = 0.25$ . Eleven basis functions were used in the expansion.

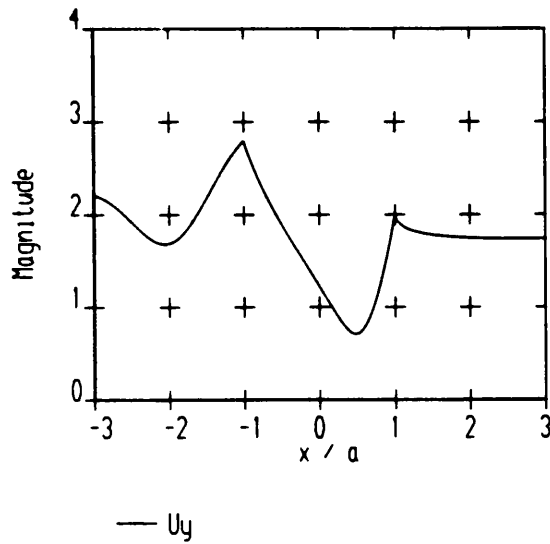


Fig. 44 : Surface displacements in the  $x-z$  plane for a horizontally polarised shear wave incident under 60 degrees on to a hemispherical surface indentation with  $\frac{2a}{\lambda_s} = 0.5$  and Poisson's ratio  $\nu = 0.25$ . Eleven basis functions were used in the expansion.

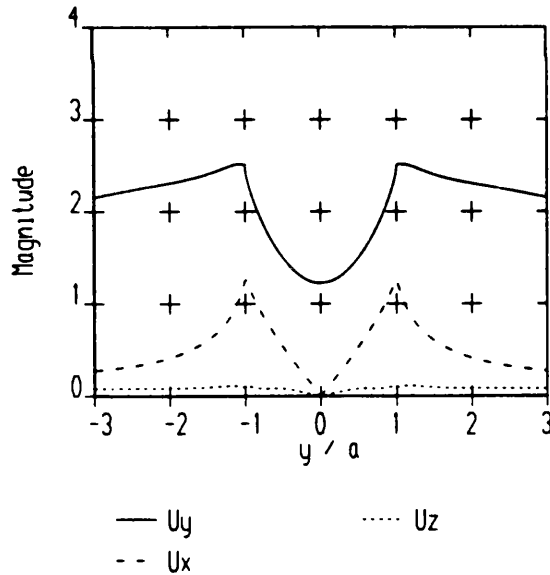


Fig. 45 : Surface displacements in the  $y-z$  plane for a horizontally polarised shear wave incident under 60 degrees on to a hemispherical surface indentation with  $\frac{2a}{\lambda_s} = 0.5$  and Poisson's ratio  $\nu = 0.25$ . Eleven basis functions were used in the expansion.

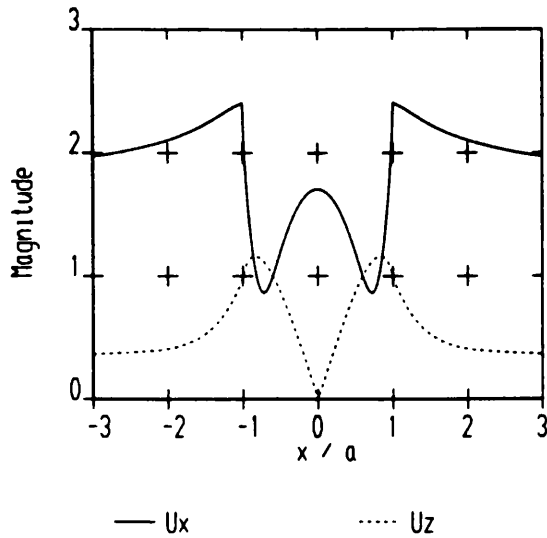


Fig. 46 : Surface displacements in the  $x-z$  plane (plane of polarisation) for a shear wave normally incident on to a hemispherical surface indentation with  $\frac{2a}{\lambda_s} = 0.5$  and Poisson's ratio  $\nu = 0.25$ . Eleven basis functions were used in the expansion.

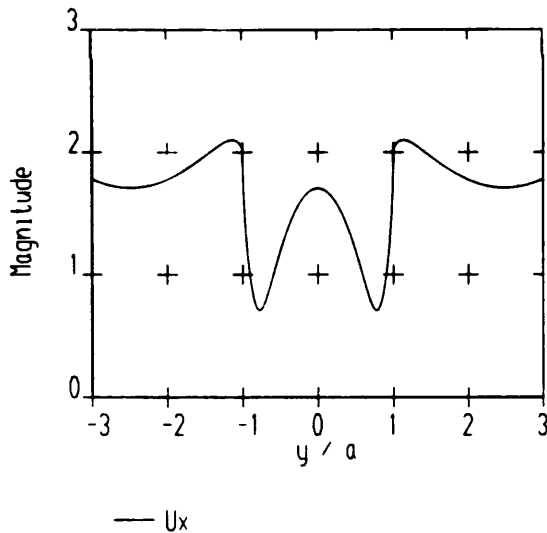


Fig. 47 : Surface displacements in the  $y-z$  plane (plane perpendicular to polarisation) for a shear wave normally incident on to a hemispherical surface indentation with  $\frac{2a}{\lambda_s} = 0.5$  and Poisson's ratio  $\nu = 0.25$ . Eleven basis functions were used in the expansion.

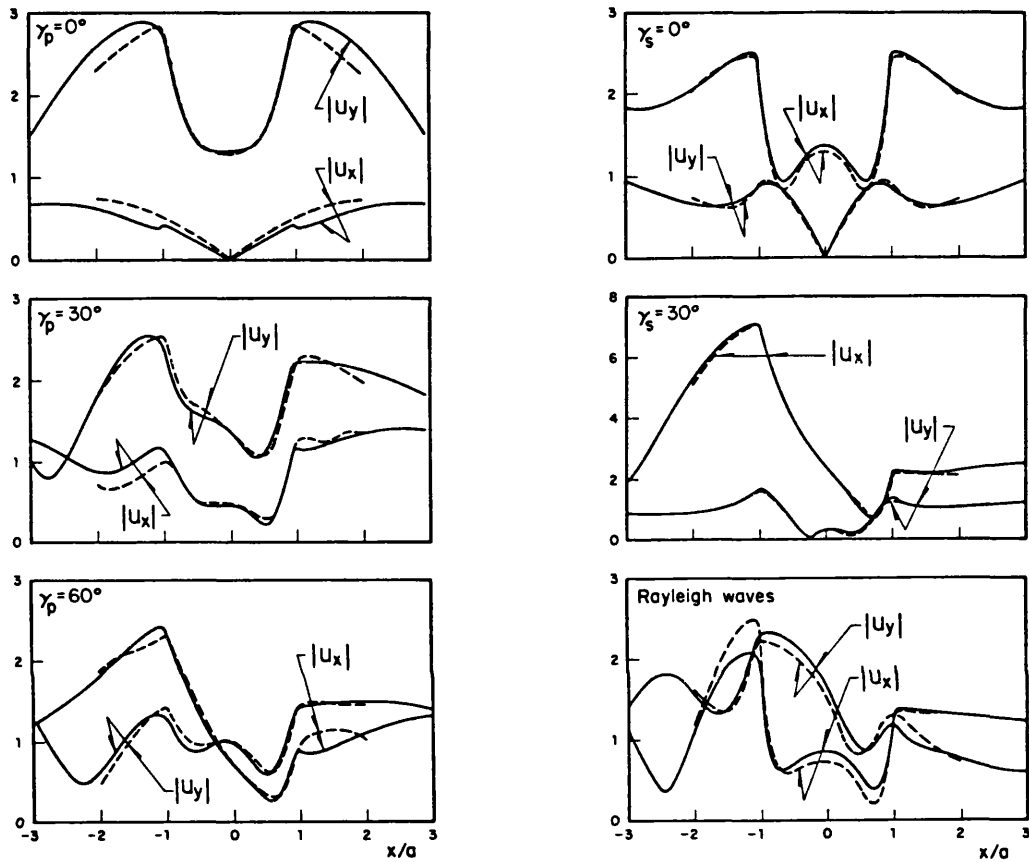


Fig. 48 : Horizontal surface displacements  $u_x$  and vertical surface displacements  $u_y$  for a compressional wave (left) and a vertically polarised shear wave (right) incident on to a semi-cylindrical canyon with  $\frac{2a}{\lambda_s} = 0.5$  and Poisson's ratio  $\nu = 0.33$ . The angle of incidence is given by  $\gamma$ . The dashed curves were calculated in [78], the straight curves were calculated by [80]. The diagram was published in [80].

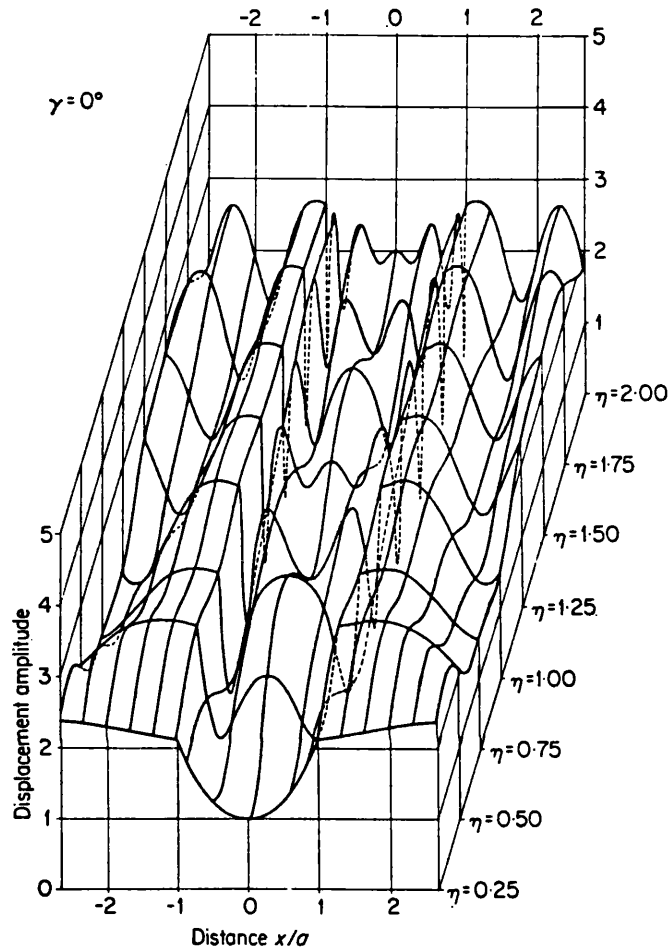


Fig. 49 : Surface displacements for a horizontally polarised shear wave normally incident on to a semi-cylindrical canyon. The diameter to shear wavelength ratio  $\frac{2a}{\lambda_s} = \eta$  is varied from 0.25 to 2.0. The diagram was published in [105].

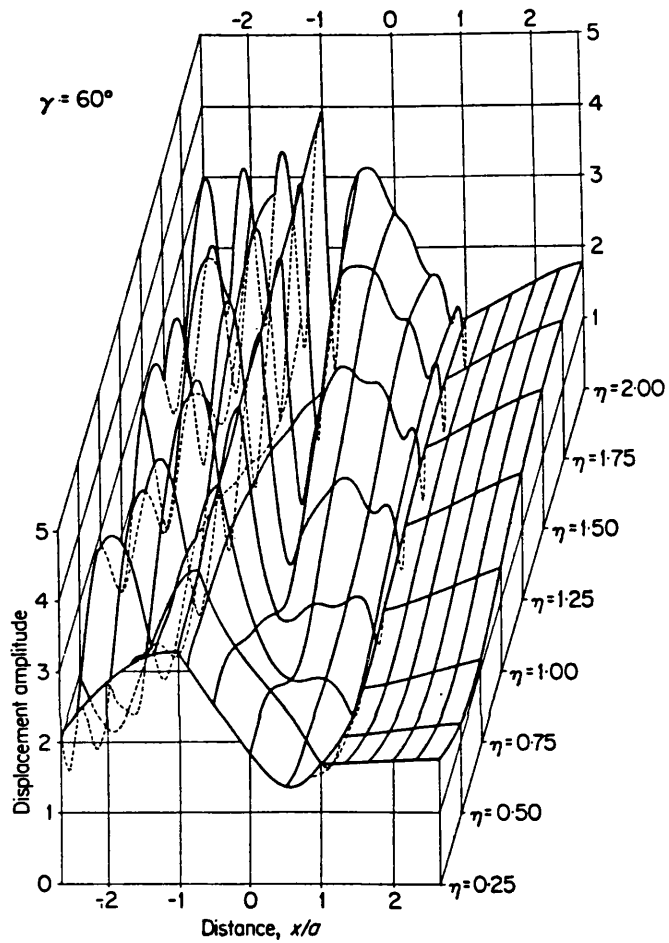


Fig. 50 : Surface displacements for a horizontally polarised shear wave incident under 60 degrees on to a semi-cylindrical canyon. The diameter to shear wavelength ratio  $\frac{2a}{\lambda_s} = \eta$  is varied from 0.25 to 2.0. The diagram was published in [105].

### 3.4 Compressional wave incident under 60 degrees and shear wave normally incident on to an axisymmetric pit at different stages of growth

This section presents the amplitude of the surface displacements, the amplitude of the far-field displacements and the differential scattering cross-section of the scattered far-field for a compressional wave incident under 60 degrees or a shear wave normally incident on to an axisymmetric pit in an aluminium half-space at different stages of growth. Poisson's ratio is  $\nu = 0.34$  and the far-field calculations were carried out at the normalised distance  $\frac{r}{a} = 1000$ . The differential scattering cross-section was calculated using equation (D3a) in Appendix D. Eight different pit shapes are considered :

- (a) a hemisphere with  $\frac{2a}{\lambda_{inc}} = 0.5$  and  $\alpha = 90^\circ$
- (b) a segment of a hemisphere with  $\frac{2a}{\lambda_{inc}} = 1.0$ ,  $\frac{d}{a} = 0.25$  and  $\alpha = 28.1^\circ$
- (c) a semi-ellipsoid with  $\frac{2a}{\lambda_{inc}} = 1.0$ ,  $\frac{d}{a} = 0.25$  and  $\alpha = 90^\circ$
- (d) a segment of a hemisphere with  $\frac{2a}{\lambda_{inc}} = 1.0$ ,  $\frac{d}{a} = 0.5$  and  $\alpha = 53.1^\circ$
- (e) a semi-ellipsoid with  $\frac{2a}{\lambda_{inc}} = 1.0$ ,  $\frac{d}{a} = 0.5$  and  $\alpha = 90^\circ$
- (f) a segment of a hemisphere with  $\frac{2a}{\lambda_{inc}} = 1.0$ ,  $\frac{d}{a} = 0.75$  and  $\alpha = 73.7^\circ$
- (g) a semi-ellipsoid with  $\frac{2a}{\lambda_{inc}} = 1.0$ ,  $\frac{d}{a} = 0.75$  and  $\alpha = 90^\circ$
- (h) a hemisphere with  $\frac{2a}{\lambda_{inc}} = 1.0$  and  $\alpha = 90^\circ$

where  $2a$  is the surface diameter and  $d$  the depth of the indentation. the angle of the corners between the indentation and the plane surface is denoted by  $\alpha$ . Feature (a) represents a hemispherical pit with a diameter of half an incident wavelength. Features (b) – (g) are shallow axisymmetric indentations with a surface diameter of one incident wavelength, but with different shapes. The depth of the pit varies from  $\frac{\lambda_{inc}}{8}$  (features (b) and (c)) over  $\frac{\lambda_{inc}}{4}$

(features (d) and (e)) to  $\frac{3}{8} \lambda_{inc}$  (features (f) and (g)). The hemispherical indentation (h) has a surface diameter of one incident wavelength and therefore a depth of  $\frac{\lambda_{inc}}{2}$ .

Case	Figure numbers for a P wave incident at 60 degrees	Figure numbers for a normally incident SV wave
(a)	Figs. 51 — 56	Figs. 99 — 104
(b)	Figs. 57 — 62	Figs. 105 — 110
(c)	Figs. 63 — 68	Figs. 111 — 116
(d)	Figs. 69 — 74	Figs. 117 — 122
(e)	Figs. 75 — 80	Figs. 123 — 128
(f)	Figs. 81 — 86	Figs. 129 — 134
(g)	Figs. 87 — 92	Figs. 135 — 140
(h)	Figs. 93 — 98	Figs. 141 — 146

Table 4 : Figure numbers of the results for the cases (a) — (h) presented in this section

The polar plots showing the angular distribution of the far-field displacements and the scattering cross-section are normalised for each case to the maximum value occurring either in the x—z or in the y—x plane. The cases relate to each other as given below, where case (a) has been chosen arbitrarily as normalisation.

case	Figure numbers	scaling factor of the far-field displacements
(a)	Figs. 53, 54	1.0
(b)	Figs. 59, 60	0.53
(c)	Figs. 65, 66	0.60
(d)	Figs. 71, 72	0.97
(e)	Figs. 77, 78	1.2
(f)	Figs. 83, 84	2.2
(g)	Figs. 89, 90	2.7
(h)	Figs. 95, 96	3.9

Table 5 : Scaling factors of the far-field displacement plots for the cases  
(a) — (h) and a P wave incident at 60 degrees

case	Figure numbers	scaling factor of the differential cross-section
(a)	Figs. 55, 56	1.0
(b)	Figs. 61, 62	0.45
(c)	Figs. 67, 68	0.58
(d)	Figs. 73, 74	3.1
(e)	Figs. 79, 80	4.3
(f)	Figs. 85, 86	7.3
(g)	Figs. 91, 92	11.3
(h)	Figs. 97, 98	24.2

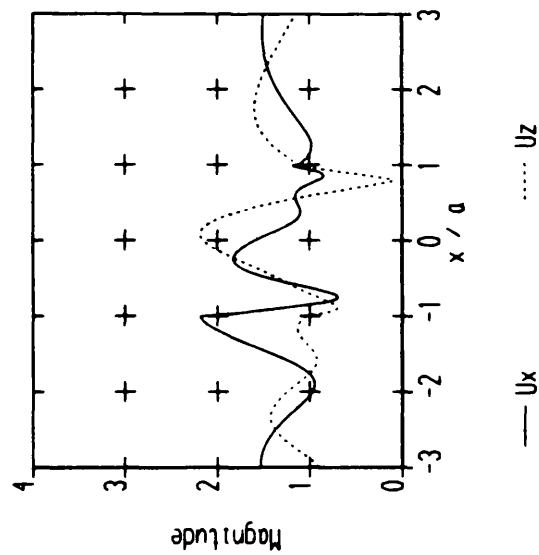
Table 6 : Scaling factors of the differential cross-section plots for the cases  
(a) — (h) and a P wave incident at 60 degrees

case	Figure numbers	scaling factor of the far-field displacements
(a)	Figs. 101, 102	1.0
(b)	Figs. 107, 108	0.37
(c)	Figs. 113, 114	0.51
(d)	Figs. 119, 120	0.72
(e)	Figs. 125, 126	0.83
(f)	Figs. 131, 132	1.2
(g)	Figs. 137, 138	1.3
(h)	Figs. 143, 144	1.8

Table 7 : Scaling factors of the far-field displacement plots for the cases  
(a) – (h) and a normally incident SV wave

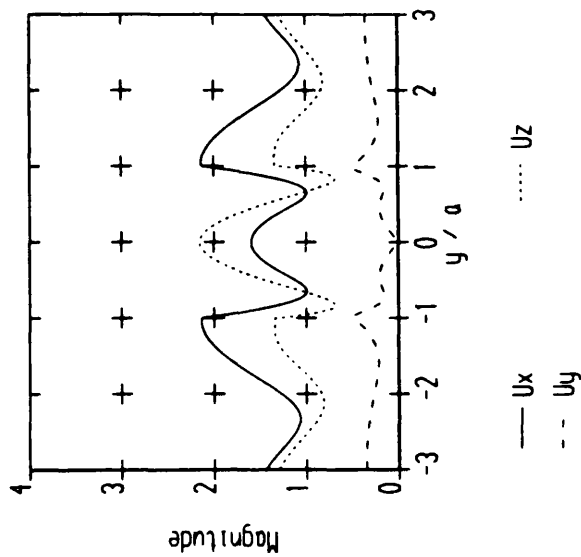
case	Figure numbers	scaling factor of the differential cross-section
(a)	Figs. 103, 104	1.0
(b)	Figs. 109, 110	0.28
(c)	Figs. 115, 116	0.53
(d)	Figs. 121, 122	1.0
(e)	Figs. 127, 128	1.4
(f)	Figs. 133, 134	3.0
(g)	Figs. 139, 140	3.4
(h)	Figs. 145, 146	6.4

Table 8 : Scaling factors of the differential cross-section plots for the cases  
(a) – (h) and a normally incident SV wave



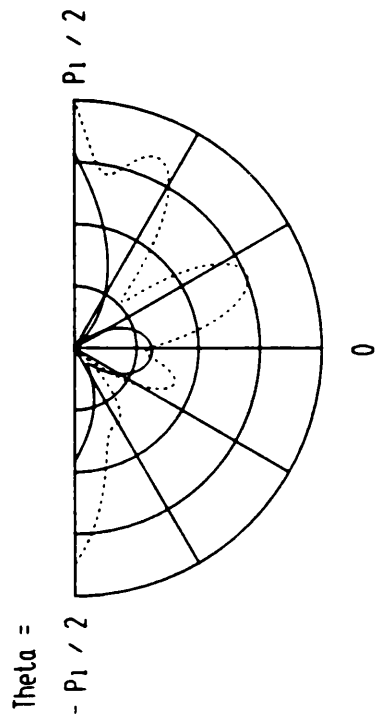
Surface displacements in x-z plane  
 Type of surface obstacle : Hemisphere  
 Order of approximation : 13  
 Incident wavetype : P  
 Incident angle : 60.00 deg  
 Poisson's ratio : 0.34  
 $2a / \lambda$  incident : 0.50  
 $d / a$  : 1.00

Fig. 51 : Amplitude of the surface displacements in the x-z plane (plane of the incident wave vector) for a compressional wave incident under 60 degrees on to a hemispherical surface indentation



Surface displacements in y-z plane  
 Type of surface obstacle : Hemisphere  
 Order of approximation : 13  
 Incident wavetype : P  
 Incident angle : 60.00 deg  
 Poisson's ratio : 0.34  
 $2a / \lambda$  incident : 0.50  
 $d / a$  : 1.00

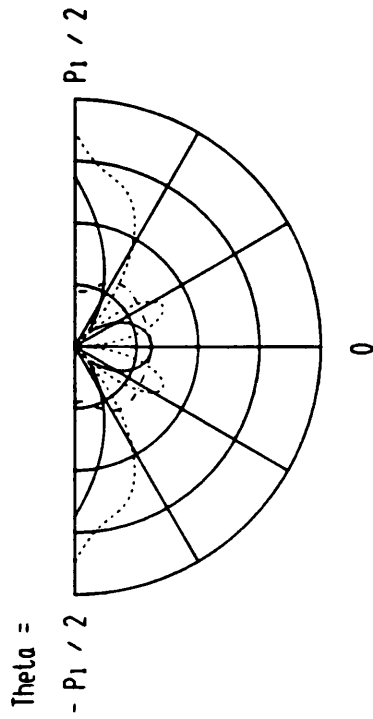
Fig. 52 : Amplitude of the surface displacements in the y-z plane (plane perpendicular to the incident wave vector) for a compressional wave incident under 60 degrees on to a hemispherical surface indentation



— R comp      ..... Theta comp

Far Field displacements in x-z plane  
 Type of surface obstacle : Hemisphere  
 Order of approximation : 13  
 Incident waveltype : P  
 Incident angle : 60.00 deg  
 Poisson's ratio : 0.34  
 $2a / \lambda$  incident : 0.50  
 $d / a$  : 1.00

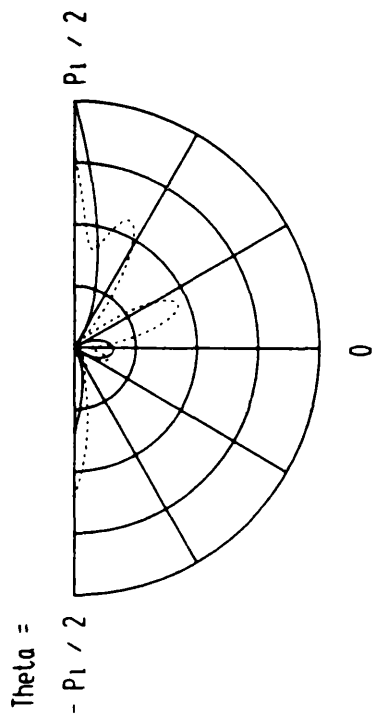
Fig. 53 : Amplitude of the far-field displacements of the scattered field in the x-z plane (plane of the incident wave vector) for a compressional wave incident under 60 degrees on to a hemispherical surface indentation



— R comp      ..... Theta comp

Far Field displacements in y-z plane  
 Type of surface obstacle : Hemisphere  
 Order of approximation : 13  
 Incident waveltype : P  
 Incident angle : 60.00 deg  
 Poisson's ratio : 0.34  
 $2a / \lambda$  incident : 0.50  
 $d / a$  : 1.00

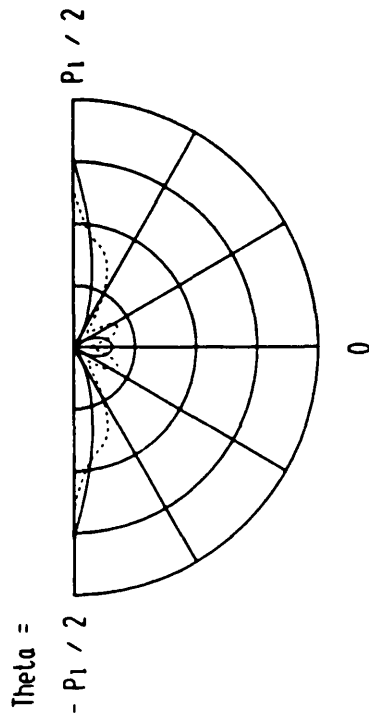
Fig. 54 : Amplitude of the far-field displacements of the scattered field in the y-z plane (plane perpendicular to the incident wave vector) for a compressional wave incident under 60 degrees on to a hemispherical surface indentation



— P component      ..... S component

Scattered energy in x-z plane  
 Type of surface obstacle : Hemisphere  
 Order of approximation : 13  
 Incident wavetype : P  
 Incident angle : 60.00 deg  
 Poisson's ratio : 0.34  
 2a / lambda incident : 0.50  
 d / a : 1.00

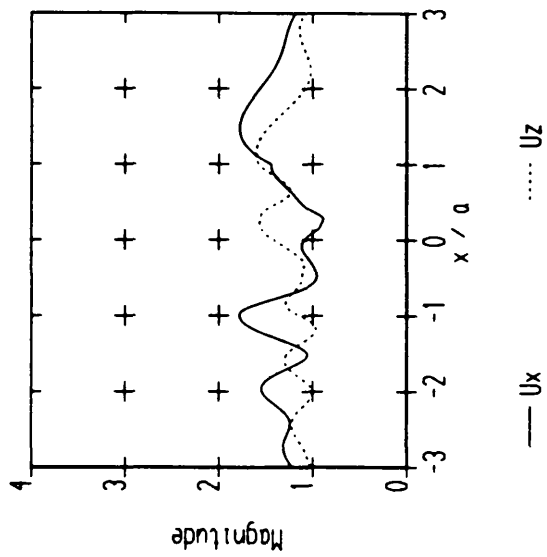
Fig. 55 : Differential cross-section of the scattered far-field in the x-z plane (plane of the incident wave vector) for a compressional wave incident under 60 degrees on to a hemispherical surface indentation



— P component      ..... S component

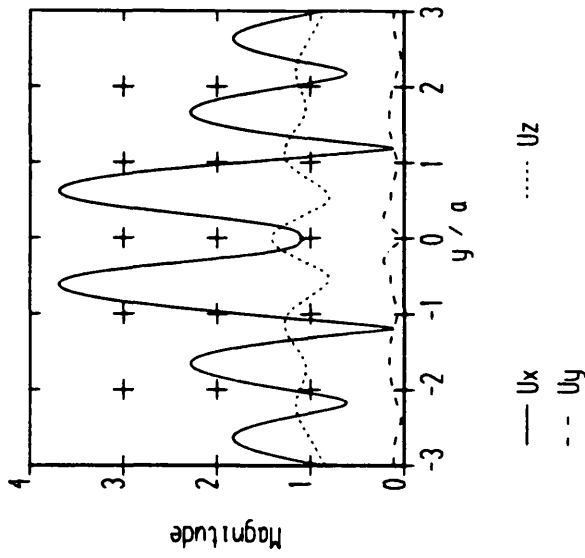
Scattered energy in y-z plane  
 Type of surface obstacle : Hemisphere  
 Order of approximation : 13  
 Incident wavetype : P  
 Incident angle : 60.00 deg  
 Poisson's ratio : 0.34  
 2a / lambda incident : 0.50  
 d / a : 1.00

Fig. 56 : Differential cross-section of the scattered far-field in the y-z plane (plane perpendicular to the incident wave vector) for a compressional wave incident under 60 degrees on to a hemispherical surface indentation



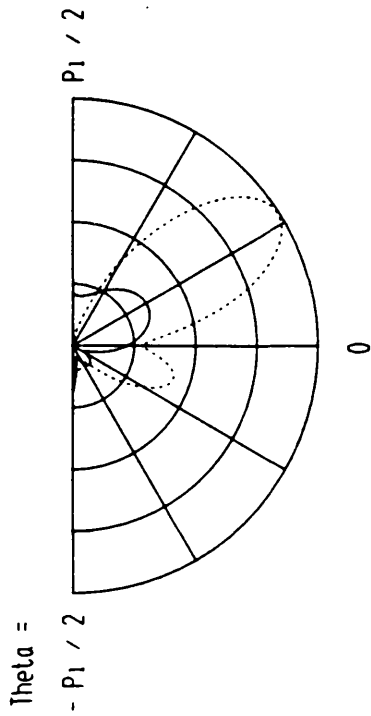
Surface displacements in x-z plane  
 Type of surface obstacle : Segment of a hemisphere  
 Order of approximation : 10  
 Incident wavetype : P  
 Incident angle : 60.00 deg  
 Poisson's ratio : 0.34  
 $2a / \lambda$  incident : 1.00  
 $d / a$  : 0.25

Fig. 57 : Amplitude of the surface displacements in the x-z plane (plane of the incident wave vector) for a compressional wave incident under 60 degrees on to a shallow axisymmetric surface indentation



Surface displacements in y-z plane  
 Type of surface obstacle : Segment of a hemisphere  
 Order of approximation : 10  
 Incident wavetype : P  
 Incident angle : 60.00 deg  
 Poisson's ratio : 0.34  
 $2a / \lambda$  incident : 1.00  
 $d / a$  : 0.25

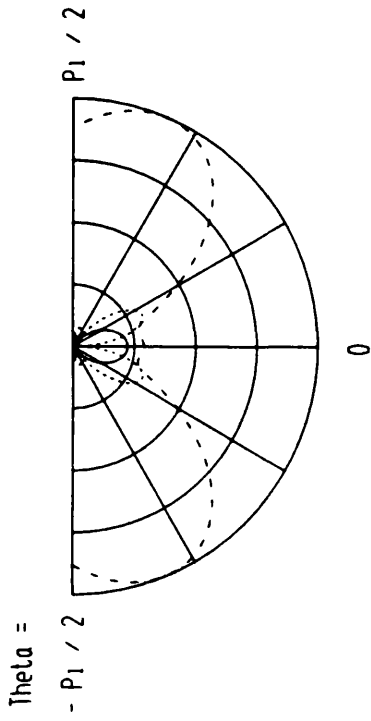
Fig. 58 : Amplitude of the surface displacements in the y-z plane (plane perpendicular to the incident wave vector) for a compressional wave incident under 60 degrees on to a shallow axisymmetric surface indentation



— R comp      ..... Theta comp

Far field displacements in x-z plane  
 Type of surface obstacle : Segment of a hemisphere  
 Order of approximation : 10  
 Incident wavetype : P  
 Incident angle : 60.00 deg  
 Poisson's ratio : 0.34  
 $2a / \lambda$  incident : 1.00  
 $d / a$  : 0.25

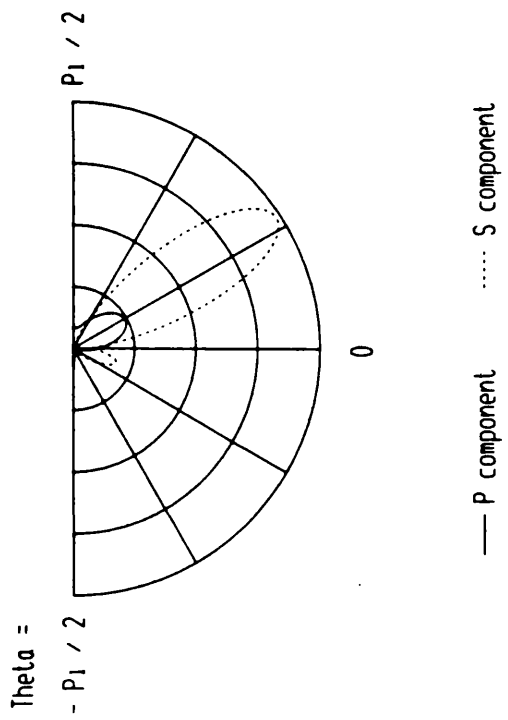
Fig. 59 : Amplitude of the far-field displacements of the scattered field in the x-z plane (plane of the incident wave vector) for a compressional wave incident under 60 degrees on to a shallow axisymmetric surface indentation



— R comp      ..... Theta comp

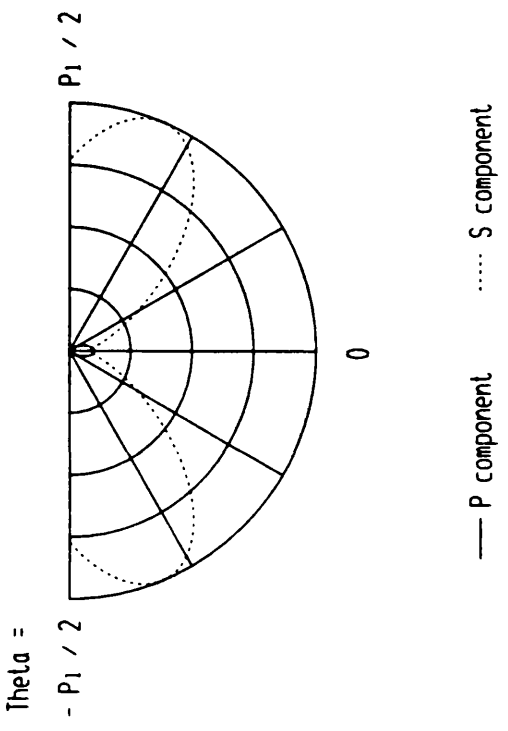
Far field displacements in y-z plane  
 Type of surface obstacle : Segment of a hemisphere  
 Order of approximation : 10  
 Incident wavetype : P  
 Incident angle : 60.00 deg  
 Poisson's ratio : 0.34  
 $2a / \lambda$  incident : 1.00  
 $d / a$  : 0.25

Fig. 60 : Amplitude of the far-field displacements of the scattered field in the y-z plane (plane perpendicular to the incident wave vector) for a compressional wave incident under 60 degrees on to a shallow axisymmetric surface indentation



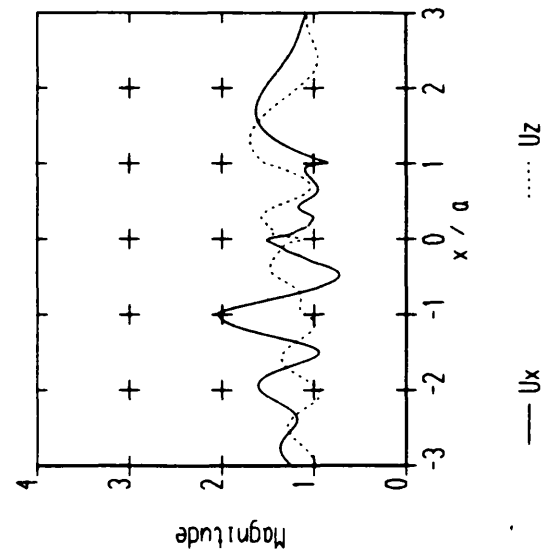
Scattered energy in x-z plane  
 Type of surface obstacle : Segment of a hemisphere  
 Order of approximation : 10  
 Incident waveltype : P  
 Incident angle : 60.00 deg  
 Poisson's ratio : 0.34  
 2a / lambda incident : 1.00  
 d / a : 0.25

Fig. 61 : Differential cross-section of the scattered far-field in the x-z plane (plane of the incident wave vector) for a compressional wave incident under 60 degrees on to a shallow axisymmetric surface indentation



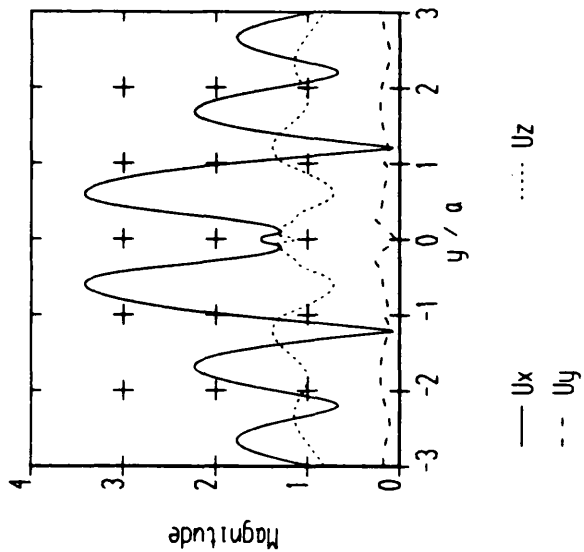
Scattered energy in y-z plane  
 Type of surface obstacle : Segment of a hemisphere  
 Order of approximation : 10  
 Incident waveltype : P  
 Incident angle : 60.00 deg  
 Poisson's ratio : 0.34  
 2a / lambda incident : 1.00  
 d / a : 0.25

Fig. 62 : Differential cross-section of the scattered far-field in the y-z plane (plane perpendicular to the incident wave vector) for a compressional wave incident under 60 degrees on to a shallow axisymmetric surface indentation



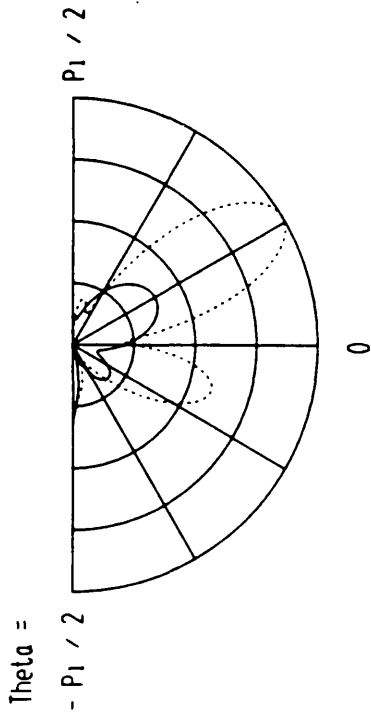
Surface displacements in x-z plane  
 Type of surface obstacle : Ellipsoid  
 Order of approximation : 10  
 Incident wavetype : P  
 Incident angle : 60.00 deg  
 Poisson's ratio : 0.34  
 $2a / \lambda$  incident : 1.00  
 $d / a$  : 0.25

Fig. 63 : Amplitude of the surface displacements in the x-z plane (plane of the incident wave vector) for a compressional wave incident under 60 degrees on to a shallow axisymmetric surface indentation



Surface displacements in y-z plane  
 Type of surface obstacle : Ellipsoid  
 Order of approximation : 10  
 Incident wavetype : P  
 Incident angle : 60.00 deg  
 Poisson's ratio : 0.34  
 $2a / \lambda$  incident : 1.00  
 $d / a$  : 0.25

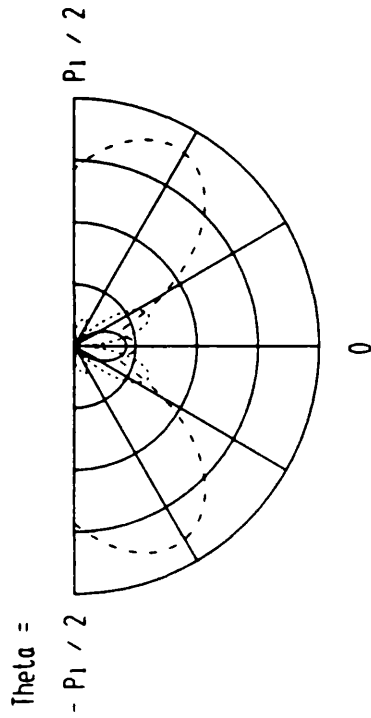
Fig. 64 : Amplitude of the surface displacements in the y-z plane (plane perpendicular to the incident wave vector) for a compressional wave incident under 60 degrees on to a shallow axisymmetric surface indentation



— R comp      ..... Theta comp

Far Field displacements in x-z plane  
 Type of surface obstacle : Ellipsoid  
 Order of approximation : 10  
 Incident waveltype : P  
 Incident angle : 60.00 deg  
 Poisson's ratio : 0.34  
 $2a / \lambda$  incident : 1.00  
 $d / a$  : 0.25

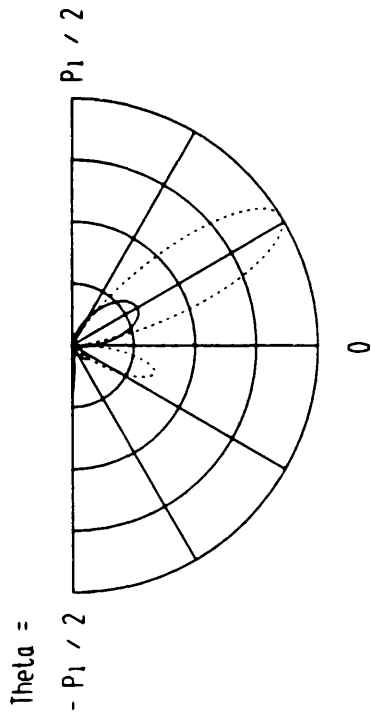
Fig. 65 : Amplitude of the far-field displacements of the scattered field in the x-z plane (plane of the incident wave vector) for a compressional wave incident under 60 degrees on to a shallow axisymmetric surface indentation



— R comp      ..... Theta comp

Far Field displacements in y-z plane  
 Type of surface obstacle : Ellipsoid  
 Order of approximation : 10  
 Incident waveltype : P  
 Incident angle : 60.00 deg  
 Poisson's ratio : 0.34  
 $2a / \lambda$  incident : 1.00  
 $d / a$  : 0.25

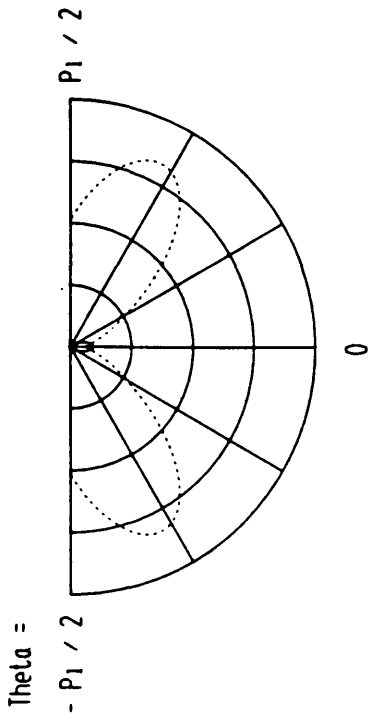
Fig. 66 : Amplitude of the far-field displacements of the scattered field in the y-z plane (plane perpendicular to the incident wave vector) for a compressional wave incident under 60 degrees on to a shallow axisymmetric surface indentation



— P component      ..... S component

Scattered energy in x-z plane  
 Type of surface obstacle : Ellipsoid  
 Order of approximation : 10  
 Incident wavetype : P  
 Incident angle : 60.00 deg  
 Poisson's ratio : 0.34  
 $2a / \lambda$  incident : 1.00  
 $d / a$  : 0.25

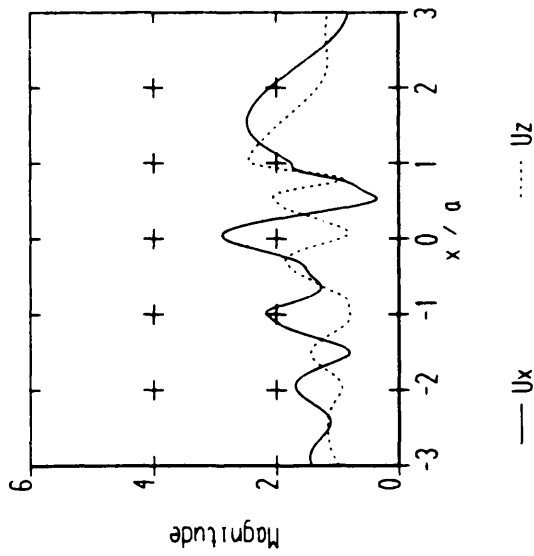
Fig. 67 : Differential cross-section of the scattered far-field in the x-z plane (plane of the incident wave vector) for a compressional wave incident under 60 degrees on to a shallow axisymmetric surface indentation



— P component      ..... S component

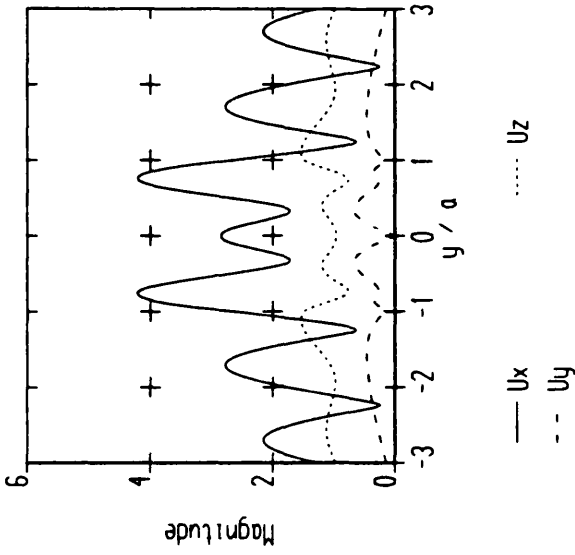
Scattered energy in y-z plane  
 Type of surface obstacle : Ellipsoid  
 Order of approximation : 10  
 Incident wavetype : P  
 Incident angle : 60.00 deg  
 Poisson's ratio : 0.34  
 $2a / \lambda$  incident : 1.00  
 $d / a$  : 0.25

Fig. 68 : Differential cross-section of the scattered far-field in the y-z plane (plane perpendicular to the incident wave vector) for a compressional wave incident under 60 degrees on to a shallow axisymmetric surface indentation



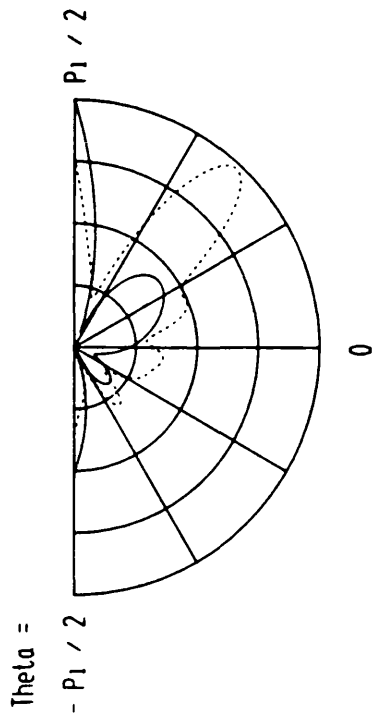
Surface displacements in x-z plane  
 Type of surface obstacle : Segment of a hemisphere  
 Order of approximation : 13  
 Incident wavetype : P  
 Incident angle : 60.00 deg  
 Poisson's ratio : 0.34  
 $2a / \lambda$  incident : 1.00  
 $d / a$  : 0.50

Fig. 69 : Amplitude of the surface displacements in the x-z plane (plane of the incident wave vector) for a compressional wave incident under 60 degrees on to a shallow axisymmetric surface indentation



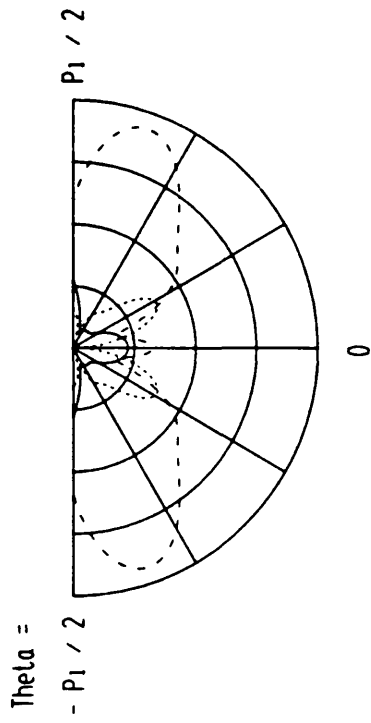
Surface displacements in y-z plane  
 Type of surface obstacle : Segment of a hemisphere  
 Order of approximation : 13  
 Incident wavetype : P  
 Incident angle : 60.00 deg  
 Poisson's ratio : 0.34  
 $2a / \lambda$  incident : 1.00  
 $d / a$  : 0.50

Fig. 70 : Amplitude of the surface displacements in the y-z plane (plane perpendicular to the incident wave vector) for a compressional wave incident under 60 degrees on to a shallow axisymmetric surface indentation



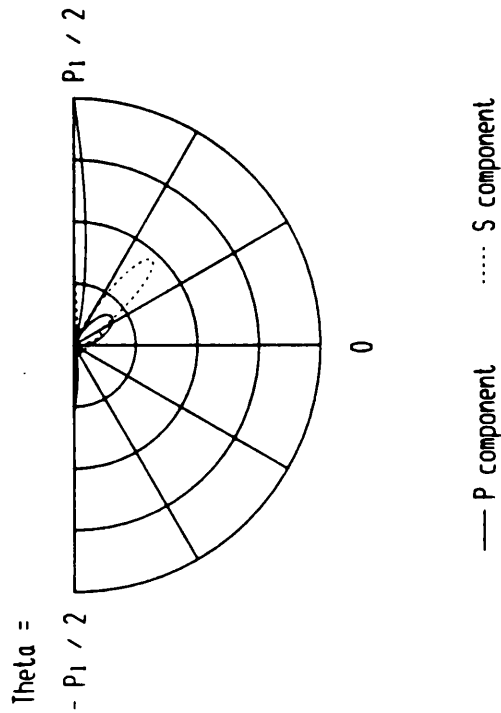
Far field displacements in x-z plane  
 Type of surface obstacle : Segment of a hemisphere  
 Order of approximation : 13  
 Incident waveltype : P  
 Incident angle : 60.00 deg  
 Poisson's ratio : 0.34  
 $2a / \lambda$  incident : 1.00  
 $d / a$  : 0.50

Fig. 71 : Amplitude of the far-field displacements of the scattered field in the x-z plane (plane of the incident wave vector) for a compressional wave incident under 60 degrees on to a shallow axisymmetric surface indentation



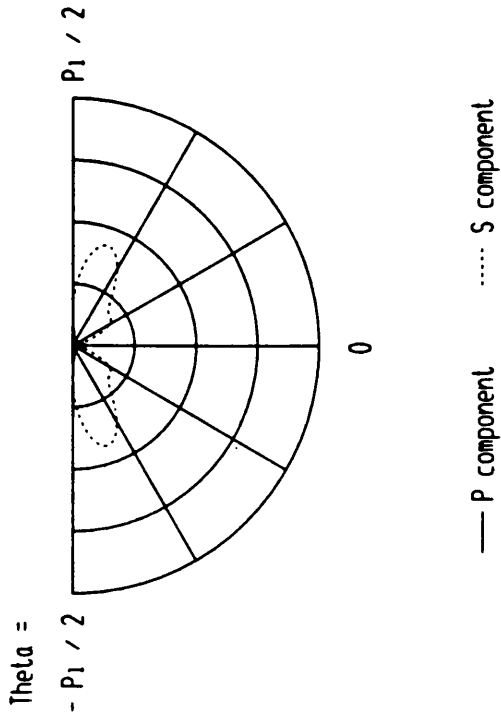
Far field displacements in y-z plane  
 Type of surface obstacle : Segment of a hemisphere  
 Order of approximation : 13  
 Incident waveltype : P  
 Incident angle : 60.00 deg  
 Poisson's ratio : 0.34  
 $2a / \lambda$  incident : 1.00  
 $d / a$  : 0.50

Fig. 72 : Amplitude of the far-field displacements of the scattered field in the y-z plane (plane perpendicular to the incident wave vector) for a compressional wave incident under 60 degrees on to a shallow axisymmetric surface indentation



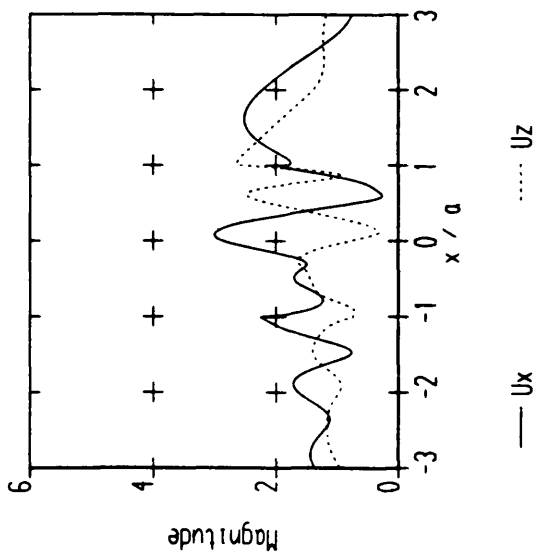
Scattered energy in x-z plane  
 Type of surface obstacle : Segment of a hemisphere  
 Order of approximation : 13  
 Incident wavetype : P  
 Incident angle : 60.00 deg  
 Poisson's ratio : 0.34  
 $2a / \lambda$  incident : 1.00  
 $d / a$  : 0.50

Fig. 73 : Differential cross-section of the scattered far-field in the x-z plane (plane of the incident wave vector) for a compressional wave incident under 60 degrees on to a shallow axisymmetric surface indentation



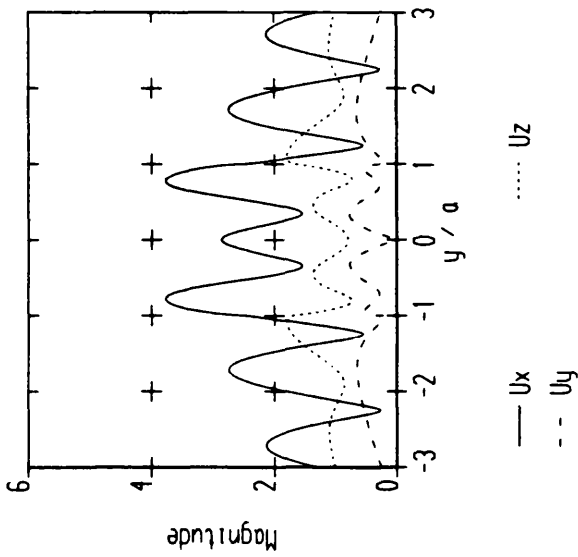
Scattered energy in y-z plane  
 Type of surface obstacle : Segment of a hemisphere  
 Order of approximation : 13  
 Incident wavetype : P  
 Incident angle : 60.00 deg  
 Poisson's ratio : 0.34  
 $2a / \lambda$  incident : 1.00  
 $d / a$  : 0.50

Fig. 74 : Differential cross-section of the scattered far-field in the y-z plane (plane perpendicular to the incident wave vector) for a compressional wave incident under 60 degrees on to a shallow axisymmetric surface indentation



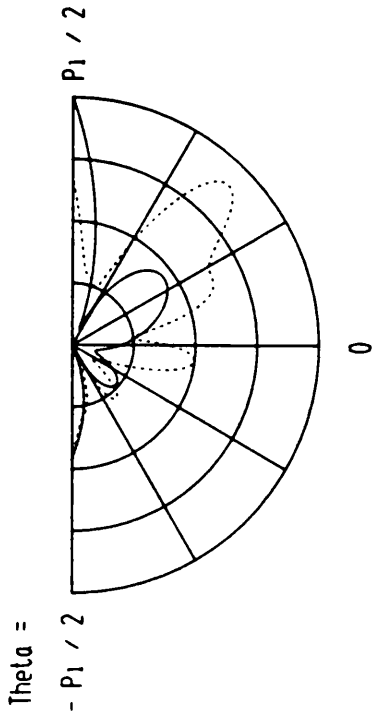
Surface displacements in x-z plane  
 Type of surface obstacle : Ellipsoid  
 Order of approximation : 13  
 Incident wavetype : P  
 Incident angle : 60.00 deg  
 Poisson's ratio : 0.34  
 $2a / \lambda$  incident : 1.00  
 $d / a$  : 0.50

Fig. 75 : Amplitude of the surface displacements in the x-z plane (plane of the incident wave vector) for a compressional wave incident under 60 degrees on to a shallow axisymmetric surface indentation



Surface displacements in y-z plane  
 Type of surface obstacle : Ellipsoid  
 Order of approximation : 13  
 Incident wavetype : P  
 Incident angle : 60.00 deg  
 Poisson's ratio : 0.34  
 $2a / \lambda$  incident : 1.00  
 $d / a$  : 0.50

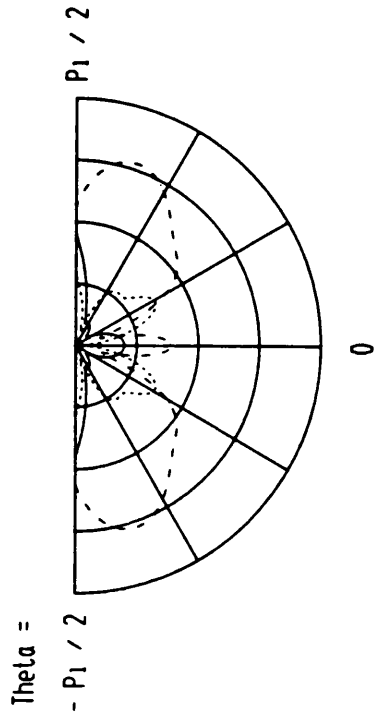
Fig. 76 : Amplitude of the surface displacements in the y-z plane (plane perpendicular to the incident wave vector) for a compressional wave incident under 60 degrees on to a shallow axisymmetric surface indentation



— R comp      ..... Theta comp

Far Field displacements in x-z plane  
 Type of surface obstacle : Ellipsoid  
 Order of approximation : 13  
 Incident waveltype : P  
 Incident angle : 60.00 deg  
 Poisson's ratio : 0.34  
 $2a / \lambda$  incident : 1.00  
 $d / a$  : 0.50

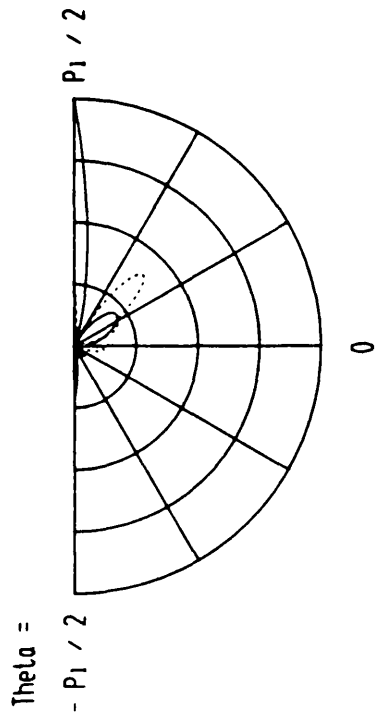
Fig. 77 : Amplitude of the far-field displacements of the scattered field in the x-z plane (plane of the incident wave vector) for a compressional wave incident under 60 degrees on to a shallow axisymmetric surface indentation



— R comp      ..... Theta comp

Far Field displacements in y-z plane  
 Type of surface obstacle : Ellipsoid  
 Order of approximation : 13  
 Incident waveltype : P  
 Incident angle : 60.00 deg  
 Poisson's ratio : 0.34  
 $2a / \lambda$  incident : 1.00  
 $d / a$  : 0.50

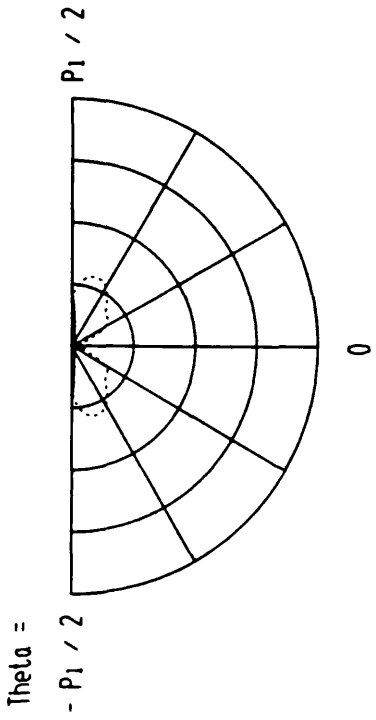
Fig. 78 : Amplitude of the far-field displacements of the scattered field in the y-z plane (plane perpendicular to the incident wave vector) for a compressional wave incident under 60 degrees on to a shallow axisymmetric surface indentation



— P component      ..... S component

Scattered energy in x-z plane  
 Type of surface obstacle : Ellipsoid  
 Order of approximation : 13  
 Incident wavetype : P  
 Incident angle : 60.00 deg  
 Poisson's ratio : 0.34  
 $2a / \lambda$  incident : 1.00  
 $d / a$  : 0.50

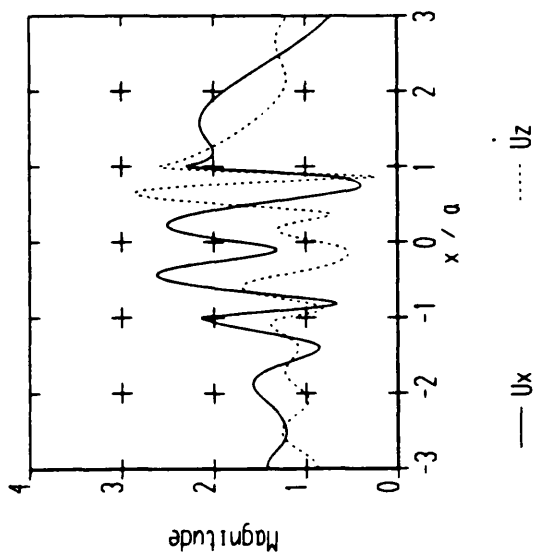
Fig. 79 : Differential cross-section of the scattered far-field in the x-z plane (plane of the incident wave vector) for a compressional wave incident under 60 degrees on to a shallow axisymmetric surface indentation



— P component      ..... S component

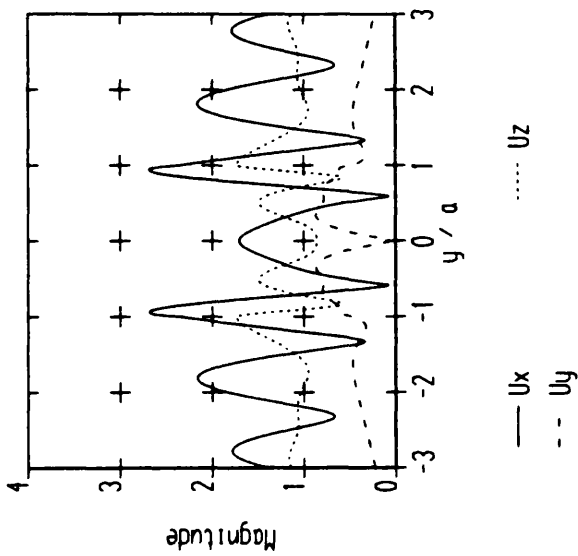
Scattered energy in y-z plane  
 Type of surface obstacle : Ellipsoid  
 Order of approximation : 13  
 Incident wavetype : P  
 Incident angle : 60.00 deg  
 Poisson's ratio : 0.34  
 $2a / \lambda$  incident : 1.00  
 $d / a$  : 0.50

Fig. 80 : Differential cross-section of the scattered far-field in the y-z plane (plane perpendicular to the incident wave vector) for a compressional wave incident under 60 degrees on to a shallow axisymmetric surface indentation



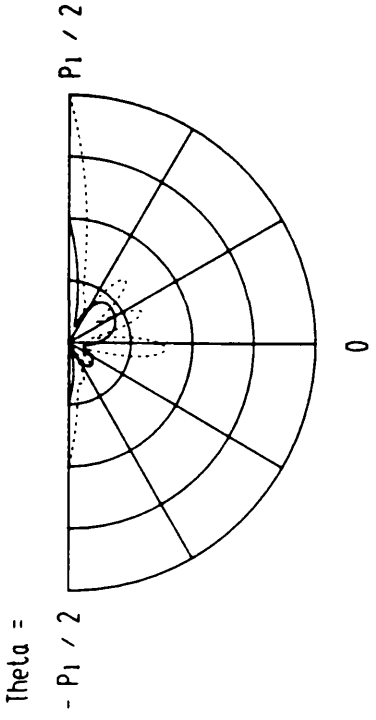
Surface displacements in x-z plane  
 Type of surface obstacle : Segment of a hemisphere  
 Order of approximation : 14  
 Incident wavetype : P  
 Incident angle : 60.00 deg  
 Poisson's ratio : 0.34  
 $2a / \lambda$  incident : 1.00  
 $d / a$  : 0.75

Fig. 81 : Amplitude of the surface displacements in the x-z plane (plane of the incident wave vector) for a compressional wave incident under 60 degrees on to a shallow axisymmetric surface indentation



Surface displacements in y-z plane  
 Type of surface obstacle : Segment of a hemisphere  
 Order of approximation : 14  
 Incident wavetype : P  
 Incident angle : 60.00 deg  
 Poisson's ratio : 0.34  
 $2a / \lambda$  incident : 1.00  
 $d / a$  : 0.75

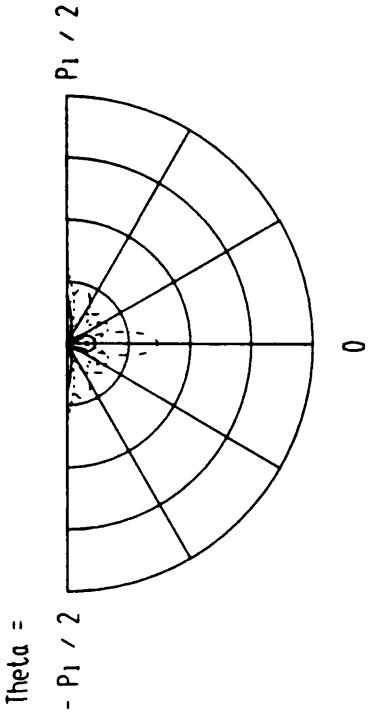
Fig. 82 : Amplitude of the surface displacements in the y-z plane (plane perpendicular to the incident wave vector) for a compressional wave incident under 60 degrees on to a shallow axisymmetric surface indentation



— R comp      ..... Theta comp

Far Field displacements in x-z plane  
 Type of surface obstacle : Segment of a hemisphere  
 Order of approximation : 14  
 Incident wavetype : P  
 Incident angle : 60.00 deg  
 Poisson's ratio : 0.34  
 $2a / \lambda$  incident : 1.00  
 $d / a$  : 0.75

Fig. 83 : Amplitude of the far-field displacements of the scattered field in the x-z plane (plane of the incident wave vector) for a compressional wave incident under 60 degrees on to a shallow axisymmetric surface indentation



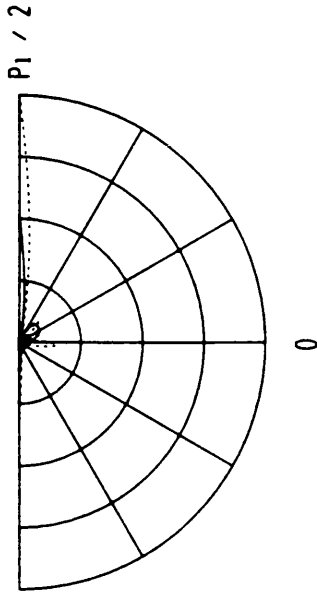
— R comp      ..... Theta comp  
 - - Phi comp

Far Field displacements in y-z plane  
 Type of surface obstacle : Segment of a hemisphere  
 Order of approximation : 14  
 Incident wavetype : P  
 Incident angle : 60.00 deg  
 Poisson's ratio : 0.34  
 $2a / \lambda$  incident : 1.00  
 $d / a$  : 0.75

Fig. 84 : Amplitude of the far-field displacements of the scattered field in the y-z plane (plane perpendicular to the incident wave vector) for a compressional wave incident under 60 degrees on to a shallow axisymmetric surface indentation

Theta =

-  $P_1 / 2$



— P component      ..... S component

Scattered energy in x-z plane

Type of surface obstacle : Segment of a hemisphere

Order of approximation : 14

Incident waveltype : P

Incident angle : 60.00 deg

Poisson's ratio : 0.34

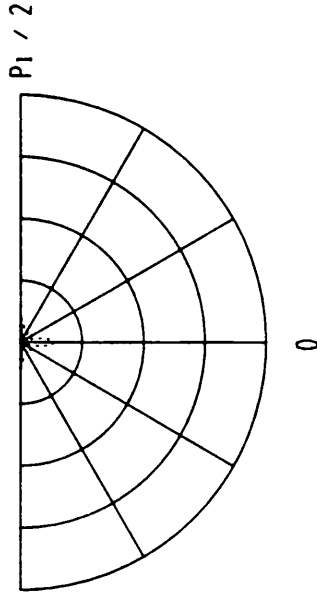
$2a / \lambda$  incident : 1.00

$d / a$  : 0.75

Fig. 85 : Differential cross-section of the scattered far-field in the x-z plane (plane of the incident wave vector) for a compressional wave incident under 60 degrees on to a shallow axisymmetric surface indentation

Theta =

-  $P_1 / 2$



— P component      ..... S component

Scattered energy in y-z plane

Type of surface obstacle : Segment of a hemisphere

Order of approximation : 14

Incident waveltype : P

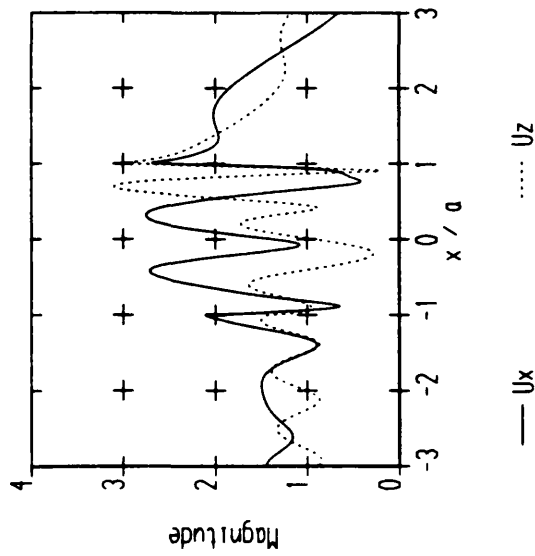
Incident angle : 60.00 deg

Poisson's ratio : 0.34

$2a / \lambda$  incident : 1.00

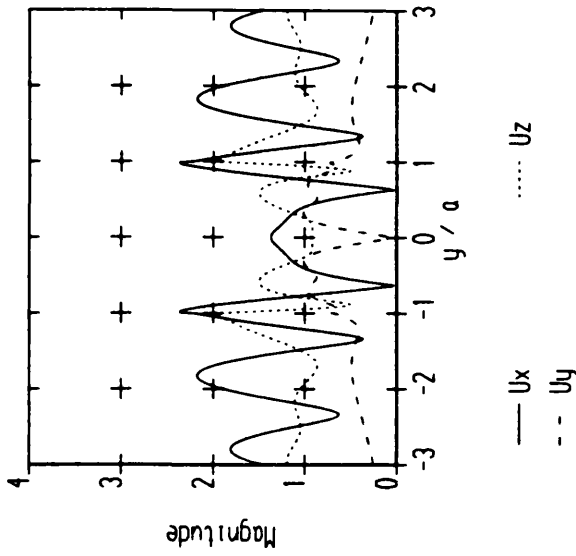
$d / a$  : 0.75

Fig. 86 : Differential cross-section of the scattered far-field in the y-z plane (plane perpendicular to the incident wave vector) for a compressional wave incident under 60 degrees on to a shallow axisymmetric surface indentation



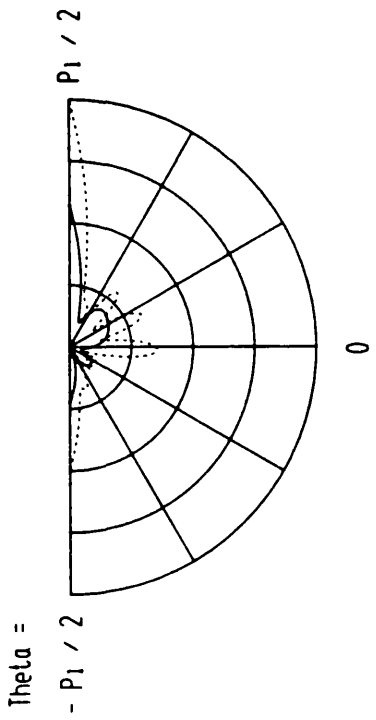
Surface displacements in x-z plane  
 Type of surface obstacle : Ellipsoid  
 Order of approximation : 14  
 Incident wavetype : P  
 Incident angle : 60.00 deg  
 Poisson's ratio : 0.34  
 $2a / \lambda$  incident : 1.00  
 $d / a$  : 0.75

Fig. 87 : Amplitude of the surface displacements in the x-z plane (plane of the incident wave vector) for a compressional wave incident under 60 degrees on to a shallow axisymmetric surface indentation



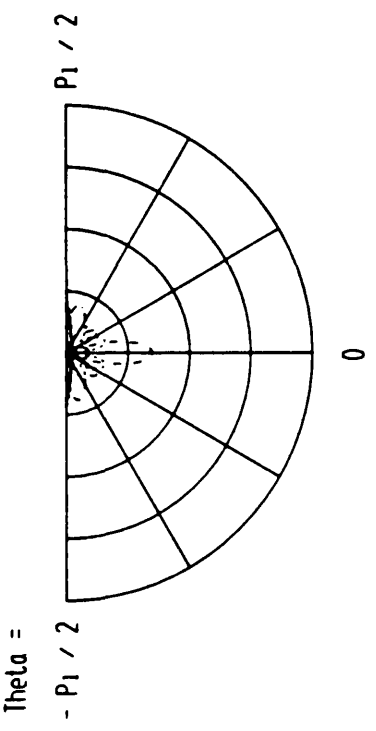
Surface displacements in y-z plane  
 Type of surface obstacle : Ellipsoid  
 Order of approximation : 14  
 Incident wavetype : P  
 Incident angle : 60.00 deg  
 Poisson's ratio : 0.34  
 $2a / \lambda$  incident : 1.00  
 $d / a$  : 0.75

Fig. 88 : Amplitude of the surface displacements in the y-z plane (plane perpendicular to the incident wave vector) for a compressional wave incident under 60 degrees on to a shallow axisymmetric surface indentation



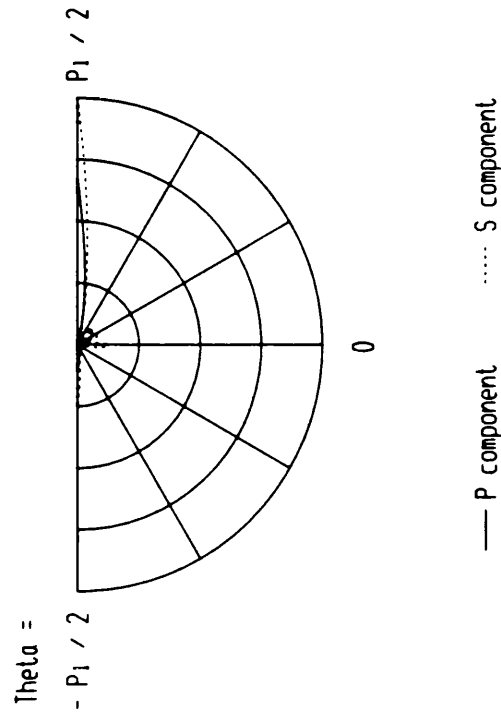
Far Field displacements in x-z plane  
 Type of surface obstacle : Ellipsoid  
 Order of approximation : 14  
 Incident wavetype : P  
 Incident angle : 60.00 deg  
 Poisson's ratio : 0.34  
 2a / lambda incident : 1.00  
 d / a : 0.75

Fig. 89 : Amplitude of the far-field displacements of the scattered field in the x-z plane (plane of the incident wave vector) for a compressional wave incident under 60 degrees on to a shallow axisymmetric surface indentation



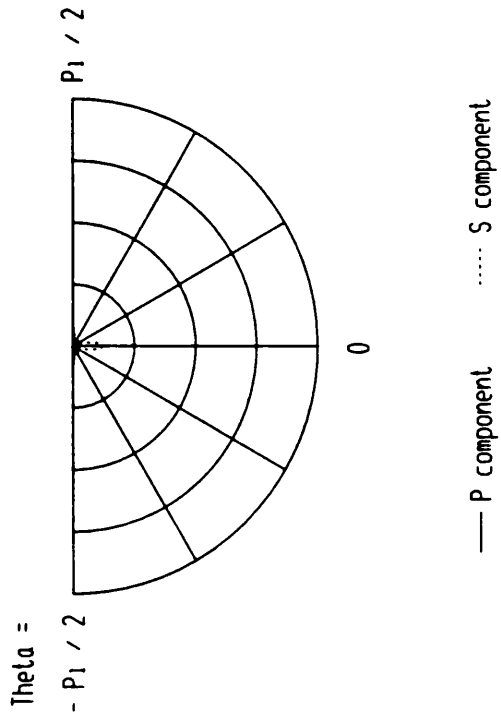
Far Field displacements in y-z plane  
 Type of surface obstacle : Ellipsoid  
 Order of approximation : 14  
 Incident wavetype : P  
 Incident angle : 60.00 deg  
 Poisson's ratio : 0.34  
 2a / lambda incident : 1.00  
 d / a : 0.75

Fig. 90 : Amplitude of the far-field displacements of the scattered field in the y-z plane (plane perpendicular to the incident wave vector) for a compressional wave incident under 60 degrees on to a shallow axisymmetric surface indentation



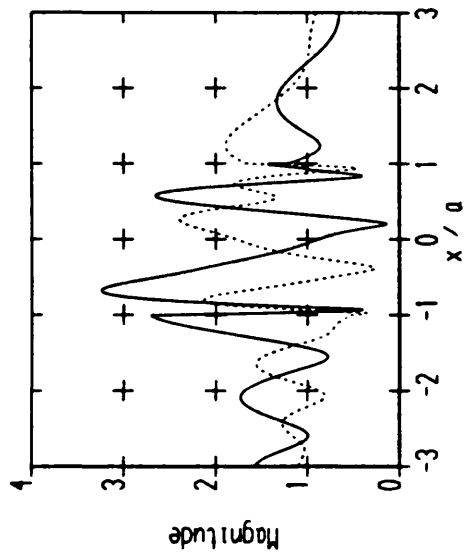
Scattered energy in x-z plane  
 Type of surface obstacle : Ellipsoid  
 Order of approximation : 14  
 Incident waveltype : P  
 Incident angle : 60.00 deg  
 Poisson's ratio : 0.34  
 $2a / \text{lambda incident}$  : 1.00  
 $d / a$  : 0.75

Fig. 91 : Differential cross-section of the scattered far-field in the x-z plane (plane of the incident wave vector) for a compressional wave incident under 60 degrees on to a shallow axisymmetric surface indentation



Scattered energy in y-z plane  
 Type of surface obstacle : Ellipsoid  
 Order of approximation : 14  
 Incident waveltype : P  
 Incident angle : 60.00 deg  
 Poisson's ratio : 0.34  
 $2a / \text{lambda incident}$  : 1.00  
 $d / a$  : 0.75

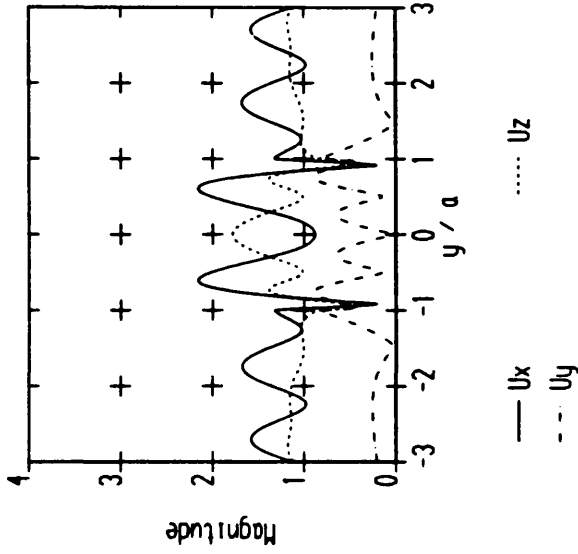
Fig. 92 : Differential cross-section of the scattered far-field in the y-z plane (plane perpendicular to the incident wave vector) for a compressional wave incident under 60 degrees on to a shallow axisymmetric surface indentation



— Ux      ..... Uz  
 - - - Uy

Surface displacements in x-z plane  
 Type of surface obstacle : Hemisphere  
 Order of approximation : 16  
 Incident wavetype : P  
 Incident angle : 60.00 deg  
 Poisson's ratio : 0.34  
 $2a / \lambda$  incident : 1.00  
 $d / a$  : 1.00

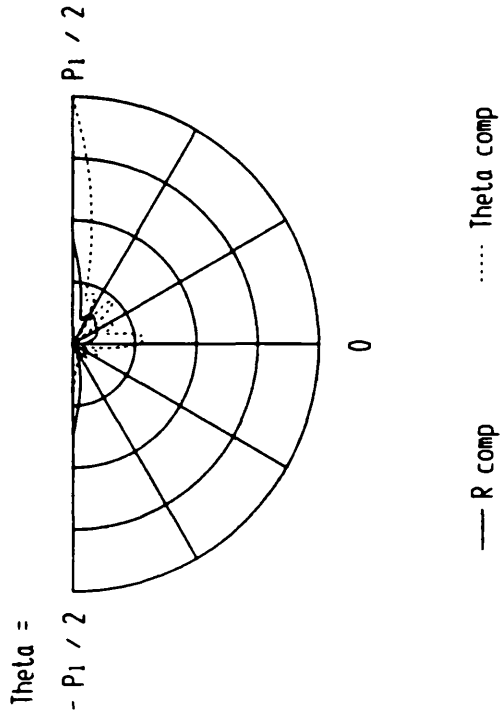
Fig. 93 : Amplitude of the surface displacements in the x-z plane (plane of the incident wave vector) for a compressional wave incident under 60 degrees on to a hemispherical surface indentation



— Ux      ..... Uz  
 - - - Uy

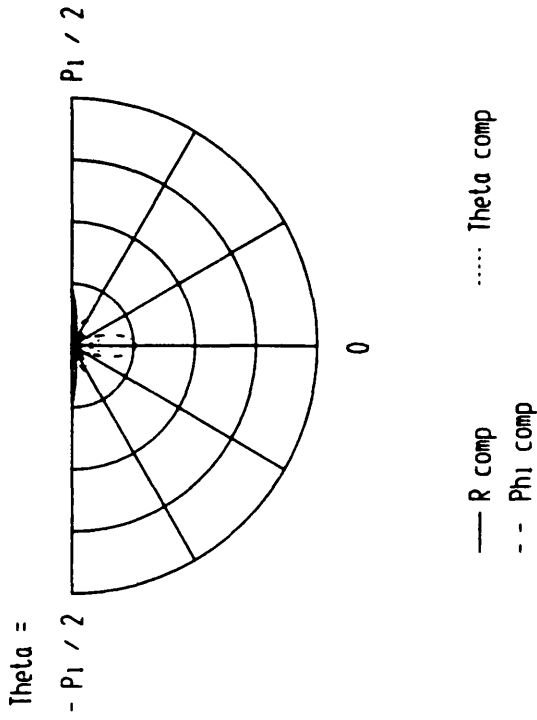
Surface displacements in y-z plane  
 Type of surface obstacle : Hemisphere  
 Order of approximation : 16  
 Incident wavetype : P  
 Incident angle : 60.00 deg  
 Poisson's ratio : 0.34  
 $2a / \lambda$  incident : 1.00  
 $d / a$  : 1.00

Fig. 94 : Amplitude of the surface displacements in the y-z plane (plane perpendicular to the incident wave vector) for a compressional wave incident under 60 degrees on to a hemispherical surface indentation



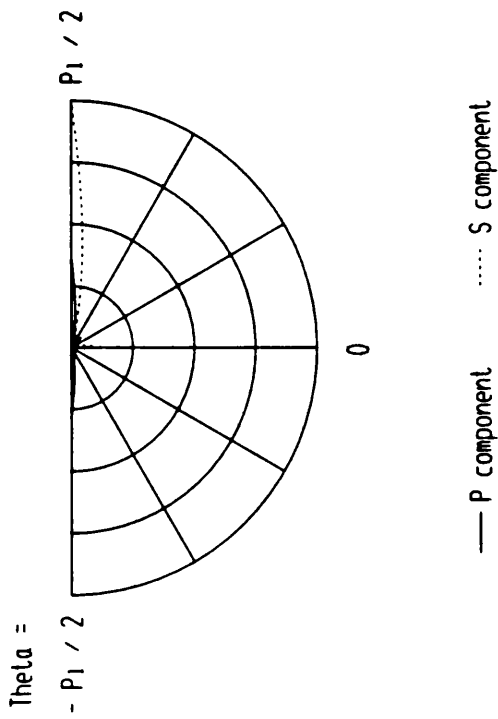
Far field displacements in x-z plane  
 Type of surface obstacle : Hemisphere  
 Order of approximation : 16  
 Incident wavetype : P  
 Incident angle : 60.00 deg  
 Poisson's ratio : 0.34  
 $2a / \lambda$  incident : 1.00  
 $d / a$  : 1.00

Fig. 95 : Amplitude of the far-field displacements of the scattered field in the x-z plane (plane of the incident wave vector) for a compressional wave incident under 60 degrees on to a hemispherical surface indentation



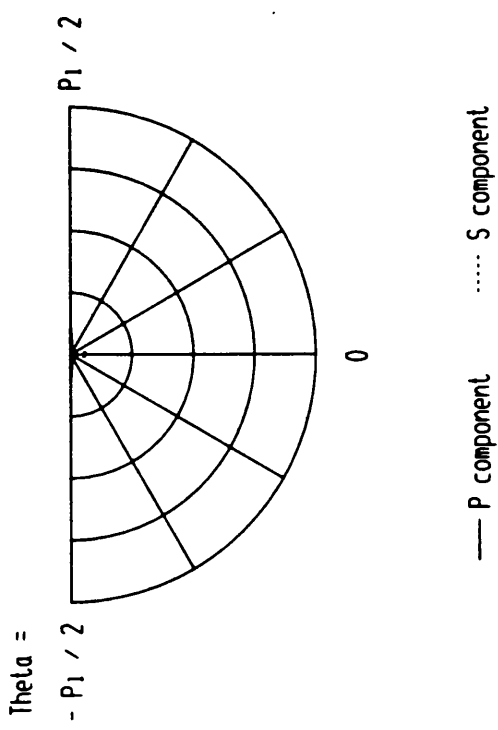
Far field displacements in y-z plane  
 Type of surface obstacle : Hemisphere  
 Order of approximation : 16  
 Incident wavetype : P  
 Incident angle : 60.00 deg  
 Poisson's ratio : 0.34  
 $2a / \lambda$  incident : 1.00  
 $d / a$  : 1.00

Fig. 96 : Amplitude of the far-field displacements of the scattered field in the y-z plane (plane perpendicular to the incident wave vector) for a compressional wave incident under 60 degrees on to a hemispherical surface indentation



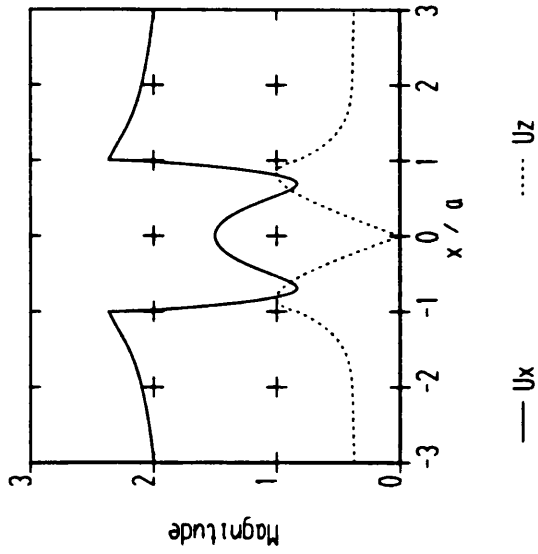
Scattered energy in x-z plane  
 Type of surface obstacle : Hemisphere  
 Order of approximation : 16  
 Incident wavetype : P  
 Incident angle : 60.00 deg  
 Poisson's ratio : 0.34  
 $2a / \lambda$  incident : 1.00  
 $d / a$  : 1.00

Fig. 97 : Differential cross-section of the scattered far-field in the x-z plane (plane of the incident wave vector) for a compressional wave incident under 60 degrees on to a hemispherical surface indentation



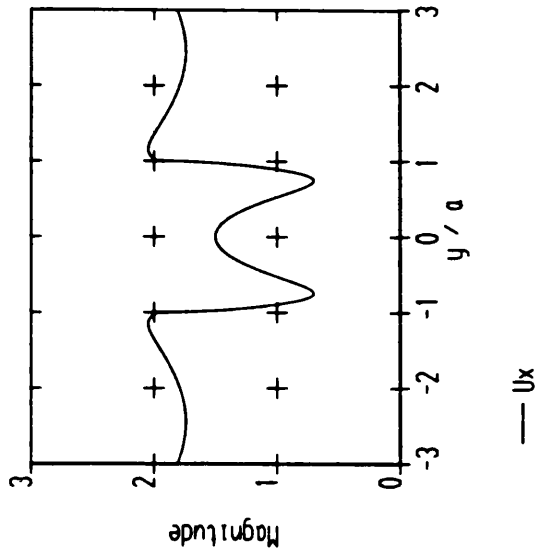
Scattered energy in y-z plane  
 Type of surface obstacle : Hemisphere  
 Order of approximation : 16  
 Incident wavetype : P  
 Incident angle : 60.00 deg  
 Poisson's ratio : 0.34  
 $2a / \lambda$  incident : 1.00  
 $d / a$  : 1.00

Fig. 98 : Differential cross-section of the scattered far-field in the y-z plane (plane perpendicular to the incident wave vector) for a compressional wave incident under 60 degrees on to a hemispherical surface indentation



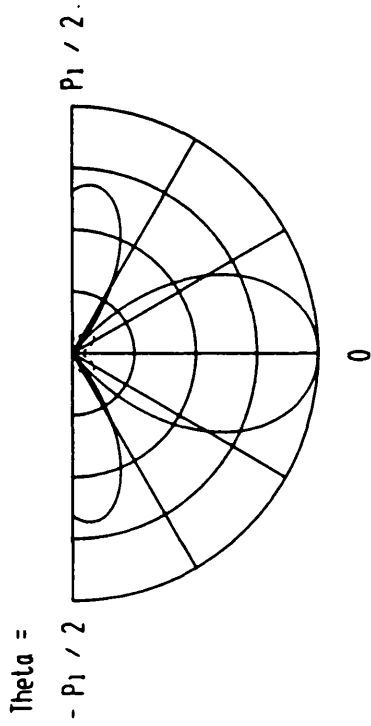
Surface displacements in x-z plane  
 Type of surface obstacle : Hemisphere  
 Order of approximation : 11  
 Incident wavetype : SV  
 Incident angle : 0.00 deg  
 Poisson's ratio : 0.34  
 $2a / \lambda$  incident : 0.50  
 $d / a$  : 1.00

Fig. 99 : Amplitude of the surface displacements in the x-z plane (plane of polarisation) for a shear wave normally incident on to a hemispherical surface indentation



Surface displacements in y-z plane  
 Type of surface obstacle : Hemisphere  
 Order of approximation : 11  
 Incident wavetype : SV  
 Incident angle : 0.00 deg  
 Poisson's ratio : 0.34  
 $2a / \lambda$  incident : 0.50  
 $d / a$  : 1.00

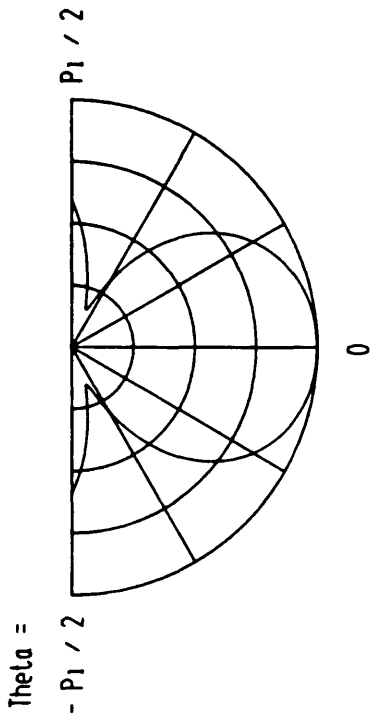
Fig. 100 : Amplitude of the surface displacements in the y-z plane (plane perpendicular to polarisation) for a shear wave normally incident on to a hemispherical surface indentation



— Theta comp      ..... R comp

Far field displacements in x-z plane  
 Type of surface obstacle : Hemisphere  
 Order of approximation : 11  
 Incident waveltype : SV  
 Incident angle : 0.00 deg  
 Poisson's ratio : 0.34  
 $2a / \lambda$  incident : 0.50  
 $d / a$  : 1.00

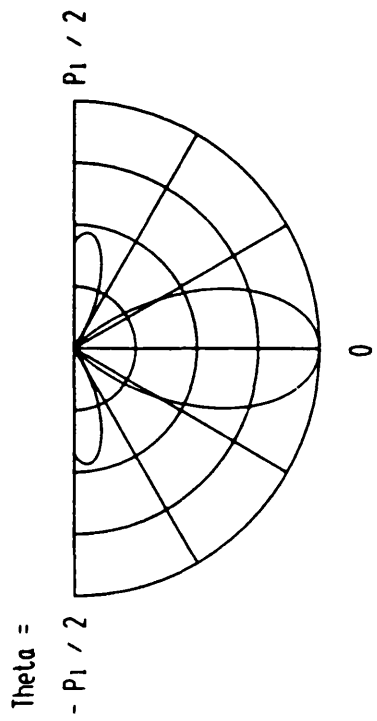
Fig. 101 : Amplitude of the far-field displacements of the scattered field in the x-z plane (plane of polarisation) for a shear wave normally incident on to a hemispherical surface indentation



— Phi comp

Far field displacements in y-z plane  
 Type of surface obstacle : Hemisphere  
 Order of approximation : 11  
 Incident waveltype : SV  
 Incident angle : 0.00 deg  
 Poisson's ratio : 0.34  
 $2a / \lambda$  incident : 0.50  
 $d / a$  : 1.00

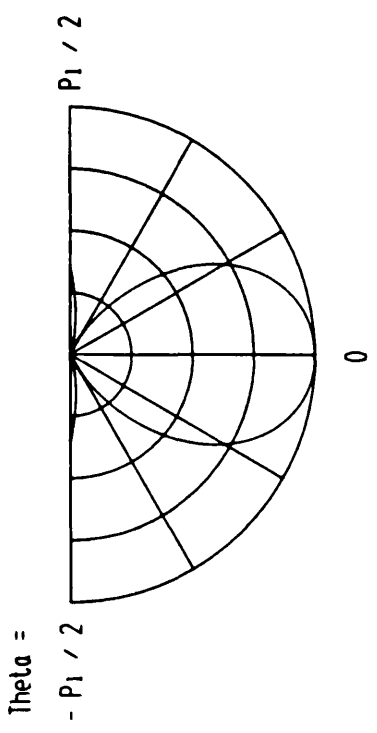
Fig. 102 : Amplitude of the far-field displacements of the scattered field in the y-z plane (plane perpendicular to polarisation) for a shear wave normally incident on to a hemispherical surface indentation



— S component      ..... P component

Scattered energy in x-z plane  
 Type of surface obstacle : Hemisphere  
 Order of approximation : 11  
 Incident wavetype : SV  
 Incident angle : 0.00 deg  
 Poisson's ratio : 0.34  
 $2a / \lambda$  incident : 0.50  
 $d / a$  : 1.00

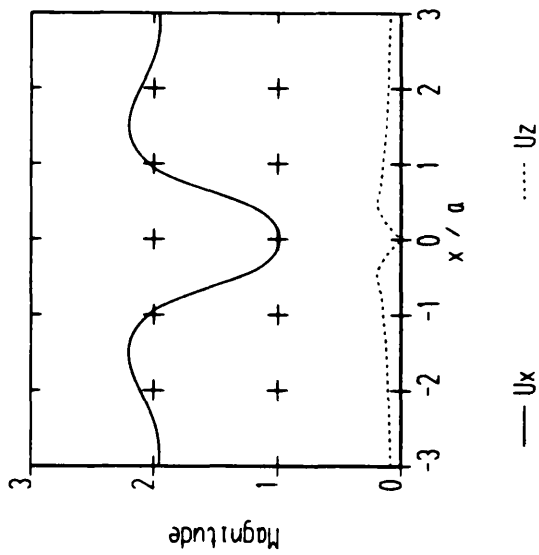
Fig. 103 : Differential cross-section of the scattered far-field in the x-z plane (plane of polarisation) for a shear wave normally incident on to a hemispherical surface indentation



— S component

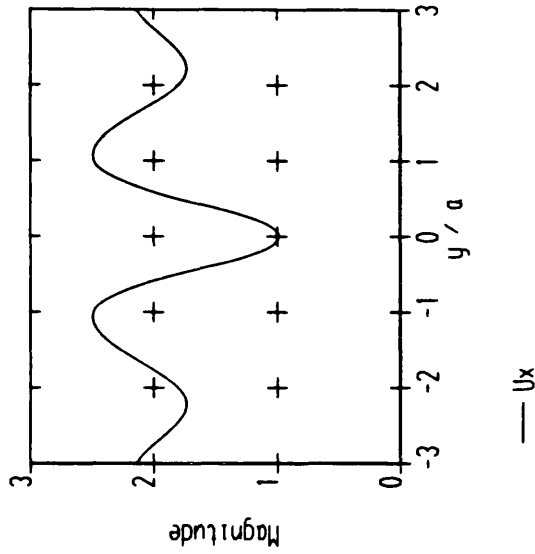
Scattered energy in y-z plane  
 Type of surface obstacle : Hemisphere  
 Order of approximation : 11  
 Incident wavetype : SV  
 Incident angle : 0.00 deg  
 Poisson's ratio : 0.34  
 $2a / \lambda$  incident : 0.50  
 $d / a$  : 1.00

Fig. 104 : Differential cross-section of the scattered far-field in the y-z plane (plane perpendicular to polarisation) for a shear wave normally incident on to a hemispherical surface indentation



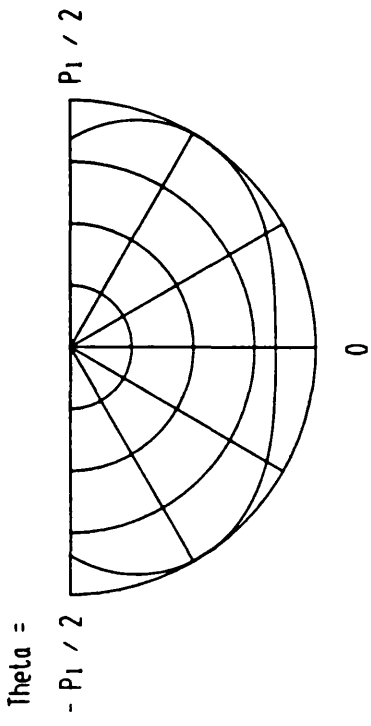
Surface displacements in x-z plane  
 Type of surface obstacle : Segment of a hemisphere  
 Order of approximation : 9  
 Incident wavetype : SV  
 Incident angle : 0.00 deg  
 Poisson's ratio : 0.34  
 $2a / \lambda$  incident : 1.00  
 $d / a$  : 0.25

Fig. 105 : Amplitude of the surface displacements in the x-z plane (plane of polarisation) for a shear wave normally incident on to a shallow axisymmetric surface indentation



Surface displacements in y-z plane  
 Type of surface obstacle : Segment of a hemisphere  
 Order of approximation : 9  
 Incident wavetype : SV  
 Incident angle : 0.00 deg  
 Poisson's ratio : 0.34  
 $2a / \lambda$  incident : 1.00  
 $d / a$  : 0.25

Fig. 106 : Amplitude of the surface displacements in the y-z plane (plane perpendicular to polarisation) for a shear wave normally incident on to a shallow axisymmetric surface indentation



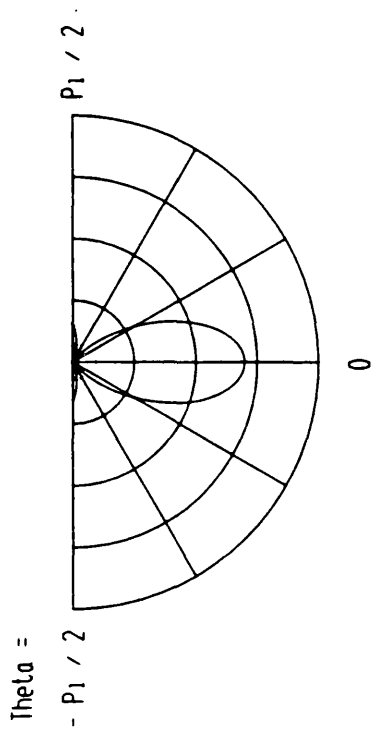
Far Field displacements in x-z plane  
 Type of surface obstacle : Segment of a hemisphere  
 Order of approximation : 9  
 Incident wavetype : SV  
 Incident angle : 0.00 deg  
 Poisson's ratio : 0.34  
 $2a / \lambda$  incident : 1.00  
 $d / a$  : 0.25

Fig. 107 : Amplitude of the far-field displacements of the scattered field in the x-z plane (plane of polarisation) for a shear wave normally incident on to a shallow axisymmetric surface indentation



Far Field displacements in y-z plane  
 Type of surface obstacle : Segment of a hemisphere  
 Order of approximation : 9  
 Incident wavetype : SV  
 Incident angle : 0.00 deg  
 Poisson's ratio : 0.34  
 $2a / \lambda$  incident : 1.00  
 $d / a$  : 0.25

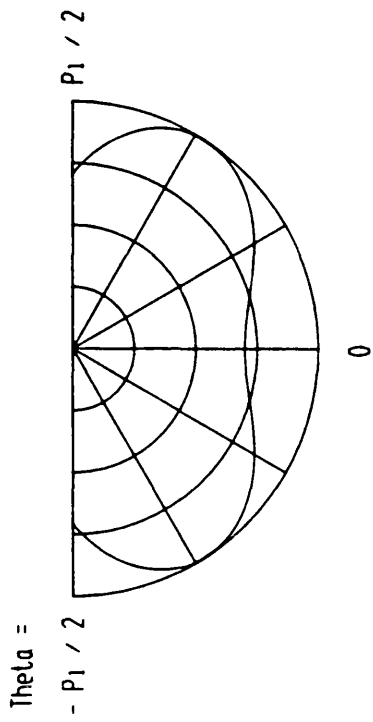
Fig. 108 : Amplitude of the far-field displacements of the scattered field in the y-z plane (plane perpendicular to polarisation) for a shear wave normally incident on to a shallow axisymmetric surface indentation



— S component      ..... P component

Scattered energy in x-z plane  
 Type of surface obstacle : Segment of a hemisphere  
 Order of approximation : 9  
 Incident waveltype : SV  
 Incident angle : 0.00 deg  
 Poisson's ratio : 0.34  
 $2a / \lambda$  incident : 1.00  
 $d / a$  : 0.25

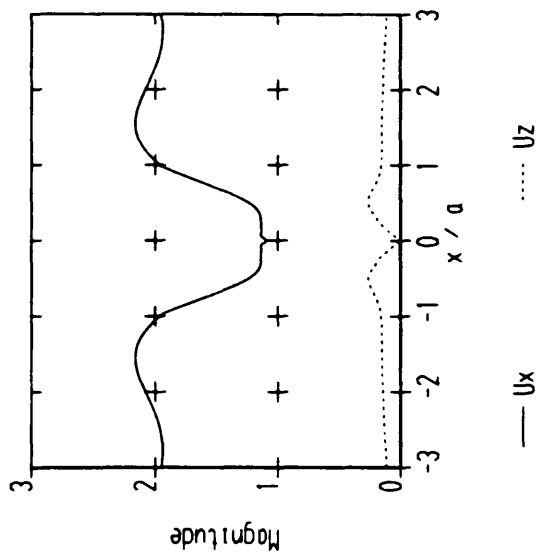
Fig. 109 : Differential cross-section of the scattered far-field in the x-z plane (plane of polarisation) for a shear wave normally incident on to a shallow axisymmetric surface indentation



— S component

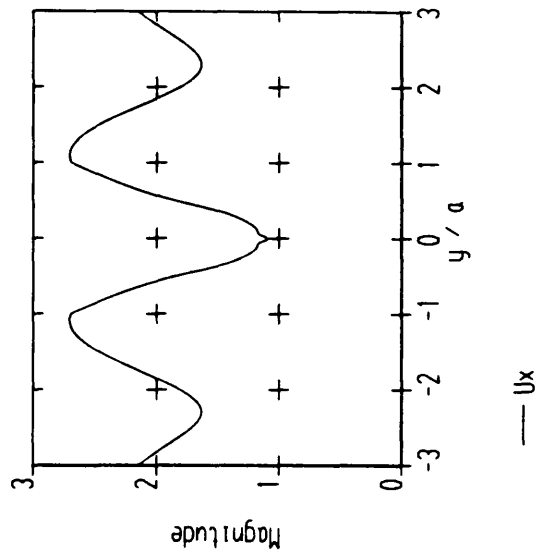
Scattered energy in y-z plane  
 Type of surface obstacle : Segment of a hemisphere  
 Order of approximation : 9  
 Incident waveltype : SV  
 Incident angle : 0.00 deg  
 Poisson's ratio : 0.34  
 $2a / \lambda$  incident : 1.00  
 $d / a$  : 0.25

Fig. 110 : Differential cross-section of the scattered far-field in the y-z plane (plane perpendicular to polarisation) for a shear wave normally incident on to a shallow axisymmetric surface indentation



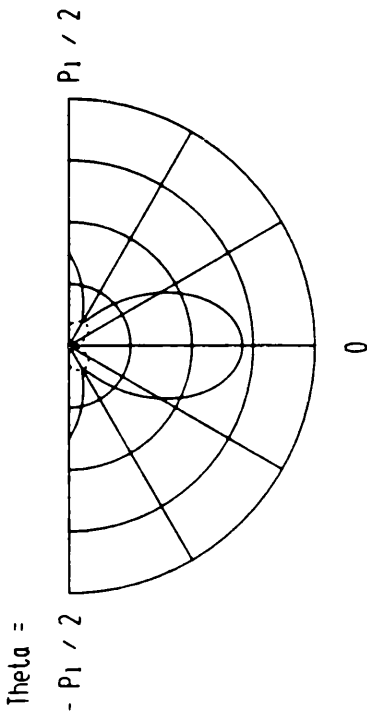
Surface displacements in x-z plane  
 Type of surface obstacle : Ellipsoid  
 Order of approximation : 9  
 Incident waveltype : SV  
 Incident angle : 0.00 deg  
 Poisson's ratio : 0.34  
 $2a / \lambda$  incident : 1.00  
 $d / a$  : 0.25

Fig. 111 : Amplitude of the surface displacements in the x-z plane (plane of polarisation) for a shear wave normally incident on to a shallow axisymmetric surface indentation



Surface displacements in y-z plane  
 Type of surface obstacle : Ellipsoid  
 Order of approximation : 9  
 Incident waveltype : SV  
 Incident angle : 0.00 deg  
 Poisson's ratio : 0.34  
 $2a / \lambda$  incident : 1.00  
 $d / a$  : 0.25

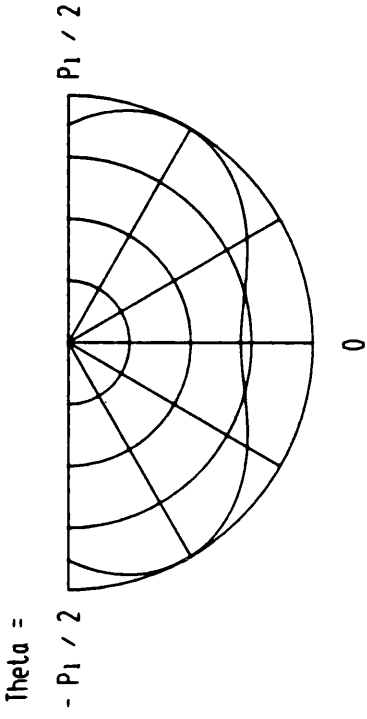
Fig. 112 : Amplitude of the surface displacements in the y-z plane (plane perpendicular to polarisation) for a shear wave normally incident on to a shallow axisymmetric surface indentation



— Theta comp      ..... R comp

Far field displacements in x-z plane  
 Type of surface obstacle : Ellipsoid  
 Order of approximation : 9  
 Incident waveltype : SV  
 Incident angle : 0.00 deg  
 Poisson's ratio : 0.34  
 2a / lambda incident : 1.00  
 d / a : 0.25

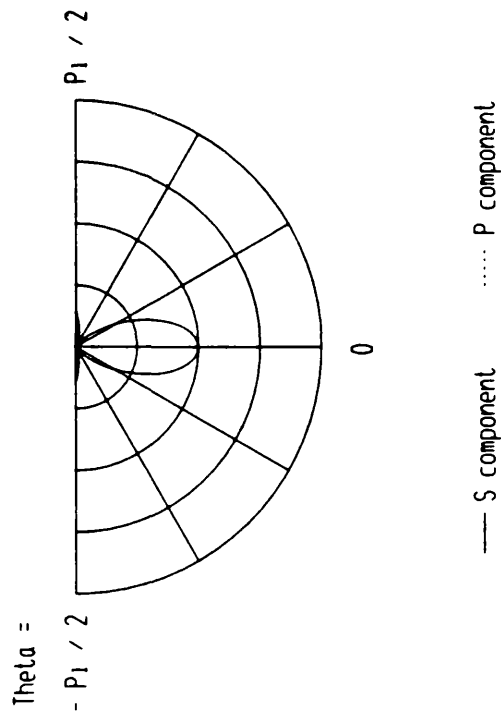
Fig. 113 : Amplitude of the far-field displacements of the scattered field in the x-z plane (plane of polarisation) for a shear wave normally incident on to a shallow axisymmetric surface indentation



— Phi comp

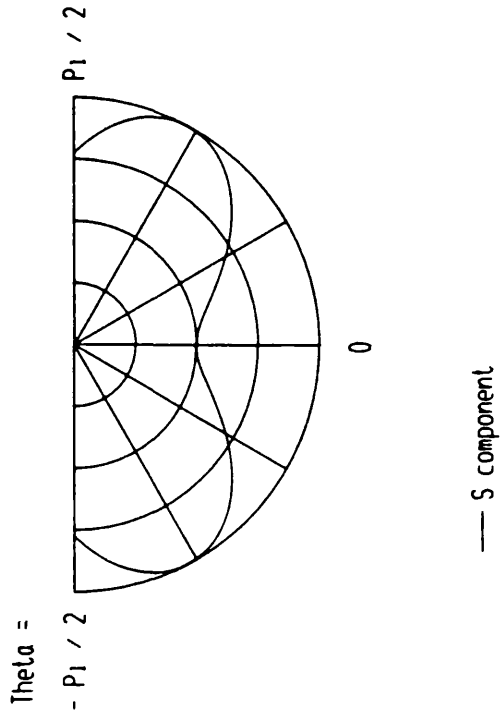
Far field displacements in y-z plane  
 Type of surface obstacle : Ellipsoid  
 Order of approximation : 9  
 Incident waveltype : SV  
 Incident angle : 0.00 deg  
 Poisson's ratio : 0.34  
 2a / lambda incident : 1.00  
 d / a : 0.25

Fig. 114 : Amplitude of the far-field displacements of the scattered field in the y-z plane (plane perpendicular to polarisation) for a shear wave normally incident on to a shallow axisymmetric surface indentation



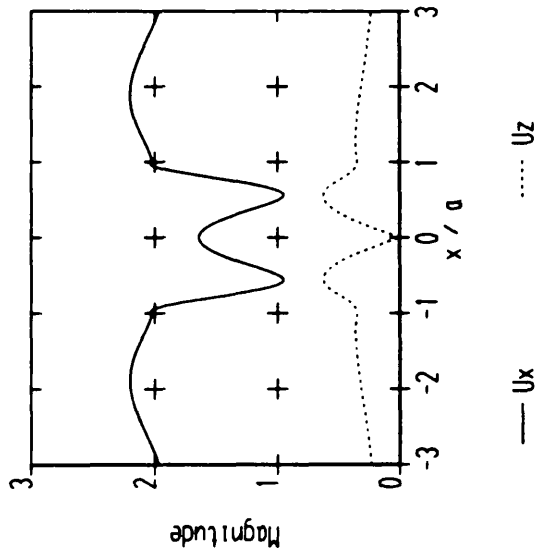
Scattered energy in x-z plane  
 Type of surface obstacle : Ellipsoid  
 Order of approximation : 9  
 Incident wavetype : SV  
 Incident angle : 0.00 deg  
 Poisson's ratio : 0.34  
 $2a / \lambda$  incident : 1.00  
 $d / a$  : 0.25

Fig. 115 : Differential cross-section of the scattered far-field in the x-z plane (plane of polarisation) for a shear wave normally incident on to a shallow axisymmetric surface indentation



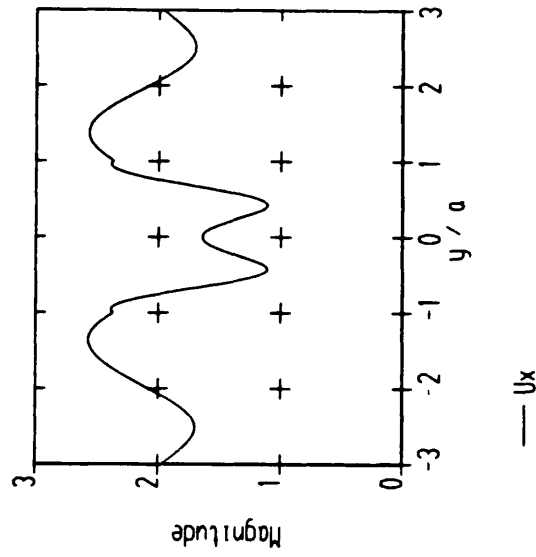
Scattered energy in y-z plane  
 Type of surface obstacle : Ellipsoid  
 Order of approximation : 9  
 Incident wavetype : SV  
 Incident angle : 0.00 deg  
 Poisson's ratio : 0.34  
 $2a / \lambda$  incident : 1.00  
 $d / a$  : 0.25

Fig. 116 : Differential cross-section of the scattered far-field in the y-z plane (plane perpendicular to polarisation) for a shear wave normally incident on to a shallow axisymmetric surface indentation



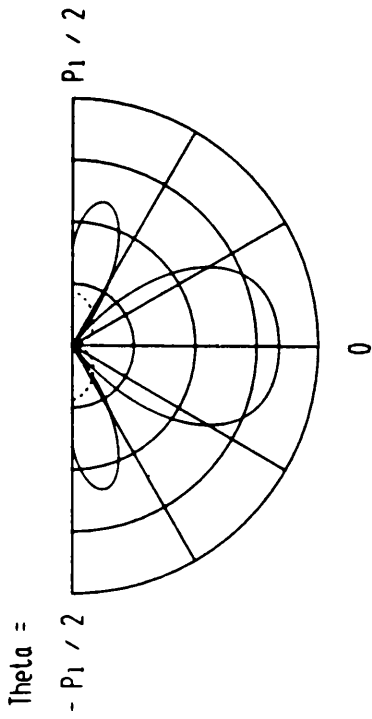
Surface displacements in x-z plane  
 Type of surface obstacle : Segment of a hemisphere  
 Order of approximation : 11  
 Incident wavetype : SV  
 Incident angle : 0.00 deg  
 Poisson's ratio : 0.34  
 $2a / \lambda$  incident : 1.00  
 $d / a$  : 0.50

Fig. 117 : Amplitude of the surface displacements in the x-z plane (plane of polarisation) for a shear wave normally incident on to a shallow axisymmetric surface indentation



Surface displacements in y-z plane  
 Type of surface obstacle : Segment of a hemisphere  
 Order of approximation : 11  
 Incident wavetype : SV  
 Incident angle : 0.00 deg  
 Poisson's ratio : 0.34  
 $2a / \lambda$  incident : 1.00  
 $d / a$  : 0.50

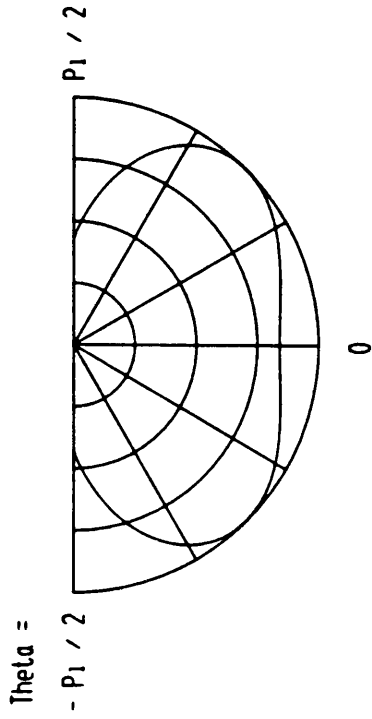
Fig. 118 : Amplitude of the surface displacements in the y-z plane (plane perpendicular to polarisation) for a shear wave normally incident on to a shallow axisymmetric surface indentation



— Theta comp      ..... R comp

Far field displacements in x-z plane  
 Type of surface obstacle : Segment of a hemisphere  
 Order of approximation : 11  
 Incident wavetype : SV  
 Incident angle : 0.00 deg  
 Poisson's ratio : 0.34  
 $2a / \lambda$  incident : 1.00  
 $d / a$  : 0.50

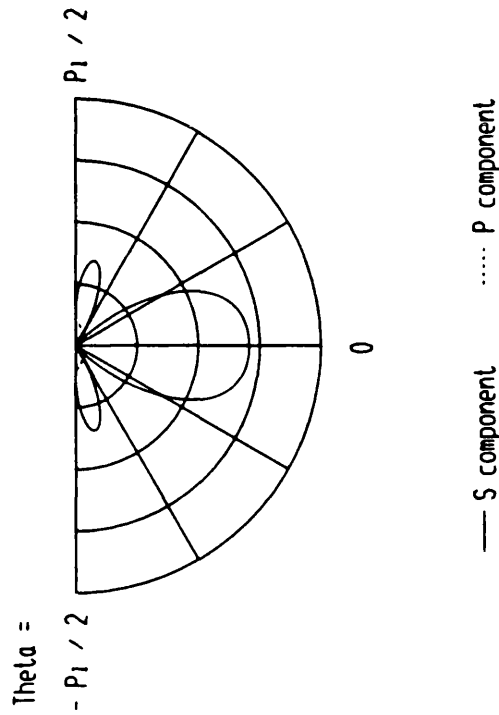
Fig. 119 : Amplitude of the far-field displacements of the scattered field in the x-z plane (plane of polarisation) for a shear wave normally incident on to a shallow axisymmetric surface indentation



— Phi comp

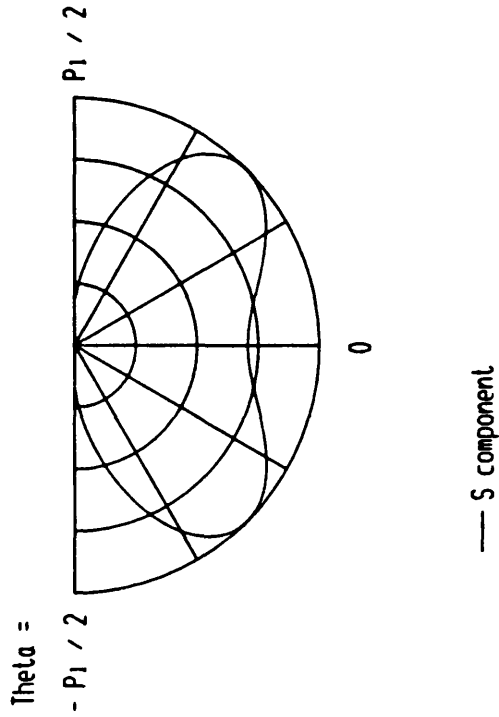
Far field displacements in y-z plane  
 Type of surface obstacle : Segment of a hemisphere  
 Order of approximation : 11  
 Incident wavetype : SV  
 Incident angle : 0.00 deg  
 Poisson's ratio : 0.34  
 $2a / \lambda$  incident : 1.00  
 $d / a$  : 0.50

Fig. 120 : Amplitude of the far-field displacements of the scattered field in the y-z plane (plane perpendicular to polarisation) for a shear wave normally incident on to a shallow axisymmetric surface indentation



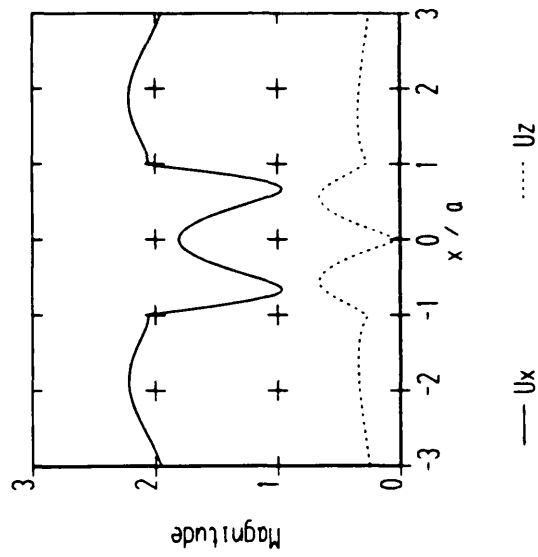
Scattered energy in x-z plane  
 Type of surface obstacle : Segment of a hemisphere  
 Order of approximation : 11  
 Incident wavetype : SV  
 Incident angle : 0.00 deg  
 Poisson's ratio : 0.34  
 $2a / \lambda$  incident : 1.00  
 $d / a$  : 0.50

Fig. 121 : Differential cross-section of the scattered far-field in the x-z plane (plane of polarisation) for a shear wave normally incident on to a shallow axisymmetric surface indentation



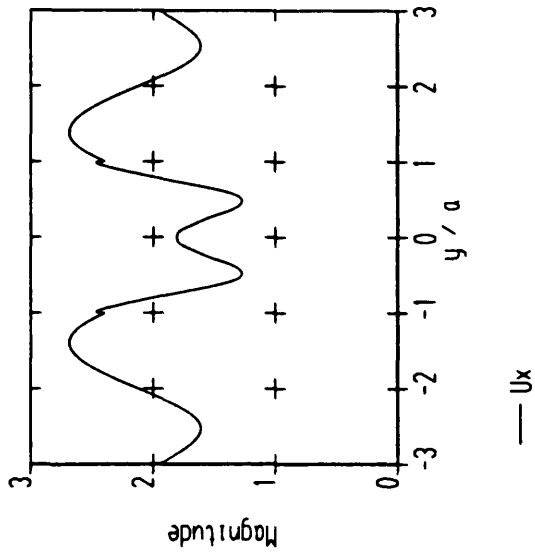
Scattered energy in y-z plane  
 Type of surface obstacle : Segment of a hemisphere  
 Order of approximation : 11  
 Incident wavetype : SV  
 Incident angle : 0.00 deg  
 Poisson's ratio : 0.34  
 $2a / \lambda$  incident : 1.00  
 $d / a$  : 0.50

Fig. 122 : Differential cross-section of the scattered far-field in the y-z plane (plane perpendicular to polarisation) for a shear wave normally incident on to a shallow axisymmetric surface indentation



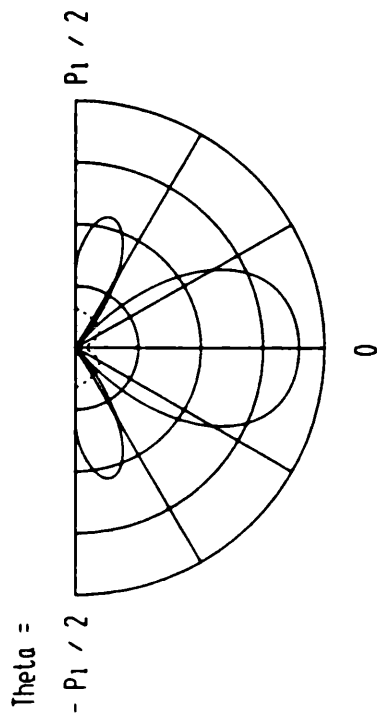
Surface displacements in x-z plane  
 Type of surface obstacle : Ellipsoid  
 Order of approximation : 11  
 Incident wavetype : SV  
 Incident angle : 0.00 deg  
 Poisson's ratio : 0.34  
 $2a / \lambda$  incident : 1.00  
 $d / a$  : 0.50

Fig. 123 : Amplitude of the surface displacements in the x-z plane (plane of polarisation) for a shear wave normally incident on to a shallow axisymmetric surface indentation



Surface displacements in y-z plane  
 Type of surface obstacle : Ellipsoid  
 Order of approximation : 11  
 Incident wavetype : SV  
 Incident angle : 0.00 deg  
 Poisson's ratio : 0.34  
 $2a / \lambda$  incident : 1.00  
 $d / a$  : 0.50

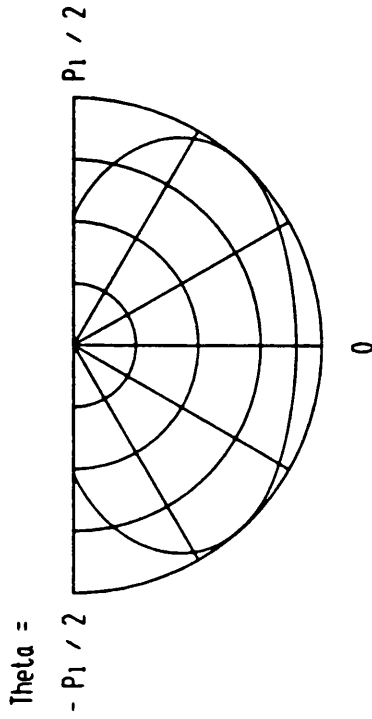
Fig. 124 : Amplitude of the surface displacements in the y-z plane (plane perpendicular to polarisation) for a shear wave normally incident on to a shallow axisymmetric surface indentation



— Theta comp      ..... R comp

Far field displacements in x-z plane  
 Type of surface obstacle : Ellipsoid  
 Order of approximation : 11  
 Incident wavetype : SV  
 Incident angle : 0.00 deg  
 Poisson's ratio : 0.34  
 $2a / \lambda$  incident : 1.00  
 $d / a$  : 0.50

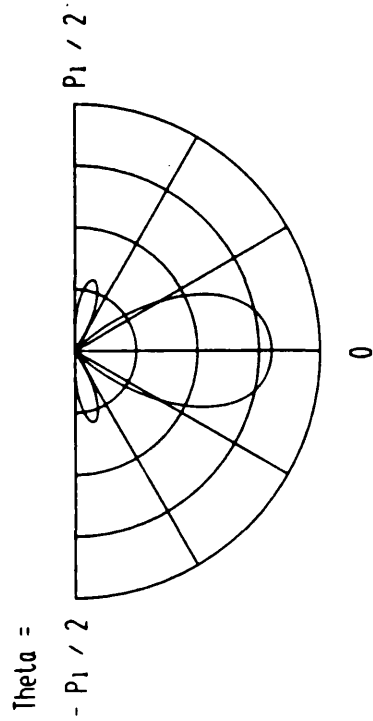
Fig. 125 : Amplitude of the far-field displacements of the scattered field in the x-z plane (plane of polarisation) for a shear wave normally incident on to a shallow axisymmetric surface indentation



— Phi comp

Far field displacements in y-z plane  
 Type of surface obstacle : Ellipsoid  
 Order of approximation : 11  
 Incident wavetype : SV  
 Incident angle : 0.00 deg  
 Poisson's ratio : 0.34  
 $2a / \lambda$  incident : 1.00  
 $d / a$  : 0.50

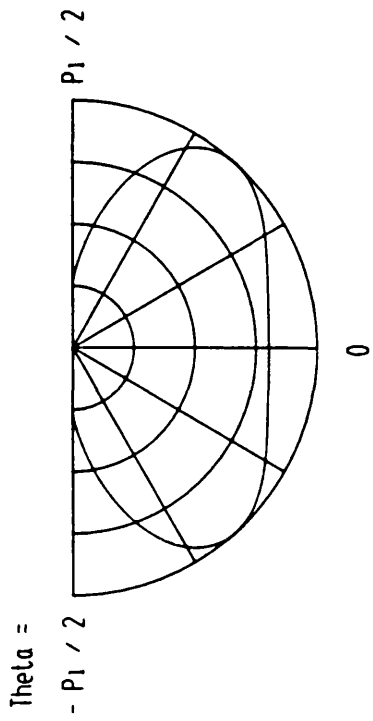
Fig. 126 : Amplitude of the far-field displacements of the scattered field in the y-z plane (plane perpendicular to polarisation) for a shear wave normally incident on to a shallow axisymmetric surface indentation



— S component    ..... P component

Scattered energy in x-z plane  
 Type of surface obstacle : Ellipsoid  
 Order of approximation : 11  
 Incident waveltype : SV  
 Incident angle : 0.00 deg  
 Poisson's ratio : 0.34  
 $2a / \lambda$  incident : 1.00  
 $d / a$  : 0.50

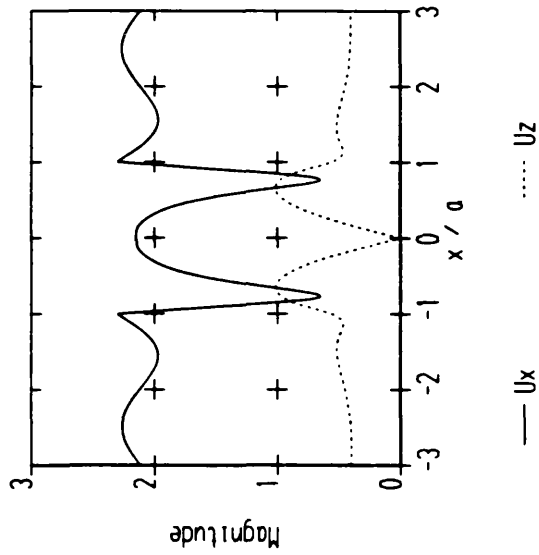
Fig. 127 : Differential cross-section of the scattered far-field in the x-z plane (plane of polarisation) for a shear wave normally incident on to a shallow axisymmetric surface indentation



— S component

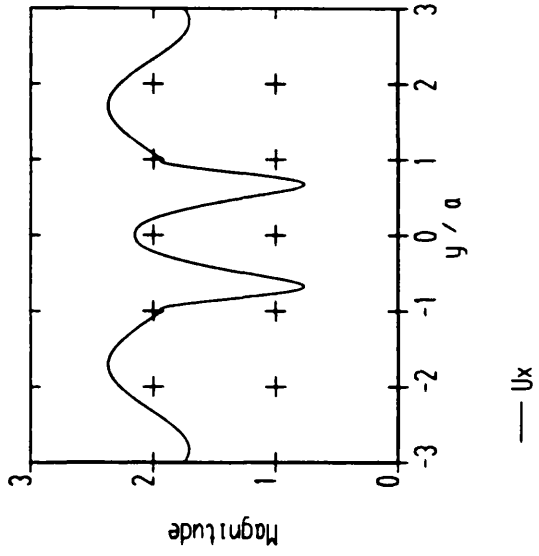
Scattered energy in y-z plane  
 Type of surface obstacle : Ellipsoid  
 Order of approximation : 11  
 Incident waveltype : SV  
 Incident angle : 0.00 deg  
 Poisson's ratio : 0.34  
 $2a / \lambda$  incident : 1.00  
 $d / a$  : 0.50

Fig. 128 : Differential cross-section of the scattered far-field in the y-z plane (plane perpendicular to polarisation) for a shear wave normally incident on to a shallow axisymmetric surface indentation



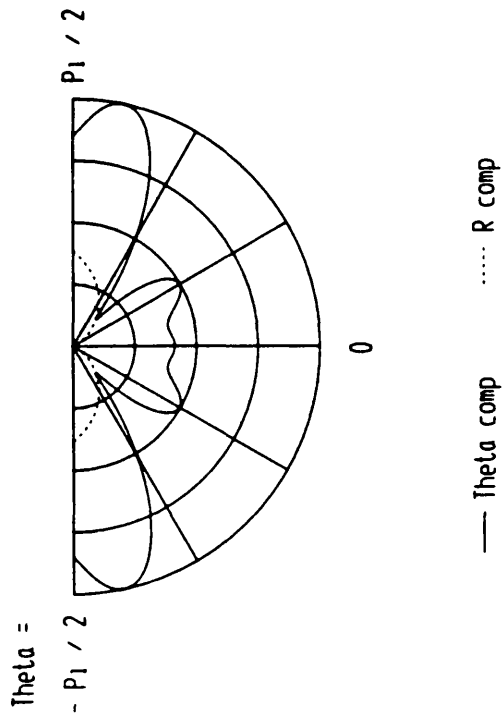
Surface displacements in x-z plane  
 Type of surface obstacle : Segment of a hemisphere  
 Order of approximation : 12  
 Incident wavetype : SV  
 Incident angle : 0.00 deg  
 Poisson's ratio : 0.34  
 $2a / \lambda$  incident : 1.00  
 $d / a$  : 0.75

Fig. 129 : Amplitude of the surface displacements in the x-z plane (plane of polarisation) for a shear wave normally incident on to a shallow axisymmetric surface indentation



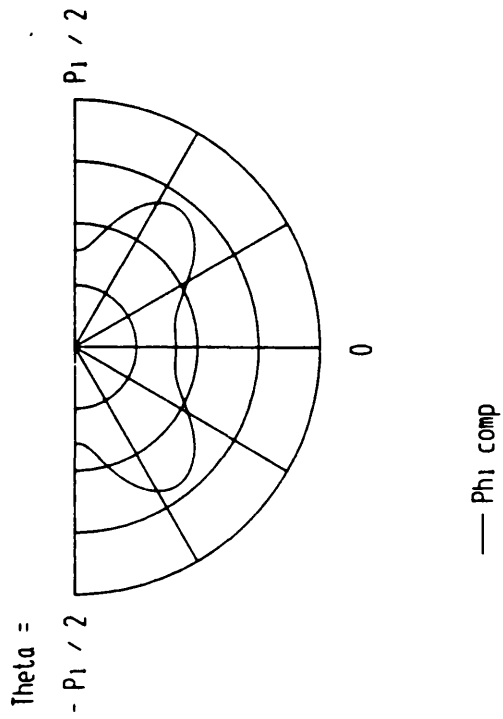
Surface displacements in y-z plane  
 Type of surface obstacle : Segment of a hemisphere  
 Order of approximation : 12  
 Incident wavetype : SV  
 Incident angle : 0.00 deg  
 Poisson's ratio : 0.34  
 $2a / \lambda$  incident : 1.00  
 $d / a$  : 0.75

Fig. 130 : Amplitude of the surface displacements in the y-z plane (plane perpendicular to polarisation) for a shear wave normally incident on to a shallow axisymmetric surface indentation



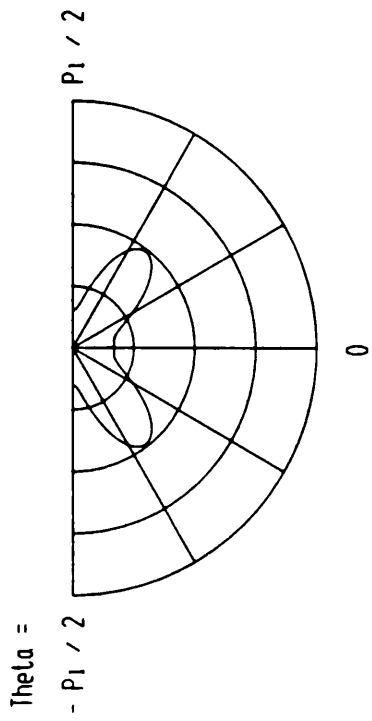
Far Field displacements in x-z plane  
 Type of surface obstacle : Segment of a hemisphere  
 Order of approximation : 12  
 Incident wavetype : SV  
 Incident angle : 0.00 deg  
 Poisson's ratio : 0.34  
 $2a / \lambda$  incident : 1.00  
 $d / a$  : 0.75

Fig. 131 : Amplitude of the far-field displacements of the scattered field in the x-z plane (plane of polarisation) for a shear wave normally incident on to a shallow axisymmetric surface indentation



Far Field displacements in y-z plane  
 Type of surface obstacle : Segment of a hemisphere  
 Order of approximation : 12  
 Incident wavetype : SV  
 Incident angle : 0.00 deg  
 Poisson's ratio : 0.34  
 $2a / \lambda$  incident : 1.00  
 $d / a$  : 0.75

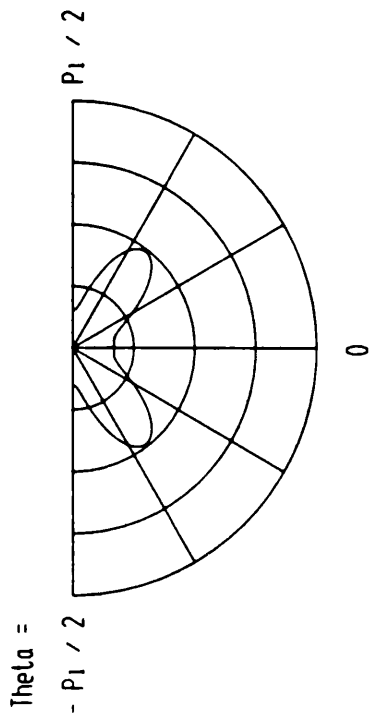
Fig. 132 : Amplitude of the far-field displacements of the scattered field in the y-z plane (plane perpendicular to polarisation) for a shear wave normally incident on to a shallow axisymmetric surface indentation



— S component      ..... P component

Scattered energy in x-z plane  
 Type of surface obstacle : Segment of a hemisphere  
 Order of approximation : 12  
 Incident waveltype : SV  
 Incident angle : 0.00 deg  
 Poisson's ratio : 0.34  
 $2a / \lambda$  incident : 1.00  
 $d / a$  : 0.75

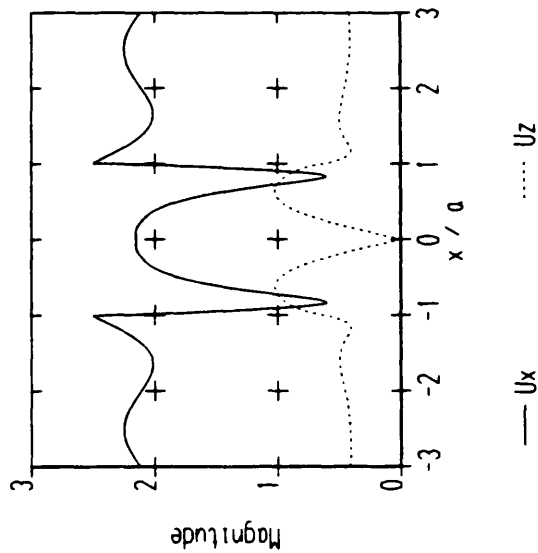
Fig. 133 : Differential cross-section of the scattered far-field in the x-z plane (plane of polarisation) for a shear wave normally incident on to a shallow axisymmetric surface indentation



— S component

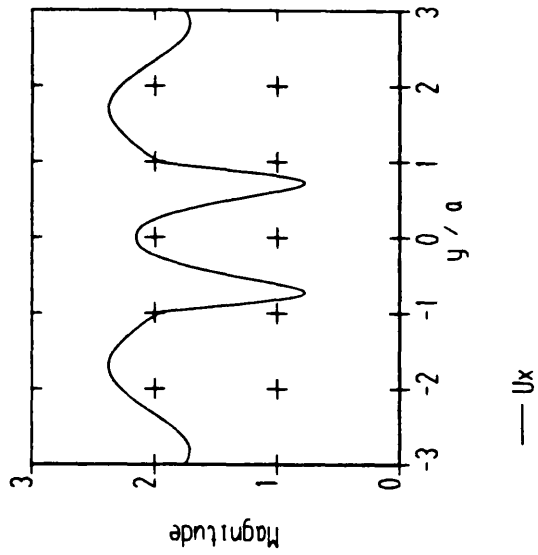
Scattered energy in y-z plane  
 Type of surface obstacle : Segment of a hemisphere  
 Order of approximation : 12  
 Incident waveltype : SV  
 Incident angle : 0.00 deg  
 Poisson's ratio : 0.34  
 $2a / \lambda$  incident : 1.00  
 $d / a$  : 0.75

Fig. 134 : Differential cross-section of the scattered far-field in the y-z plane (plane perpendicular to polarisation) for a shear wave normally incident on to a shallow axisymmetric surface indentation



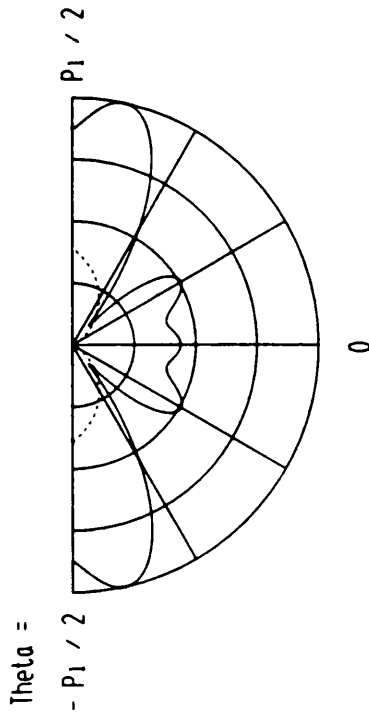
Surface displacements in x-z plane  
 Type of surface obstacle : Ellipsoid  
 Order of approximation : 12  
 Incident wavetype : SV  
 Incident angle : 0.00 deg  
 Poisson's ratio : 0.34  
 $2a / \lambda$  incident : 1.00  
 $d / a$  : 0.75

Fig. 135 : Amplitude of the surface displacements in the x-z plane (plane of polarisation) for a shear wave normally incident on to a shallow axisymmetric surface indentation



Surface displacements in y-z plane  
 Type of surface obstacle : Ellipsoid  
 Order of approximation : 12  
 Incident wavetype : SV  
 Incident angle : 0.00 deg  
 Poisson's ratio : 0.34  
 $2a / \lambda$  incident : 1.00  
 $d / a$  : 0.75

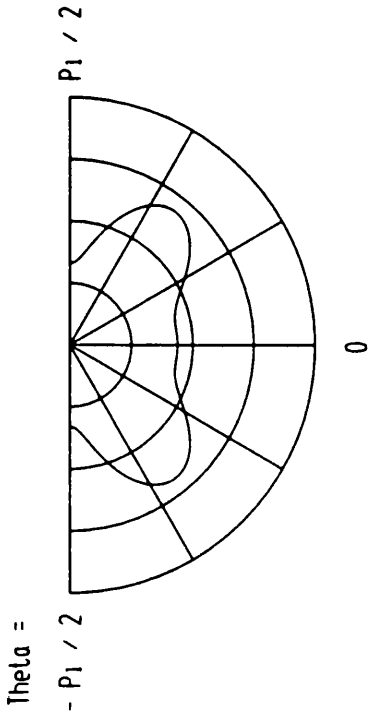
Fig. 136 : Amplitude of the surface displacements in the y-z plane (plane perpendicular to polarisation) for a shear wave normally incident on to a shallow axisymmetric surface indentation



— Theta comp      ..... R comp

Far Field displacements in x-z plane  
 Type of surface obstacle : Ellipsoid  
 Order of approximation : 12  
 Incident waveltype : SV  
 Incident angle : 0.00 deg  
 Poisson's ratio : 0.34  
 $2a / \lambda$  incident : 1.00  
 $d / a$  : 0.75

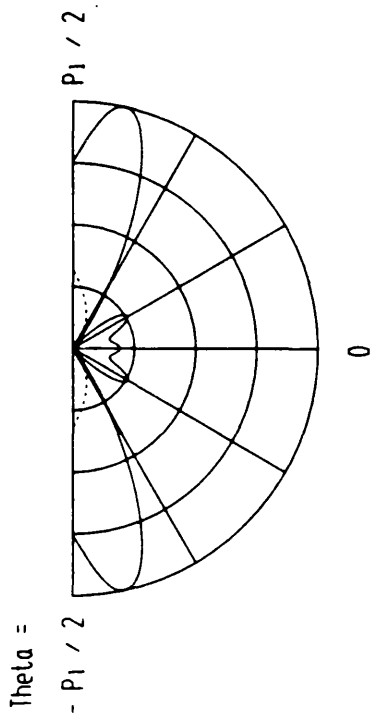
Fig. 137 : Amplitude of the far-field displacements of the scattered field in the x-z plane (plane of polarisation) for a shear wave normally incident on to a shallow axisymmetric surface indentation



— Phi comp

Far Field displacements in y-z plane  
 Type of surface obstacle : Ellipsoid  
 Order of approximation : 12  
 Incident waveltype : SV  
 Incident angle : 0.00 deg  
 Poisson's ratio : 0.34  
 $2a / \lambda$  incident : 1.00  
 $d / a$  : 0.75

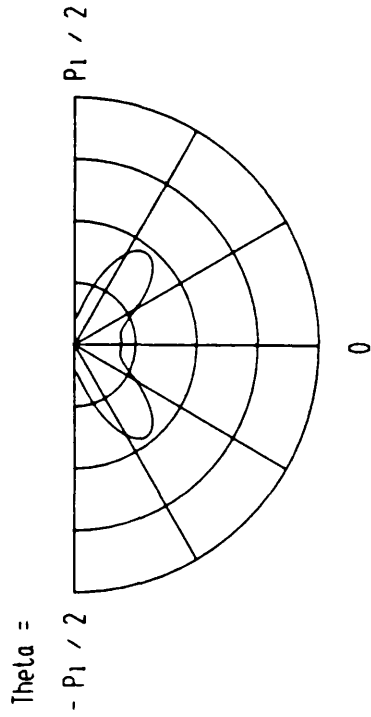
Fig. 138 : Amplitude of the far-field displacements of the scattered field in the y-z plane (plane perpendicular to polarisation) for a shear wave normally incident on to a shallow axisymmetric surface indentation



— S component      ..... P component

Scattered energy in x-z plane  
 Type of surface obstacle : Ellipsoid  
 Order of approximation : 12  
 Incident wavetype : SV  
 Incident angle : 0.00 deg  
 Poisson's ratio : 0.34  
 $2a / \lambda$  incident : 1.00  
 $d / a$  : 0.75

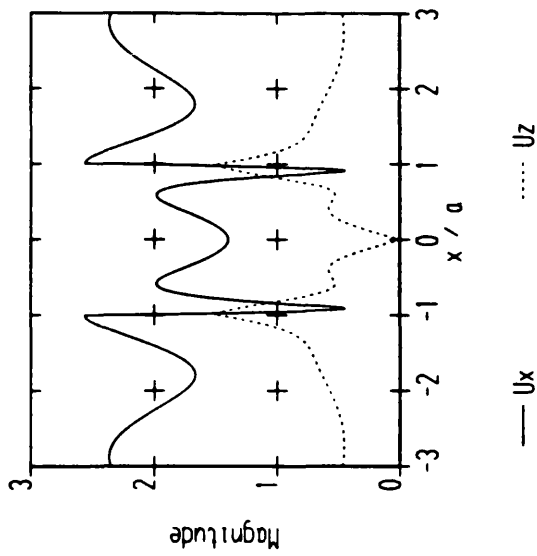
Fig. 139 : Differential cross-section of the scattered far-field in the x-z plane (plane of polarisation) for a shear wave normally incident on to a shallow axisymmetric surface indentation



— S component

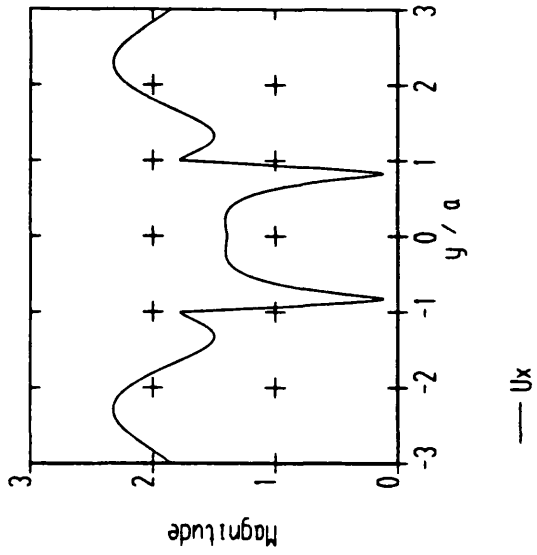
Scattered energy in y-z plane  
 Type of surface obstacle : Ellipsoid  
 Order of approximation : 12  
 Incident wavetype : SV  
 Incident angle : 0.00 deg  
 Poisson's ratio : 0.34  
 $2a / \lambda$  incident : 1.00  
 $d / a$  : 0.75

Fig. 140 : Differential cross-section of the scattered far-field in the y-z plane (plane perpendicular to polarisation) for a shear wave normally incident on to a shallow axisymmetric surface indentation



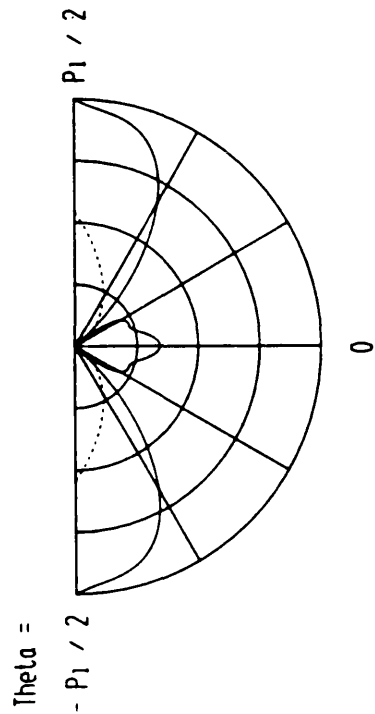
Surface displacements in x-z plane  
 Type of surface obstacle : Hemisphere  
 Order of approximation : 13  
 Incident wavetype : SV  
 Incident angle : 0.00 deg  
 Poisson's ratio : 0.34  
 $2a / \lambda$  incident : 1.00  
 $d / a$  : 1.00

Fig. 141 : Amplitude of the surface displacements in the x-z plane (plane of polarisation) for a shear wave normally incident on to a hemispherical surface indentation



Surface displacements in y-z plane  
 Type of surface obstacle : Hemisphere  
 Order of approximation : 13  
 Incident wavetype : SV  
 Incident angle : 0.00 deg  
 Poisson's ratio : 0.34  
 $2a / \lambda$  incident : 1.00  
 $d / a$  : 1.00

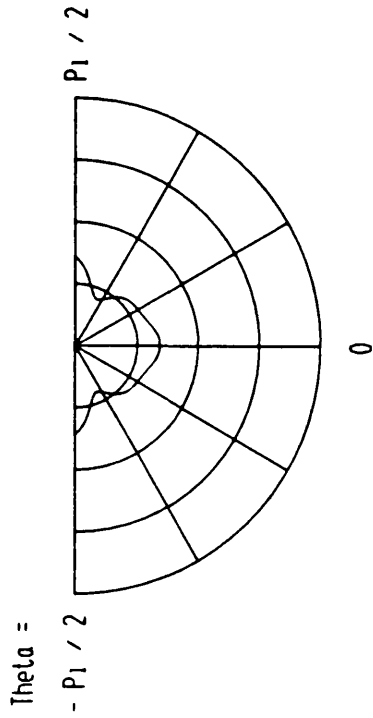
Fig. 142 : Amplitude of the surface displacements in the y-z plane (plane perpendicular to polarisation) for a shear wave normally incident on to a hemispherical surface indentation



— Theta comp      ..... R comp

Far field displacements in x-z plane  
 Type of surface obstacle : Hemisphere  
 Order of approximation : 13  
 Incident waveltype : SV  
 Incident angle : 0.00 deg  
 Poisson's ratio : 0.34  
 2a / lambda incident : 1.00  
 d / a : 1.00

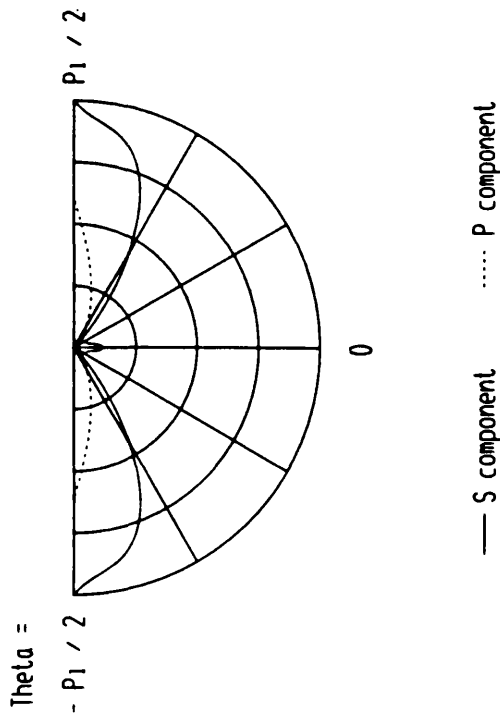
Fig. 143 : Amplitude of the far-field displacements of the scattered field in the x-z plane (plane of polarisation) for a shear wave normally incident on to a hemispherical surface indentation



— Phi comp

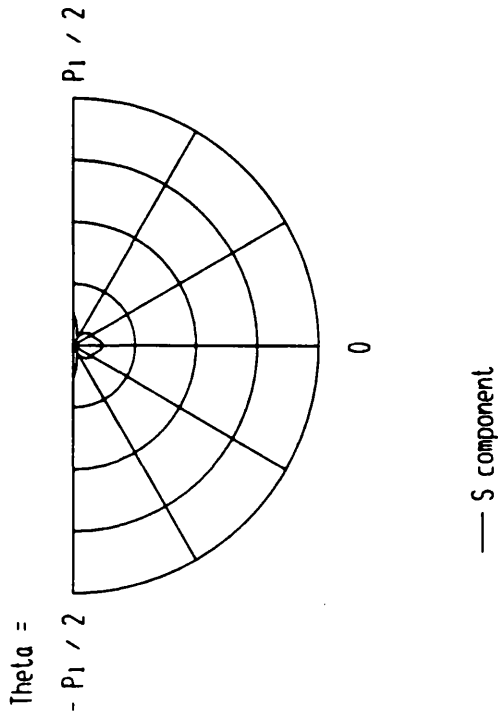
Far field displacements in y-z plane  
 Type of surface obstacle : Hemisphere  
 Order of approximation : 13  
 Incident waveltype : SV  
 Incident angle : 0.00 deg  
 Poisson's ratio : 0.34  
 2a / lambda incident : 1.00  
 d / a : 1.00

Fig. 144 : Amplitude of the far-field displacements of the scattered field in the y-z plane (plane perpendicular to polarisation) for a shear wave normally incident on to a hemispherical surface indentation



Scattered energy in x-z plane  
 Type of surface obstacle : Hemisphere  
 Order of approximation : 13  
 Incident waveltype : SV  
 Incident angle : 0.00 deg  
 Poisson's ratio : 0.34  
 $2a / \lambda$  incident : 1.00  
 $d / a$  : 1.00

Fig. 145 : Differential cross-section of the scattered far-field in the x-z plane (plane of polarisation) for a shear wave normally incident on to a hemispherical surface indentation



Scattered energy in y-z plane  
 Type of surface obstacle : Hemisphere  
 Order of approximation : 13  
 Incident waveltype : SV  
 Incident angle : 0.00 deg  
 Poisson's ratio : 0.34  
 $2a / \lambda$  incident : 1.00  
 $d / a$  : 1.00

Fig. 146 : Differential cross-section of the scattered far-field in the y-z plane (plane perpendicular to polarisation) for a shear wave normally incident on to a hemispherical surface indentation

### 3.5 Comparison between numerical predictions and measurements

In order to check the calculations of the numerical model a range of measurements were carried out. The available equipment was an ultrasound pulser-receiver "Panametrics Pulser Receiver Model 5052 PR", two compressional wave transducers with a centre frequency of 1 MHz, one shear wave transducer with a centre frequency of 2 MHz and normal beam direction and a wide band Rayleigh wave transducer with a centre frequency of 1 MHz. Two aluminium blocks were designed in order to allow the measurement of the field scattered from a hemispherical indentation in the plane rectangular side of each block. The shape of the blocks can be seen in Fig. 147. All facetes have the same distance from the hemisphere and were machined in order to create a flat surface for the transducers at multiples of 15 degrees. The experimental configuration is shown in Fig. 148. A compressional or shear wave is normally incident on to the surface indentation (1), the scattered body waves are measured every 15 degrees along the facetes (2), and the Rayleigh waves can be measured on the plane surface (3) in which the hemispherical indentation (4) was machined. Both aluminium blocks were 100.0 mm in depth and the distance of each facet from the indentation was 142.5 mm. The indentation machined in the first block had a diameter of 1.6 mm, the indentation in the second block was 3.2 mm in diameter.

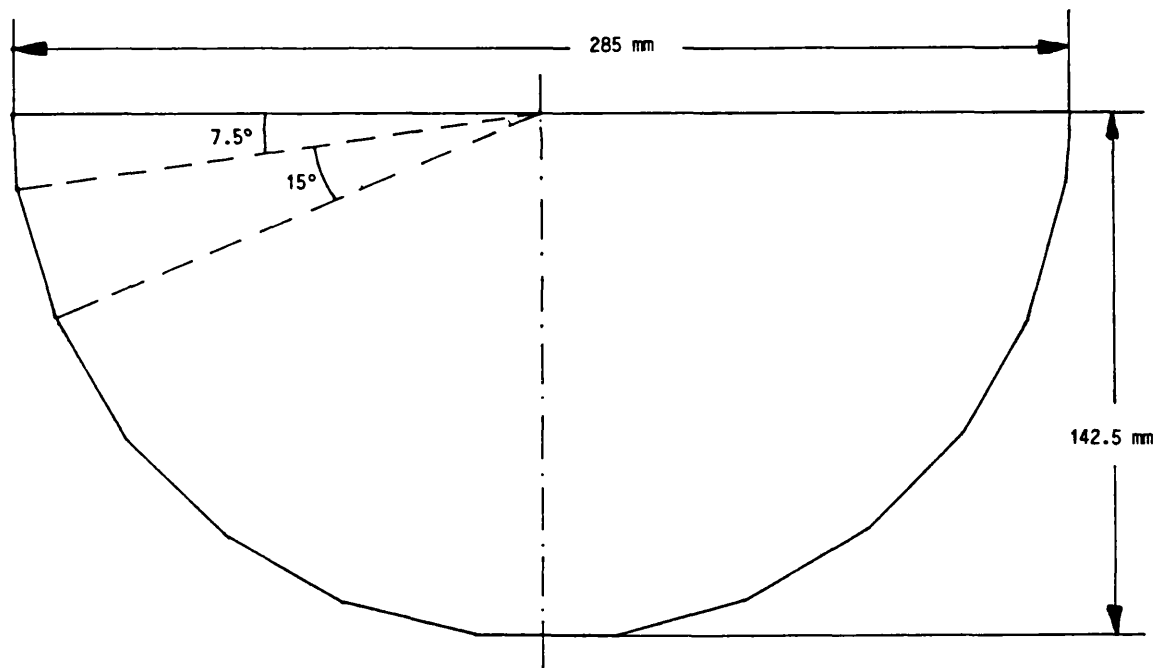
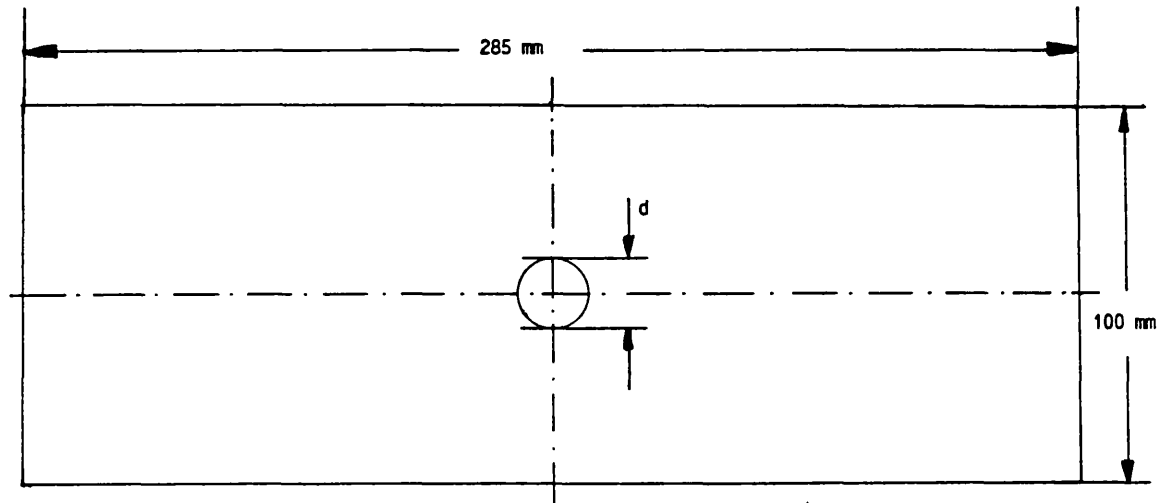


Fig. 147 : Shape and dimensions of the aluminium test block in top view and side view. The diameter of the hemispherical indentation is  $d = 3.2 \text{ mm}$  or  $d = 1.6 \text{ mm}$

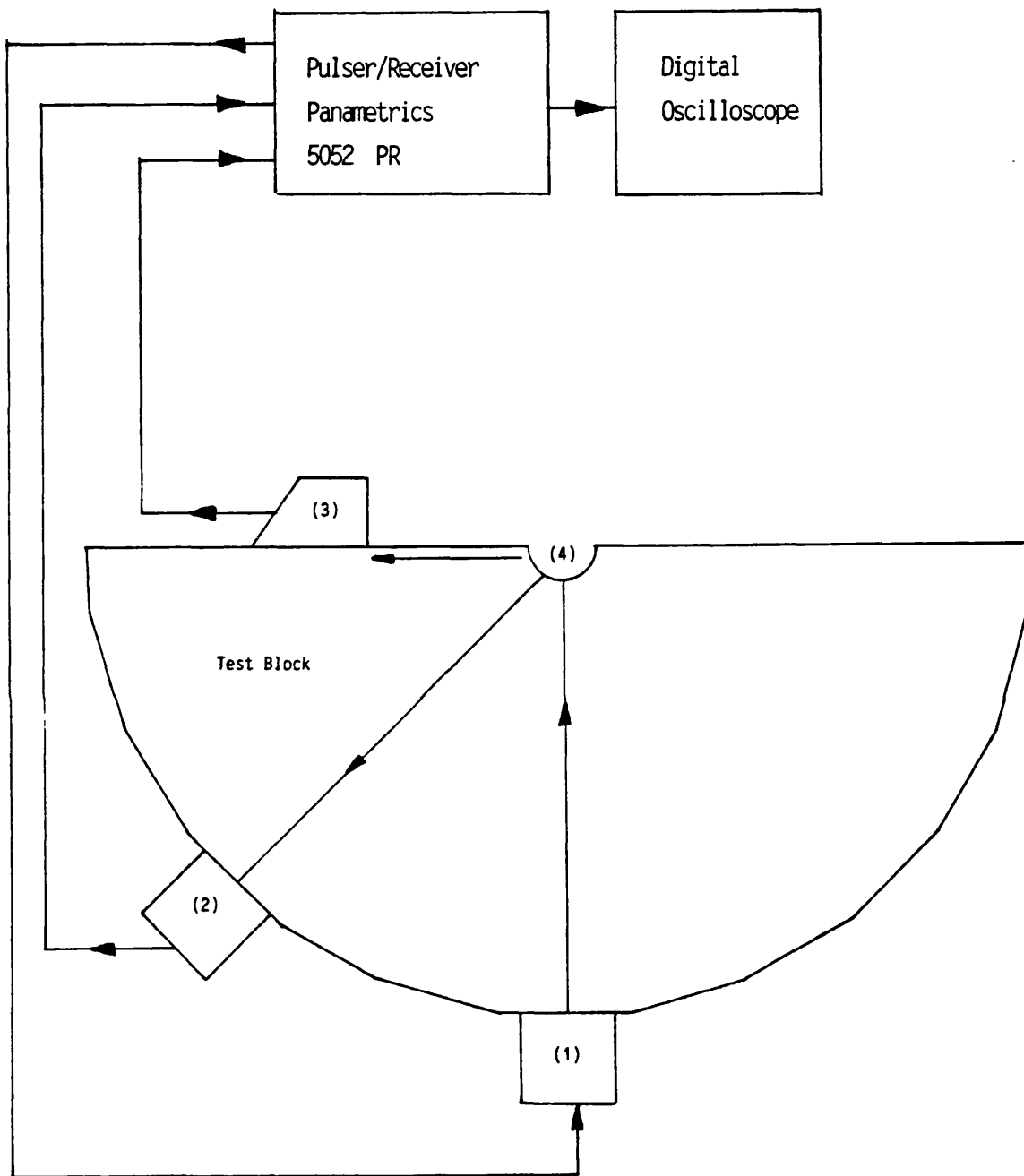


Fig. 148 : Experimental configuration for the measurement of the ultrasonic field scattered from a hemispherical surface indentation in an aluminium block

The compressional and shear wavelength at 1 MHz and 2 MHz are :

1 MHz :  $\lambda_p = 6.398$  mm,  $\lambda_s = 3.122$  mm

2 MHz :  $\lambda_p = 3.199$  mm,  $\lambda_s = 1.561$  mm

and therefore the diameter to incident wavelength ratios were

a) incident compressional wave at 1 MHz,  $\lambda_p = 6.398$  mm

	block 1	block 2
diameter 2a	1.575 mm	3.175 mm
$\frac{2a}{\lambda_p}$	0.25	0.5

b) incident shear wave at 2 MHz,  $\lambda_s = 1.561$  mm

	block 1	block 2
diameter 2a	1.575 mm	3.175 mm
$\frac{2a}{\lambda_s}$	1.0	2.0

The far-field displacements calculated with the numerical method at the appropriate distance (142.5 mm) for these diameter to wavelength ratios are shown on the next three pages. The polar plots are normalised for each case and the maximum values relate to each other as follows :

a) normally incident compressional wave

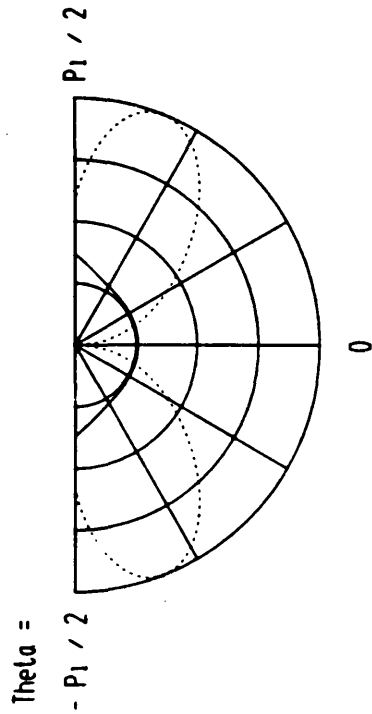
$\frac{2a}{\lambda_p}$	Figure numbers	scaling factor of the far-field displacements
0.25	Fig. 149	1.0
0.5	Fig. 150	7.4

b) normally incident compressional wave

$\frac{2a}{\lambda_s}$	Figure numbers	scaling factor of the far-field displacements
1.0	Figs. 151, 152	1.0
2.0	Figs. 153, 154	7.8

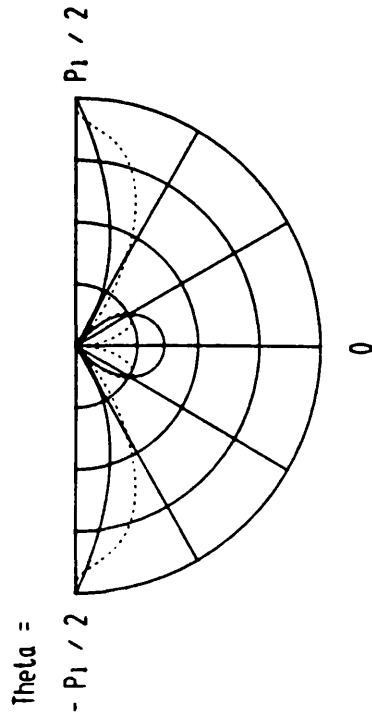
The numerical results indicate that the scattering process is stronger for the larger indentation, and that for all four cases the scattered field is largely confined to a layer close to the plane surface with a small amount of energy scattered into the bulk material. For a normally incident compressional wave the scattered field is axisymmetric and the presence of a compressional as well as a shear wave component oriented along the surface gives rise to an axisymmetric Rayleigh wave propagating away from the hemispherical indentation (Figs. 149, 150). For a normally incident shear wave the scattered field is no longer axisymmetric (see chapter 2.2.4). The displacement components in the plane of polarisation of the incident wave (here chosen as the  $x-z$  plane, Figs. 151, 153)) show an azimuth dependence of  $\cos \phi$ , i.e. have their maxima in the  $x-z$  plane and vanish in the  $y-z$  plane. The displacement components in the plane perpendicular to the polarisation (here the  $y-z$  plane, Figs. 152, 154) show an azimuth dependence of  $\sin \phi$ , i.e. they have their maxima in the  $y-z$  plane and vanish in the  $x-z$  plane. The numerical results for a normally incident shear wave indicate that scattered field in the plane of polarisation ( $x-z$  plane) consists of a compressional and a shear wave component along the surface, therefore giving rise to a Rayleigh wave propagating in the direction of polarisation. The scattered field in the plane perpendicular to the plane of polarisation has a shear wave component only, and therefore no Rayleigh wave should be observed in this

plane. The experiments carried out support these results. The measurement of the amplitude of the Rayleigh wave component at a constant radius around the hemispherical indentation for angles of multiples of 22.5 degrees is presented in Figs. 155 — 158. The azimuth dependence of the Rayleigh wave component has the predicted shape. For a normally incident compressional wave the Rayleigh amplitude is virtually independent from the azimuth angle  $\phi$  (Figs. 155, 156), for a normally incident shear wave the Rayleigh amplitude has a  $\cos \phi$  dependence with its maxima in the plane of polarisation and different polarity for each of the two lobes (Figs. 157, 158). The numerical calculations predict that the amplitude of the surface wave components for an incident shear wave will be about 8 times larger for the wavefield scattered from the large hemisphere than the amplitudes of the wavefield scattered from the small hemisphere, and the ratio is even larger for the case of an incident compressional wave. The experimental results show that the Rayleigh wave amplitudes for an incident P wave as well as for an incident SV wave are approximately twice as large for the large surface indentation compared to the Rayleigh waves generated by the small hemisphere. This discrepancy between theory and experiment can be explained by the fact that the numerical model does not explicitly include Rayleigh waves in the expansion of the scattered field, and becomes inaccurate in a qualitative sense when the scattered field consists predominantly of surface wave components (see also Chapter 4 and Appendix D).



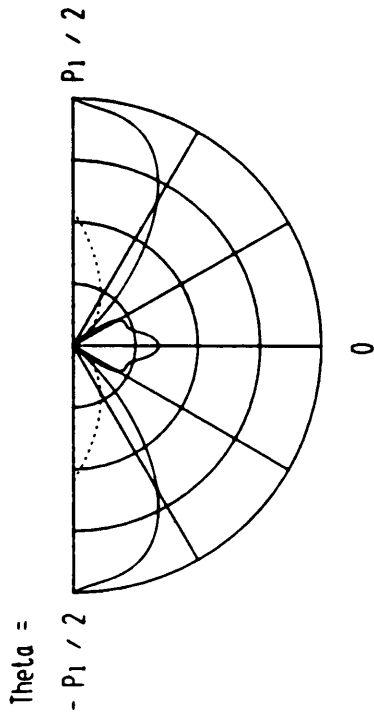
Far field displacements in x-z plane  
 Type of surface obstacle : Hemisphere  
 Order of approximation : 11  
 Incident wavetype : P  
 Incident angle : 0.00 deg  
 Poisson's ratio : 0.34  
 $2a / \lambda$  incident : 0.25  
 $d / a$  : 1.00

Fig. 149 : Amplitude of the far-field displacements of the scattered field for a compressional wave normally incident on to a hemispherical surface indentation in an aluminium half-space



Far field displacements in x-z plane  
 Type of surface obstacle : Hemisphere  
 Order of approximation : 13  
 Incident wavetype : P  
 Incident angle : 0.00 deg  
 Poisson's ratio : 0.34  
 $2a / \lambda$  incident : 0.50  
 $d / a$  : 1.00

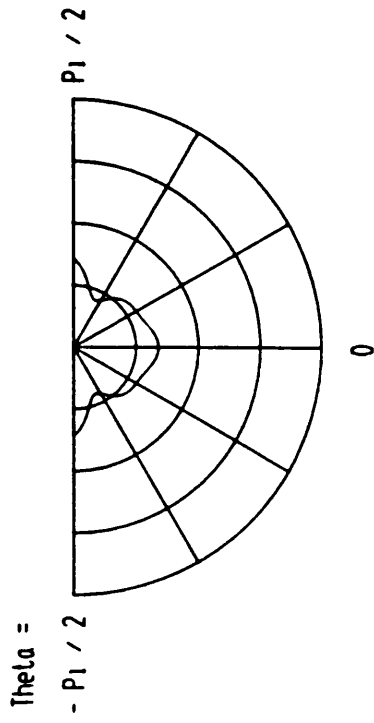
Fig. 150 : Amplitude of the far-field displacements of the scattered field for a compressional wave normally incident on to a hemispherical surface indentation in an aluminium half-space



— Theta comp      ..... R comp

Far Field displacements in x-z plane  
 Type of surface obstacle : Hemisphere  
 Order of approximation : 13  
 Incident wavetype : SV  
 Incident angle : 0.00 deg  
 Poisson's ratio : 0.34  
 $2a / \lambda$  incident : 1.00  
 $d / a$  : 1.00

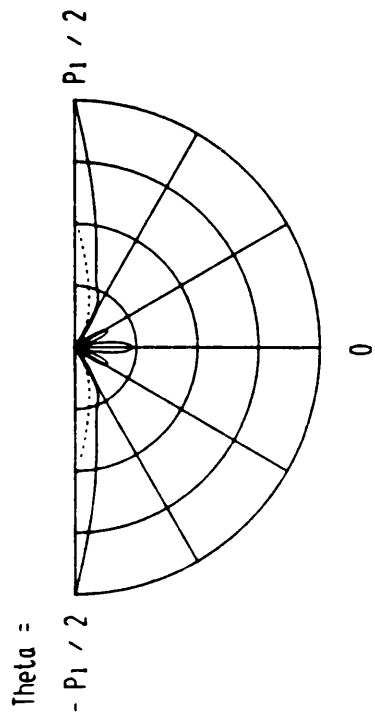
Fig. 151 : Amplitude of the far-field displacements of the scattered field in the x-z plane (plane of polarisation) for a shear wave normally incident on to a hemispherical surface indentation in an aluminium half-space



— Phi comp

Far Field displacements in y-z plane  
 Type of surface obstacle : Hemisphere  
 Order of approximation : 13  
 Incident wavetype : SV  
 Incident angle : 0.00 deg  
 Poisson's ratio : 0.34  
 $2a / \lambda$  incident : 1.00  
 $d / a$  : 1.00

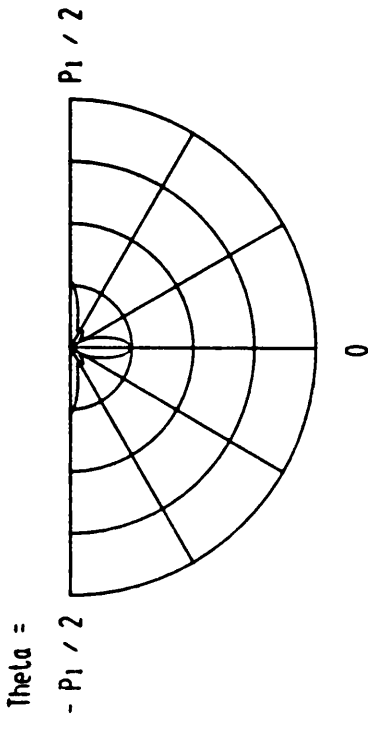
Fig. 152 : Amplitude of the far-field displacements of the scattered field in the y-z plane (plane perpendicular to polarisation) for a shear wave normally incident on to a hemispherical surface indentation in an aluminium half-space



— Theta comp  
..... R comp

Far field displacements in x-z plane  
 Type of surface obstacle : Hemisphere  
 Order of approximation : 16  
 Incident waveltype : SV  
 Incident angle : 0.00 deg  
 Poisson's ratio : 0.34  
 2a / lambda incident : 2.00  
 d / a : 1.00

Fig. 153 : Amplitude of the far-field displacements of the scattered field in the x-z plane (plane of polarisation) for a shear wave normally incident on to a hemispherical surface indentation in an aluminium half-space



— Phi comp

Far field displacements in y-z plane  
 Type of surface obstacle : Hemisphere  
 Order of approximation : 16  
 Incident waveltype : SV  
 Incident angle : 0.00 deg  
 Poisson's ratio : 0.34  
 2a / lambda incident : 2.00  
 d / a : 1.00

Fig. 154 : Amplitude of the far-field displacements of the scattered field in the y-z plane (plane perpendicular to polarisation) for a shear wave normally incident on to a hemispherical surface indentation in an aluminium half-space

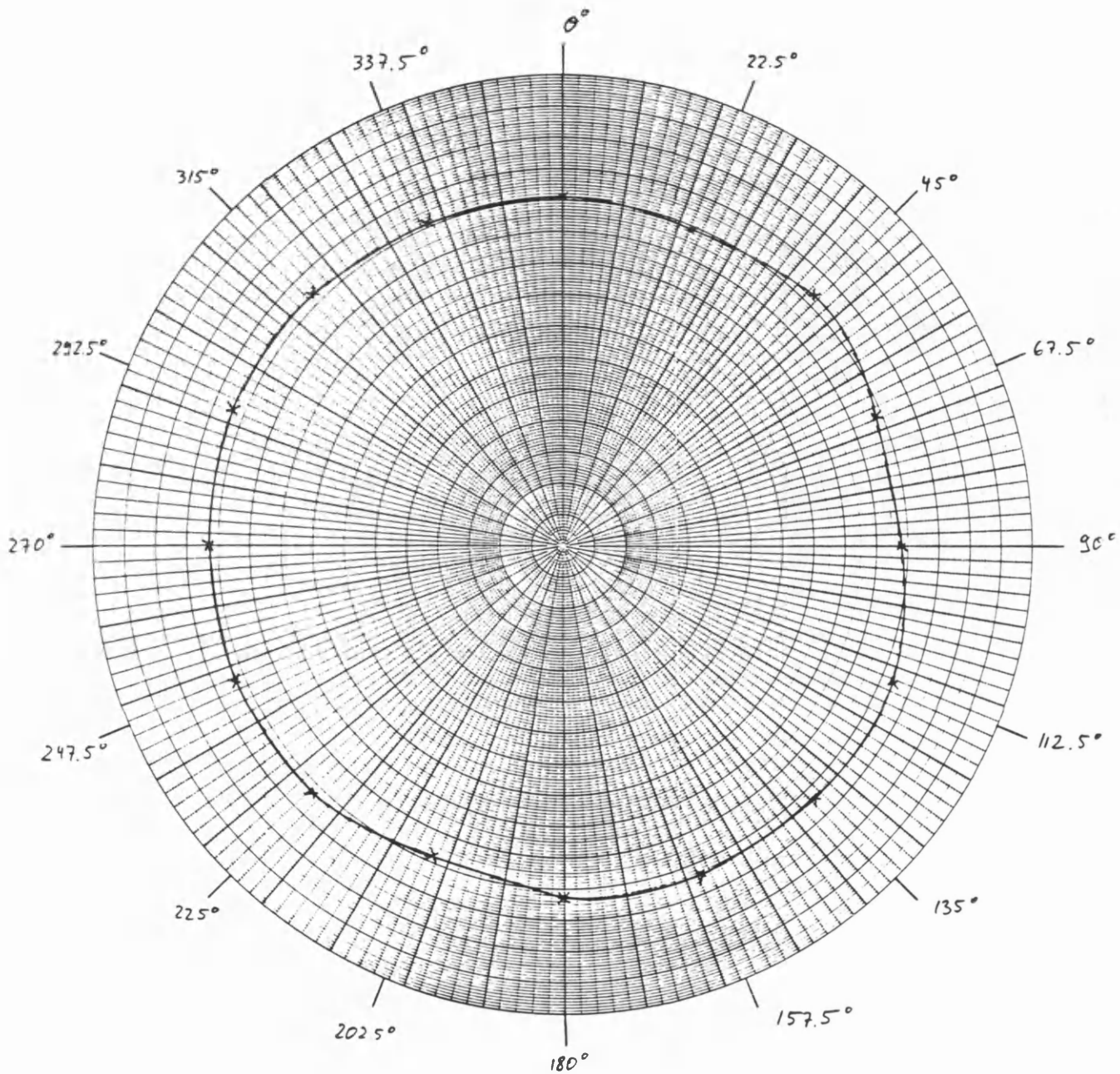


Fig. 155 : Rayleigh wave amplitude as function of the azimuth angle  $\phi$  for a compressional wave with a frequency of 1 MHz normally incident on to a small hemispherical surface indentation with a diameter of 1.6 mm. The original scale was 10 mm = 0.01 V.

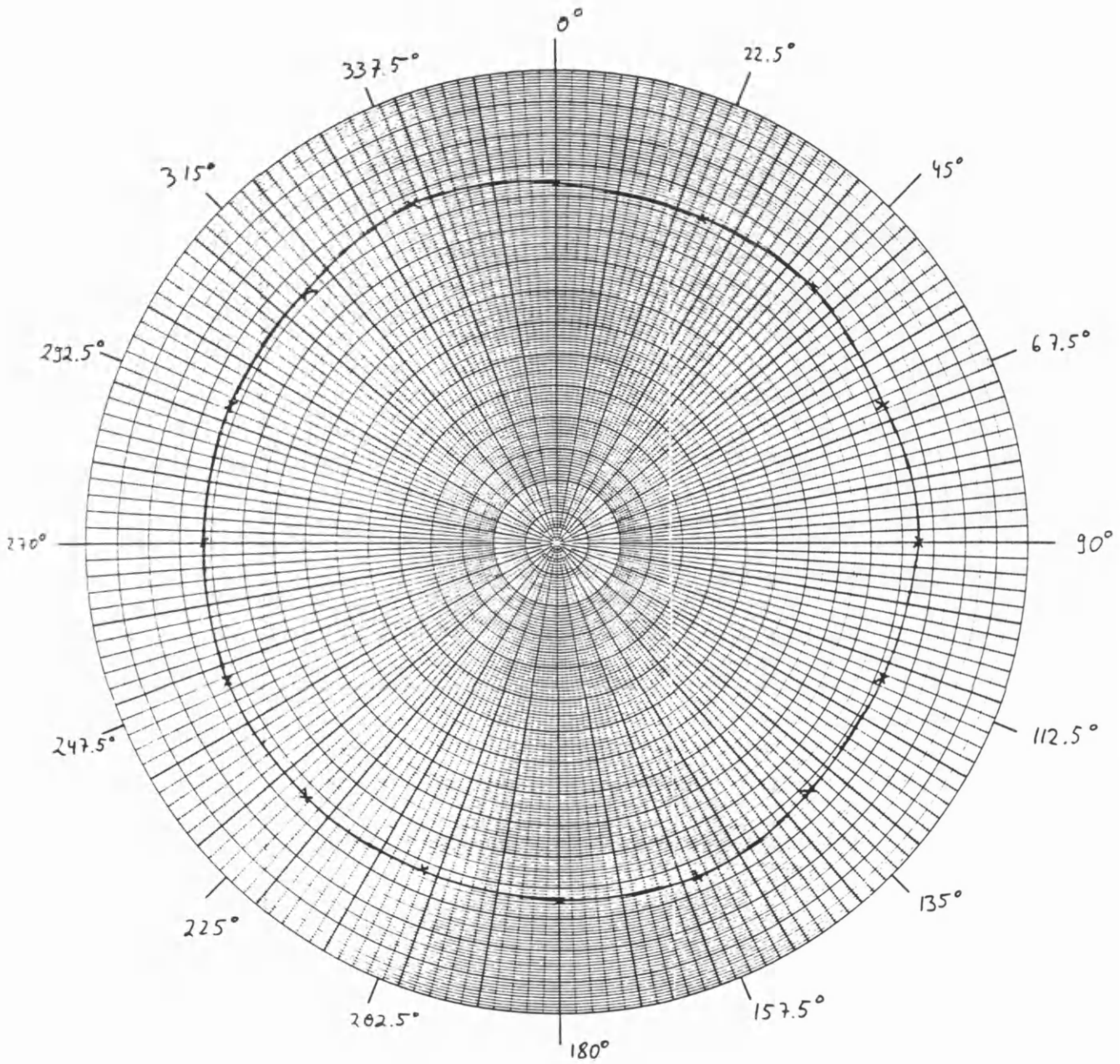


Fig. 156 : Rayleigh wave amplitude as function of the azimuth angle  $\phi$  for a compressional wave with a frequency of 1 MHz normally incident on to a large hemispherical surface indentation with a diameter of 3.2 mm. The original scale was 10 mm = 0.02 V.

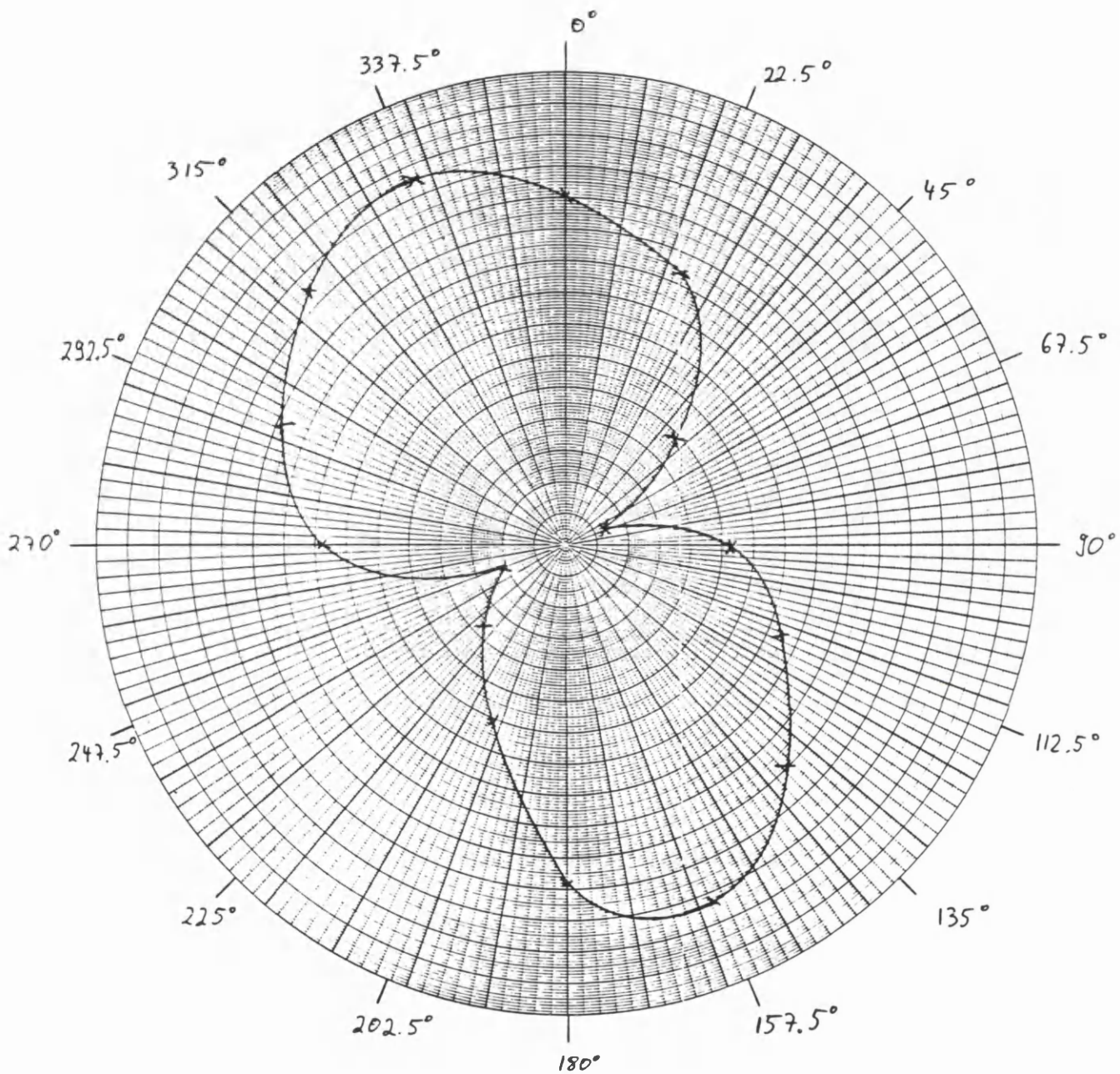


Fig. 157 : Rayleigh wave amplitude as function of the azimuth angle  $\phi$  for a shear wave with a frequency of 2 MHz normally incident on to a small hemispherical surface indentation with a diameter of 1.6 mm. The original scale was 10 mm = 0.01 V.

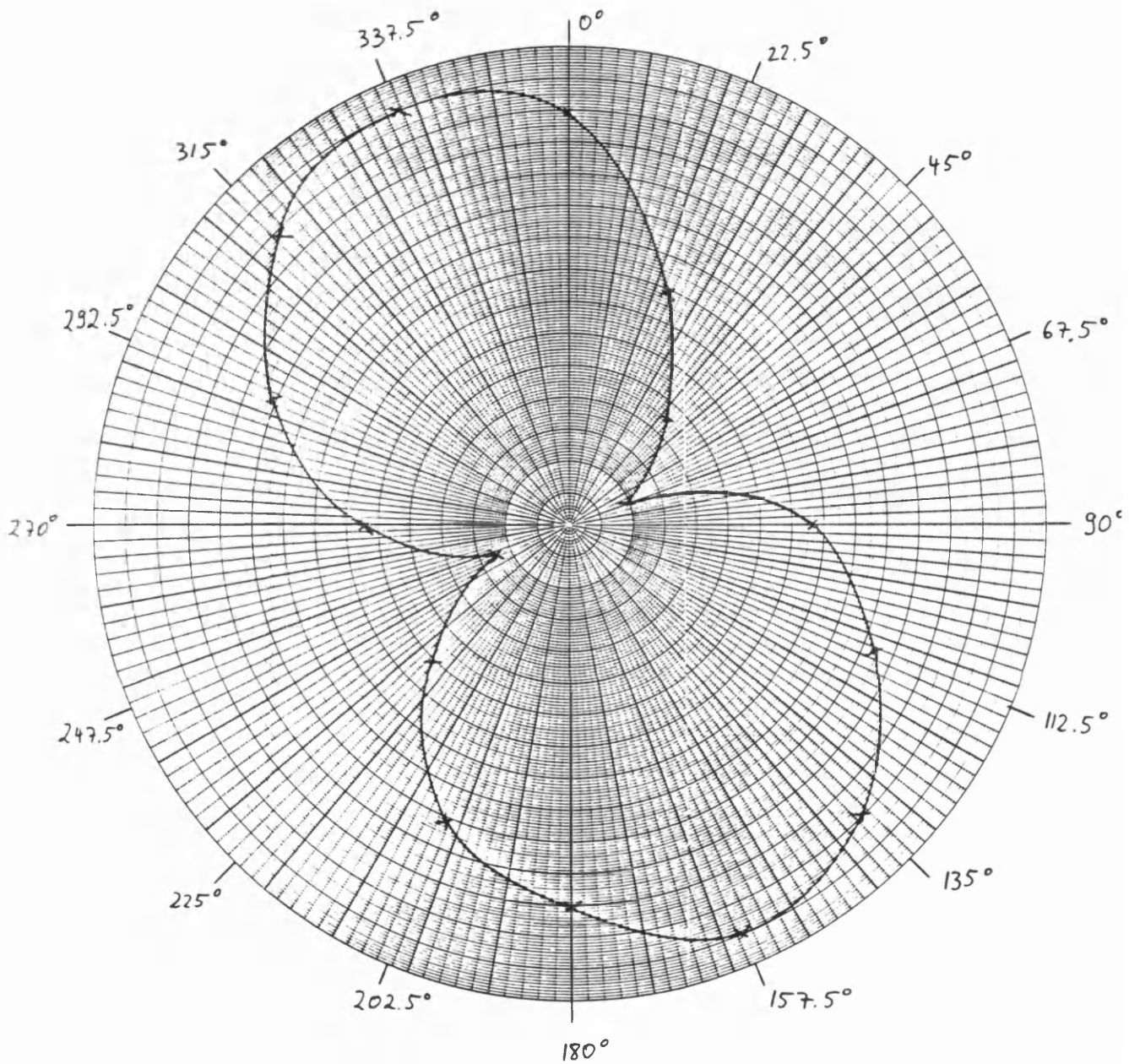


Fig. 158 : Rayleigh wave amplitude as function of the azimuth angle  $\phi$  for a shear wave with a frequency of 2 MHz normally incident on to a large hemispherical surface indentation with a diameter of 3.2 mm. The original scale was 10 mm = 0.02 V.

The measurement of body wave components along the facets of the aluminium blocks did not give any information on the field scattered from the surface indentation. The following reasons are believed to be the explanation for this :

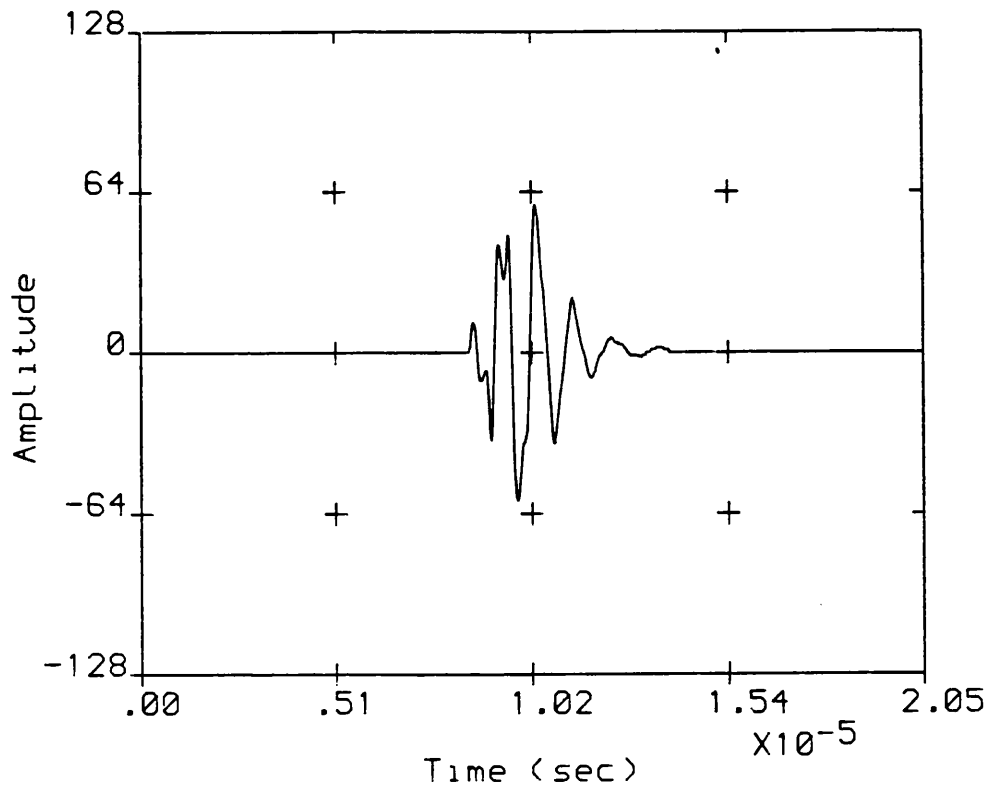
a) The beam width of the transducers were very wide and any incident wave was reflected by the plane surface into a range of angles up to 45 degrees away from the normal, therefore effectively drowning any signal due to the scatterer. Due to the strong signal reflected back normally (in the direction of incidence) from the plane surface it was also not possible to separate out any component scattered back normally from the indentation. This can be seen in Figs. 159 — 162, where the rf traces of the pulses reflected back normally for a normally incident compressional and shear wave are shown together with their spectra. For angles beyond 45 degrees the signal to noise ratio of the measured signal was very poor and it was not possible to identify any scattered wave components in the rf traces.

b) The frequency spectrum of the compressional wave transducer has a minimum at 2 MHz (the centre frequency of the shear wave transducer), and the frequency component of the shear wave spectrum is 10 dB down at 1 MHz (the centre frequency of the compressional wave transducer) compared to its maximum at 2 MHz (see Figs. 160, 162). The overlap of the two spectra therefore does not seem to be sufficient for an effective measurement of compressional wave components due to an incident shear wave and vice versa.

c) The numerical predictions indicate that for three of the four investigated cases the surface components are much stronger than the body wave components. The fourth case, a compressional wave incident on to the small hemisphere (with a diameter to wavelength ratio of  $\frac{2a}{\lambda_p} = 0.25$ ) generates a shear wave component with a maximum at approximately 80 degrees. This

component can be thought of as an approximation of the shear component of a Rayleigh surface wave.

d) A comparison of experimental and theoretical results has to take account of the fact that the computations were carried out using a single frequency model whereas the measurements employed ultrasound pulses containing a range of frequencies. The spectra of the compressional and shear wave transducers show strong maxima at the centre frequency of each transducer and have a narrow bandwidth (Figs. 160, 162). This allows a comparison of experimental and theoretical results as long as the calculations are carried out for frequency components near the centre frequency of the transducers. This was done in this study, where the results for an incident compressional wave were calculated for a frequency component at 1MHz (Figs. 149, 150) and the plots for an incident shear wave were obtained for a frequency component of 2 MHz (Figs. 151 — 154).



— Ultrasound pulse

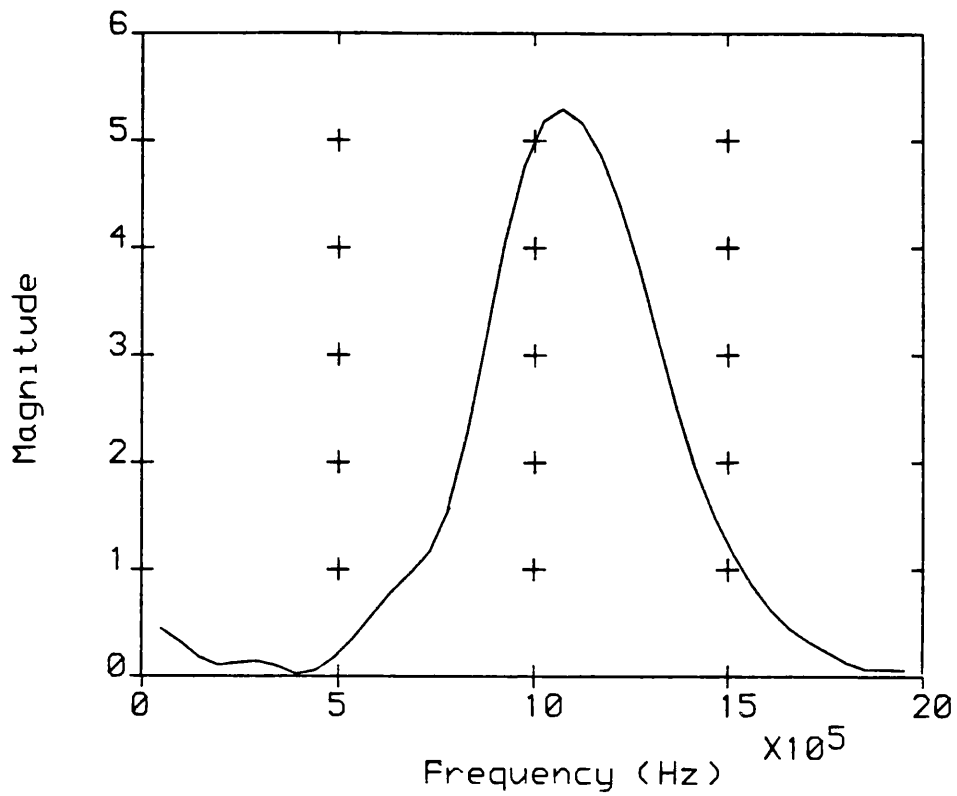
Time domain

Number of points : 1024

Sampling interval : .2E -7 sec / sample

Displayed signal : Measured signal

**Fig. 159 : Rf trace of a compressional wave pulse reflected back normally from a plane surface with a hemispherical surface indentation of 3.2 mm diameter for a normally incident compressional wave pulse with a centre frequency of 1 MHz**



— Frequency spectrum

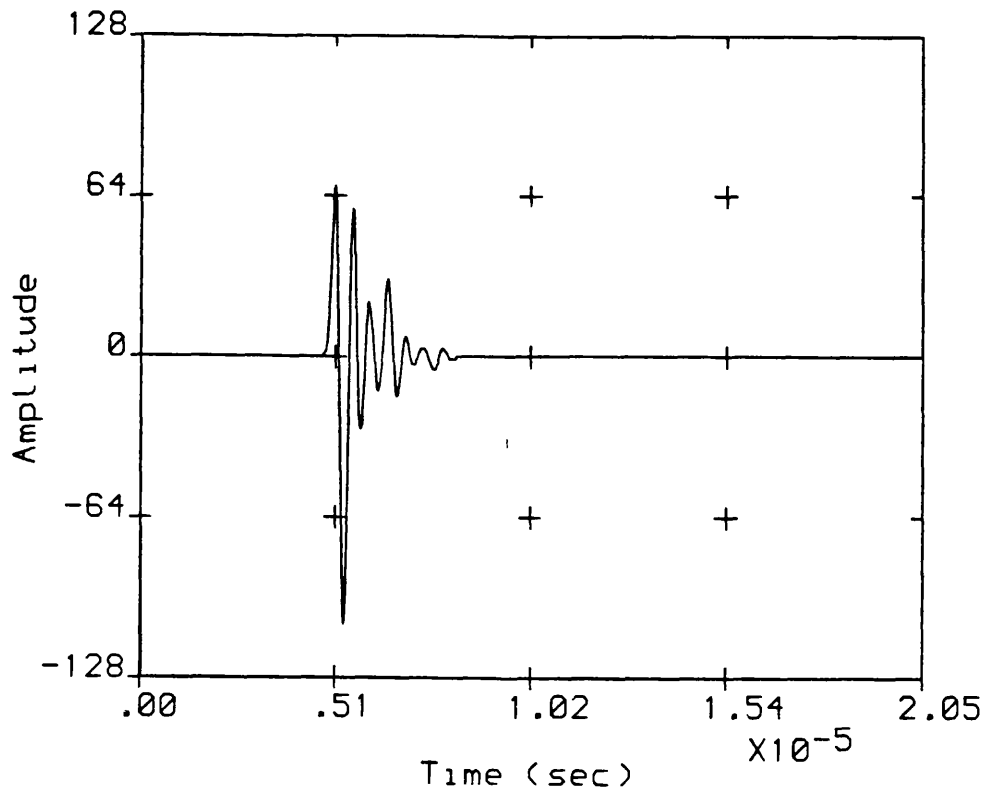
Frequency domain

Number of points : 1024

Sampling interval : .2E -7 sec / sample

Displayed signal : Measured signal

**Fig. 160 : Frequency spectrum of a compressional wave pulse reflected back normally from a plane surface with a hemispherical surface indentation of 3.2 mm diameter for a normally incident compressional wave pulse with a centre frequency of 1 MHz**



— Ultrasound pulse

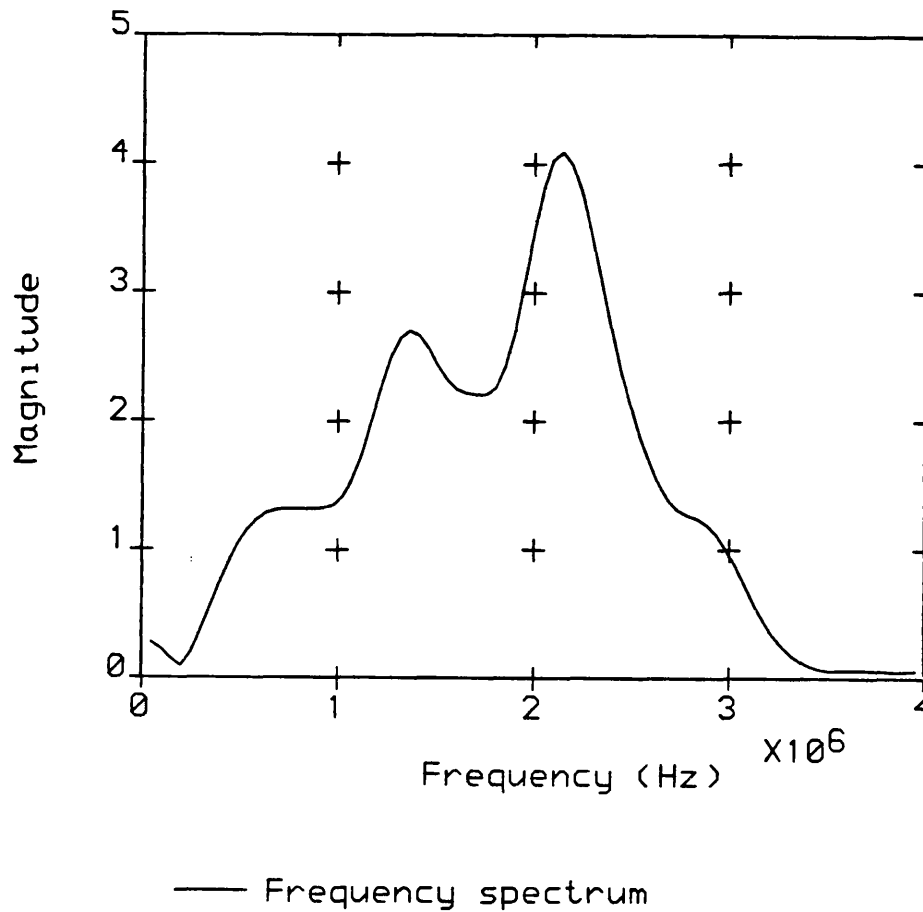
Time domain

Number of points : 1024

Sampling interval : .2E -7 sec / sample

Displayed signal : Measured signal

**Fig. 161 : Rf trace of a shear wave pulse reflected back normally from a plane surface with a hemispherical surface indentation of 3.2 mm diameter for a normally incident shear wave pulse with a centre frequency of 2 MHz**



Frequency domain

Number of points : 1024

Sampling interval : .2E -7 sec / sample

Displayed signal : Measured signal

**Fig. 162 : Frequency spectrum of a shear wave pulse reflected back normally from a plane surface with a hemispherical surface indentation of 3.2 mm diameter for a normally incident shear wave pulse with a centre frequency of 2 MHz**

## 4 Discussion and Conclusion

### 4.1 Discussion of the numerical and experimental results

This section is divided into three parts. The first part looks into the performance of the numerical method and comments on its advantages and limitations. The second part discusses the far-field results together with the experimental results and its implications for the detection of pitting corrosion. The third part looks at the surface movements in the near field.

#### 4.1.1 Performance of the numerical method presented in this study

The indirect boundary method presented in this study is a powerful tool for the numerical simulation of elastic wave scattering from axisymmetric surface indentations in three dimensions. It requires far less computer memory and cpu time than three-dimensional finite element or finite difference methods, and it is possible to use mini computers or work stations in order to obtain simulation results. An extension to non-axisymmetric surface indentations is straightforward, but it is then no longer possible to decompose the three-dimensional problem into two dimensional sub-problems, and the computation time and storage requirements will rise by an order of magnitude.

The main drawback of this method is that it is based on time harmonic wave motion and provides only single frequency results. In order to obtain results for time dependent (pulsed) incident wave fields the simulation program could be employed several times for different diameter to wavelength ratios with subsequent Fourier synthesis in the time domain.

There are two limitations to the method presented here that need further attention :

a) The method is applicable to incident P and SH waves at all angles, but is, for the time being, restricted to SV waves below the critical angle. This is due to the chosen expansion of the incident wavefield. An extension of the numerical method to SV waves beyond the critical angle is possible by using an expansion given in [9].

b) The scattered field is expanded in terms of a finite number of spherical vector functions, which have a far-field dependence of  $\frac{1}{r}$ . This expansion is no longer accurate when the far-field contains a significant surface wave component, which has a far-field dependence of  $\frac{1}{\sqrt{r}}$ . The far-field results for this case will be qualitatively accurate, but do no longer give a quantitative analysis of the different contributions to the far field due to Rayleigh waves, compressional waves and shear waves. This problem can be overcome by including surface wave terms explicitly in the expansion of the scattered field (see also Appendix D).

Remedies to the problems outlined above together with further possible improvements and extensions of the numerical method will be discussed in chapter 4.2.

#### 4.1.2 Discussion of the far-field results and measurements

The far-field results obtained by the numerical model together with the experimental results presented in chapter 3.5 give a good understanding into the difficulties of detecting pitting corrosion in early stages. From the plots in section 3.4 it can be seen that the depth of the indentation has some influence on the scattering behaviour. Shallow indentations with a depth smaller than one incident wavelength generate body waves scattered back approximately into the direction of incidence (e.g. Figs. 71, 72, 119, 120), whereas hemispherical indentations with a diameter of the order of one incident wavelength generate strong surface wave components with very little energy scattered back into the bulk material (Figs. 95, 96, 143, 144). It seems that hemispherical surface features give strong body to Rayleigh wave mode conversion.

Due to the normalisation of surface diameter and depth of the indentation with respect to the incident wavelength the scattering of shear waves does not appear to be as strong as the scattering of compressional waves (in aluminium  $\lambda_p \approx 2 \lambda_s$ ), but it can generally be observed that the amplitudes of the scattered wave components increase with the size of the scatterer (see Tables 5 – 8).

By comparing the far-field plots of two different cross-sectional shapes (a segment of a hemisphere and a semi-ellipsoid) with the same surface diameter and depth it can be seen that the directional pattern of the scattered far-field displacements and energy have not changed drastically (e.g. Figs. 71, 72 compared to Figs. 77, 78). It can, however, be observed that amplitudes of the scattered field have increased for the semi-ellipsoidal

indentation with sharp 90 degrees corners between the obstacle and the plane surface compared to the indentation with the shape of a segment of a hemisphere, where the corners are not as sharp (Tables 5 — 8).

For very shallow indentations (with a depth of an eighth of an incident wavelength) the sharpness of the the corners is reflected in the least squares residual of the numerical matching procedure, which is much higher for the semi-ellipsoid (Figs. 63 — 68 for an incident P wave and Figs. 111 — 116 for an incident SV wave) than for the segment of a hemisphere (Figs. 57 — 62 for an incident P wave and Figs. 105 — 110 For an incident SV wave). This implies a loss in accuracy for shallow surface indentations with sharp corners and is to be expected due to the choice of an expansion of the scattered field into spherical functions which are unsuitable for this geometry. For increasing depth of the indentations these differences in accuracy disappear as the angles between the indentation and the plane surface approach 90 degrees.

The directional patterns of shallow surface obstacles change quite smoothly to the directional pattern of a hemisphere when the depth of the shallow indentations is increased and the shape of the indentation approaches a hemisphere. This can be seen for the case of a compressional wave incident at 60 degrees in Figs. 59, 60 (with  $\frac{d}{a} = 0.25$ ), Figs. 71, 72 (with  $\frac{d}{a} = 0.5$ ), Figs. 83, 84 (with  $\frac{d}{a} = 0.75$ ) and Figs. 95, 96 (hemisphere with  $\frac{d}{a} = 1.0$ ). The same transition can be observed for the case of a normally incident shear wave in Figs. 107, 108 (with  $\frac{d}{a} = 0.25$ ), Figs. 119, 120 (with  $\frac{d}{a} = 0.5$ ), Figs. 131, 132 (with  $\frac{d}{a} = 0.75$ ) and Figs. 143, 144 (hemisphere with  $\frac{d}{a} = 1.0$ ). The energy scattered into body waves decreases, whereas the energy travelling along the plane surface as Rayleigh waves increases.

An interesting observation is that for most cases the scattered shear wave components dominate the scattered field not only for an incident shear wave but also for an incident compressional wave. This is especially noticeable for a compressional wave non-normally incident on to shallow indentations, where a strong shear wave component can be observed in the plane perpendicular to the plane of the incident wave vector (Figs. 60 and 72), which also results in strong surface movements in the near field (Figs. 58 and 70). This is a three-dimensional phenomenon and can not be deduced from two-dimensional simulations of elastic waves scattered from canyons. It can not be observed for shear waves non-normally incident on to shallow surface indentations (Figs. 231 — 242 in Appendix E).

The experimental results presented in chapter 3.5 support the findings of the numerical simulations. For compressional and shear waves normally incident on hemispherical surface indentations strong Rayleigh waves are generated. These Rayleigh wave were measured and they showed the predicted azimuth dependence. Body waves reflected back into the bulk material could not be observed.

These findings lead to the following suggestions for the development of new experimental procedures for use in detecting pitting corrosion on the remote side of aluminium plates :

- The frequency of the incident wave should be chosen so that the wavelength is smaller than the depth of the expected corrosion pits. This will avoid the predominant scattering into Rayleigh waves.
- Shear wave transducers should be used rather than compressional wave transducers. As can be seen from the numerical simulations, the shear wave components dominate the scattered field, and it should be easier to

measure them rather than measuring the scattered compressional wave components.

- The ultrasonic beam should be non-normally incident at angles around 45 degrees on to the corroded surface, see Fig. 163. Successful applications of this technique have been reported in [6]. The use of pitch-catch tandem configurations can avoid that the signal generated by the corrosion pits is drowned by the ultrasound pulse reflected from the uncorroded parts of the surface, see Fig. 164.
- The detection of a hemispherical pit with a diameter of 1 mm in an aluminium plate will require a shear wavelength below 0.5mm, therefore frequencies above 6 MHz should be used.

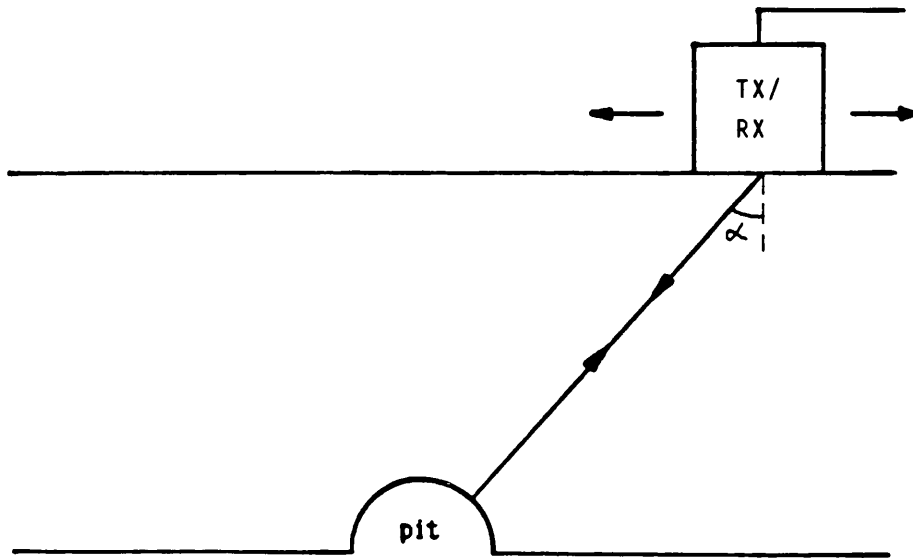


Fig. 163 : Ultrasonic inspection of a corrosion pit using a pulse-echo configuration with an ultrasound pulse incident at  $\alpha = 45^\circ$

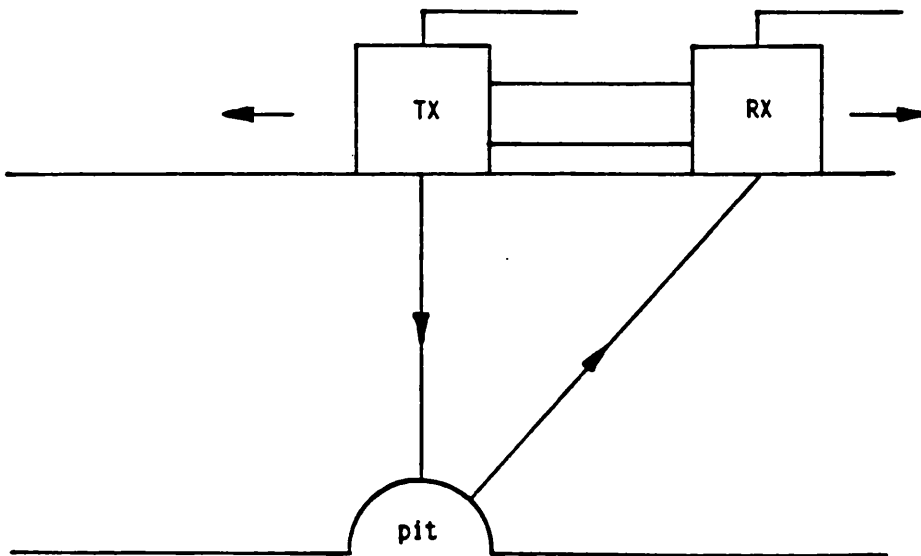


Fig. 164 : Ultrasonic inspection of a corrosion pit using a pitch-catch tandem configuration

#### 4.1.3 Discussion of the surface displacements in the near-field

It can be seen that the strength of the surface movements increases with increasing size of the indentation (e.g. Figs. 51, 52 compared to Figs. 93, 94). For normally incident shear waves there are significant vertical surface movements near the rim of the indentation (e.g. Figs. 99, 129) if the depth of the indentation approaches the order of an incident wavelength. For normally incident compressional waves strong horizontal surface movements can be observed (Figs. 165, 166 in Appendix E, see also [9]). There is some influence of the rim of the indentation on the surface movements, which results in a less smooth behaviour of the displacements near the rim and a slight increase of the surface movements for the indentations with sharp 90 degrees corners (semi-ellipsoids, Figs. 75, 76, 87, 88) compared to the indentations that have corners below 90 degrees (segments of hemispheres, Figs. 69, 70, 81, 82).

An interesting observation is that for non-normally incident compressional waves on to shallow surface indentations there is a resonance phenomenon of the horizontal displacements in the plane perpendicular to the plane of the incident wave vector, resulting in a standing wave pattern (Figs. 58, 70, 82). The surface movements are especially strong for a surface indentation with a surface diameter of one incident wavelength and a depth of a quarter of an incident wavelength (Fig. 70), although the resonances can also be observed for other shallow indentations. The resonances diminish with increasing depth of the indentation and are no longer significant for the case of a hemispherical surface obstacle (Fig. 94). The phenomenon seems to be independent of the sharpness of the rim, since it can be observed for indentations with the shape of a segment of a hemisphere (e.g. Fig. 70) as well as for indentations shaped as a semi-ellipsoid (e.g. Fig. 76). The strong

surface movements result in strong shear wave components in the far-field for that plane (Fig. 72). The resonance phenomenon is absent for the case of non-normally incident shear waves incident on to shallow indentations, see Fig. 232 in Appendix E.

## 4.2 Suggested further improvements to the numerical simulation model

As already indicated in section 4.1.1, there are several possibilities for improving and extending the work presented here by :

a) investigating the scattering of SH waves incident at all angles on to axisymmetric surface indentations. Although implemented in the existing computer program, this feature has so far not been exploited.

b) examining the influence of smooth corners on the scattering process

This can easily be achieved by altering the sampling path so as to create smooth corners between the surface indentation and the plane surface.

c) taking account of incident SV waves beyond the critical angle and incident Rayleigh waves

This can be achieved by following the strategy outlined in [9]. The incident and reflected waves in the unperturbed half-space are expanded in cylindrical coordinates with subsequent coordinate transformation rather than expanded directly in spherical coordinates. Surface waves with field components exponentially decaying away from the plane surface are then easily described, and a Fourier decomposition of incident, reflected and scattered field components with respect to the azimuth component  $\phi$  is still possible.

d) taking account of an outwardly propagating Rayleigh wave in the scattered field expansion

This can be achieved by including surface wave terms explicitly (one for each azimuth component) in the expansion used to describe the scattered field. It would then be possible to get quantitatively accurate values for the scattered far-field and the scattering cross-section, because surface wave terms (with a far-field dependence  $\sim \frac{1}{\sqrt{r}}$ ) are no longer approximated by body waves (with a far-field dependence  $\sim \frac{1}{r}$ ).

e) taking account of incident wave fields other than plane waves (e.g. point sources below the surface)

This can be achieved by either superimposing a set of incident plane waves or by expanding the incident wave field appropriately. It is, for example, possible to expand a point source at a given location in terms of spherical vector functions centered at another location, see [108].

f) taking account of incident wave fields with a given time dependence

This can be achieved by implementing the computer programs on the Cray supercomputer available at the University of London Computer Centre. The programs will then require very little computing time, and for a given geometry several runs for different frequencies with subsequent Fourier synthesis in the time domain are possible.

g) taking account of irregularly shaped axisymmetric surface indentations (e.g. flat bottomed hole)

This can be achieved by using a hybrid finite element / boundary method, see [86, 89]. The scattering is split into two regions : an inner region, bounded by a hemisphere, and an outer region. The (multiple) scattering inside the inner region can easily be modelled with finite elements. The radiation condition is fulfilled by an expansion of the wave field into spherical vector functions in the outer region, and continuity of displacements and stresses combines the two regions.

h) comparing numerically obtained near-field results for shallow surface indentations with perturbation theory

Shallow surface indentations with the shape of segments of a hemisphere can be considered as small perturbations of an elastic half-space, as long as the depth of the indentation is much smaller than the incident wavelength. The surface displacements in the vicinity of such a shallow indentation could then be compared to displacement results obtained with perturbation theory [72].

i) taking account of non-axisymmetric surface indentations

At the time of completion of this work a study dealing with elastic wave scattering from non-axisymmetric surface indentations was published in [109]. The study employs the wave function expansion approach that is also presented here, without restricting the geometry to axisymmetric features, where a decomposition of the three-dimensional scattering problem into two-

dimensional sub-problems is no longer possible. The computer program written in the course of this work can, at the expense of computing time and memory capacity, be extended to non-axisymmetric features in a straightforward manner.

## Appendix A

The potentials  $\varphi$ ,  $\psi$  and  $\chi$  in the appendices A and B are assumed to be given by the expansions (A.6) – (A.8). Equations (A.5) and (A.10) give the contribution of the individual potential components  $\varphi_{m,n}$ ,  $\psi_{m,n}$  and  $\chi_{m,n}$  to the displacement and stress components, and equations (A.11) and (B.1) – (B.3) are written down for the individual components of the potentials  $\varphi_{m,n}$ ,  $\psi_{m,n}$  and  $\chi_{m,n}$ . The indices (m,n) in equations (A.5), (A.10), (A.11) and (B.1) – (B.3) were omitted and are implied.

Displacement and stress components in spherical coordinates

The displacement vector  $\vec{u}$  that satisfies the time harmonic elastic wave equation in spherical coordinates can be written as superposition of the spherical vector wave functions  $\vec{L}$ ,  $\vec{M}$  and  $\vec{N}$ , see [41, 94]

$$\vec{u} = \vec{L}(k_p, r, \theta, \phi) + \vec{M}(k_s, r, \theta, \phi) + \vec{N}(k_s, r, \theta, \phi) \quad (\text{A.1})$$

where

$$\vec{L}(k_p, r, \theta, \phi) = \text{grad } \varphi(k_p, r, \theta, \phi) \quad (\text{A.2a})$$

$$\nabla^2 \varphi + k_p^2 \varphi = 0 \quad (\text{A.2b})$$

$$\vec{M}(k_s, r, \theta, \phi) = \text{curl}(r \psi(k_s, r, \theta, \phi) \vec{e}_r) \quad (\text{A.3a})$$

$$= \text{grad}(r \psi) \times \vec{e}_r \quad (\text{A.3b})$$

$$\nabla^2 \psi + k_s^2 \psi = 0 \quad (\text{A.3c})$$

$$\vec{N}(k_s, r, \theta, \phi) = \frac{1}{k_s} \text{curl curl}(r \chi(k_s, r, \theta, \phi) \vec{e}_r) \quad (\text{A.4a})$$

$$= \frac{1}{k_s} \text{grad} \frac{\partial(r\chi)}{\partial r} + k_s r \chi \vec{e}_r \quad (\text{A.4b})$$

$$\nabla^2 \chi + k_s^2 \chi = 0 \quad (\text{A.4c})$$

with

$\vec{e}_r$  : unit vector in radial direction

$k_p$  : compressional wave number

$k_s$  : shear wave number

The components of the displacement vector are therefore dependent on the scalar potentials  $\varphi$ ,  $\psi$  and  $\chi$  [41]

$$u_r = \frac{\partial \varphi}{\partial r} + \frac{n(n+1)}{k_s r} \chi \quad (\text{A.5a})$$

$$u_\theta = \frac{1}{r} \frac{\partial \varphi}{\partial \theta} + \frac{1}{r \sin \theta} \frac{\partial(r\psi)}{\partial \phi} + \frac{1}{k_s r} \frac{\partial^2(r\chi)}{\partial \theta \partial r} \quad (\text{A.5b})$$

$$u_\phi = \frac{1}{r \sin \theta} \frac{\partial \varphi}{\partial \phi} - \frac{1}{r} \frac{\partial(r\psi)}{\partial \theta} + \frac{1}{k_s r \sin \theta} \frac{\partial^2(r\chi)}{\partial \phi \partial r} \quad (\text{A.5c})$$

The scalar potentials, being solutions to the scalar wave equation in spherical coordinates, can be written down explicitly as a series of spherical Bessel functions, Legendre polynomials and trigonometric functions, see [41, 94 – 96]

$$\varphi(k_p, r, \theta, \phi) = \sum_{n=0}^{\infty} \sum_{m=0}^n \sum_{\sigma=e}^o a_{\sigma,m,n} V_{\sigma,m,n}(k_p, r, \theta, \phi) \quad (\text{A.6})$$

$$\psi(k_s, r, \theta, \phi) = \sum_{n=0}^{\infty} \sum_{m=0}^n \sum_{\sigma=e}^o b_{\sigma,m,n} V_{\sigma,m,n}(k_s, r, \theta, \phi) \quad (\text{A.7})$$

$$\chi(k_s, r, \theta, \phi) = \sum_{n=0}^{\infty} \sum_{m=0}^n \sum_{\sigma=e}^o c_{\sigma,m,n} V_{\sigma,m,n}(k_s, r, \theta, \phi) \quad (\text{A.8})$$

$$V_{e,m,n}(k, r, \theta, \phi) = z_n(kr) P_n^m(\cos \theta) \cos(m\phi) \quad (\text{A.9a})$$

$$V_{o,m,n}(k, r, \theta, \phi) = z_n(kr) P_n^m(\cos \theta) \sin(m\phi) \quad (\text{A.9b})$$

with the following meaning for the subscripts

' $\sigma$ ': index for the azimuth dependence

'e': even azimuth dependence

'o': odd azimuth dependence

'm': order of solution in the azimuth direction

'n': order of solution in the colatitude direction

$z_n$  is a spherical Bessel function of the first, second or third kind

and of order  $n$

$P_n^m$  is the associated Legendre Polynomial of order  $(n, m)$ .

The stress components in spherical can also be expressed as functions of the scalar potentials  $\varphi$ ,  $\psi$  and  $\chi$

$$\sigma_{rr} = -\lambda k_p^2 \varphi + 2\mu \frac{\partial^2 \varphi}{\partial r^2} + \frac{2\mu}{k_s} \frac{\partial}{\partial r} \left( \frac{\partial^2 (r\chi)}{\partial r^2} + k_s^2 r \chi \right) \quad (\text{A.10a})$$

$$\begin{aligned} \sigma_{\theta\theta} = & -\lambda k_p^2 \varphi + \frac{2\mu}{r^2} \left( r \frac{\partial \varphi}{\partial r} + \frac{\partial^2 \varphi}{\partial \theta^2} \right) - \frac{2\mu}{r \sin^2 \theta} \left( \cos \theta \frac{\partial \psi}{\partial \phi} - \sin \theta \frac{\partial^2 \psi}{\partial \theta \partial \phi} \right) \\ & + \frac{2\mu}{k_s r^2} \left( \frac{\partial^3 (r\chi)}{\partial^2 \theta \partial r} + n(n+1) \chi \right) \end{aligned} \quad (\text{A.10b})$$

$$\begin{aligned} \sigma_{\phi\phi} = & -\lambda k_p^2 \varphi + \frac{2\mu}{r^2} \left( \frac{1}{\sin^2 \theta} \frac{\partial^2 \varphi}{\partial \phi^2} + r \frac{\partial \varphi}{\partial r} + \frac{\cos \theta}{\sin \theta} \frac{\partial \varphi}{\partial \theta} \right) \\ & + \frac{2\mu}{r \sin \theta} \left( \frac{\cos \theta}{\sin \theta} \frac{\partial \psi}{\partial \phi} - \frac{\partial^2 \psi}{\partial \theta \partial \phi} \right) + \frac{2\mu}{k_s r^2 \sin^2 \theta} \\ & \times \left( \frac{\partial^3 (r\chi)}{\partial^2 \phi \partial r} + n(n+1) \sin^2 \theta \chi + \cos \theta \sin \theta \frac{\partial^2 (r\chi)}{\partial r \partial \theta} \right) \end{aligned} \quad (\text{A.10c})$$

$$\begin{aligned} \sigma_{r\theta} = & + \frac{2\mu}{r^2} \left( r \frac{\partial^2 \varphi}{\partial r \partial \theta} - \frac{\partial \varphi}{\partial \theta} \right) - \frac{\mu}{r \sin \theta} \left( \frac{\partial \psi}{\partial \phi} - r \frac{\partial^2 \psi}{\partial r \partial \phi} \right) \\ & + \frac{2\mu}{k_s r^2} \left( n(n+1) \frac{\partial \chi}{\partial \theta} - \frac{\partial^2 (r\chi)}{\partial r \partial \theta} - \frac{(k_s r)}{2} \frac{\partial \chi}{\partial \theta} \right) \end{aligned} \quad (\text{A.10d})$$

$$\begin{aligned} \sigma_{r\phi} = & + \frac{2\mu}{r^2 \sin \theta} \left( r \frac{\partial^2 \varphi}{\partial r \partial \phi} - \frac{\partial \varphi}{\partial \phi} \right) + \frac{\mu}{r} \left( \frac{\partial \psi}{\partial \theta} - r \frac{\partial^2 \psi}{\partial r \partial \theta} \right) \\ & + \frac{2\mu}{k_s r^2 \sin \theta} \left( n(n+1) \frac{\partial \chi}{\partial \phi} - \frac{(k_s r)^2}{2} \frac{\partial \chi}{\partial \phi} - \frac{\partial^2 (r\chi)}{\partial r \partial \phi} \right) \end{aligned} \quad (\text{A.10e})$$

$$\begin{aligned}
\sigma_{\theta\phi} = & + \frac{2\mu}{r^2 \sin^2\theta} \left( \sin \theta \frac{\partial^2 \varphi}{\partial \theta \partial \phi} - \cos \theta \frac{\partial \varphi}{\partial \phi} \right) \\
& + \frac{\mu}{r \sin^2\theta} \left( \cos \theta \sin \theta \frac{\partial \psi}{\partial \theta} - \sin^2\theta \frac{\partial^2 \psi}{\partial \theta^2} + \frac{\partial^2 \psi}{\partial \phi^2} \right) \\
& + \frac{2\mu}{k_s r^2 \sin^2\theta} \left( r \sin \theta \frac{\partial^3 \chi}{\partial r \partial \theta \partial \phi} - r \cos \theta \frac{\partial^2 \chi}{\partial r \partial \phi} \right) \tag{A.10f}
\end{aligned}$$

These equations are derived from equations found in [41]. They have been expanded using the relations (A.2b), (A.3b) and (A.4c) as well as

$$\frac{\partial^2(r\chi)}{\partial r^2} - r \nabla^2 \chi = \frac{n(n+1)}{r} \chi \tag{A.11}$$

which can be found in [96].

## Appendix B

### Numerical treatment of the displacement and stress components

The implementation of equations (A.5) and (A.10) into a computer program requires the elimination of any derivatives occurring. This can be done in a very elegant manner by using some properties of the scalar potentials and its components, largely resulting from equations (A.2b), (A.3b), (A.4c) and (A.9). The the following set of equations was compiled from [41, 96].

$$\frac{\partial^2 \varphi}{\partial r^2} = \frac{1}{r^2} \left( - 2r \frac{\partial \varphi}{\partial r} - k_p^2 r^2 \varphi + n(n+1) \varphi \right) \quad (\text{B.1})$$

$$\frac{\partial^2 \varphi}{\partial \theta^2} = - \frac{\cos \theta}{\sin \theta} \frac{\partial \varphi}{\partial \theta} - n(n+1) \varphi + \frac{m^2}{\sin^2 \theta} \varphi \quad (\text{B.2})$$

$$- \lambda k_p^2 \varphi = \frac{2\mu}{r^2} \left( - \frac{(k_s r)^2}{2} + (k_p r)^2 \right) \varphi \quad (\text{B.3})$$

$$\frac{\partial z_n(kr)}{\partial r} = \frac{n}{r} z_n(kr) - k z_{n+1}(kr) \quad (\text{B.4})$$

$$\frac{\partial (r z_n(kr))}{\partial r} = (n+1) z_n(kr) - k r z_{n+1}(kr) \quad (\text{B.5})$$

$$\frac{\partial P_n^m(\cos \theta)}{\partial \theta} = \frac{1}{\sin \theta} \left( - (n+m) P_{n-1}^m(\cos \theta) + n \cos \theta P_n^m(\cos \theta) \right) \quad (\text{B.6a})$$

$$\frac{\partial P_n^m(\cos \theta)}{\partial \theta} = \frac{1}{\sin \theta} \left( - (n+1) \cos \theta P_n^m(\cos \theta) + (n-m+1) P_{n+1}^m(\cos \theta) \right) \quad (\text{B.6b})$$

The incorporation of (B.1) – (B.5) and (B.6b) into (A.5) and (A.10) leads to a set of equations that is easy to implement on a computer. For the sake of transparency the contribution from each potential to the displacement and stress components is listed separately. A corresponding set of equations is obtained when instead of recurrence relation (B.6b) the alternative equation (B.6a) is used. Such a set can be found in [41, 95]. However, for computational reasons it was preferred to employ equation (B.6b). The azimuth dependence of the displacement and stress components is given at the end of each component in vector component form, the upper part denotes even azimuth dependence of the corresponding scalar potential, the lower part denotes odd azimuth dependence.

$u_r$  due to  $\varphi$  ( $= L_r$ ) :

$$u_{r,\varphi,m,n} = \left( \frac{n}{r} Z_n(k_p r) - k_p Z_{n+1}(k_p r) \right) P_n^m(\cos \theta) \begin{bmatrix} \cos(m\phi) \\ \sin(m\phi) \end{bmatrix} \quad (\text{B.7a})$$

$u_r$  due to  $\psi$  ( $= M_r$ ) :

$$u_{r,\psi,m,n} = 0 \quad (\text{B.7b})$$

$u_r$  due to  $\chi$  ( $= N_r$ ) :

$$u_{r,\chi,m,n} = \frac{n(n+1)}{k_s r} Z_n(k_s r) P_n^m(\cos \theta) \begin{bmatrix} \cos(m\phi) \\ \sin(m\phi) \end{bmatrix} \quad (\text{B.7c})$$

$u_\theta$  due to  $\varphi$  ( $= L_\theta$ ) :

$$u_{\theta,\varphi,m,n} = \frac{z_n(k_p r)}{r \sin \theta} \left( - (n + 1) \cos \theta P_n^m(\cos \theta) + (n - m + 1) P_{n+1}^m(\cos \theta) \right) \\ \times \begin{bmatrix} \cos(m\phi) \\ \sin(m\phi) \end{bmatrix} \quad (\text{B.8a})$$

$u_\theta$  due to  $\psi$  ( $= M_\theta$ ) :

$$u_{\theta,\psi,m,n} = \frac{m}{\sin \theta} z_n(k_s r) P_n^m(\cos \theta) \begin{bmatrix} - \sin(m\phi) \\ \cos(m\phi) \end{bmatrix} \quad (\text{B.8b})$$

$u_\theta$  due to  $\chi$  ( $= N_\theta$ ) :

$$u_{\theta,\chi,m,n} = \frac{1}{\sin \theta} \left( \frac{n + 1}{k_s r} z_n(k_s r) - z_{n+1}(k_s r) \right) \\ \times \left( - (n + 1) \cos \theta P_n^m(\cos \theta) + (n - m + 1) P_{n+1}^m(\cos \theta) \right) \\ \times \begin{bmatrix} \cos(m\phi) \\ \sin(m\phi) \end{bmatrix} \quad (\text{B.8c})$$

$u_\phi$  due to  $\varphi$  ( $= L_\phi$ ) :

$$u_{\phi,\varphi,m,n} = \frac{m}{r \sin \theta} z_n(k_p r) P_n^m(\cos \theta) \begin{bmatrix} - \sin(m\phi) \\ \cos(m\phi) \end{bmatrix} \quad (\text{B.9a})$$

$u_\phi$  due to  $\psi$  ( $= M_\phi$ ) :

$$u_{\phi,\psi,m,n} = - \frac{z_n(k_s r)}{\sin \theta} \left( - (n + 1) \cos \theta P_n^m(\cos \theta) + (n - m + 1) P_{n+1}^m(\cos \theta) \right) \\ \times \begin{bmatrix} \cos(m\phi) \\ \sin(m\phi) \end{bmatrix} \quad (\text{B.9b})$$

$u_\phi$  due to  $\chi$  ( $= N_\phi$ ) :

$$u_{\phi,\chi,m,n} = \frac{m}{\sin \theta} \left( \frac{n+1}{k_s r} z_n(k_s r) - z_{n+1}(k_s r) \right) P_n^m(\cos \theta) \begin{bmatrix} -\sin(m\phi) \\ \cos(m\phi) \end{bmatrix} \quad (\text{B.9c})$$

$\sigma_{rr}$  due to  $\varphi$  :

$$\sigma_{rr,\varphi,m,n} = \frac{2\mu}{r^2} \left[ \left( n^2 - n - \frac{(k_s r)^2}{2} \right) z_n(k_p r) + 2 k_p r z_{n+1}(k_p r) \right] P_n^m(\cos \theta) \times \begin{bmatrix} \cos(m\phi) \\ \sin(m\phi) \end{bmatrix} \quad (\text{B.10a})$$

$\sigma_{rr}$  due to  $\psi$  :

$$\sigma_{rr,\psi,m,n} = 0 \quad (\text{B.10b})$$

$\sigma_{rr}$  due to  $\chi$  :

$$\sigma_{rr,\chi,m,n} = \frac{2\mu}{k_s} \frac{n(n+1)}{r^2} \left[ (n-1) z_n(k_s r) - k_s r z_{n+1}(k_s r) \right] P_n^m(\cos \theta) \times \begin{bmatrix} \cos(m\phi) \\ \sin(m\phi) \end{bmatrix} \quad (\text{B.10c})$$

$\sigma_{\theta\theta}$  due to  $\varphi$  :

$$\sigma_{\theta\theta,\varphi,m,n} = \frac{2\mu}{r^2} \left[ \left( -n^2 - \frac{(k_s r)^2}{2} + (k_p r)^2 \right) z_n(k_p r) - k_p r z_{n+1}(k_p r) \right] P_n^m(\cos \theta) + \frac{1}{\sin^2 \theta} \left[ (m^2 + (n+1) \cos^2 \theta) P_n^m(\cos \theta) - (n-m+1) \cos \theta P_{n+1}^m(\cos \theta) \right] z_n(k_p r) \begin{bmatrix} \cos(m\phi) \\ \sin(m\phi) \end{bmatrix} \quad (\text{B.11a})$$

$\sigma_{\theta\theta}$  due to  $\psi$  :

$$\sigma_{\theta\theta,\psi,m,n} = \frac{2\mu m}{r \sin^2\theta} z_n(k_s r) \left( - (n + 2) \cos \theta P_n^m(\cos \theta) \right. \\ \left. + (n - m + 1) P_{n+1}^m(\cos \theta) \right) \begin{bmatrix} - \sin(m\phi) \\ \cos(m\phi) \end{bmatrix} \quad (\text{B.11b})$$

$\sigma_{\theta\theta}$  due to  $\chi$  :

$$\sigma_{\theta\theta,\chi,m,n} = \frac{2\mu}{k_s r^2} \left( - (n^2 + n) [n z_n(k_s r) - k_s r z_{n+1}(k_s r)] P_n^m(\cos \theta) \right. \\ \left. + \frac{1}{\sin^2} [(n + 1) z_n(k_s r) - k_s r z_{n+1}(k_s r)] \right. \\ \left. \times \left[ (m^2 + (n + 1) \cos^2\theta) P_n^m(\cos \theta) \right. \right. \\ \left. \left. - (n - m + 1) \cos \theta P_{n+1}^m(\cos \theta) \right] \right) \begin{bmatrix} \cos(m\phi) \\ \sin(m\phi) \end{bmatrix} \quad (\text{B.11c})$$

$\sigma_{\phi\phi}$  due to  $\varphi$  :

$$\sigma_{\phi\phi,\varphi,m,n} = \frac{2\mu}{r^2} \left( \left[ \left[ n - \frac{(k_s r)^2}{2} + (k_p r)^2 \right] z_n(k_p r) - k_p r z_{n+1}(k_p r) \right] P_n^m(\cos \theta) \right. \\ \left. + \frac{1}{\sin^2\theta} \left[ - (m^2 + (n + 1) \cos^2\theta) P_n^m(\cos \theta) \right. \right. \\ \left. \left. + (n - m + 1) \cos \theta P_{n+1}^m(\cos \theta) \right] z_n(k_p r) \right) \begin{bmatrix} \cos(m\phi) \\ \sin(m\phi) \end{bmatrix} \quad (\text{B.12a})$$

$\sigma_{\phi\phi}$  due to  $\psi$  :

$$\begin{aligned} \sigma_{\phi\phi,\psi,m,n} &= \frac{2\mu m}{r \sin^2\theta} z_n(k_s r) \left[ (n+2) \cos\theta P_n^m(\cos\theta) - (n-m+1) P_{n+1}^m(\cos\theta) \right] \\ &\quad \times \begin{bmatrix} -\sin(m\phi) \\ \cos(m\phi) \end{bmatrix} \end{aligned} \quad (\text{B.12b})$$

$\sigma_{\phi\phi}$  due to  $\chi$  :

$$\begin{aligned} \sigma_{\phi\phi,\chi,m,n} &= \frac{2\mu}{k_s r^2 \sin^2\theta} \left[ n(n+1) \sin^2\theta P_n^m(\cos\theta) z_n(k_s r) \right. \\ &\quad \left. + \left[ (n+1) z_n(k_s r) - k_s r z_{n+1}(k_s r) \right] \right. \\ &\quad \times \left[ - \left[ (n+1) \cos^2\theta + m^2 \right] P_n^m(\cos\theta) \right. \\ &\quad \left. \left. + \left[ n-m+1 \right] \cos\theta P_{n+1}^m(\cos\theta) \right] \right] \begin{bmatrix} \cos(m\phi) \\ \sin(m\phi) \end{bmatrix} \end{aligned} \quad (\text{B.12c})$$

$\sigma_{r\theta}$  due to  $\varphi$  :

$$\begin{aligned} \sigma_{r\theta,\varphi,m,n} &= \frac{2\mu}{r^2 \sin\theta} \left[ \left[ (n-1) z_n(k_p r) - k_p r z_{n+1}(k_p r) \right] \right. \\ &\quad \left. \times \left[ - (n+1) \cos\theta P_n^m(\cos\theta) + (n-m+1) P_{n+1}^m(\cos\theta) \right] \right] \\ &\quad \times \begin{bmatrix} \cos(m\phi) \\ \sin(m\phi) \end{bmatrix} \end{aligned} \quad (\text{B.13a})$$

$\sigma_{r\theta}$  due to  $\psi$  :

$$\begin{aligned} \sigma_{r\theta,\psi,m,n} &= \frac{\mu m}{r \sin \theta} \left[ (n-1) z_n(k_s r) - k_s r z_{n+1}(k_s r) \right] P_n^m(\cos \theta) \\ &\quad \times \begin{bmatrix} -\sin(m\phi) \\ \cos(m\phi) \end{bmatrix} \end{aligned} \quad (\text{B.13b})$$

$\sigma_{r\theta}$  due to  $\chi$  :

$$\begin{aligned} \sigma_{r\theta,\chi,m,n} &= \frac{2\mu}{k_s r^2 \sin \theta} \left[ \left( n^2 - 1 - \frac{(k_s r)^2}{2} \right) z_n(k_s r) + k_s r z_{n+1}(k_s r) \right] \\ &\quad \times \left[ - (n+1) \cos \theta P_n^m(\cos \theta) + (n-m+1) P_{n+1}^m(\cos \theta) \right] \\ &\quad \times \begin{bmatrix} \cos(m\phi) \\ \sin(m\phi) \end{bmatrix} \end{aligned} \quad (\text{B.13c})$$

$\sigma_{r\phi}$  due to  $\varphi$  :

$$\begin{aligned} \sigma_{r\phi,\varphi,m,n} &= \frac{2\mu m}{r^2 \sin \theta} \left[ (n-1) z_n(k_p r) - k_p r z_{n+1}(k_p r) \right] P_n^m(\cos \theta) \\ &\quad \times \begin{bmatrix} -\sin(m\phi) \\ \cos(m\phi) \end{bmatrix} \end{aligned} \quad (\text{B.14a})$$

$\sigma_{r\phi}$  due to  $\psi$  :

$$\begin{aligned} \sigma_{r\phi,\psi,m,n} &= \frac{\mu}{r \sin \theta} \left[ \left( (n-1) z_n(k_s r) - k_s r z_{n+1}(k_s r) \right) \right. \\ &\quad \left. \times \left[ (n+1) \cos \theta P_n^m(\cos \theta) - (n-m+1) P_{n+1}^m(\cos \theta) \right] \right] \\ &\quad \times \begin{bmatrix} \cos(m\phi) \\ \sin(m\phi) \end{bmatrix} \end{aligned} \quad (\text{B.14b})$$

$\sigma_{r\phi}$  due to  $\chi$  :

$$\sigma_{r\phi,\chi,m,n} = \frac{2\mu m}{k_s r^2 \sin \theta} \left[ \left( n^2 - 1 - \frac{(k_s r)^2}{2} \right) z_n(k_s r) + k_s r z_{n+1}(k_s r) \right] \\ \times P_n^m(\cos \theta) \begin{bmatrix} -\sin(m\phi) \\ \cos(m\phi) \end{bmatrix} \quad (\text{B.14c})$$

$\sigma_{\theta\phi}$  due to  $\varphi$  :

$$\sigma_{\theta\phi,\varphi,m,n} = \frac{2\mu m}{r^2 \sin^2 \theta} \left[ -(n+2) \cos \theta P_n^m(\cos \theta) + (n-m+1) P_{n+1}^m(\cos \theta) \right] \\ \times z_n(k_p r) \begin{bmatrix} -\sin(m\phi) \\ \cos(m\phi) \end{bmatrix} \quad (\text{B.15a})$$

$\sigma_{\theta\phi}$  due to  $\psi$  :

$$\sigma_{\theta\phi,\psi,m,n} = \frac{2\mu}{r \sin^2 \theta} \left[ \left( \frac{n^2 + 3n + 2}{2} \sin^2 \theta - n - 1 - m^2 \right) P_n^m(\cos \theta) \right. \\ \left. + (n-m+1) \cos \theta P_{n+1}^m(\cos \theta) \right] z_n(k_s r) \begin{bmatrix} \cos(m\phi) \\ \sin(m\phi) \end{bmatrix} \quad (\text{B.15b})$$

$\sigma_{\theta\phi}$  due to  $\chi$  :

$$\sigma_{\theta\phi,\chi,m,n} = \frac{2\mu m}{k_s r^2 \sin^2 \theta} \left[ (n+1) z_n(k_s r) - k_s r z_{n+1}(k_s r) \right] \\ \times \left[ -(n+2) \cos \theta P_n^m(\cos \theta) + (n-m+1) P_{n+1}^m(\cos \theta) \right] \\ \times \begin{bmatrix} -\sin(m\phi) \\ \cos(m\phi) \end{bmatrix} \quad (\text{B.15c})$$

Due to the occurrence of the terms  $\sin^{-1}\theta$  and  $\sin^{-2}\theta$  equations (B.7) – (B.15) are, in the numerical sense, singular at  $\theta = 0$  and  $\pi$ . They are, however, not singular in the analytical sense, since they describe physical phenomena that are continuous in space. Also, the singular terms have largely appeared due to the elimination of derivatives of Legendre polynomials, see (B.6b). It can be shown that, if proper limiting procedures are applied, equations (B.7) – (B.15) are finite at  $\theta = 0, \pi$ . This limiting process has been applied to the displacement components (B.7) – (B.9) in order to allow for continuous displacement everywhere. The stress components (B.10) – (B.15) were not modified since they do not need to be computed at the numerical singularity. For the limiting procedure some properties of the Legendre polynomials have to be employed. The following equations were used, they can be found in [96].

$$\frac{m P_n^m(\cos \theta)}{\sin \theta} = \frac{\cos \theta}{2} \left[ (n - m + 1)(n + m) P_n^{m-1}(\cos \theta) + P_n^{m+1}(\cos \theta) \right] + m \sin \theta P_n^m(\cos \theta) \quad (\text{B.16})$$

$$\frac{\partial P_n^m(\cos \theta)}{\partial \theta} = \frac{1}{2} \left[ (n - m + 1)(n + m) P_n^{m-1}(\cos \theta) - P_n^{m+1}(\cos \theta) \right] \quad (\text{B.17})$$

$$P_n^m(\cos \theta)|_{\theta=0} = \begin{cases} 0 & m \neq 0 \\ 1 & m = 0 \end{cases} \quad (\text{B.18a})$$

$$P_n^m(\cos \theta)|_{\theta=\pi} = \begin{cases} 0 & m \neq 0 \\ (-1)^n & m = 0 \end{cases} \quad (\text{B.18b})$$

With equations (B.18) it follows that (B.16) is zero at  $\theta = 0, \pi$  for all  $m$  apart from  $m = 1$

$$\left. \frac{P_n^1(\cos \theta)}{\sin \theta} \right|_{\theta=0} = \frac{n(n+1)}{2} \quad (\text{B.19a})$$

$$\left. \frac{P_n^1(\cos \theta)}{\sin \theta} \right|_{\theta=\pi} = (-1)^n \frac{n(n+1)}{2} \quad (\text{B.19b})$$

Also equation (B.17) is non-zero only for  $m = 1$

$$\left. \frac{\partial P_n^1(\cos \theta)}{\partial \theta} \right|_{\theta=0} = \frac{n(n+1)}{2} \quad (\text{B.20a})$$

$$\left. \frac{\partial P_n^1(\cos \theta)}{\partial \theta} \right|_{\theta=\pi} = (-1)^n \frac{n(n+1)}{2} \quad (\text{B.20b})$$

The contribution of the scalar potentials to the displacement components at  $\theta = 0$  can therefore be written as follows

$u_r$  due to  $\varphi$  :

contribution for  $m = 0$  only

$$u_{r,\varphi,0,n} = \left( \frac{n}{r} z_n(k_p r) - k_p z_{n+1}(k_p r) \right) \begin{bmatrix} 1 \\ 0 \end{bmatrix} \quad (\text{B.21a})$$

$u_r$  due to  $\psi$  :

$$u_{r,\psi,m,n} = 0 \quad (\text{B.21b})$$

$u_r$  due to  $\chi$  :

contribution for  $m = 0$  only

$$u_{r,\chi,0,n} = \frac{n(n+1)}{k_s r} z_n(k_s r) \begin{bmatrix} 1 \\ 0 \end{bmatrix} \quad (\text{B.21c})$$

$u_\theta$  due to  $\varphi$  :

contribution for  $m = 1$  only

$$u_{\theta,\varphi,1,n} = \frac{n(n+1)}{2} \frac{z_n(k_p r)}{r} \begin{bmatrix} \cos \phi \\ \sin \phi \end{bmatrix} \quad (\text{B.22a})$$

$u_\theta$  due to  $\psi$  :

contribution for  $m = 1$  only

$$u_{\theta,\psi,1,n} = \frac{n(n+1)}{2} z_n(k_s r) \begin{bmatrix} -\sin \phi \\ \cos \phi \end{bmatrix} \quad (\text{B.22b})$$

$u_\theta$  due to  $\chi$  :

contribution for  $m = 1$  only

$$u_{\theta,\chi,1,n} = \frac{n(n+1)}{2} \left( \frac{n+1}{k_s r} z_n(k_s r) - z_{n+1}(k_s r) \right) \begin{bmatrix} \cos \phi \\ \sin \phi \end{bmatrix} \quad (\text{B.22c})$$

$u_\phi$  due to  $\varphi$  :

contribution for  $m = 1$  only

$$u_{\phi,\varphi,1,n} = \frac{n(n+1)}{2} \frac{z_n(k_p r)}{r} \begin{bmatrix} -\sin \phi \\ \cos \phi \end{bmatrix} \quad (\text{B.23a})$$

$u_\phi$  due to  $\psi$  :

contribution for  $m = 1$  only

$$u_{\phi,\psi,1,n} = - \frac{n(n+1)}{2} z_n(k_{sr}) \begin{bmatrix} \cos \phi \\ \sin \phi \end{bmatrix} \quad (\text{B.23b})$$

$u_\phi$  due to  $\chi$  :

contribution for  $m = 1$  only

$$u_{\phi,\chi,1,n} = \frac{n(n+1)}{2} \left( \frac{n+1}{k_{sr}} z_n(k_{sr}) - z_{n+1}(k_{sr}) \right) \begin{bmatrix} -\sin \phi \\ \cos \phi \end{bmatrix} \quad (\text{B.23c})$$

The component  $u_r$  is independent of  $\phi$  and vanishes for scalar potentials with an odd azimuth dependence. The displacement components at  $\theta = \pi$  are obtained by multiplying (B.21) – (B.23) with the factor  $(-1)^n$ , see equations (B.18) – (B.20).

## Appendix C

### Expansion of a vector plane wave using spherical vector functions

It is possible to represent a vector plane wave as an infinite series of the spherical vector wave functions  $\vec{L}$ ,  $\vec{M}$  and  $\vec{N}$ . In order to write down this expansion in a compact form three new vector functions have to be introduced, the so-called spherical vector harmonics [94, 110]. The variables  $\alpha$  and  $\beta$  denote colatitude and azimuth, respectively. As in Appendix B, the even and odd azimuth dependence is given by the components in square brackets, upper part meaning even and lower part meaning odd  $\beta$  dependence.

$$\vec{P}_{mn}(\alpha, \beta) = P_n^m(\cos \alpha) \begin{bmatrix} \cos(m\beta) \\ \sin(m\beta) \end{bmatrix} \vec{e}_r \quad (\text{C.1})$$

$$\vec{B}_{mn}(\alpha, \beta) = \frac{r}{\sqrt{n(n+1)}} \text{grad} \left( P_n^m(\cos \alpha) \begin{bmatrix} \cos(m\beta) \\ \sin(m\beta) \end{bmatrix} \right) \quad (\text{C.2a})$$

$$= \frac{1}{\sqrt{n(n+1)}} \left( \frac{\partial P_n^m(\cos \alpha)}{\partial \alpha} \begin{bmatrix} \cos(m\beta) \\ \sin(m\beta) \end{bmatrix} \vec{e}_\theta + \frac{m}{\sin \alpha} P_n^m(\cos \alpha) \begin{bmatrix} -\sin(m\beta) \\ \cos(m\beta) \end{bmatrix} \vec{e}_\phi \right) \quad (\text{C.2b})$$

$$\vec{C}_{mn}(\alpha, \beta) = \frac{r}{\sqrt{n(n+1)}} \text{curl} \left( P_n^m(\cos \alpha) \begin{bmatrix} \cos(m\beta) \\ \sin(m\beta) \end{bmatrix} \vec{e}_r \right) - \frac{r}{\sqrt{n(n+1)}} \left( \text{grad} \left( P_n^m(\cos \alpha) \begin{bmatrix} \cos(m\beta) \\ \sin(m\beta) \end{bmatrix} \right) \times \vec{e}_r \right) \quad (\text{C.3a})$$

$$= \frac{1}{\sqrt{n(n+1)}} \left( + \frac{m}{\sin \alpha} P_n^m(\cos \alpha) \begin{bmatrix} -\sin(m\beta) \\ \cos(m\beta) \end{bmatrix} \vec{e}_\theta - \frac{\partial P_n^m(\cos \alpha)}{\partial \alpha} \begin{bmatrix} \cos(m\beta) \\ \sin(m\beta) \end{bmatrix} \vec{e}_\phi \right) \quad (\text{C.3b})$$

The derivatives occurring in (C.2) and (C.3) can be eliminated using some of the equations given in Appendix B

$$\begin{aligned} \tilde{B}_{m\alpha}(\alpha, \beta) = & \frac{1}{\sqrt{n(n+1)\sin\alpha}} \left\{ (n+1-m) P_{n+1}^m(\cos\alpha) \right. \\ & \left. - (n+1)\cos\alpha P_n^m(\cos\alpha) \right\} \begin{bmatrix} \cos(m\beta) \\ \sin(m\beta) \end{bmatrix} \tilde{e}_\theta \\ & + m P_n^m(\cos\alpha) \begin{bmatrix} -\sin(m\beta) \\ \cos(m\beta) \end{bmatrix} \tilde{e}_\phi \end{aligned} \quad (C.4a)$$

The apparent singularity of (C.4a) for  $n = 0$  is misleading. It can be shown (see [94]) that<sup>5</sup>

$$\tilde{B}_{00}(\alpha, \beta) = 0 \quad (C.4b)$$

$$\begin{aligned} \tilde{C}_{m\alpha}(\alpha, \beta) = & \frac{1}{\sqrt{n(n+1)\sin\alpha}} \left\{ m P_n^m(\cos\alpha) \begin{bmatrix} -\sin(m\beta) \\ \cos(m\beta) \end{bmatrix} \tilde{e}_\theta \right. \\ & \left. - [(n+1-m) P_{n+1}^m(\cos\alpha) - (n+1)\cos\alpha P_n^m(\cos\alpha)] \right. \\ & \left. \times \begin{bmatrix} \cos(m\beta) \\ \sin(m\beta) \end{bmatrix} \tilde{e}_\phi \right\} \end{aligned} \quad (C.5a)$$

$$\tilde{C}_{00}(\alpha, \beta) = 0 \quad (C.5b)$$

For  $\alpha = 0, \pi$  the equations (C.4) and (C.5) are numerically singular. A limitation process yields for  $\alpha = 0$

---

<sup>5</sup> The case  $n = 0$  implies that also  $m = 0$ , since always  $n \geq |m|$

$$\vec{P}_{0n}(\alpha, \beta) = \begin{bmatrix} 1 \\ 0 \end{bmatrix} \vec{e}_r \quad (C.6a)$$

$$\vec{P}_{mn}(\alpha, \beta) = 0 \quad \text{otherwise} \quad (C.6b)$$

$$\vec{B}_{1n}(\alpha, \beta) = \frac{1}{2} \sqrt{n(n+1)} \left( \begin{bmatrix} \cos \beta \\ \sin \beta \end{bmatrix} \vec{e}_\theta + \begin{bmatrix} -\sin \beta \\ \cos \beta \end{bmatrix} \vec{e}_\phi \right) \quad (C.7a)$$

$$\vec{B}_{mn}(\alpha, \beta) = 0 \quad \text{otherwise} \quad (C.7b)$$

$$\vec{C}_{1n}(\alpha, \beta) = \frac{1}{2} \sqrt{n(n+1)} \left( \begin{bmatrix} -\sin \beta \\ \cos \beta \end{bmatrix} \vec{e}_\theta - \begin{bmatrix} \cos \beta \\ \sin \beta \end{bmatrix} \vec{e}_\phi \right) \quad (C.8a)$$

$$\vec{C}_{mn}(\alpha, \beta) = 0 \quad \text{otherwise} \quad (C.8b)$$

For  $\alpha = \pi$  equations (C.6a), (C.7a) and (C.8a) have to be multiplied by the factor  $(-1)^n$

The vector harmonics  $\vec{P}$ ,  $\vec{B}$  and  $\vec{C}$  are orthogonal functions and closely related to the spherical vector wave functions  $\vec{L}$ ,  $\vec{M}$  and  $\vec{N}$ , many details may be found in [94, 110].

It is now possible to write a vector plane wave as

$$\begin{aligned} \vec{e} e^{i\vec{k}\vec{r}} &= \sum_{n=0}^{\infty} \sum_{m=0}^n \sum_{\sigma=e}^{\circ} \epsilon_m i^n (2n+1) \frac{(n-m)!}{(n+m)!} \\ &\times \left\{ -\frac{i}{k_p} \left[ \vec{e} \cdot \vec{P}_{\sigma,m,n}(\alpha, \beta) \right] \vec{L}_{\sigma,m,n}(k_p, \theta, \phi) + \right. \\ &\quad \frac{1}{\sqrt{n(n+1)}} \left[ \left[ \vec{e} \cdot \vec{C}_{\sigma,m,n}(\alpha, \beta) \right] \vec{M}_{\sigma,m,n}(k_s, \theta, \phi) \right. \\ &\quad \left. \left. - i \left[ \vec{e} \cdot \vec{B}_{\sigma,m,n}(\alpha, \beta) \right] \vec{N}_{\sigma,m,n}(k_s, \theta, \phi) \right] \right\} \quad (C.9) \end{aligned}$$

where the index ' $\sigma$ ' stands for even or odd azimuth dependence and  $\vec{e}$  gives the polarisation of the plane wave. The radial dependence of the potentials  $\varphi$ ,  $\psi$  and  $\chi$  (and therefore also the radial dependence of the  $\vec{L}$ ,  $\vec{M}$  and  $\vec{N}$ ) in expansion (C.9) is given by spherical Bessel functions of the first kind in order to ensure the boundedness of the displacement at the origin. Also

$$\epsilon_m = \begin{cases} 1 & m > 0 \\ 2 & m = 0 \end{cases} \quad (\text{C.10})$$

Two different spherical coordinate systems are employed in equation (C.9)

- $(k, \alpha, \beta)$  denotes the coordinates of the wave vector
- $(r, \theta, \phi)$  denotes the coordinates of the point of observation

Plane waves with three different polarisations are possible

- compressional plane waves (P waves) :

$$\vec{e} = \vec{e}_p \quad \text{and} \quad \vec{k} = \vec{k}_p \quad \text{with} \quad \vec{e}_p \text{ being parallel to } \vec{k}_p$$

- shear horizontally polarised plane waves (SH waves) :

$$\vec{e} = \vec{e}_{sh} \quad \text{and} \quad \vec{k} = \vec{k}_s \quad \text{with} \quad \vec{e}_{sh} \text{ being perpendicular to } \vec{k}_s$$

- shear vertically polarised plane waves (SV waves) :

$$\vec{e} = \vec{e}_{sv} \quad \text{and} \quad \vec{k} = \vec{k}_s \quad \text{with} \quad \vec{e}_{sv} \text{ being perpendicular to } \vec{e}_{sh} \text{ and } \vec{k}_s$$

In spherical coordinates the wave vector points in  $\vec{e}_r$  direction

$$\vec{k} = k \vec{e}_r \quad (\text{C.11})$$

The polarisation vector  $\vec{e}_p$  then also points in  $\vec{e}_r$  direction

$$\vec{e}_p = \vec{e}_r \quad (\text{C.12})$$

Without loss of generality it can be assumed that the wave vector  $\vec{k}$  lies in the  $x-z$  plane, i.e.

$$\beta = 0 \quad (\text{C.13})$$

Then  $\vec{e}_p$  and  $\vec{e}_{sv}$  will be in the  $x-z$  plane (they will also be perpendicular) whereas  $\vec{e}_{sh}$  will be in  $\vec{e}_y$  direction. The shear wave polarisation vectors can

now be written as

$$\vec{e}_{sh} = \vec{e}_\phi \quad (\text{C.14})$$

and

$$\vec{e}_{sv} = -\vec{e}_\theta \quad (\text{C.15})$$

see also Fig. 8. The minus sign in equation (C.15) appears in order to turn (C.12), (C.14) and (C.15) into a right handed orthogonal coordinate system (i.e.  $\vec{e}_r \times \vec{e}_{sh} = \vec{e}_{sv}$ ). It can now be seen from equation (C.9) that a compressional plane wave is generated as a series of  $\vec{L}_{\sigma,m,n}$  only and an arbitrarily polarised shear wave consists of  $\vec{M}_{\sigma,m,n}$  and  $\vec{N}_{\sigma,m,n}$  without contribution from any  $\vec{L}_{\sigma,m,n}$ . A derivation of equation (C.9) can be found in [111] for the longitudinal part (i.e. compressional waves) and in [112] for the transverse part (i.e. shear waves), for details see also [108].

Due to equation (C.13) the azimuth dependence of the field components in (C.9) will be either even or odd, not a linear combination of both (since  $\sin(m\beta) \equiv 0$ ). This and (C.12), (C.14) and (C.15) can be used to write down a simplified expansion in place of (C.9) where each plane wave type can be considered separately. The tilde ( $\tilde{\phantom{x}}$ ) above the spherical vector harmonics and the displacement components signals that the azimuth dependence has been factorized out<sup>6</sup>.

---

<sup>6</sup> The following definition is intended to simplify the notation of a diagonal matrix

$$\text{diag} \begin{bmatrix} a \\ b \\ c \end{bmatrix} := \begin{bmatrix} a & 0 & 0 \\ 0 & b & 0 \\ 0 & 0 & c \end{bmatrix}$$

$$\begin{aligned} \vec{e}_p e^{i\vec{k}_p \vec{r}} &= - \sum_{n=0}^{\infty} \sum_{m=0}^n \epsilon_m (2n+1) \frac{(n-m)!}{(n+m)!} \\ &\times \text{diag} \begin{bmatrix} \cos(m\phi) \\ \cos(m\phi) \\ -\sin(m\phi) \end{bmatrix} \frac{i^{n+1}}{k_p} \tilde{P}_{r,m,n}(\alpha) \begin{bmatrix} \tilde{u}_{r,\phi,m,n} \\ \tilde{u}_{\theta,\phi,m,n} \\ \tilde{u}_{\phi,\phi,m,n} \end{bmatrix} \end{aligned} \quad (\text{C16a})$$

$$\begin{aligned} \vec{e}_{sh} e^{i\vec{k}_s \vec{r}} &= \sum_{n=0}^{\infty} \sum_{m=0}^n \epsilon_m (2n+1) \frac{(n-m)!}{(n+m)!} \\ &\times \text{diag} \begin{bmatrix} \sin(m\phi) \\ \sin(m\phi) \\ \cos(m\phi) \end{bmatrix} \left( \frac{i^n}{\sqrt{n(n+1)}} \tilde{C}_{\phi,m,n}(\alpha) \begin{bmatrix} 0 \\ -\tilde{u}_{\theta,\phi,m,n} \\ \tilde{u}_{\phi,\phi,m,n} \end{bmatrix} \right. \\ &\left. - \frac{i^{n+1}}{\sqrt{n(n+1)}} \tilde{B}_{\phi,m,n}(\alpha) \begin{bmatrix} \tilde{u}_{r,\chi,m,n} \\ \tilde{u}_{\theta,\chi,m,n} \\ \tilde{u}_{\phi,\chi,m,n} \end{bmatrix} \right) \end{aligned} \quad (\text{C16b})$$

$$\begin{aligned} \vec{e}_{sv} e^{i\vec{k}_s \vec{r}} &= - \sum_{n=0}^{\infty} \sum_{m=0}^n \epsilon_m (2n+1) \frac{(n-m)!}{(n+m)!} \\ &\times \text{diag} \begin{bmatrix} \cos(m\phi) \\ \cos(m\phi) \\ -\sin(m\phi) \end{bmatrix} \left( \frac{i^n}{\sqrt{n(n+1)}} \tilde{C}_{\theta,m,n}(\alpha) \begin{bmatrix} 0 \\ \tilde{u}_{\theta,\phi,m,n} \\ -\tilde{u}_{\phi,\phi,m,n} \end{bmatrix} \right. \\ &\left. - \frac{i^{n+1}}{\sqrt{n(n+1)}} \tilde{B}_{\theta,m,n}(\alpha) \begin{bmatrix} \tilde{u}_{r,\chi,m,n} \\ \tilde{u}_{\theta,\chi,m,n} \\ \tilde{u}_{\phi,\chi,m,n} \end{bmatrix} \right) \end{aligned} \quad (\text{C16c})$$

The stresses generated by a plane compressional or shear wave can be obtained by the same decomposition as the displacement components. Due to the symmetry of the stress tensor ( $\sigma_{ij} = \sigma_{ji}$ ) it is possible to write the

stress components in vector form. This is mathematically not entirely correct, but it simplifies the notation substantially. Hence, instead of

$$\vec{\sigma} = \begin{bmatrix} \sigma_{rr} & \sigma_{r\theta} & \sigma_{r\phi} \\ \sigma_{r\theta} & \sigma_{\theta\theta} & \sigma_{\theta\phi} \\ \sigma_{r\phi} & \sigma_{\theta\phi} & \sigma_{\phi\phi} \end{bmatrix} \quad (\text{C.17a})$$

the notation

$$\vec{\sigma} = \begin{bmatrix} \sigma_{rr} \\ \sigma_{\theta\theta} \\ \sigma_{\phi\phi} \\ \sigma_{r\theta} \\ \sigma_{r\phi} \\ \sigma_{\theta\phi} \end{bmatrix} \quad (\text{C.17b})$$

will be used. The stress components due to a compressional plane wave are then given as

$$\vec{\sigma}_p = - \sum_{n=0}^{\infty} \sum_{m=0}^n \epsilon_m (2n + 1) \frac{(n - m)!}{(n + m)!}$$

$$\times \text{diag} \begin{bmatrix} \cos(m\phi) \\ \cos(m\phi) \\ \cos(m\phi) \\ \cos(m\phi) \\ -\sin(m\phi) \\ -\sin(m\phi) \end{bmatrix}$$

$$\times \frac{i^{n+1}}{k_p} \tilde{P}_{r,m,n}(\alpha) \begin{bmatrix} \tilde{\sigma}_{rr,\varphi,m,n} \\ \tilde{\sigma}_{\theta\theta,\varphi,m,n} \\ \tilde{\sigma}_{\phi\phi,\varphi,m,n} \\ \tilde{\sigma}_{r\theta,\varphi,m,n} \\ \tilde{\sigma}_{r\phi,\varphi,m,n} \\ \tilde{\sigma}_{\theta\phi,\varphi,m,n} \end{bmatrix} \quad (\text{C.18a})$$

The stress components due to a horizontally polarised shear plane wave are written as

$$\begin{aligned}
 \vec{\sigma}_{sh} = & \sum_{n=0}^{\infty} \sum_{m=0}^n \epsilon_m (2n + 1) \frac{(n - m)!}{(n + m)!} \\
 & \times \text{diag} \begin{bmatrix} \sin(m\phi) \\ \sin(m\phi) \\ \sin(m\phi) \\ \sin(m\phi) \\ \cos(m\phi) \\ \cos(m\phi) \end{bmatrix} \\
 & \times \left( \frac{i^n}{\sqrt{n(n+1)}} \tilde{C}_{\phi, m, n}(\alpha) \begin{bmatrix} 0 \\ -\tilde{\sigma}_{\theta\theta, \psi, m, n} \\ -\tilde{\sigma}_{\phi\phi, \psi, m, n} \\ -\tilde{\sigma}_{r\theta, \psi, m, n} \\ \tilde{\sigma}_{r\phi, \psi, m, n} \\ \tilde{\sigma}_{\theta\phi, \psi, m, n} \end{bmatrix} \right. \\
 & \left. - \frac{i^{n+1}}{\sqrt{n(n+1)}} \tilde{B}_{\phi, m, n}(\alpha) \begin{bmatrix} \tilde{\sigma}_{rr, \chi, m, n} \\ \tilde{\sigma}_{\theta\theta, \chi, m, n} \\ \tilde{\sigma}_{\phi\phi, \chi, m, n} \\ \tilde{\sigma}_{r\theta, \chi, m, n} \\ \tilde{\sigma}_{r\phi, \chi, m, n} \\ \tilde{\sigma}_{\theta\phi, \chi, m, n} \end{bmatrix} \right) \quad (C.18b)
 \end{aligned}$$

and the stress components due to a vertically polarised shear plane wave can be expanded as

$$\begin{aligned}
 \tilde{\sigma}_{sv} = & - \sum_{n=0}^{\infty} \sum_{m=0}^n \epsilon_m (2n + 1) \frac{(n - m)!}{(n + m)!} \\
 & \times \text{diag} \begin{bmatrix} \cos(m\phi) \\ \cos(m\phi) \\ \cos(m\phi) \\ \cos(m\phi) \\ -\sin(m\phi) \\ -\sin(m\phi) \end{bmatrix} \\
 & \times \left( \frac{i^n}{\sqrt{n(n+1)}} \tilde{C}_{\theta,m,n}(\alpha) \begin{bmatrix} 0 \\ \tilde{\sigma}_{\theta\theta,\psi,m,n} \\ \tilde{\sigma}_{\phi\phi,\psi,m,n} \\ \tilde{\sigma}_{r\theta,\psi,m,n} \\ -\tilde{\sigma}_{r\phi,\psi,m,n} \\ -\tilde{\sigma}_{\theta\phi,\psi,m,n} \end{bmatrix} \right. \\
 & \left. - \frac{i^{n+1}}{\sqrt{n(n+1)}} \tilde{B}_{\theta,m,n}(\alpha) \begin{bmatrix} \tilde{\sigma}_{rr,\chi,m,n} \\ \tilde{\sigma}_{\theta\theta,\chi,m,n} \\ \tilde{\sigma}_{\phi\phi,\chi,m,n} \\ \tilde{\sigma}_{r\theta,\chi,m,n} \\ \tilde{\sigma}_{r\phi,\chi,m,n} \\ \tilde{\sigma}_{\theta\phi,\chi,m,n} \end{bmatrix} \right) \quad (C.18c)
 \end{aligned}$$

where the tilde indicates that the azimuth dependence has been factorized out of the stress components and the defined notation for a diagonal matrix is employed.

## Appendix D

### Far-field approximation and differential scattering cross-section

A close look at equations (B.7) – (B.15) in Appendix B reveals that the following displacement components decay with  $\frac{1}{r}$  and will therefore be the dominant part in the far-field (all other components decay with  $\frac{1}{r^2}$  or stronger and can therefore be neglected) :

- $u_r$  due to potential  $\varphi$ , this constitutes an outward propagating spherical longitudinal (compressional) wave

$$u_{r,\varphi,m,n} \approx -k_p z_{n+1}(k_p r) P_n^m(\cos \theta) \begin{bmatrix} \cos(m\phi) \\ \sin(m\phi) \end{bmatrix} \quad (D.1a)$$

- $u_\theta$  due to the potentials  $\psi$  and  $\chi$ , this gives the first polarisation component of an outward propagating spherical transverse (shear) wave

$$u_{\theta,\psi,m,n} \approx \frac{m}{\sin \theta} z_n(k_s r) P_n^m(\cos \theta) \begin{bmatrix} -\sin(m\phi) \\ \cos(m\phi) \end{bmatrix} \quad (D.1b)$$

$$u_{\theta,\chi,m,n} \approx -\frac{z_{n+1}(k_s r)}{\sin \theta} \left( - (n+1) \cos \theta P_n^m(\cos \theta) + (n-m+1) P_{n+1}^m(\cos \theta) \right) \begin{bmatrix} \cos(m\phi) \\ \sin(m\phi) \end{bmatrix} \quad (D.1c)$$

- $u_\phi$  due to the potentials  $\psi$  and  $\chi$ , this gives the second polarisation component of an outward propagating spherical transverse (shear) wave

$$\mathbf{u}_{\phi, \psi, m, n} \approx - \frac{Z_n(k_s r)}{\sin \theta} \left[ - (n + 1) \cos \theta P_n^m(\cos \theta) \right. \\ \left. + (n - m + 1) P_{n+1}^m(\cos \theta) \right] \begin{bmatrix} \cos(m\phi) \\ \sin(m\phi) \end{bmatrix} \quad (\text{D.1d})$$

$$\mathbf{u}_{\phi, \chi, m, n} \approx - \frac{m}{\sin \theta} Z_{n+1}(k_s r) P_n^m(\cos \theta) \begin{bmatrix} - \sin(m\phi) \\ \cos(m\phi) \end{bmatrix} \quad (\text{D.1e})$$

Hankel functions of the first kind have a simple asymptotic form for large arguments [113] :

$$z_n(kr) = h_n^{(1)}(kr) \approx -i \frac{e^{i(kr - \frac{n\pi}{2})}}{kr} \quad (\text{D.2a})$$

$$z_{n+1}(kr) = h_{n+1}^{(1)}(kr) \approx - \frac{e^{i(kr - \frac{n\pi}{2})}}{kr} \quad (\text{D.2b})$$

$$kr \gg 1 \quad (\text{D.2c})$$

and combining equations (D.1) with (D.2) allows very efficient computations in the far-field.

The differential cross-section  $R$  is defined as the average rate per unit area at which energy is scattered into the radial direction by the surface obstacle. It is equivalent to the Poynting vector in electromagnetic theory<sup>7</sup> [114]

$$R = \Im \left( \frac{\omega}{2} \left( \mathbf{u}_r^* \sigma_{rr} + \mathbf{u}_\theta^* \sigma_{r\theta} + \mathbf{u}_\phi^* \sigma_{r\phi} \right) \right) \Big|_{r, \theta, \phi} \quad (\text{D.3a})$$

$$r \gg 1, \theta \text{ and } \phi \text{ fixed} \quad (\text{D3.b})$$

---

<sup>7</sup> the superscript '\*' indicates the complex conjugate

The displacement and stress components in (D.3a) are given by the expansion (2.14) of the scattered field due to the surface indentation in the far-field. Equation (D.3a) can be evaluated separately for the scattered compressional wave components (due to the potential  $\varphi$ ) and for the scattered shear wave components (due to the potentials  $\psi$  and  $\chi$ ).

The differential scattering cross-section defined by (D.3) will be quantitatively accurate as long as there is no significant scattering into surface wave modes. Representation (2.14) does consist of a finite number of body waves with a far-field dependence of  $\frac{1}{r}$ , whereas surface waves propagate with  $\frac{1}{\sqrt{r}}$  in the far-field and their energy is confined to a thin layer along the surface. Expansion (2.14) is sufficient for a qualitative analysis of the scattered far-field energy, but it gives inaccurate quantitative results when most of the energy is scattered into Rayleigh waves. This could be remedied by including surface wave terms explicitly in (2.14) and treating them separately when evaluating the scattering cross-section, as was done in [115].

## Appendix E

### Supplementary results

This appendix introduces further results obtained by the numerical method presented above and is included for the sake of completeness.

#### Normally incident compressional and shear waves

This section presents the amplitude of the surface displacements, the amplitude of the far-field displacements and the differential scattering cross-section of the scattered far-field for a compressional or shear wave normally incident on to a hemispherical or shallow surface indentation in a half-space with Poisson's ratio  $\nu = 0.25$ . The far-field calculations were carried out at the normalised distance  $\frac{r}{a} = 1000$ . Four different surface indentations are considered :

- (a) a hemisphere with  $\frac{2a}{\lambda_{inc}} = 0.5$  and  $\alpha = 90^\circ$
- (b) a segment of a hemisphere with  $\frac{2a}{\lambda_{inc}} = 1.0$ ,  $\frac{d}{a} = 0.5$  and  $\alpha = 53.1^\circ$
- (c) a semi-ellipsoid with  $\frac{2a}{\lambda_{inc}} = 1.0$ ,  $\frac{d}{a} = 0.5$  and  $\alpha = 90^\circ$
- (d) a hemisphere with  $\frac{2a}{\lambda_{inc}} = 1.0$  and  $\alpha = 90^\circ$

where  $2a$  is the surface diameter and  $d$  the depth of the indentation. The angle of the corners between the indentation and the plane surface is denoted by  $\alpha$ . Features (a) and (d) represent hemispherical pits with a diameter of half an incident wavelength and one incident wavelength respectively. Features (b) and (c) are shallow axisymmetric indentations with a surface diameter of one incident wavelength and a depth of a quarter of an incident wavelength each, but with different shape.

	Figure numbers for a normally incident P wave	Figure numbers for a normally incident SV wave
Case		
(a)	Figs. 165, 167, 169	Figs. 177 — 182
(b)	Figs. 171, 173, 175	Figs. 183 — 188
(c)	Figs. 172, 174, 176	Figs. 189 — 194
(d)	Figs. 166, 168, 170	Figs. 195 — 200

Table 9 : Figure numbers of the results for the cases (a) — (d) presented in this section for a normally incident P or SV wave

The polar plots showing the angular distribution of the far-field displacements and the scattering cross-section are normalised for each case in the way described in chapter 3. The maximum values of each case cases relate to each other as given below, where case (a) has been chosen arbitrarily as normalisation.

case	Figure numbers	scaling factor of the far-field displacements
(a)	Fig. 167	1.0
(b)	Fig. 173	0.62
(c)	Fig. 174	0.58
(d)	Fig. 168	4.0

Table 10 : Scaling factors of the far-field displacement plots for the cases  
(a) — (d) and a normally incident P wave

case	Figure numbers	scaling factor of the differential cross-section
(a)	Fig. 169	1.0
(b)	Fig. 175	1.2
(c)	Fig. 176	1.0
(d)	Fig. 170	48.0

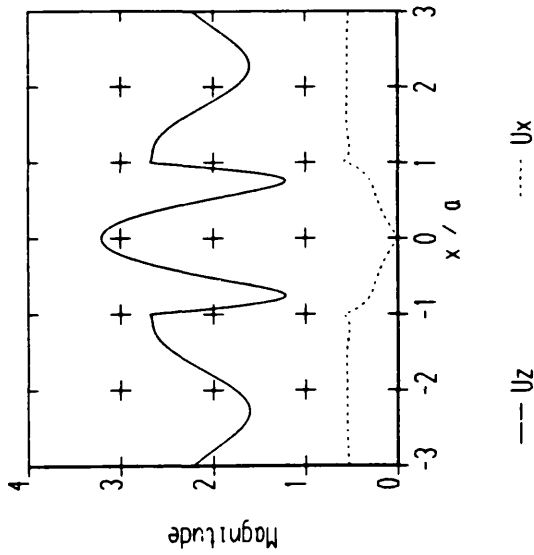
Table 11 : Scaling factors of the differential cross-section plots for the cases  
(a) — (d) and a normally incident P wave

case	Figure numbers	scaling factor of the far-field displacements
(a)	Figs. 179, 180	1.0
(b)	Figs. 185, 186	0.63
(c)	Figs. 191, 192	0.73
(d)	Figs. 197, 198	2.1

Table 12 : Scaling factors of the far-field displacement plots for the cases  
(a) — (d) and a normally incident SV wave

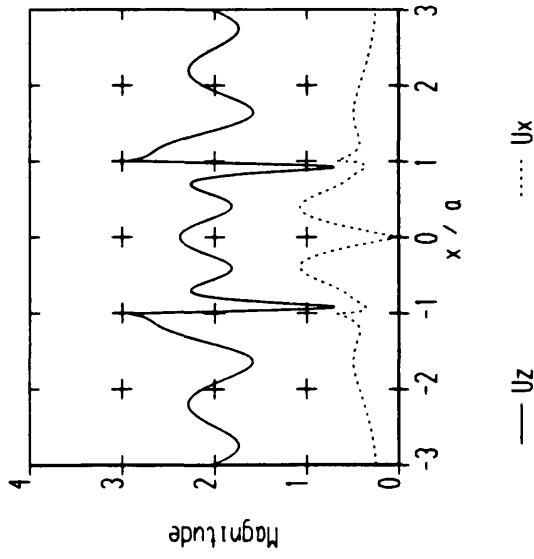
case	Figure numbers	scaling factor of the differential cross-section
(a)	Figs. 181, 182	1.0
(b)	Figs. 187, 188	0.79
(c)	Figs. 193, 194	1.1
(h)	Figs. 199, 200	8.9

Table 13 : Scaling factors of the differential cross-section plots for the cases  
(a) — (d) and a normally incident SV wave



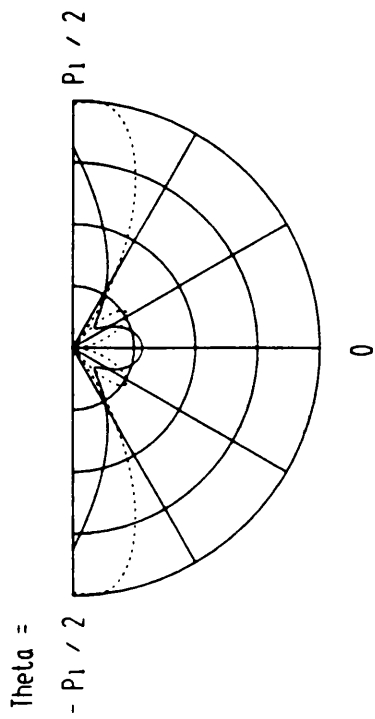
Surface displacements in x-z plane  
 Type of surface obstacle : Hemisphere  
 Order of approximation : 13  
 Incident wavetype : P  
 Incident angle : 0.00 deg  
 Poisson's ratio : 0.25  
 $2a / \lambda$  incident : 0.50  
 $d / a$  : 1.00

Fig. 165 : Amplitude of the surface displacements for a compressional wave normally incident on to a hemispherical surface indentation



Surface displacements in x-z plane  
 Type of surface obstacle : Hemisphere  
 Order of approximation : 17  
 Incident wavetype : P  
 Incident angle : 0.00 deg  
 Poisson's ratio : 0.25  
 $2a / \lambda$  incident : 1.00  
 $d / a$  : 1.00

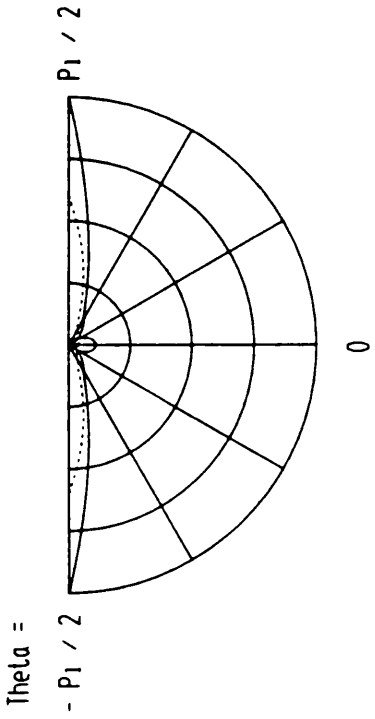
Fig. 166 : Amplitude of the surface displacements for a compressional wave normally incident on to a hemispherical surface indentation



— R comp      ..... Theta comp

Far field displacements in x-z plane  
 Type of surface obstacle : Hemisphere  
 Order of approximation : 13  
 Incident waveltype : P  
 Incident angle : 0.00 deg  
 Poisson's ratio : 0.25  
 $2a / \lambda$  incident : 0.50  
 $d / a$  : 1.00

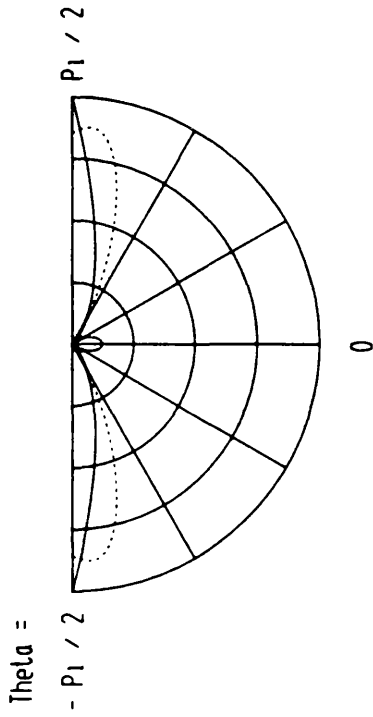
Fig. 167 : Amplitude of the far-field displacements of the scattered field for a compressional wave normally incident on to a hemispherical surface indentation



— R comp      ..... Theta comp

Far field displacements in x-z plane  
 Type of surface obstacle : Hemisphere  
 Order of approximation : 17  
 Incident waveltype : P  
 Incident angle : 0.00 deg  
 Poisson's ratio : 0.25  
 $2a / \lambda$  incident : 1.00  
 $d / a$  : 1.00

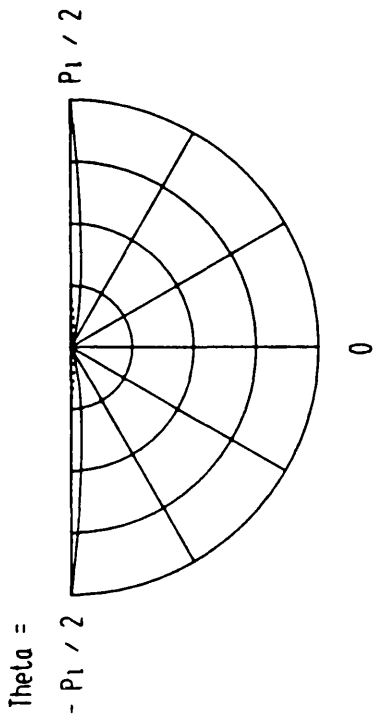
Fig. 168 : Amplitude of the far-field displacements of the scattered field for a compressional wave normally incident on to a hemispherical surface indentation



— P component      ..... S component

Scattered energy in x-z plane  
 Type of surface obstacle : Hemisphere  
 Order of approximation : 13  
 Incident wavetype : P  
 Incident angle : 0.00 deg  
 Poisson's ratio : 0.25  
 $2a / \lambda$  incident : 0.50  
 $d / a$  : 1.00

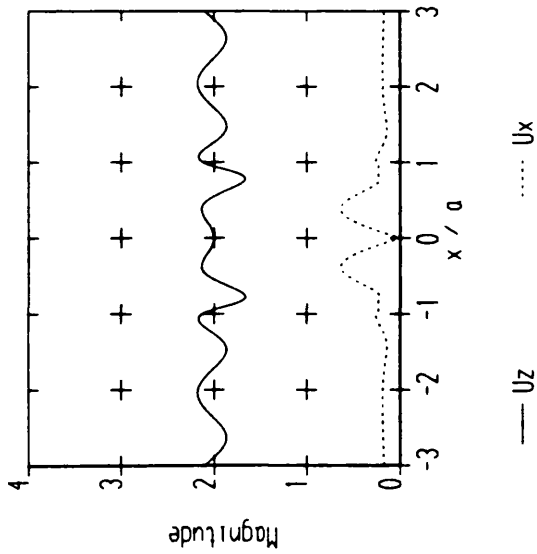
Fig. 169 : Differential cross-section of the scattered far-field for a compressional wave normally incident on to a hemispherical surface indentation



— P component      ..... S component

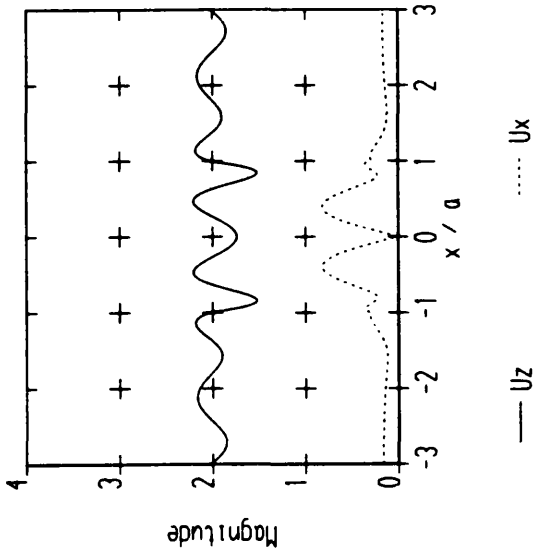
Scattered energy in x-z plane  
 Type of surface obstacle : Hemisphere  
 Order of approximation : 17  
 Incident wavetype : P  
 Incident angle : 0.00 deg  
 Poisson's ratio : 0.25  
 $2a / \lambda$  incident : 1.00  
 $d / a$  : 1.00

Fig. 170 : Differential cross-section of the scattered far-field for a compressional wave normally incident on to a hemispherical surface indentation



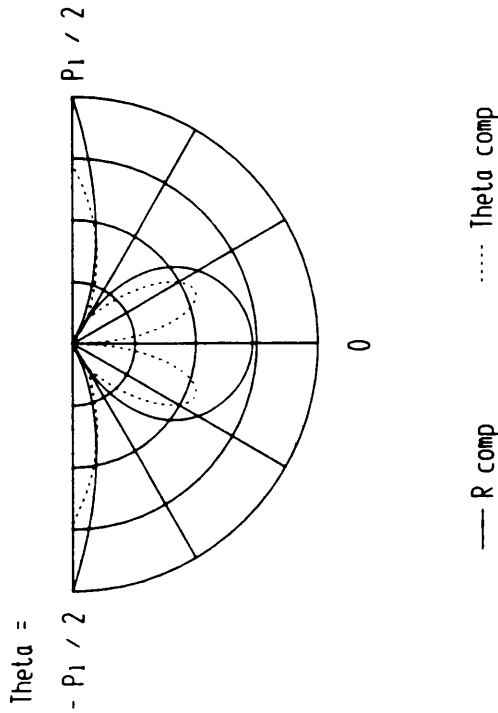
Surface displacements in x-z plane  
 Type of surface obstacle : Segment of a hemisphere  
 Order of approximation : 13  
 Incident wavetype : P  
 Incident angle : 0.00 deg  
 Poisson's ratio : 0.25  
 $2a / \lambda$  incident : 1.00  
 $d / a$  : 0.50

Fig. 171 : Amplitude of the surface displacements for a compressional wave normally incident on to a shallow axisymmetric surface indentation



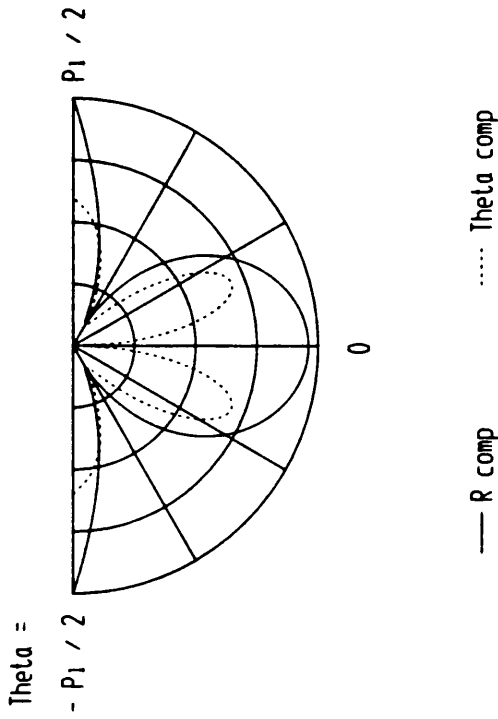
Surface displacements in x-z plane  
 Type of surface obstacle : Ellipsoid  
 Order of approximation : 13  
 Incident wavetype : P  
 Incident angle : 0.00 deg  
 Poisson's ratio : 0.25  
 $2a / \lambda$  incident : 1.00  
 $d / a$  : 0.50

Fig. 172 : Amplitude of the surface displacements for a compressional wave normally incident on to a shallow axisymmetric surface indentation



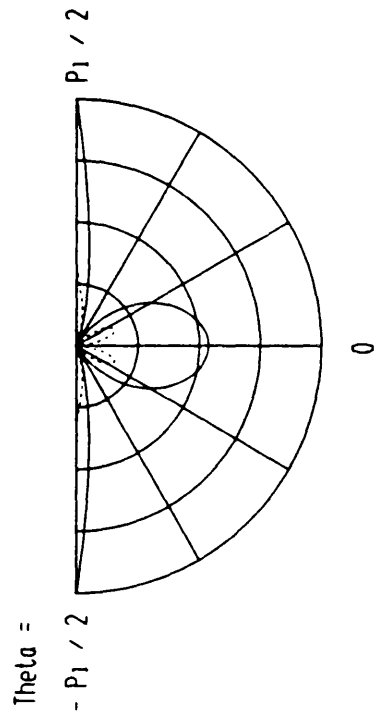
Far Field displacements in x-z plane  
 Type of surface obstacle : Segment of a hemisphere  
 Order of approximation : 13  
 Incident wavetype : P  
 Incident angle : 0.00 deg  
 Poisson's ratio : 0.25  
 $2a / \lambda$  incident : 1.00  
 $d / a$  : 0.50

Fig. 173 : Amplitude of the far-field displacements of the scattered field for a compressional wave normally incident on to a shallow axisymmetric surface indentation



Far Field displacements in x-z plane  
 Type of surface obstacle : Ellipsoid  
 Order of approximation : 13  
 Incident wavetype : P  
 Incident angle : 0.00 deg  
 Poisson's ratio : 0.25  
 $2a / \lambda$  incident : 1.00  
 $d / a$  : 0.50

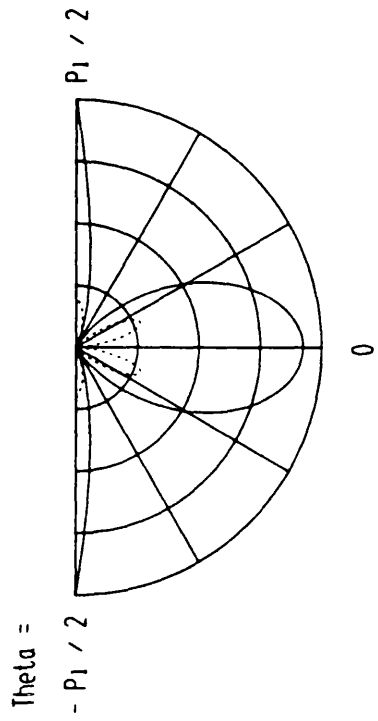
Fig. 174 : Amplitude of the far-field displacements of the scattered field for a compressional wave normally incident on to a shallow axisymmetric surface indentation



— P component      ..... S component

Scattered energy in x-z plane  
 Type of surface obstacle : Segment of a hemisphere  
 Order of approximation : 13  
 Incident waveltype : P  
 Incident angle : 0.00 deg  
 Poisson's ratio : 0.25  
 2a / lambda incident : 1.00  
 d / a : 0.50

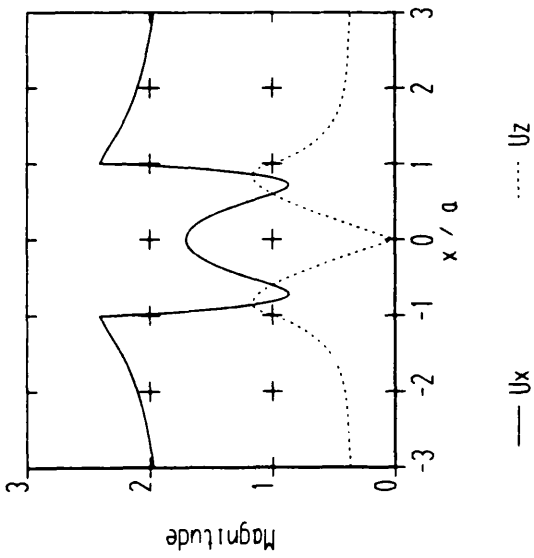
Fig. 175 : Differential cross-section of the scattered far-field for a compressional wave normally incident on to a shallow axisymmetric surface indentation



— P component      ..... S component

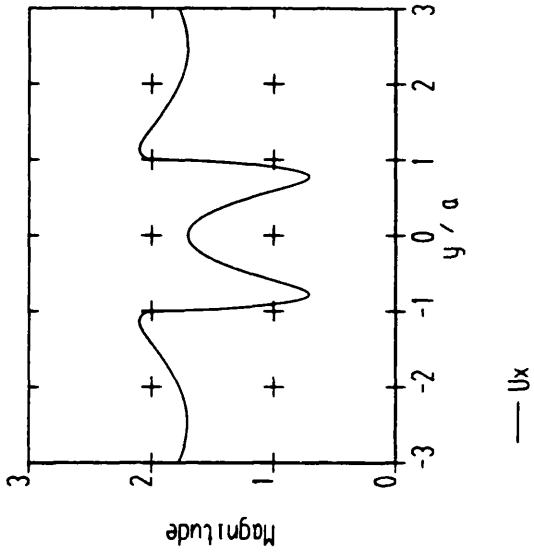
Scattered energy in x-z plane  
 Type of surface obstacle : Ellipsoid  
 Order of approximation : 13  
 Incident waveltype : P  
 Incident angle : 0.00 deg  
 Poisson's ratio : 0.25  
 2a / lambda incident : 1.00  
 d / a : 0.50

Fig. 176 : Differential cross-section of the scattered far-field for a compressional wave normally incident on to a shallow axisymmetric surface indentation



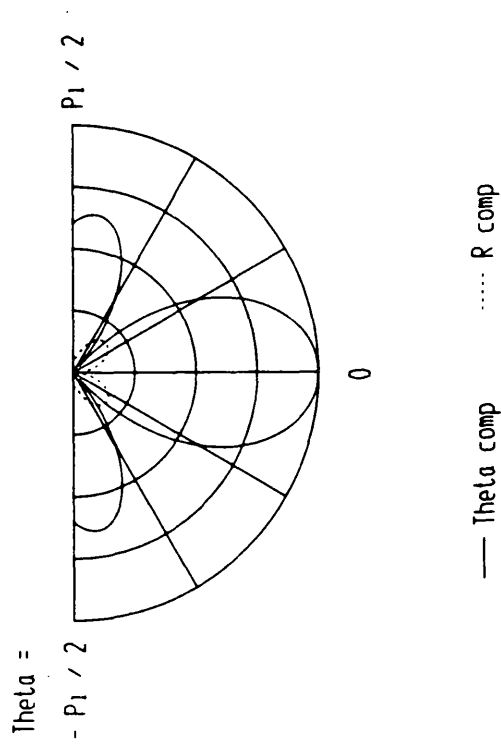
Surface displacements in  $x-z$  plane  
 Type of surface obstacle : Hemisphere  
 Order of approximation : 11  
 Incident wavetype : SV  
 Incident angle : 0.00 deg  
 Poisson's ratio : 0.25  
 $2a / \lambda$  incident : 0.50  
 $d / a$  : 1.00

Fig. 177 : Amplitude of the surface displacements in the  $x-z$  plane (plane of polarisation) for a shear wave normally incident on to a hemispherical surface indentation



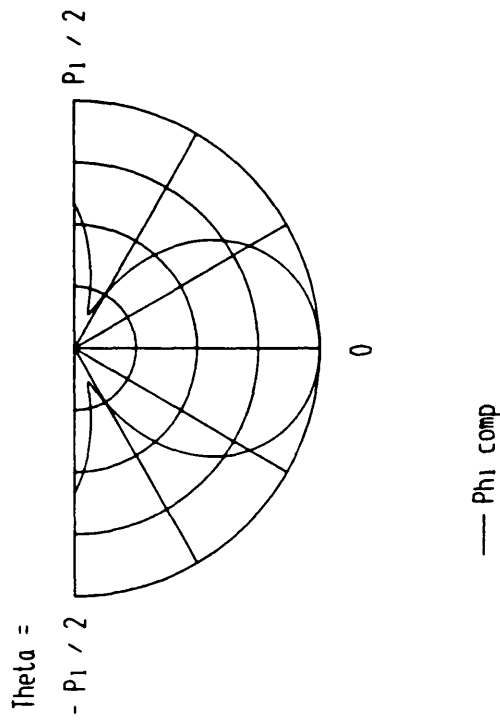
Surface displacements in  $y-z$  plane  
 Type of surface obstacle : Hemisphere  
 Order of approximation : 11  
 Incident wavetype : SV  
 Incident angle : 0.00 deg  
 Poisson's ratio : 0.25  
 $2a / \lambda$  incident : 0.50  
 $d / a$  : 1.00

Fig. 178 : Amplitude of the surface displacements in the  $y-z$  plane (plane perpendicular to polarisation) for a shear wave normally incident on to a hemispherical surface indentation



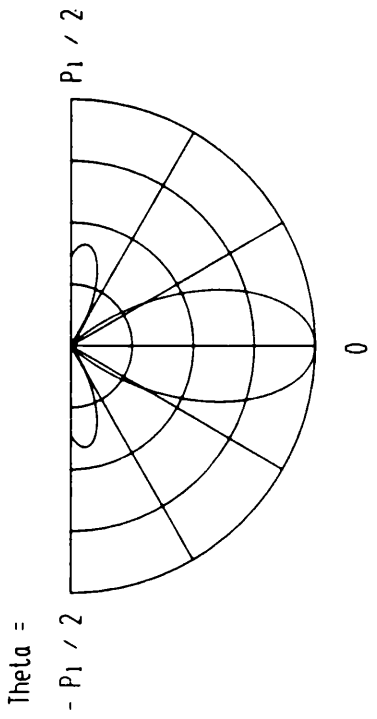
Far Field displacements in x-z plane  
 Type of surface obstacle : Hemisphere  
 Order of approximation : 11  
 Incident wavetype : SV  
 Incident angle : 0.00 deg  
 Poisson's ratio : 0.25  
 $2a / \lambda$  incident : 0.50  
 $d / a$  : 1.00

Fig. 179 : Amplitude of the far-field displacements of the scattered field in the x-z plane (plane of polarisation) for a shear wave normally incident on to a hemispherical surface indentation



Far Field displacements in y-z plane  
 Type of surface obstacle : Hemisphere  
 Order of approximation : 11  
 Incident wavetype : SV  
 Incident angle : 0.00 deg  
 Poisson's ratio : 0.25  
 $2a / \lambda$  incident : 0.50  
 $d / a$  : 1.00

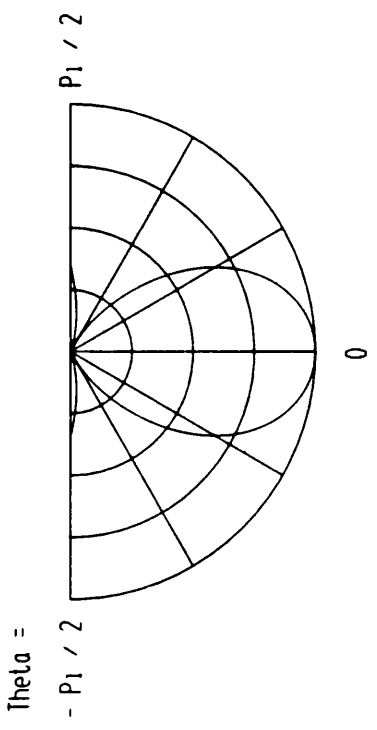
Fig. 180 : Amplitude of the far-field displacements of the scattered field in the y-z plane (plane perpendicular to polarisation) for a shear wave normally incident on to a hemispherical surface indentation



— S component      ..... P component

Scattered energy in x-z plane  
 Type of surface obstacle : Hemisphere  
 Order of approximation : 11  
 Incident wavetype : SV  
 Incident angle : 0.00 deg  
 Poisson's ratio : 0.25  
 $2a / \lambda$  incident : 0.50  
 $d / a$  : 1.00

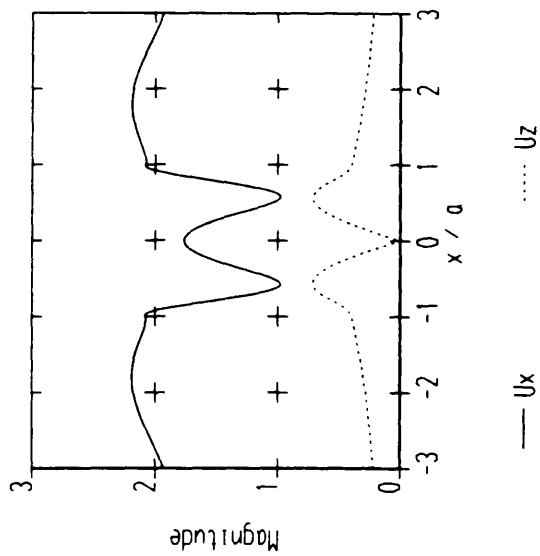
Fig. 181 : Differential cross-section of the scattered far-field in the x-z plane (plane of polarisation) for a shear wave normally incident on to a hemispherical surface indentation



— S component

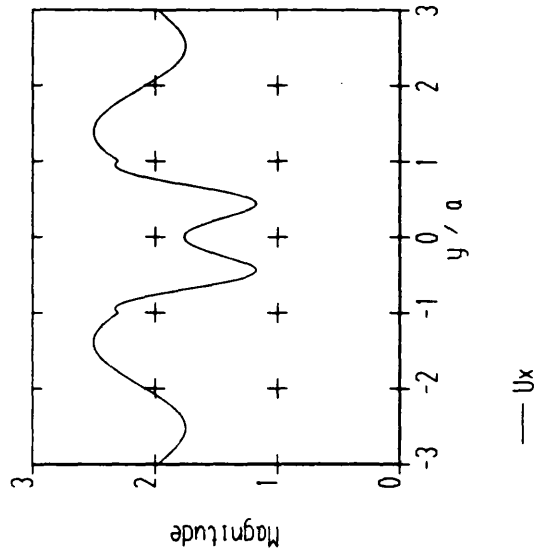
Scattered energy in y-z plane  
 Type of surface obstacle : Hemisphere  
 Order of approximation : 11  
 Incident wavetype : SV  
 Incident angle : 0.00 deg  
 Poisson's ratio : 0.25  
 $2a / \lambda$  incident : 0.50  
 $d / a$  : 1.00

Fig. 182 : Differential cross-section of the scattered far-field in the y-z plane (plane perpendicular to polarisation) for a shear wave normally incident on to a hemispherical surface indentation



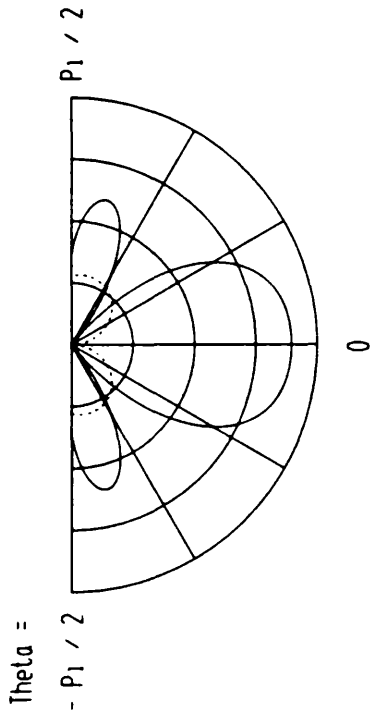
Surface displacements in x-z plane  
 Type of surface obstacle : Segment of a hemisphere  
 Order of approximation : 11  
 Incident waveltype : SV  
 Incident angle : 0.00 deg  
 Poisson's ratio : 0.25  
 $2a / \lambda$  incident : 1.00  
 $d / a$  : 0.50

Fig. 183 : Amplitude of the surface displacements in the x-z plane (plane of polarisation) for a shear wave normally incident on to a shallow axisymmetric surface indentation



Surface displacements in y-z plane  
 Type of surface obstacle : Segment of a hemisphere  
 Order of approximation : 11  
 Incident waveltype : SV  
 Incident angle : 0.00 deg  
 Poisson's ratio : 0.25  
 $2a / \lambda$  incident : 1.00  
 $d / a$  : 0.50

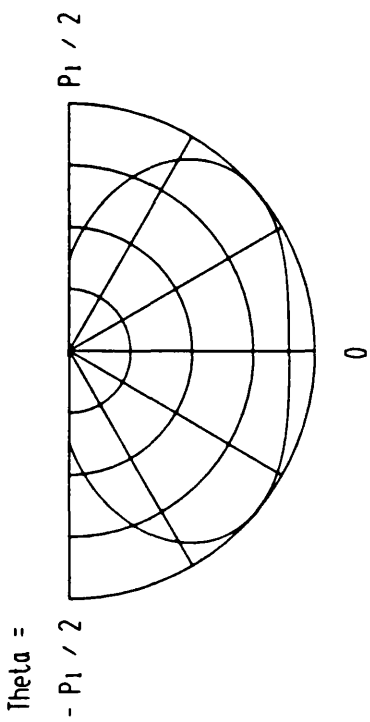
Fig. 184 : Amplitude of the surface displacements in the y-z plane (plane perpendicular to polarisation) for a shear wave normally incident on to a shallow axisymmetric surface indentation



— Theta comp      ..... R comp

Far field displacements in x-z plane  
 Type of surface obstacle : Segment of a hemisphere  
 Order of approximation : 11  
 Incident wavetype : SV  
 Incident angle : 0.00 deg  
 Poisson's ratio : 0.25  
 $2a / \lambda$  incident : 1.00  
 $d / a$  : 0.50

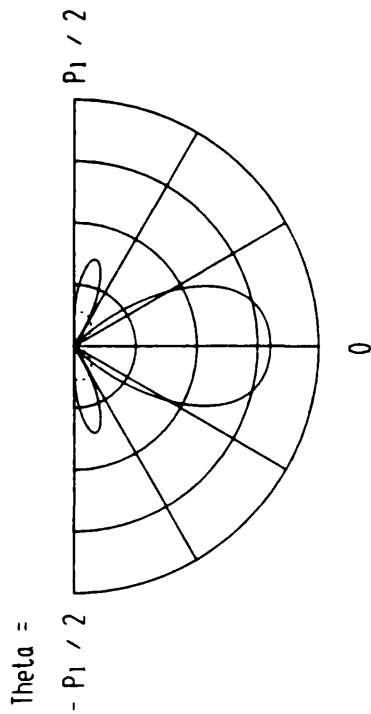
Fig. 185 : Amplitude of the far-field displacements of the scattered field in the x-z plane (plane of polarisation) for a shear wave normally incident on to a shallow axisymmetric surface indentation



— Phi comp

Far field displacements in y-z plane  
 Type of surface obstacle : Segment of a hemisphere  
 Order of approximation : 11  
 Incident wavetype : SV  
 Incident angle : 0.00 deg  
 Poisson's ratio : 0.25  
 $2a / \lambda$  incident : 1.00  
 $d / a$  : 0.50

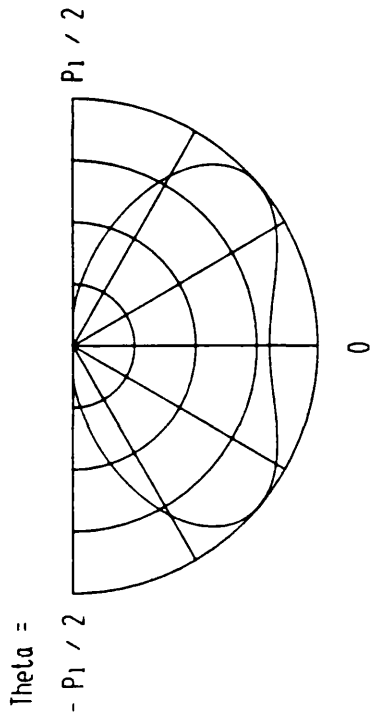
Fig. 186 : Amplitude of the far-field displacements of the scattered field in the y-z plane (plane perpendicular to polarisation) for a shear wave normally incident on to a shallow axisymmetric surface indentation



— S component      ..... P component

Scattered energy in x-z plane  
 Type of surface obstacle : Segment of a hemisphere  
 Order of approximation : 11  
 Incident wavetype : SV  
 Incident angle : 0.00 deg  
 Poisson's ratio : 0.25  
 2a / lambda incident : 1.00  
 d / a : 0.50

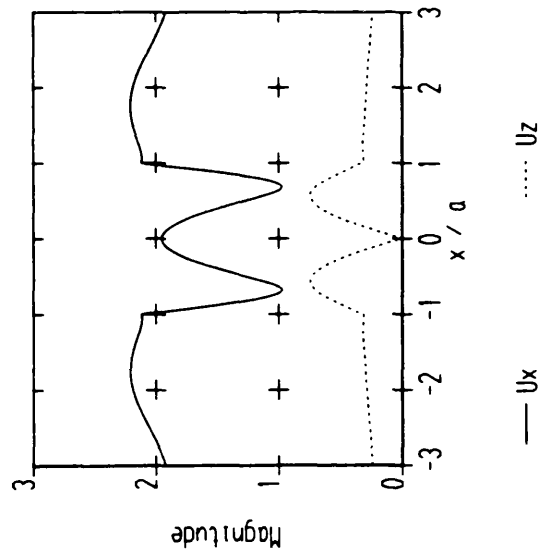
Fig. 187 : Differential cross-section of the scattered far-field in the x-z plane (plane of polarisation) for a shear wave normally incident on to a shallow axisymmetric surface indentation



— S component

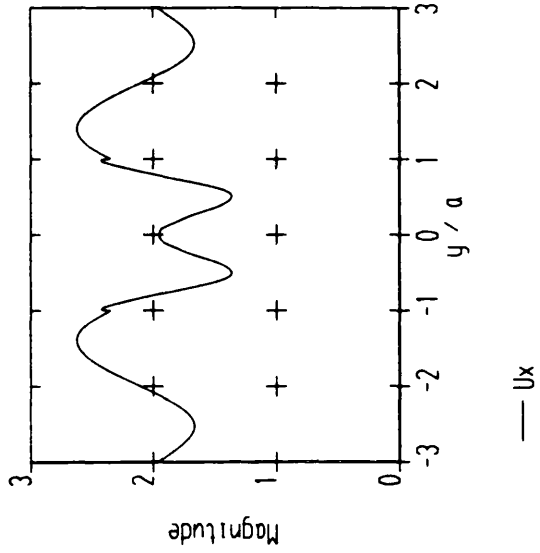
Scattered energy in y-z plane  
 Type of surface obstacle : Segment of a hemisphere  
 Order of approximation : 11  
 Incident wavetype : SV  
 Incident angle : 0.00 deg  
 Poisson's ratio : 0.25  
 2a / lambda incident : 1.00  
 d / a : 0.50

Fig. 188 : Differential cross-section of the scattered far-field in the y-z plane (plane perpendicular to polarisation) for a shear wave normally incident on to a shallow axisymmetric surface indentation



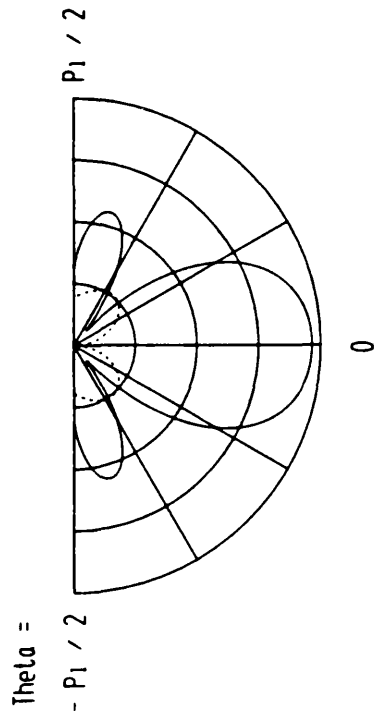
Surface displacements in x-z plane  
 Type of surface obstacle : Ellipsoid  
 Order of approximation : 11  
 Incident wavetype : SV  
 Incident angle : 0.00 deg  
 Poisson's ratio : 0.25  
 $2a / \lambda$  incident : 1.00  
 $d / a$  : 0.50

Fig. 189 : Amplitude of the surface displacements in the x-z plane (plane of polarisation) for a shear wave normally incident on to a shallow axisymmetric surface indentation



Surface displacements in y-z plane  
 Type of surface obstacle : Ellipsoid  
 Order of approximation : 11  
 Incident wavetype : SV  
 Incident angle : 0.00 deg  
 Poisson's ratio : 0.25  
 $2a / \lambda$  incident : 1.00  
 $d / a$  : 0.50

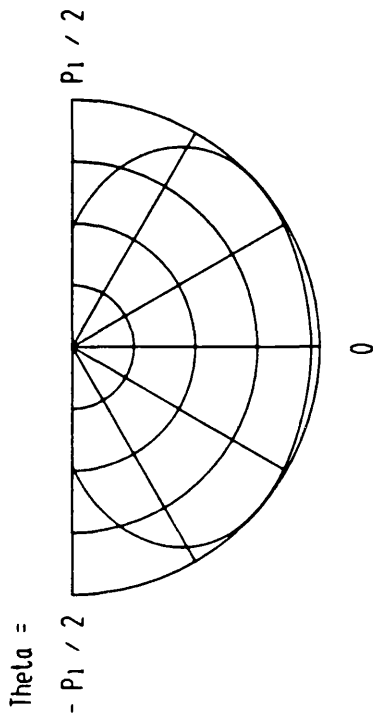
Fig. 190 : Amplitude of the surface displacements in the y-z plane (plane perpendicular to polarisation) for a shear wave normally incident on to a shallow axisymmetric surface indentation



— Theta comp      ..... R comp

Far field displacements in x-z plane  
 Type of surface obstacle : Ellipsoid  
 Order of approximation : 11  
 Incident waveltype : SV  
 Incident angle : 0.00 deg  
 Poisson's ratio : 0.25  
 $2a / \lambda$  incident : 1.00  
 $d / a$  : 0.50

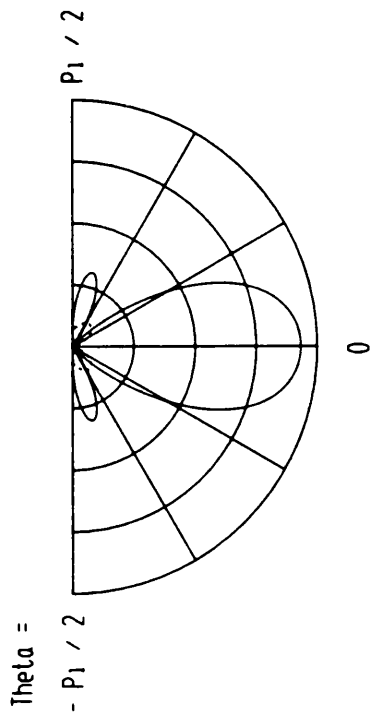
Fig. 191 : Amplitude of the far-field displacements of the scattered field in the x-z plane (plane of polarisation) for a shear wave normally incident on to a shallow axisymmetric surface indentation



— Phi comp

Far field displacements in y-z plane  
 Type of surface obstacle : Ellipsoid  
 Order of approximation : 11  
 Incident waveltype : SV  
 Incident angle : 0.00 deg  
 Poisson's ratio : 0.25  
 $2a / \lambda$  incident : 1.00  
 $d / a$  : 0.50

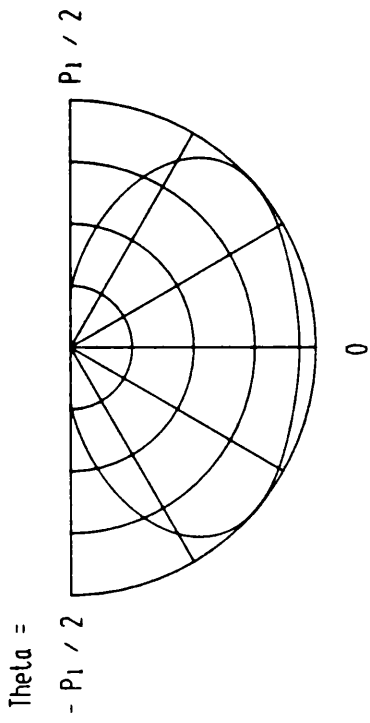
Fig. 192 : Amplitude of the far-field displacements of the scattered field in the y-z plane (plane perpendicular to polarisation) for a shear wave normally incident on to a shallow axisymmetric surface indentation



— S component      ..... P component

Scattered energy in x-z plane  
 Type of surface obstacle : Ellipsoid  
 Order of approximation : 11  
 Incident wavetype : SV  
 Incident angle : 0.00 deg  
 Poisson's ratio : 0.25  
 $2a / \lambda$  incident : 1.00  
 $d / a$  : 0.50

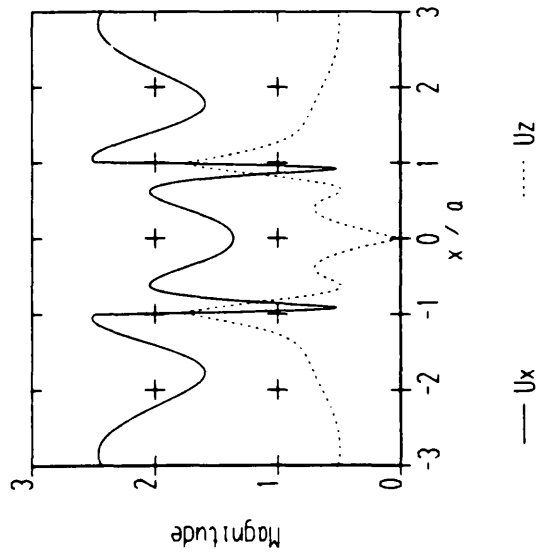
Fig. 193 : Differential cross-section of the scattered far-field in the x-z plane (plane of polarisation) for a shear wave normally incident on to a shallow axisymmetric surface indentation



— S component

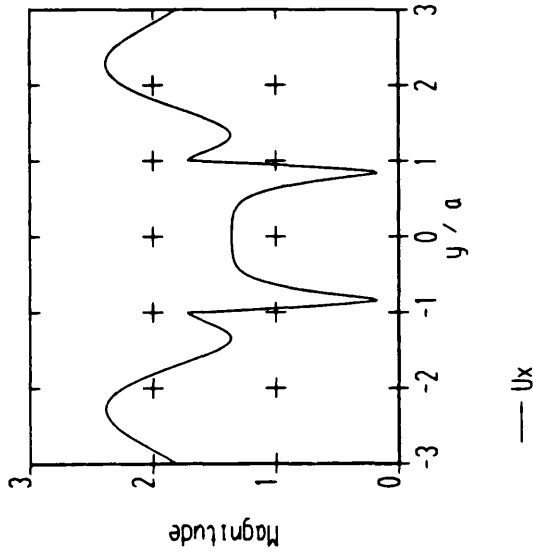
Scattered energy in y-z plane  
 Type of surface obstacle : Ellipsoid  
 Order of approximation : 11  
 Incident wavetype : SV  
 Incident angle : 0.00 deg  
 Poisson's ratio : 0.25  
 $2a / \lambda$  incident : 1.00  
 $d / a$  : 0.50

Fig. 194 : Differential cross-section of the scattered far-field in the y-z plane (plane perpendicular to polarisation) for a shear wave normally incident on to a shallow axisymmetric surface indentation



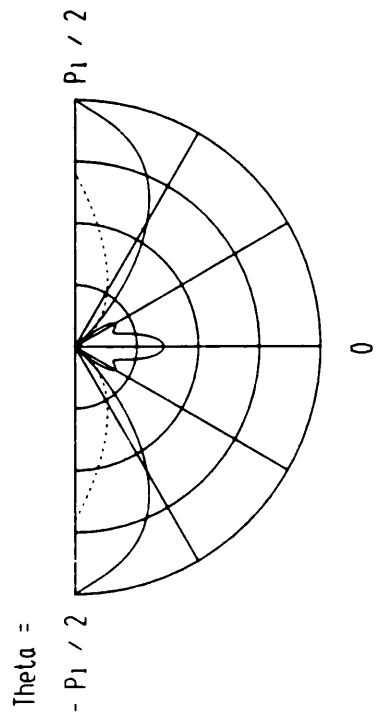
Surface displacements in x-z plane  
 Type of surface obstacle : Hemisphere  
 Order of approximation : 14  
 Incident wavetype : SV  
 Incident angle : 0.00 deg  
 Poisson's ratio : 0.25  
 $2a / \lambda$  incident : 1.00  
 $d / a$  : 1.00

Fig. 195 : Amplitude of the surface displacements in the x-z plane (plane of polarisation) for a shear wave normally incident on to a hemispherical surface indentation



Surface displacements in y-z plane  
 Type of surface obstacle : Hemisphere  
 Order of approximation : 14  
 Incident wavetype : SV  
 Incident angle : 0.00 deg  
 Poisson's ratio : 0.25  
 $2a / \lambda$  incident : 1.00  
 $d / a$  : 1.00

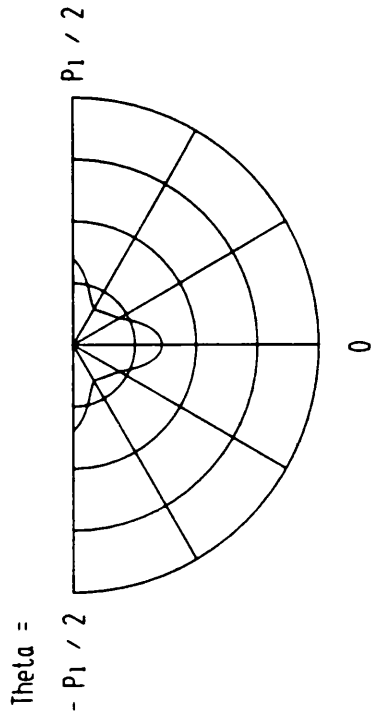
Fig. 196 : Amplitude of the surface displacements in the y-z plane (plane perpendicular to polarisation) for a shear wave normally incident on to a hemispherical surface indentation



— Theta comp      ..... R comp

Far Field displacements in x-z plane  
 Type of surface obstacle : Hemisphere  
 Order of approximation : 14  
 Incident wavetype : SV  
 Incident angle : 0.00 deg  
 Poisson's ratio : 0.25  
 $2a / \lambda$  incident : 1.00  
 $d / a$  : 1.00

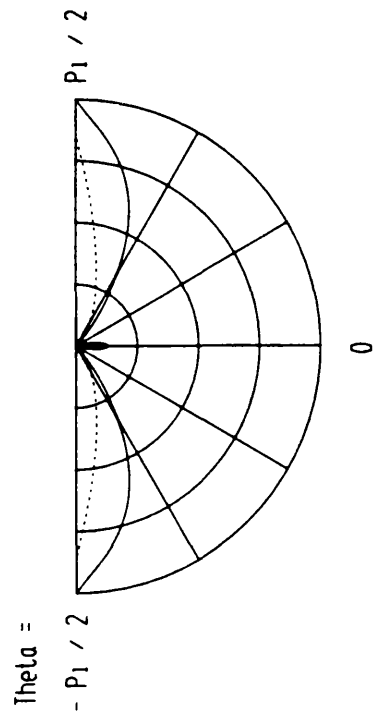
Fig. 197 : Amplitude of the far-field displacements of the scattered field in the x-z plane (plane of polarisation) for a shear wave normally incident on to a hemispherical surface indentation



— Phi comp

Far Field displacements in y-z plane  
 Type of surface obstacle : Hemisphere  
 Order of approximation : 14  
 Incident wavetype : SV  
 Incident angle : 0.00 deg  
 Poisson's ratio : 0.25  
 $2a / \lambda$  incident : 1.00  
 $d / a$  : 1.00

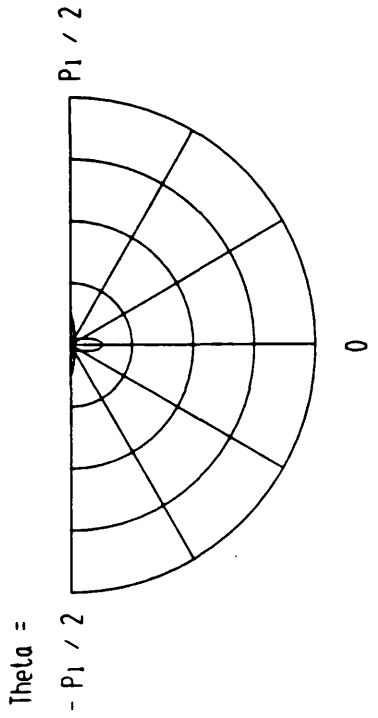
Fig. 198 : Amplitude of the far-field displacements of the scattered field in the y-z plane (plane perpendicular to polarisation) for a shear wave normally incident on to a hemispherical surface indentation



— S component      ..... P component

Scattered energy in x-z plane  
 Type of surface obstacle : Hemisphere  
 Order of approximation : 14  
 Incident wavetype : SV  
 Incident angle : 0.00 deg  
 Poisson's ratio : 0.25  
 2a / lambda incident : 1.00  
 d / a : 1.00

Fig. 199 : Differential cross-section of the scattered far-field in the x-z plane (plane of polarisation) for a shear wave normally incident on to a hemispherical surface indentation



— S component

Scattered energy in y-z plane  
 Type of surface obstacle : Hemisphere  
 Order of approximation : 14  
 Incident wavetype : SV  
 Incident angle : 0.00 deg  
 Poisson's ratio : 0.25  
 2a / lambda incident : 1.00  
 d / a : 1.00

Fig. 200 : Differential cross-section of the scattered far-field in the y-z plane (plane perpendicular to polarisation) for a shear wave normally incident on to a hemispherical surface indentation

Compressional and shear waves incident at 30 degrees

This section presents the amplitude of the surface displacements, the amplitude of the far-field displacements and the differential scattering cross-section of the scattered far-field for a compressional or shear wave incident under 30 degrees on to the surface indentations considered above. The polar plots are again normalised and the maximum values relate to each other as given below.

Case	Figure numbers for a P wave incident at 30 degrees	Figure numbers for SV wave incident at 30 degrees
(a)	Figs. 201 — 206	Figs. 225 — 230
(b)	Figs. 207 — 212	Figs. 231 — 236
(c)	Figs. 213 — 218	Figs. 237 — 242
(d)	Figs. 219 — 224	Figs. 243 — 248

Table 14 : Figure numbers of the results for the cases (a) — (d) presented in this section for a P or SV wave incident at 30 degrees

case	Figure numbers	scaling factor of the far-field displacements
(a)	Figs. 203, 204	1.0
(b)	Figs. 209, 210	1.3
(c)	Figs. 215, 216	1.6
(d)	Figs. 221, 222	3.9

Table 15 : Scaling factors of the far-field displacement plots for the cases

(a) — (d) and a P wave incident at 30 degrees

case	Figure numbers	scaling factor of the differential cross-section
(a)	Fig. 205, 206	1.0
(b)	Fig. 211, 212	4.5
(c)	Fig. 217, 218	7.6
(d)	Fig. 223, 224	44.5

Table 16 : Scaling factors of the differential cross-section plots for the cases

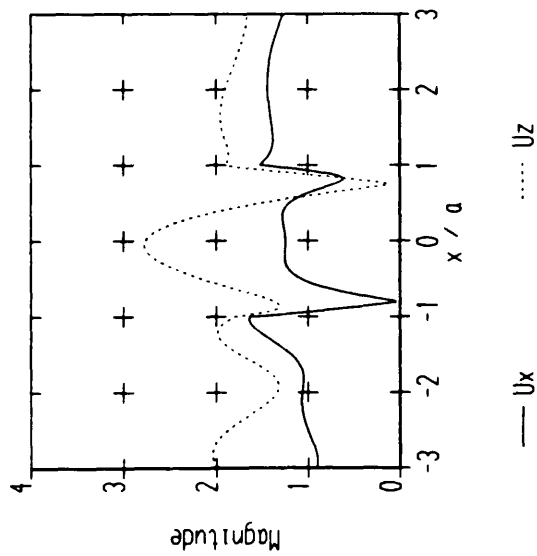
(a) — (d) and a P wave incident at 30 degrees

case	Figure numbers	scaling factor of the far-field displacements
(a)	Figs. 227, 228	1.0
(b)	Figs. 233, 234	0.76
(c)	Figs. 239, 240	0.76
(d)	Figs. 245, 246	3.1

Table 17 : Scaling factors of the far-field displacement plots for the cases  
(a) – (d) and a SV wave incident at 30 degrees

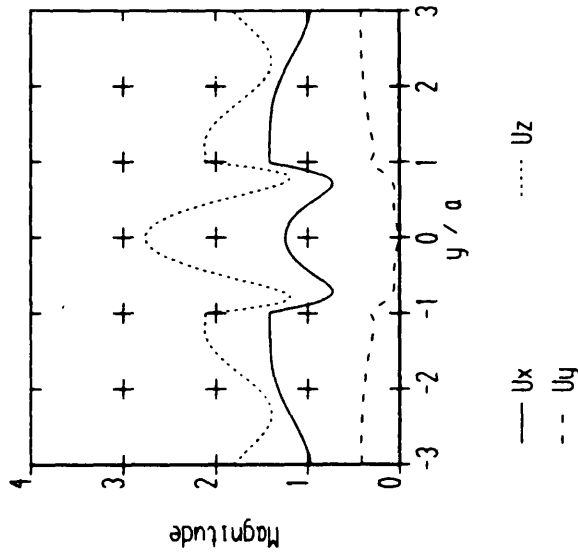
case	Figure numbers	scaling factor of the differential cross-section
(a)	Figs. 229, 230	1.0
(b)	Figs. 235, 236	1.2
(c)	Figs. 241, 242	2.0
(h)	Figs. 247, 248	26.7

Table 18 : Scaling factors of the differential cross-section plots for the cases  
(a) – (d) and a SV wave incident at 30 degrees



Surface displacements in x-z plane  
 Type of surface obstacle : Hemisphere  
 Order of approximation : 13  
 Incident wavetype : P  
 Incident angle : 30.00 deg  
 Poisson's ratio : 0.25  
 $2a / \lambda$  incident : 0.50  
 $d / a$  : 1.00

Fig. 201 : Amplitude of the surface displacements in the x-z plane (plane of the incident wave vector) for a compressional wave incident under 30 degrees on to a hemispherical surface indentation



Surface displacements in y-z plane  
 Type of surface obstacle : Hemisphere  
 Order of approximation : 13  
 Incident wavetype : P  
 Incident angle : 30.00 deg  
 Poisson's ratio : 0.25  
 $2a / \lambda$  incident : 0.50  
 $d / a$  : 1.00

Fig. 202 : Amplitude of the surface displacements in the y-z plane (plane perpendicular to the incident wave vector) for a compressional wave incident under 30 degrees on to a hemispherical surface indentation

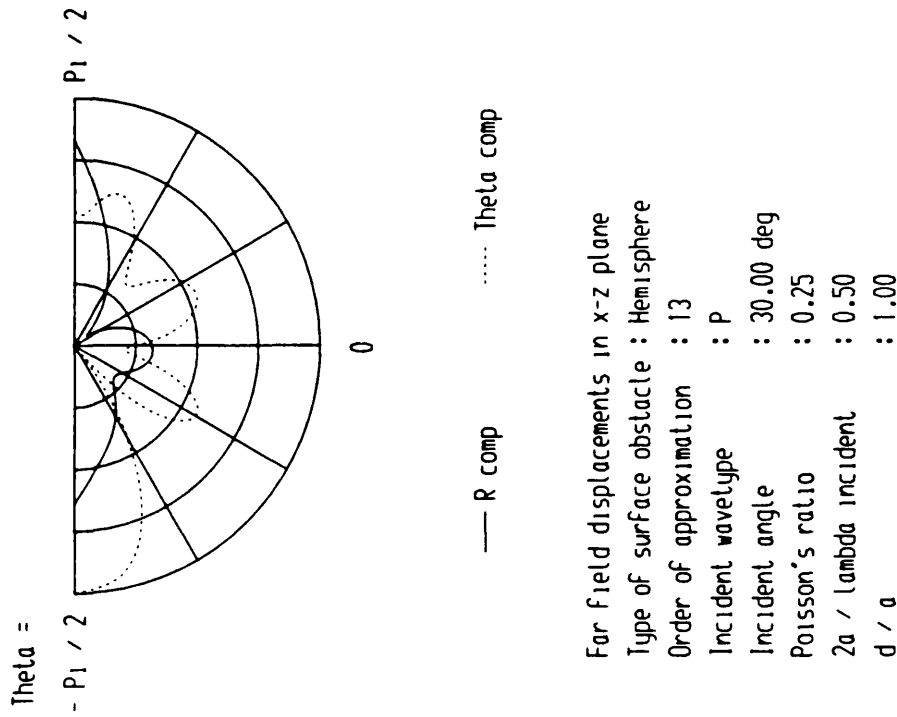


Fig. 203 : Amplitude of the far-field displacements of the scattered field in the x-z plane (plane of the incident wave vector) for a compressional wave incident under 30 degrees on to a hemispherical surface indentation

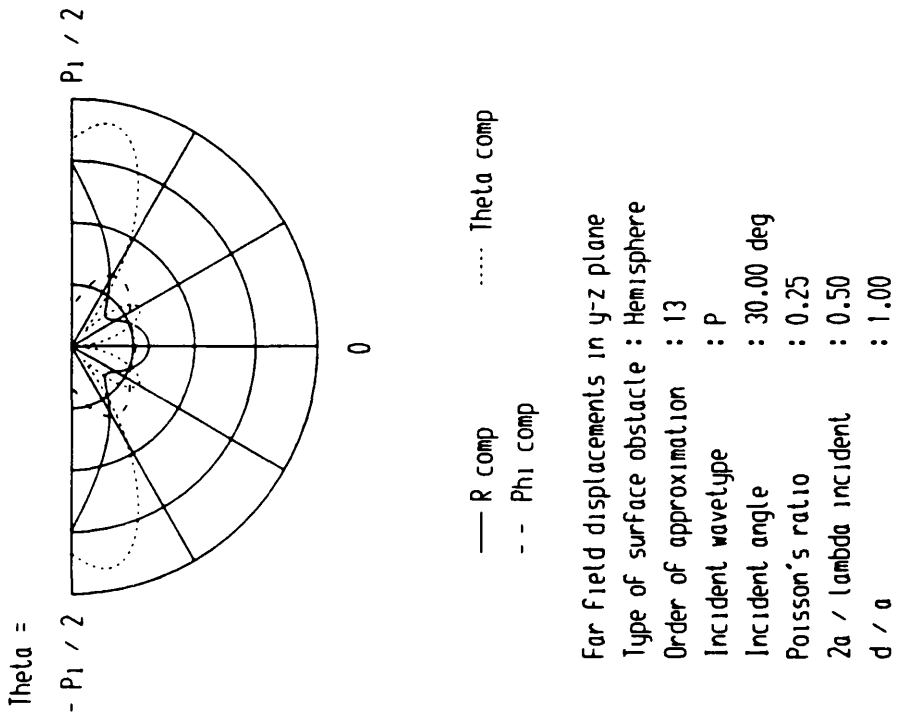
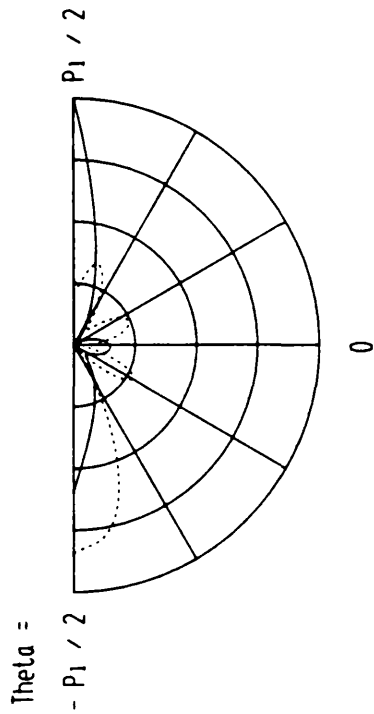


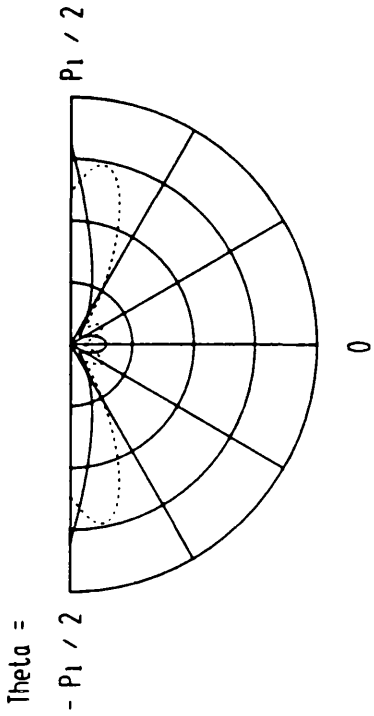
Fig. 204 : Amplitude of the far-field displacements of the scattered field in the y-z plane (plane perpendicular to the incident wave vector) for a compressional wave incident under 30 degrees on to a hemispherical surface indentation



— P component      ..... S component

Scattered energy in x-z plane  
 Type of surface obstacle : Hemisphere  
 Order of approximation : 13  
 Incident wavetype : P  
 Incident angle : 30.00 deg  
 Poisson's ratio : 0.25  
 $2a / \lambda$  incident : 0.50  
 $d / a$  : 1.00

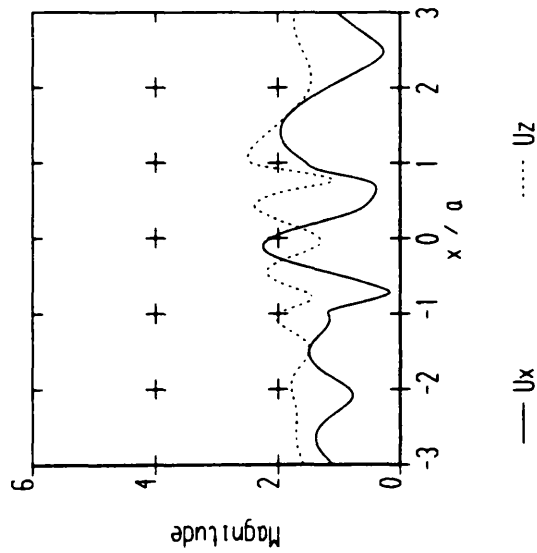
Fig. 205 : Differential cross-section of the scattered far-field in the x-z plane (plane of the incident wave vector) for a compressional wave incident under 30 degrees on to a hemispherical surface indentation



— P component      ..... S component

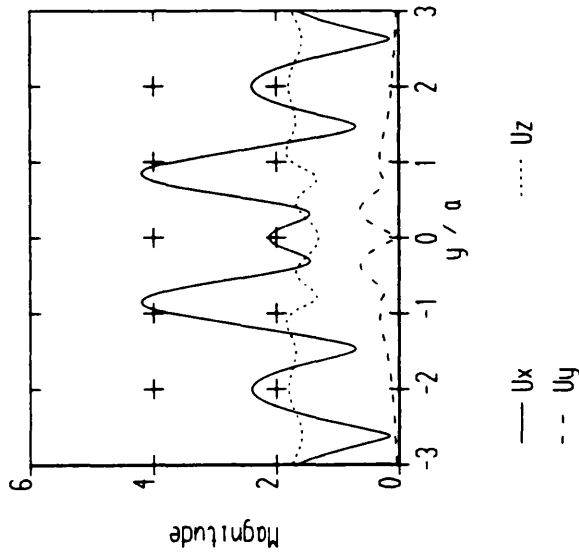
Scattered energy in y-z plane  
 Type of surface obstacle : Hemisphere  
 Order of approximation : 13  
 Incident wavetype : P  
 Incident angle : 30.00 deg  
 Poisson's ratio : 0.25  
 $2a / \lambda$  incident : 0.50  
 $d / a$  : 1.00

Fig. 206 : Differential cross-section of the scattered far-field in the y-z plane (plane perpendicular to the incident wave vector) for a compressional wave incident under 30 degrees on to a hemispherical surface indentation



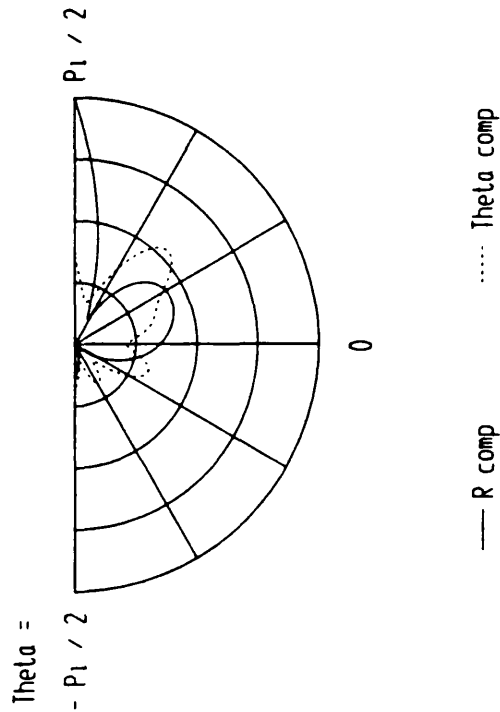
Surface displacements in x-z plane  
 Type of surface obstacle : Segment of a hemisphere  
 Order of approximation : 13  
 Incident wavetype : P  
 Incident angle : 30.00 deg  
 Poisson's ratio : 0.25  
 $2a / \lambda$  incident : 1.00  
 $d / a$  : 0.50

Fig. 207 : Amplitude of the surface displacements in the x-z plane (plane of the incident wave vector) for a compressional wave incident under 30 degrees on to a shallow axisymmetric surface indentation



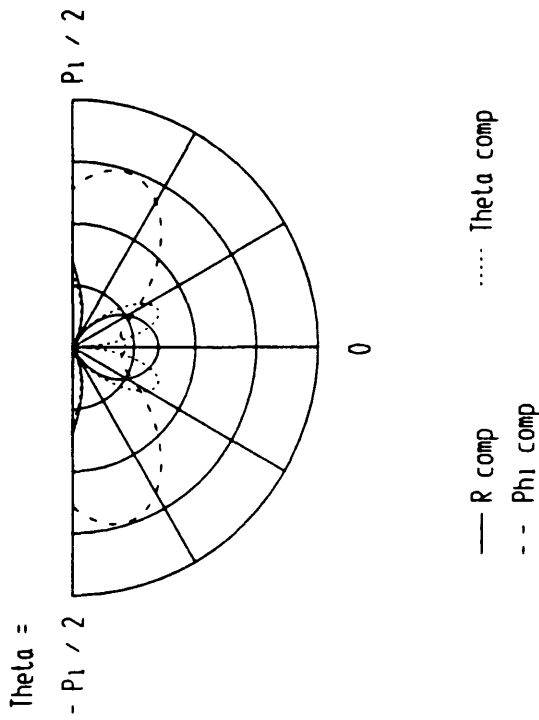
Surface displacements in y-z plane  
 Type of surface obstacle : Segment of a hemisphere  
 Order of approximation : 13  
 Incident wavetype : P  
 Incident angle : 30.00 deg  
 Poisson's ratio : 0.25  
 $2a / \lambda$  incident : 1.00  
 $d / a$  : 0.50

Fig. 208 : Amplitude of the surface displacements in the y-z plane (plane perpendicular to the incident wave vector) for a compressional wave incident under 30 degrees on to a shallow axisymmetric surface indentation



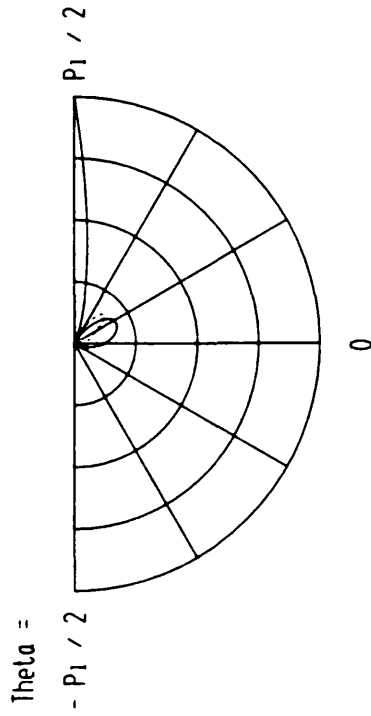
Far Field displacements in x-z plane  
 Type of surface obstacle : Segment of a hemisphere  
 Order of approximation : 13  
 Incident waveltype : P  
 Incident angle : 30.00 deg  
 Poisson's ratio : 0.25  
 $2a / \lambda$  incident : 1.00  
 $d / a$  : 0.50

Fig. 209 : Amplitude of the far-field displacements of the scattered field in the x-z plane (plane of the incident wave vector) for a compressional wave incident under 30 degrees on to a shallow axisymmetric surface indentation



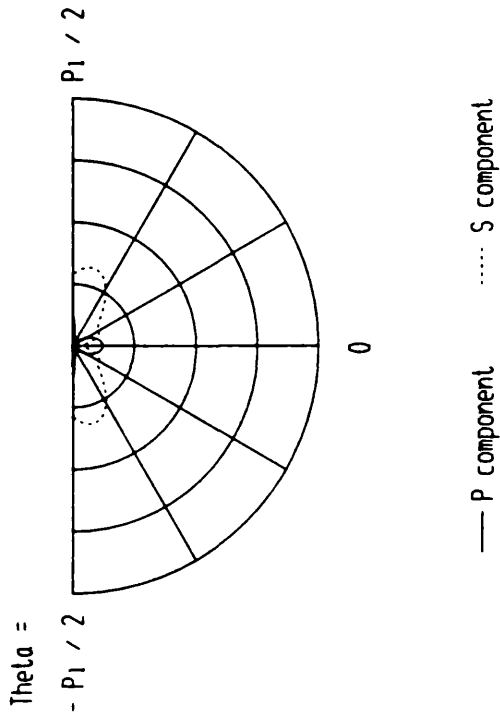
Far Field displacements in y-z plane  
 Type of surface obstacle : Segment of a hemisphere  
 Order of approximation : 13  
 Incident waveltype : P  
 Incident angle : 30.00 deg  
 Poisson's ratio : 0.25  
 $2a / \lambda$  incident : 1.00  
 $d / a$  : 0.50

Fig. 210 : Amplitude of the far-field displacements of the scattered field in the y-z plane (plane perpendicular to the incident wave vector) for a compressional wave incident under 30 degrees on to a shallow axisymmetric surface indentation



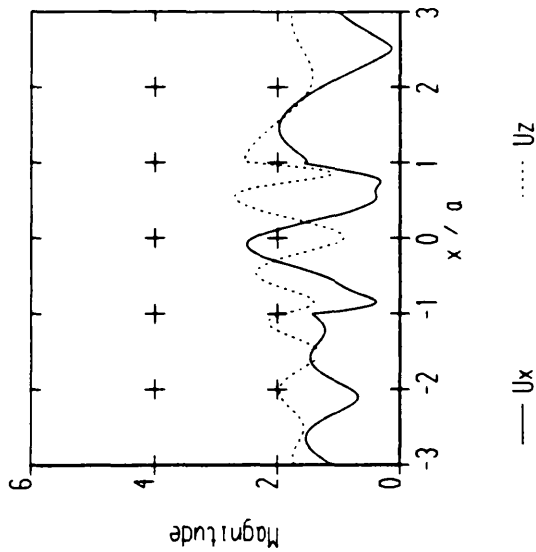
Scattered energy in x-z plane  
 Type of surface obstacle : Segment of a hemisphere  
 Order of approximation : 13  
 Incident waveltype : P  
 Incident angle : 30.00 deg  
 Poisson's ratio : 0.25  
 $2a / \lambda$  incident : 1.00  
 $d / a$  : 0.50

Fig. 211 : Differential cross-section of the scattered far-field in the x-z plane (plane of the incident wave vector) for a compressional wave incident under 30 degrees on to a shallow axisymmetric surface indentation



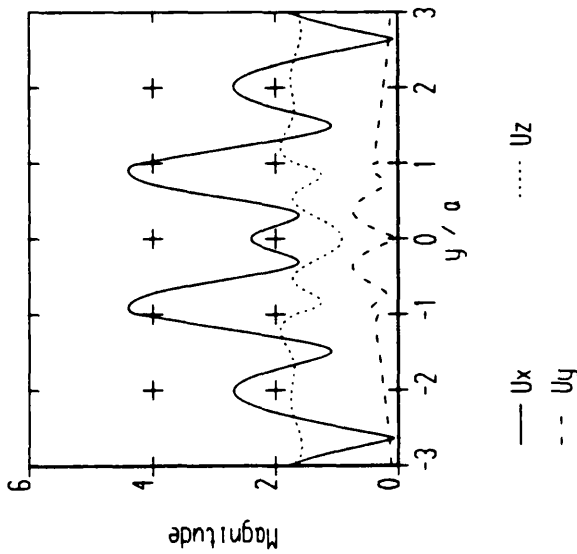
Scattered energy in y-z plane  
 Type of surface obstacle : Segment of a hemisphere  
 Order of approximation : 13  
 Incident waveltype : P  
 Incident angle : 30.00 deg  
 Poisson's ratio : 0.25  
 $2a / \lambda$  incident : 1.00  
 $d / a$  : 0.50

Fig. 212 : Differential cross-section of the scattered far-field in the y-z plane (plane perpendicular to the incident wave vector) for a compressional wave incident under 30 degrees on to a shallow axisymmetric surface indentation



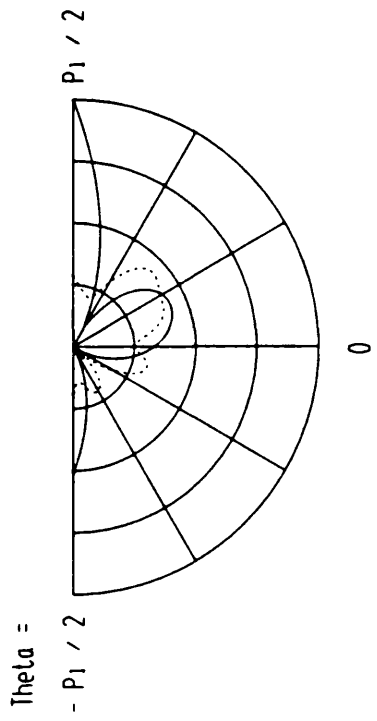
Surface displacements in x-z plane  
 Type of surface obstacle : Ellipsoid  
 Order of approximation : 13  
 Incident waveltype : P  
 Incident angle : 30.00 deg  
 Poisson's ratio : 0.25  
 $2a / \lambda$  incident : 1.00  
 $d / a$  : 0.50

Fig. 213 : Amplitude of the surface displacements in the x-z plane (plane of the incident wave vector) for a compressional wave incident under 30 degrees on to a shallow axisymmetric surface indentation



Surface displacements in y-z plane  
 Type of surface obstacle : Ellipsoid  
 Order of approximation : 13  
 Incident waveltype : P  
 Incident angle : 30.00 deg  
 Poisson's ratio : 0.25  
 $2a / \lambda$  incident : 1.00  
 $d / a$  : 0.50

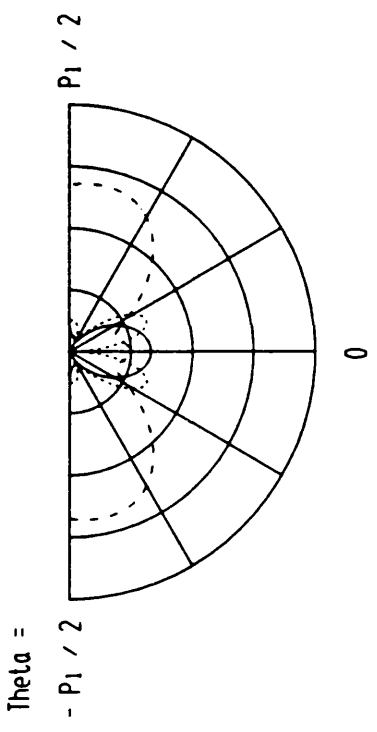
Fig. 214 : Amplitude of the surface displacements in the y-z plane (plane perpendicular to the incident wave vector) for a compressional wave incident under 30 degrees on to a shallow axisymmetric surface indentation



— R comp      ..... Theta comp

Far field displacements in x-z plane  
 Type of surface obstacle : Ellipsoid  
 Order of approximation : 13  
 Incident wavetype : P  
 Incident angle : 30.00 deg  
 Poisson's ratio : 0.25  
 2a / lambda incident : 1.00  
 d / a : 0.50

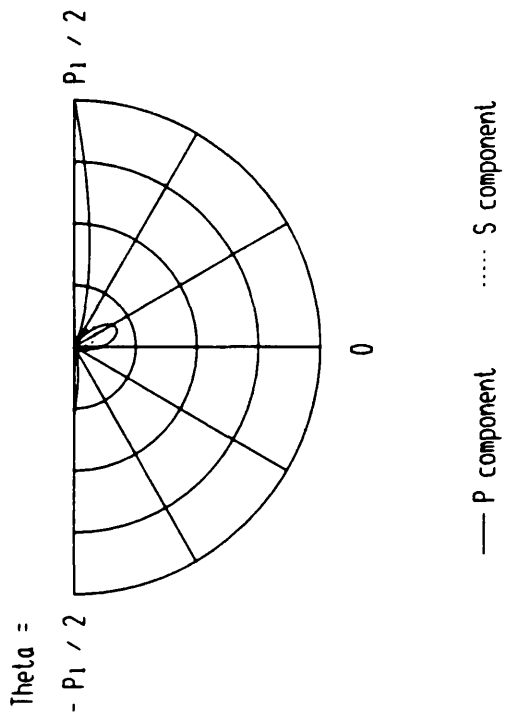
Fig. 215 : Amplitude of the far-field displacements of the scattered field in the x-z plane (plane of the incident wave vector) for a compressional wave incident under 30 degrees on to a shallow axisymmetric surface indentation



— R comp      ..... Theta comp

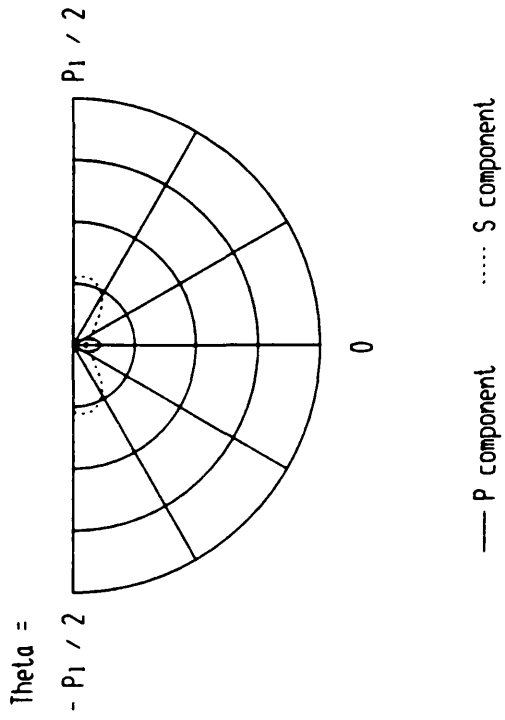
Far field displacements in y-z plane  
 Type of surface obstacle : Ellipsoid  
 Order of approximation : 13  
 Incident wavetype : P  
 Incident angle : 30.00 deg  
 Poisson's ratio : 0.25  
 2a / lambda incident : 1.00  
 d / a : 0.50

Fig. 216 : Amplitude of the far-field displacements of the scattered field in the y-z plane (plane perpendicular to the incident wave vector) for a compressional wave incident under 30 degrees on to a shallow axisymmetric surface indentation



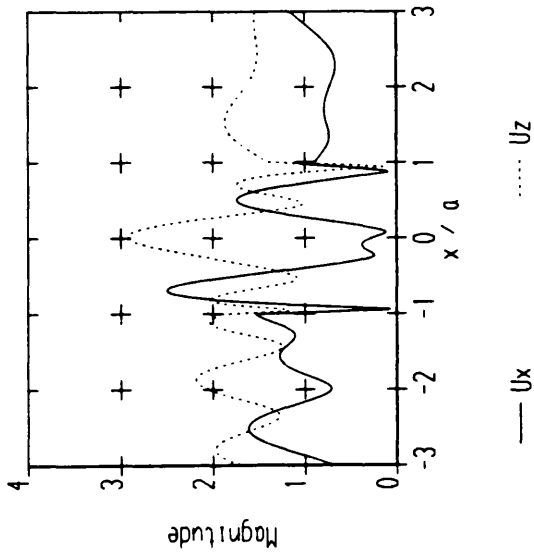
Scattered energy in x-z plane  
 Type of surface obstacle : Ellipsoid  
 Order of approximation : 13  
 Incident wavetype : P  
 Incident angle : 30.00 deg  
 Poisson's ratio : 0.25  
 2a / lambda incident : 1.00  
 d / a : 0.50

Fig. 217 : Differential cross-section of the scattered far-field in the x-z plane (plane of the incident wave vector) for a compressional wave incident under 30 degrees on to a shallow axisymmetric surface indentation



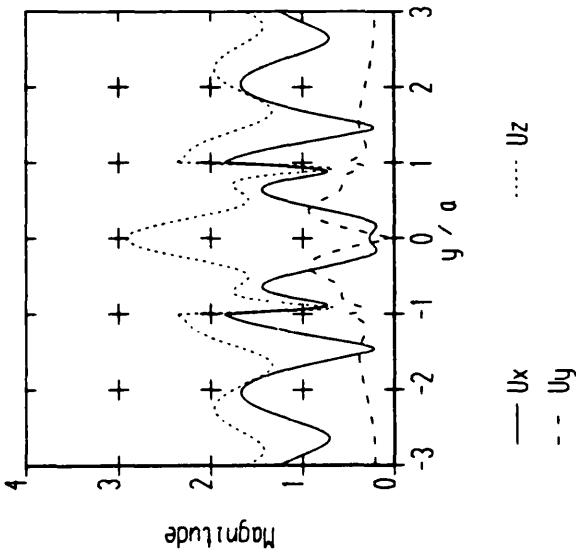
Scattered energy in y-z plane  
 Type of surface obstacle : Ellipsoid  
 Order of approximation : 13  
 Incident wavetype : P  
 Incident angle : 30.00 deg  
 Poisson's ratio : 0.25  
 2a / lambda incident : 1.00  
 d / a : 0.50

Fig. 218 : Differential cross-section of the scattered far-field in the y-z plane (plane perpendicular to the incident wave vector) for a compressional wave incident under 30 degrees on to a shallow axisymmetric surface indentation



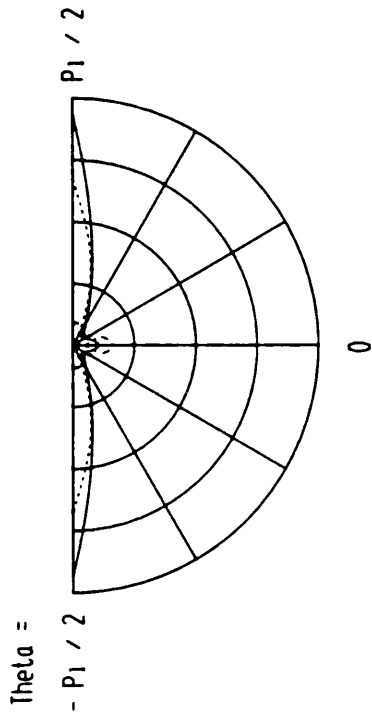
Surface displacements in x-z plane  
 Type of surface obstacle : Hemisphere  
 Order of approximation : 16  
 Incident wavetype : P  
 Incident angle : 30.00 deg  
 Poisson's ratio : 0.25  
 $2a / \lambda$  incident : 1.00  
 $d / a$  : 1.00

Fig. 219 : Amplitude of the surface displacements in the x-z plane (plane of the incident wave vector) for a compressional wave incident under 30 degrees on to a hemispherical surface indentation



Surface displacements in y-z plane  
 Type of surface obstacle : Hemisphere  
 Order of approximation : 16  
 Incident wavetype : P  
 Incident angle : 30.00 deg  
 Poisson's ratio : 0.25  
 $2a / \lambda$  incident : 1.00  
 $d / a$  : 1.00

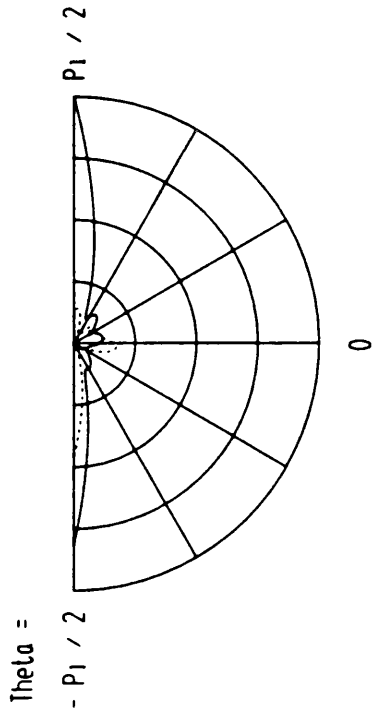
Fig. 220 : Amplitude of the surface displacements in the y-z plane (plane perpendicular to the incident wave vector) for a compressional wave incident under 30 degrees on to a hemispherical surface indentation



— R comp      ..... Theta comp  
- - - Phi comp

Far Field displacements in y-z plane  
 Type of surface obstacle : Hemisphere  
 Order of approximation : 16  
 Incident wavetype : P  
 Incident angle : 30.00 deg  
 Poisson's ratio : 0.25  
 $2a / \lambda$  incident : 1.00  
 $d / a$  : 1.00

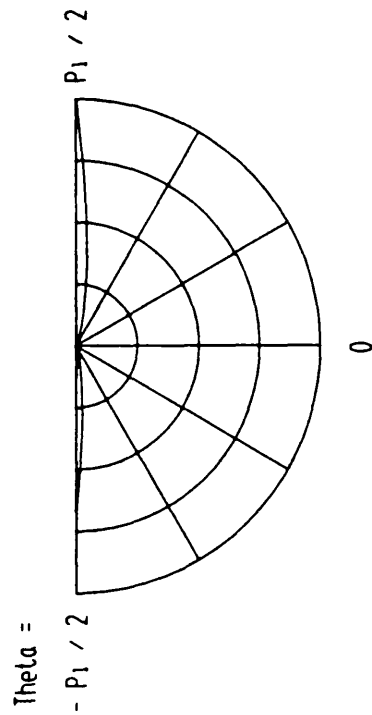
Fig. 222 : Amplitude of the far-field displacements of the scattered field in the y-z plane (plane perpendicular to the incident wave vector) for a compressional wave incident under 30 degrees on to a hemispherical surface indentation



— R comp      ..... Theta comp

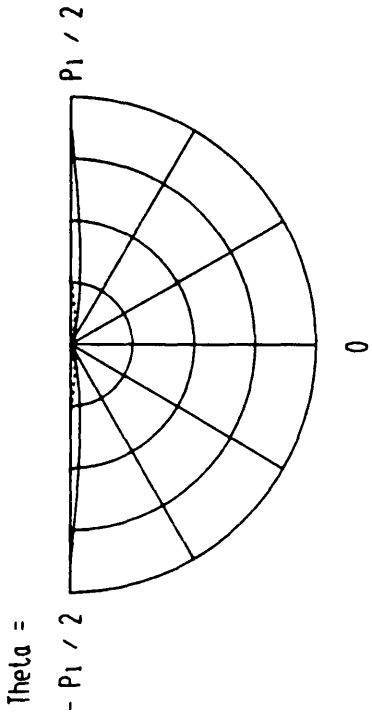
Far Field displacements in x-z plane  
 Type of surface obstacle : Hemisphere  
 Order of approximation : 16  
 Incident wavetype : P  
 Incident angle : 30.00 deg  
 Poisson's ratio : 0.25  
 $2a / \lambda$  incident : 1.00  
 $d / a$  : 1.00

Fig. 221 : Amplitude of the far-field displacements of the scattered field in the x-z plane (plane of the incident wave vector) for a compressional wave incident under 30 degrees on to a hemispherical surface indentation



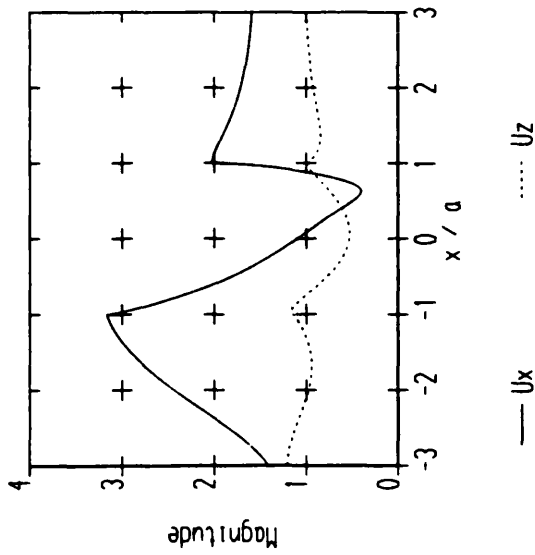
Scattered energy in x-z plane  
 Type of surface obstacle : Hemisphere  
 Order of approximation : 16  
 Incident waveltype : P  
 Incident angle : 30.00 deg  
 Poisson's ratio : 0.25  
 2a / lambda incident : 1.00  
 d / a : 1.00

Fig. 223 : Differential cross-section of the scattered far-field in the x-z plane (plane of the incident wave vector) for a compressional wave incident under 30 degrees on to a hemispherical surface indentation



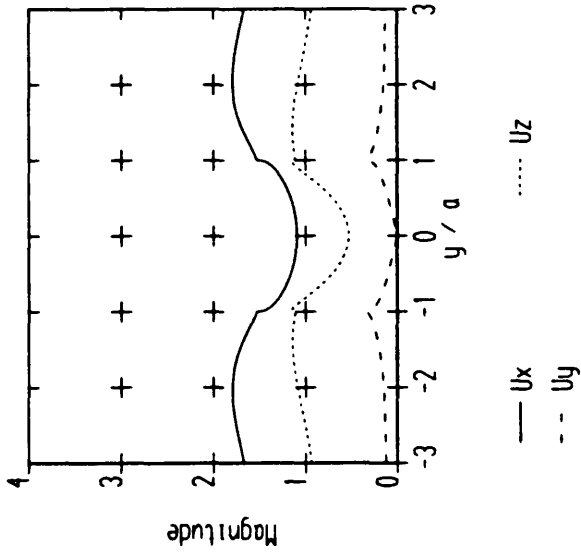
Scattered energy in y-z plane  
 Type of surface obstacle : Hemisphere  
 Order of approximation : 16  
 Incident waveltype : P  
 Incident angle : 30.00 deg  
 Poisson's ratio : 0.25  
 2a / lambda incident : 1.00  
 d / a : 1.00

Fig. 224 : Differential cross-section of the scattered far-field in the y-z plane (plane perpendicular to the incident wave vector) for a compressional wave incident under 30 degrees on to a hemispherical surface indentation



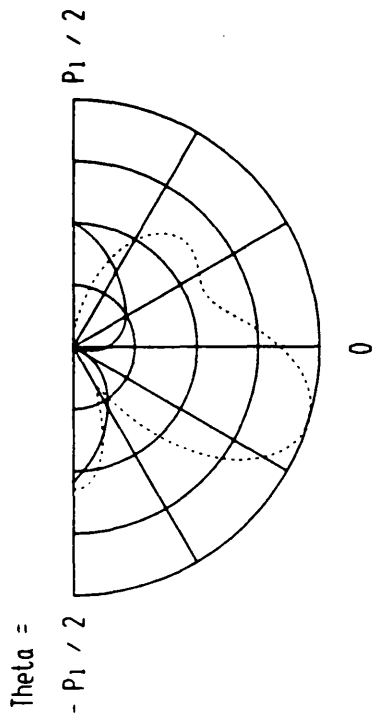
Surface displacements in x-z plane  
 Type of surface obstacle : Hemisphere  
 Order of approximation : 11  
 Incident wavetype : SV  
 Incident angle : 30.00 deg  
 Poisson's ratio : 0.25  
 $2a / \lambda$  incident : 0.50  
 $d / a$  : 1.00

Fig. 225 : Amplitude of the surface displacements in the x-z plane (plane of the incident wave vector) for a shear wave incident under 30 degrees on to a hemispherical surface indentation



Surface displacements in y-z plane  
 Type of surface obstacle : Hemisphere  
 Order of approximation : 11  
 Incident wavetype : SV  
 Incident angle : 30.00 deg  
 Poisson's ratio : 0.25  
 $2a / \lambda$  incident : 0.50  
 $d / a$  : 1.00

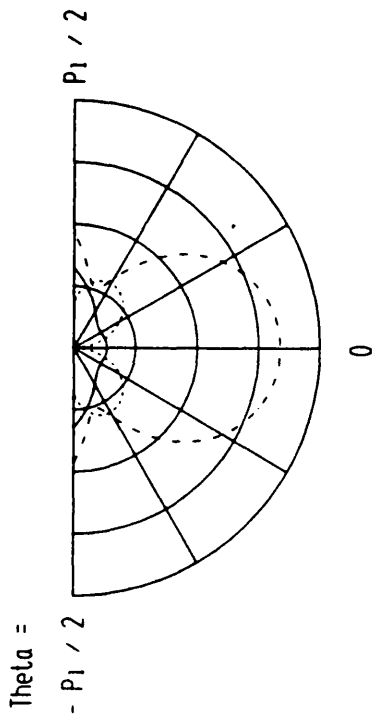
Fig. 226 : Amplitude of the surface displacements in the y-z plane (plane perpendicular to the incident wave vector) for a shear wave incident under 30 degrees on to a hemispherical surface indentation



— R comp      ..... Theta comp

Far field displacements in x-z plane  
 Type of surface obstacle : Hemisphere  
 Order of approximation : 11  
 Incident wavetype : SV  
 Incident angle : 30.00 deg  
 Poisson's ratio : 0.25  
 $2a / \lambda$  incident : 0.50  
 $d / a$  : 1.00

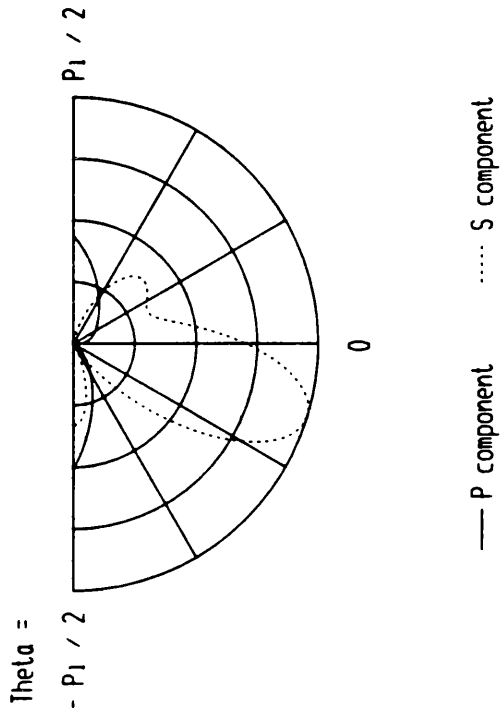
Fig. 227 : Amplitude of the far-field displacements of the scattered field in the x-z plane (plane of the incident wave vector) for a shear wave incident under 30 degrees on to a hemispherical surface indentation



— R comp      ..... Theta comp  
 - - Phi comp

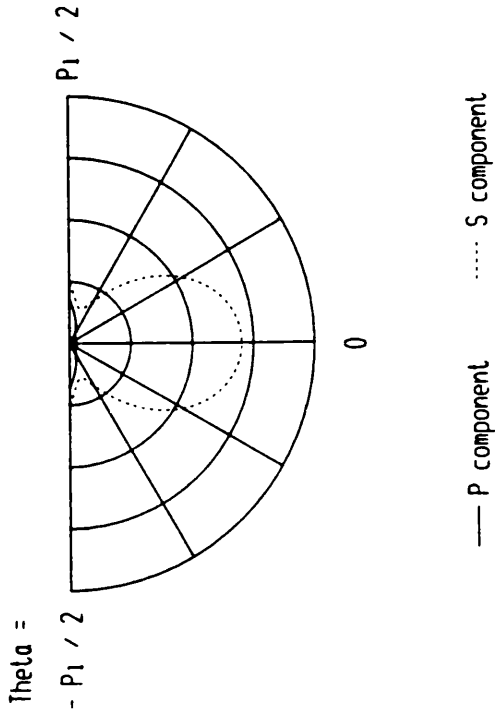
Far field displacements in y-z plane  
 Type of surface obstacle : Hemisphere  
 Order of approximation : 11  
 Incident wavetype : SV  
 Incident angle : 30.00 deg  
 Poisson's ratio : 0.25  
 $2a / \lambda$  incident : 0.50  
 $d / a$  : 1.00

Fig. 228 : Amplitude of the far-field displacements of the scattered field in the y-z plane (plane perpendicular to the incident wave vector) for a shear wave incident under 30 degrees on to a hemispherical surface indentation



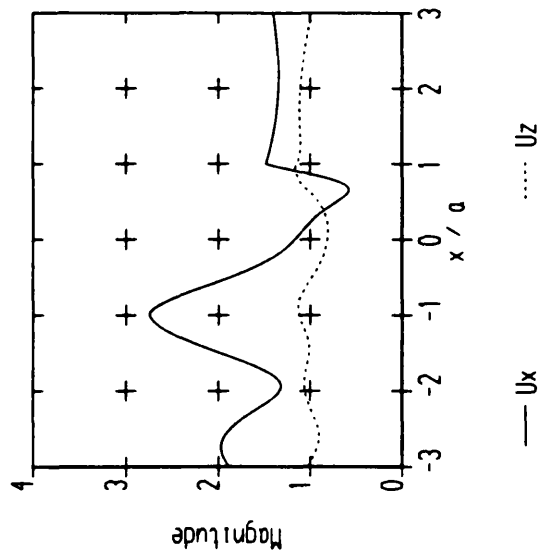
Scattered energy in x-z plane  
 Type of surface obstacle : Hemisphere  
 Order of approximation : 11  
 Incident waveltype : SV  
 Incident angle : 30.00 deg  
 Poisson's ratio : 0.25  
 $2a / \lambda$  incident : 0.50  
 $d / a$  : 1.00

Fig. 229 Differential cross-section of the scattered far-field in the x-z plane (plane of the incident wave vector) for a shear wave incident under 30 degrees on to a hemispherical surface indentation



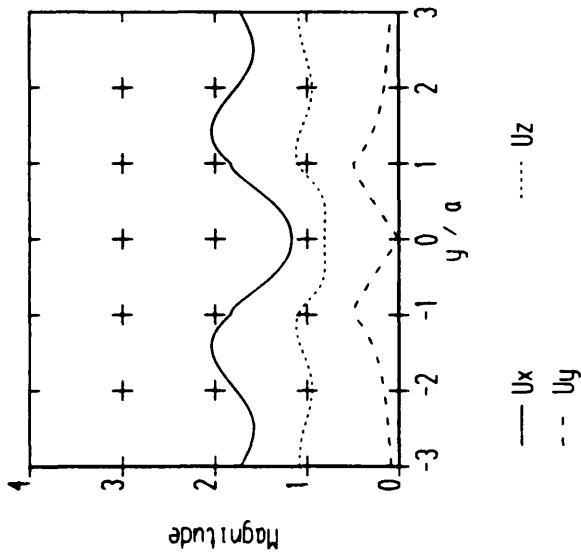
Scattered energy in y-z plane  
 Type of surface obstacle : Hemisphere  
 Order of approximation : 11  
 Incident waveltype : SV  
 Incident angle : 30.00 deg  
 Poisson's ratio : 0.25  
 $2a / \lambda$  incident : 0.50  
 $d / a$  : 1.00

Fig. 230 : Differential cross-section of the scattered far-field in the y-z plane (plane perpendicular to the incident wave vector) for a shear wave incident under 30 degrees on to a hemispherical surface indentation



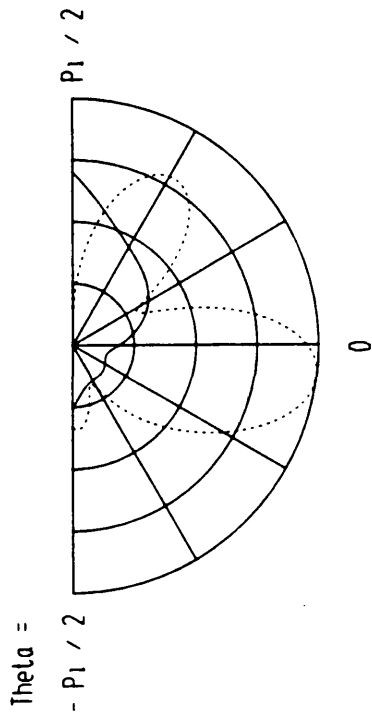
Surface displacements in x-z plane  
 Type of surface obstacle : Segment of a hemisphere  
 Order of approximation : 11  
 Incident wavetype : SV  
 Incident angle : 30.00 deg  
 Poisson's ratio : 0.25  
 $2a / \lambda$  incident : 1.00  
 $d / a$  : 0.50

Fig. 231 : Amplitude of the surface displacements in the x-z plane (plane of the incident wave vector) for a shear wave incident under 30 degrees on to a shallow axisymmetric surface indentation



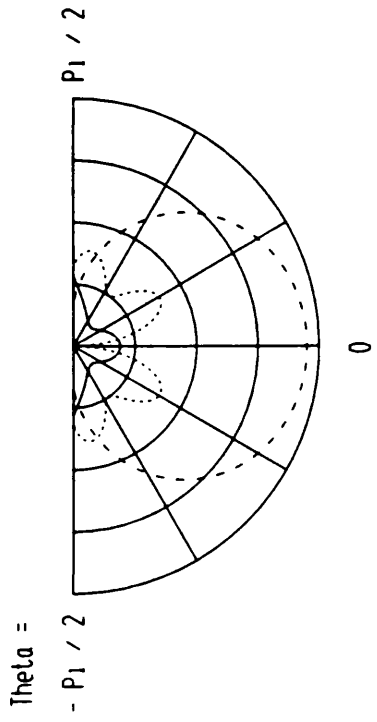
Surface displacements in y-z plane  
 Type of surface obstacle : Segment of a hemisphere  
 Order of approximation : 11  
 Incident wavetype : SV  
 Incident angle : 30.00 deg  
 Poisson's ratio : 0.25  
 $2a / \lambda$  incident : 1.00  
 $d / a$  : 0.50

Fig. 232 : Amplitude of the surface displacements in the y-z plane (plane perpendicular to the incident wave vector) for a shear wave incident under 30 degrees on to a shallow axisymmetric surface indentation



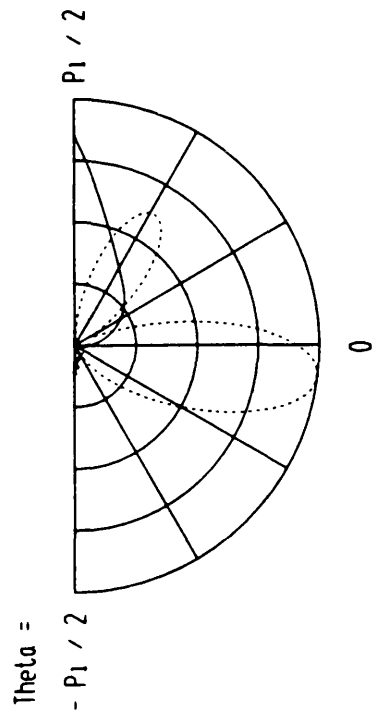
Far field displacements in x-z plane  
 Type of surface obstacle : Segment of a hemisphere  
 Order of approximation : 11  
 Incident wavetype : SV  
 Incident angle : 30.00 deg  
 Poisson's ratio : 0.25  
 $2a / \lambda$  incident : 1.00  
 $d / a$  : 0.50

Fig. 233 : Amplitude of the far-field displacements of the scattered field in the x-z plane (plane of the incident wave vector) for a shear wave incident under 30 degrees on to a shallow axisymmetric surface indentation



Far field displacements in y-z plane  
 Type of surface obstacle : Segment of a hemisphere  
 Order of approximation : 11  
 Incident wavetype : SV  
 Incident angle : 30.00 deg  
 Poisson's ratio : 0.25  
 $2a / \lambda$  incident : 1.00  
 $d / a$  : 0.50

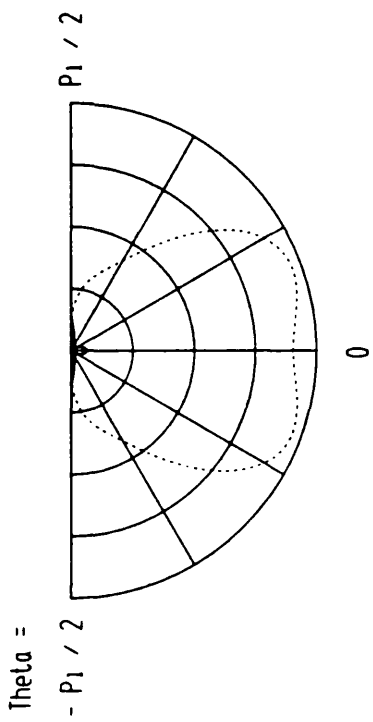
Fig. 234 : Amplitude of the far-field displacements of the scattered field in the y-z plane (plane perpendicular to the incident wave vector) for a shear wave incident under 30 degrees on to a shallow axisymmetric surface indentation



— P component      ..... S component

Scattered energy in x-z plane  
 Type of surface obstacle : Segment of a hemisphere  
 Order of approximation : 11  
 Incident wavetype : SV  
 Incident angle : 30.00 deg  
 Poisson's ratio : 0.25  
 $2a / \lambda$  incident : 1.00  
 $d / a$  : 0.50

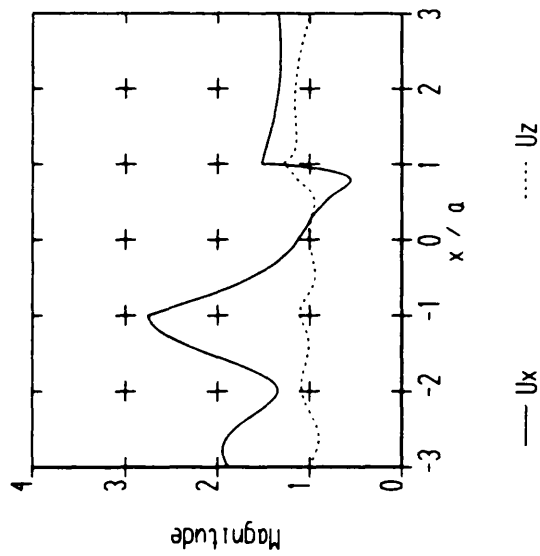
Fig. 235 : Differential cross-section of the scattered far-field in the x-z plane (plane of the incident wave vector) for a shear wave incident under 30 degrees on to a shallow axisymmetric surface indentation



— P component      ..... S component

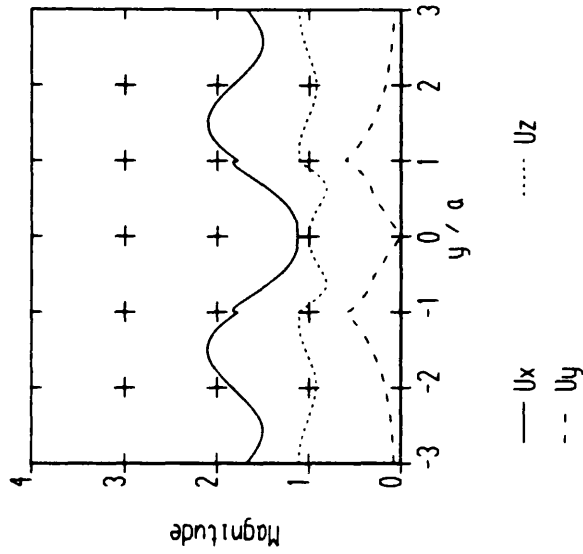
Scattered energy in y-z plane  
 Type of surface obstacle : Segment of a hemisphere  
 Order of approximation : 11  
 Incident wavetype : SV  
 Incident angle : 30.00 deg  
 Poisson's ratio : 0.25  
 $2a / \lambda$  incident : 1.00  
 $d / a$  : 0.50

Fig. 236 : Differential cross-section of the scattered far-field in the y-z plane (plane perpendicular to the incident wave vector) for a shear wave incident under 30 degrees on to a shallow axisymmetric surface indentation



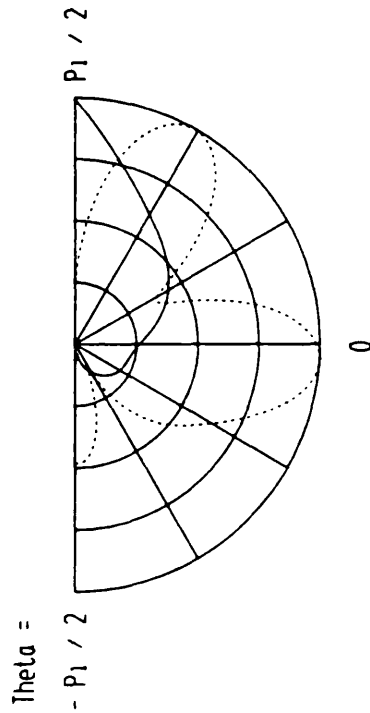
Surface displacements in x-z plane  
 Type of surface obstacle : Ellipsoid  
 Order of approximation : 11  
 Incident wavetype : SV  
 Incident angle : 30.00 deg  
 Poisson's ratio : 0.25  
 $2a / \lambda$  incident : 1.00  
 $d / a$  : 0.50

Fig. 237 : Amplitude of the surface displacements in the x-z plane (plane of the incident wave vector) for a shear wave incident under 30 degrees on to a shallow axisymmetric surface indentation



Surface displacements in y-z plane  
 Type of surface obstacle : Ellipsoid  
 Order of approximation : 11  
 Incident wavetype : SV  
 Incident angle : 30.00 deg  
 Poisson's ratio : 0.25  
 $2a / \lambda$  incident : 1.00  
 $d / a$  : 0.50

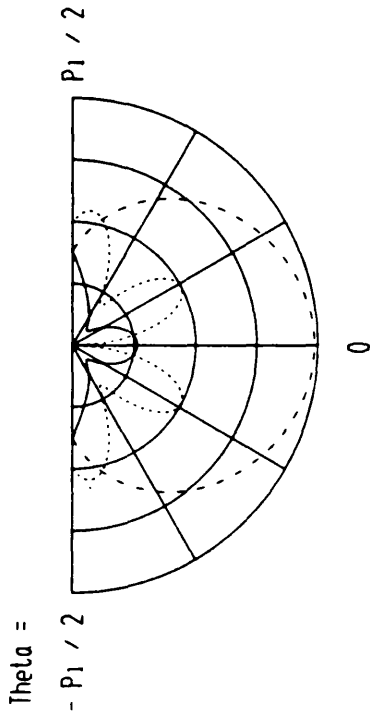
Fig. 238 : Amplitude of the surface displacements in the y-z plane (plane perpendicular to the incident wave vector) for a shear wave incident under 30 degrees on to a shallow axisymmetric surface indentation



— R comp      ..... Theta comp

Far field displacements in x-z plane  
 Type of surface obstacle : Ellipsoid  
 Order of approximation : 11  
 Incident waveltype : SV  
 Incident angle : 30.00 deg  
 Poisson's ratio : 0.25  
 $2a / \lambda$  incident : 1.00  
 $d / a$  : 0.50

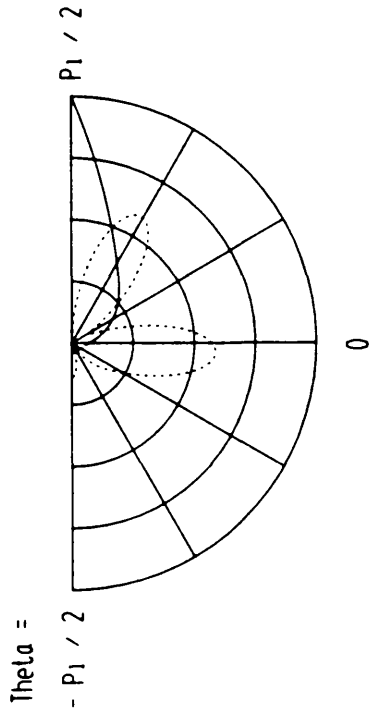
Fig. 239 : Amplitude of the far-field displacements of the scattered field in the x-z plane (plane of the incident wave vector) for a shear wave incident under 30 degrees on to a shallow axisymmetric surface indentation



— R comp      ..... Theta comp  
 - - Phi comp

Far field displacements in y-z plane  
 Type of surface obstacle : Ellipsoid  
 Order of approximation : 11  
 Incident waveltype : SV  
 Incident angle : 30.00 deg  
 Poisson's ratio : 0.25  
 $2a / \lambda$  incident : 1.00  
 $d / a$  : 0.50

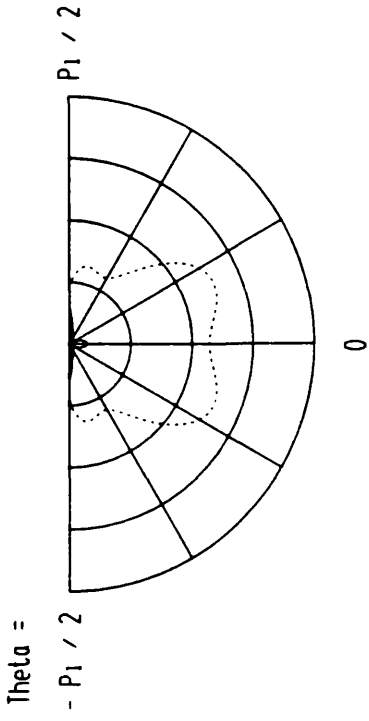
Fig. 240 : Amplitude of the far-field displacements of the scattered field in the y-z plane (plane perpendicular to the incident wave vector) for a shear wave incident under 30 degrees on to a shallow axisymmetric surface indentation



— P component      ..... S component

Scattered energy in x-z plane  
 Type of surface obstacle : Ellipsoid  
 Order of approximation : 11  
 Incident waveltype : SV  
 Incident angle : 30.00 deg  
 Poisson's ratio : 0.25  
 $2a / \lambda$  incident : 1.00  
 $d / a$  : 0.50

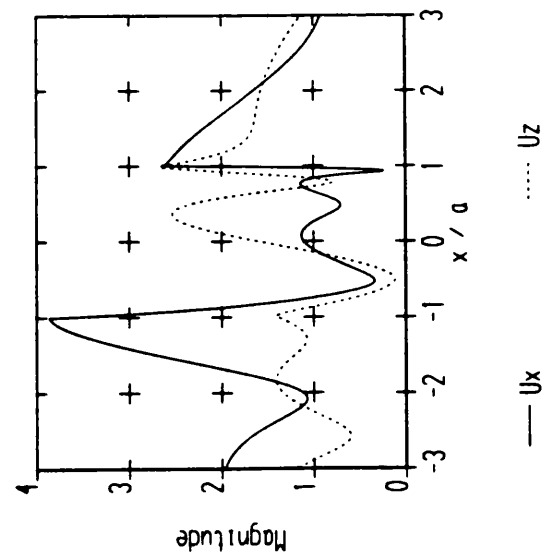
Fig. 241 : Differential cross-section of the scattered far-field in the x-z plane (plane of the incident wave vector) for a shear wave incident under 30 degrees on to a shallow axisymmetric surface indentation



— P component      ..... S component

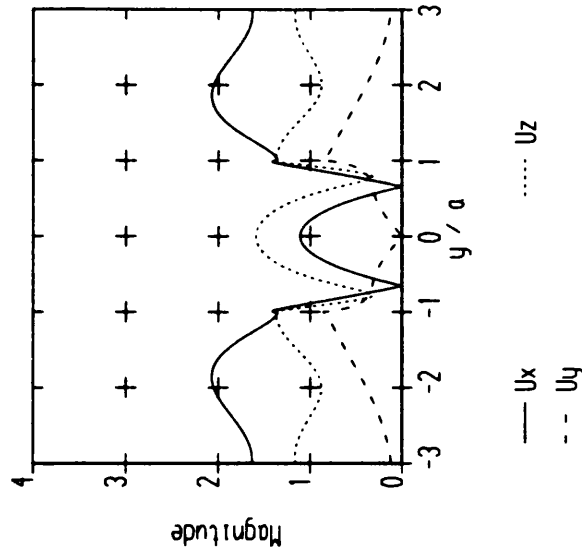
Scattered energy in y-z plane  
 Type of surface obstacle : Ellipsoid  
 Order of approximation : 11  
 Incident waveltype : SV  
 Incident angle : 30.00 deg  
 Poisson's ratio : 0.25  
 $2a / \lambda$  incident : 1.00  
 $d / a$  : 0.50

Fig. 242 : Differential cross-section of the scattered far-field in the y-z plane (plane perpendicular to the incident wave vector) for a shear wave incident under 30 degrees on to a shallow axisymmetric surface indentation



Surface displacements in x-z plane  
 Type of surface obstacle : Hemisphere  
 Order of approximation : 14  
 Incident wavetype : SV  
 Incident angle : 30.00 deg  
 Poisson's ratio : 0.25  
 $2a / \lambda$  incident : 1.00  
 $d / a$  : 1.00

Fig. 243 : Amplitude of the surface displacements in the x-z plane (plane of the incident wave vector) for a shear wave incident under 30 degrees on to a hemispherical surface indentation

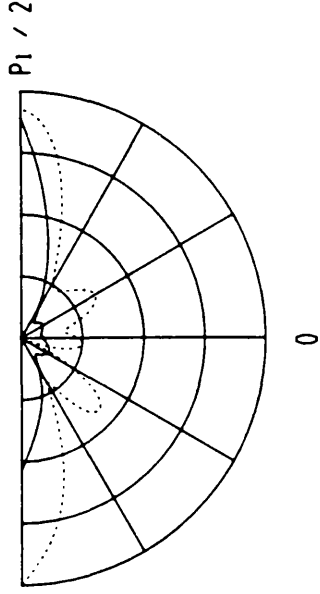


Surface displacements in y-z plane  
 Type of surface obstacle : Hemisphere  
 Order of approximation : 14  
 Incident wavetype : SV  
 Incident angle : 30.00 deg  
 Poisson's ratio : 0.25  
 $2a / \lambda$  incident : 1.00  
 $d / a$  : 1.00

Fig. 244 : Amplitude of the surface displacements in the y-z plane (plane perpendicular to the incident wave vector) for a shear wave incident under 30 degrees on to a hemispherical surface indentation

Theta =

-  $\pi / 2$



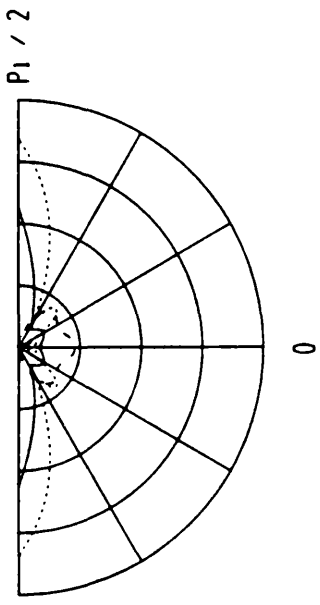
— R comp      ..... Theta comp

Far Field displacements in x-z plane  
 Type of surface obstacle : Hemisphere  
 Order of approximation : 14  
 Incident wavetype : SV  
 Incident angle : 30.00 deg  
 Poisson's ratio : 0.25  
 $2a / \lambda$  incident : 1.00  
 $d / a$  : 1.00

Fig. 245 : Amplitude of the far-field displacements of the scattered field in the x-z plane (plane of the incident wave vector) for a shear wave incident under 30 degrees on to a hemispherical surface indentation

Theta =

-  $\pi / 2$

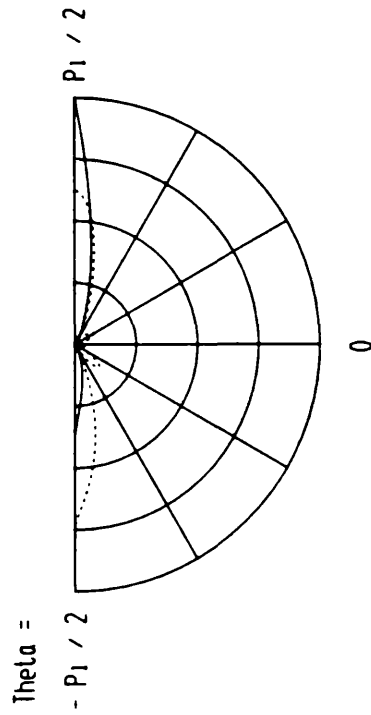


— R comp      ..... Theta comp

-- Phi comp

Far Field displacements in y-z plane  
 Type of surface obstacle : Hemisphere  
 Order of approximation : 14  
 Incident wavetype : SV  
 Incident angle : 30.00 deg  
 Poisson's ratio : 0.25  
 $2a / \lambda$  incident : 1.00  
 $d / a$  : 1.00

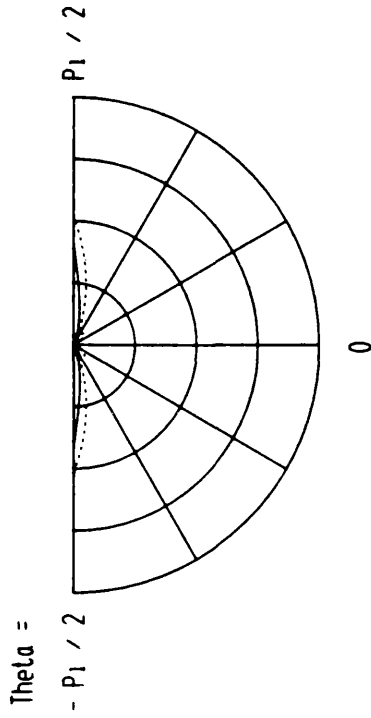
Fig. 246 : Amplitude of the far-field displacements of the scattered field in the y-z plane (plane perpendicular to the incident wave vector) for a shear wave incident under 30 degrees on to a hemispherical surface indentation



— P component      ..... S component

Scattered energy in x-z plane  
 Type of surface obstacle : Hemisphere  
 Order of approximation : 14  
 Incident wavetype : SV  
 Incident angle : 30.00 deg  
 Poisson's ratio : 0.25  
 $2a / \lambda$  incident : 1.00  
 $d / a$  : 1.00

Fig. 247 : Differential cross-section of the scattered far-field in the x-z plane (plane of the incident wave vector) for a shear wave incident under 30 degrees on to a hemispherical surface indentation



— P component      ..... S component

Scattered energy in y-z plane  
 Type of surface obstacle : Hemisphere  
 Order of approximation : 14  
 Incident wavetype : SV  
 Incident angle : 30.00 deg  
 Poisson's ratio : 0.25  
 $2a / \lambda$  incident : 1.00  
 $d / a$  : 1.00

Fig. 248 : Differential cross-section of the scattered far-field in the y-z plane (plane perpendicular to the incident wave vector) for a shear wave incident under 30 degrees on to a hemispherical surface indentation

## Bibliography

- [1] R. B. Thompson, Quantitative Ultrasonic Nondestructive Evaluation Methods, Transactions of the ASME, Journal of Applied Mechanics, Vol. 50, pp 1191 — 1201, December 1983
  
- [2] R. B. Thompson and D. O. Thompson, Ultrasonics in Nondestructive Evaluation, Proceedings of the IEEE, Vol. 73, pp 1716 — 1755, December 1985
  
- [3] L. J. Bond, Review of existing NDT technologies and their capabilities, AGARD Structures and Materials Panel, Spring Meeting, 5 — 6th May 1988, AGARD, SMP TX103 Workshop on NDE, AGARD Report No 768
  
- [4] D. J. Hagemaiier, Nondestructive Detection of Exfoliation Corrosion around Fastener Holes in Aluminium Wing Skins, Materials Evaluation, Vol. 40, pp 682 — 685, May 1982
  
- [5] R. E. Beissner and A. S. Birring, Nondestructive Evaluation Methods for Characterization of Corrosion, State-of-the-Art-Review, SwRI Project 17—7958—508, Nondestructive Testing Information Analysis Center, Southwest Research Institute, San Antonio, Texas, December 1988
  
- [6] D. J. Hagemaiier, A. H. Wendelbo, Jr., and Y. Bar-Cohen, Aircraft Corrosion and Detection Methods, Materials Evaluation, Vol. 43, pp 426 — 437, March 1985

- [7] Leonard J. Bond, Numerical techniques and their use to study wave propagation and scattering — a review, in : IUTAM Symposium on Elastic Wave Propagation and Ultrasonic Nondestructive Evaluation, 1989, Elsevier Science Publishers, in print
- [8] Francisco J. Sánchez-Sesma, Site effects on strong ground motion, Soil Dynamics and Earthquake Engineering, Vol. 6, pp 124 — 132, 1987
- [9] Francisco J. Sánchez-Sesma, Diffraction of elastic waves by three-dimensional surface irregularities, Bulletin of the Seismological Society of America, Vol. 73, pp 1621 — 1636, December 1983
- [10] Francisco J. Sánchez-Sesma, Sergio Chávez-Pérez and Javier Avilés, Scattering of elastic waves by three-dimensional topographies, Proc. World Conf. Earthquake Engrg., 8th, Vol. 2, San Francisco, California, pp 639 — 646, 1984
- [11] T. P. Smith and H. G. Beech, The Application and Use of Eddy-Currents in Non-Destructive Testing, British Journal of NDT, pp 137 — 143, Vol. 18, September 1976
- [12] D. A. Constantinis, Corrosion Condition Monitoring, State of the Art, in : NDT 86, Editors J. M. Farley and P. D. Hanstead, pp 61 — 69, EMAS, 1987
- [13] T. P. Hobin, Survey of Corrosion Monitoring and the Requirements, British Journal of NDT, Vol. 20, pp 284 — 290, November 1978

- [14] A. R. Bond, Corrosion Detection and Evaluation by NDT, British Journal of NDT, Vol 17, pp 46 — 52, March 1975
  
- [15] A. R. Bond, The Use of Eddy Currents in Corrosion Monitoring, British Journal of NDT, Vol. 20, pp 227 — 231, September 1978
  
- [16] D. J. Hagemmaier, Eddy Current Impedance Plane Analysis, Materials Evaluation, Vol. 41, pp 211 — 218, February 1983
  
- [17] D. J. Hagemmaier, Application of Eddy Current Impedance Plane Testing, Materials Evaluation, Vol. 42, pp 1035 — 1040, July 1984
  
- [18] D. J. Hagemmaier, Aircraft Corrosion and Detection Methods, in : Proceedings of the AFWAL / ML Workshop on Nondestructive Evaluation of Aircraft Corrosion, pp 41 — 51, May 1983
  
- [19] M. G. Fontana and N. D. Greene, Corrosion Engineering, McGraw-Hill, Singapore, 1978
  
- [20] R. N. Parkins, Corrosion Processes, Applied Science Publishers, London and New York, 1982
  
- [21] J. A. Ogilvy, A review of literature on wave scattering from rough surfaces, United Kingdom Atomic Energy Authority, Harwell Laboratory Report AERE R 12237, June 1986

- [22] A. A. Maraduin and D. L. Mills, The attenuation of Rayleigh Surface Waves by Surface Roughness, *Annals of Physics*, Vol. 100, pp 262 — 309, 1976
- [23] J. A. G. Temple, Calculations of the reflection and transmission of ultrasound by rough, planar defects containing water, manganese sulphide or alumina, in a steel host, United Kingdom Atomic Energy Authority, Harwell Laboratory Report AERE R 10110, June 1981
- [24] J. A. G. Temple, Calculations of the reflection and transmission of ultrasound by rough, sodium-filled defects in steel, United Kingdom Atomic Energy Authority, Harwell Laboratory Report AERE R 10095, July 1981
- [25] J. A. G. Temple, private communication
- [26] J. A. Ogilvy, Ultrasonic wave scattering from rough defects : the elastic Kirchhoff approximation, United Kingdom Atomic Energy Authority, Harwell Laboratory Report AERE R 11866, June 1985
- [27] J. A. Ogilvy, Theoretical comparison of ultrasonic signal amplitudes from smooth and rough defects, *NDT International*, Vol. 19, pp 371 — 385, December 1986

- [28] M. de Billy, J. Doucet and G. Quentin, Angular dependence of the backscattered intensity of acoustic waves from rough surfaces, Ultrasonics International 1975, Conference Proceedings, pp 218 — 223, I.P.C. Science Publication, London 1975
- [29] G. Quentin, M. de Billy, F. Cohen-Ténoudji, J. Doucet and A. Jungman, Experimental results on the scattering of ultrasound by randomly or periodically rough surfaces in the frequency range 2 to 25 MHz, Ultrasonics Symposium Proceedings, IEEE, pp 102 — 106, 1975
- [30] M. de Billy, F. Cohen-Ténoudji, A. Jungman and G. Quentin, The possibility of Assigning a Signature to Rough Surfaces Using Ultrasonic Backscattering Diagrams, IEEE Transactions on Sonics and Ultrasonics, Vol. SU-23, pp 356 — 363, September 1976
- [31] M. de Billy, F. Cohen-Ténoudji, G. Quentin, K. Lewis and L. Adler, Ultrasonic Evaluation of Geometrical and Surface Parameters of Rough Defects in Solids, Journal of Nondestructive Evaluation, Vol. 1, pp 249 — 261, 1980
- [32] M. de Billy and G. Quentin, Backscattering of acoustic waves by randomly rough surfaces of elastic solids immersed in water, Journal of the Acoustical Society of America, Vol. 72, pp 591 — 601, August 1982

- [33] F. Cohen-Ténoudji and G. Quentin, Characterisation of surfaces by deconvolution of ultrasonic echoes using extended bandwidth, *Journal of Applied Physics*, Vol. 53, pp 4057 — 4063, June 1982
- [34] Yih-Hsing Pao, *Elastic Wave in Solids*, Transactions of the ASME, *Journal of Applied Mechanics*, Vol. 50, pp 1152 — 1164, December 1983
- [35] G. A. Georgiou and M. Blakemore, *Mathematical Modelling and NDT : A State of the Art*, in : *Proceedings of the Sixth International Offshore Mechanics and Arctic Engineering Symposium (OMAE)*, pp 531 — 545, 1987
- [36] A. H. Harker, *Elastic Waves in Solids*, Adam Hilger, Bristol and Philadelphia, 1988
- [37] J. D. Achenbach, A. K. Gautesen and H. McMaken, *Ray Methods for Waves in Elastic Solids*, Pitman Books Ltd, London, 1982
- [38] William M. Visscher, Theory of scattering of elastic waves from flat cracks of arbitrary shape, *Wave Motion*, Vol. 5, pp 15 — 32, 1983
- [39] William M. Visscher, Elastic wave scattering by a surface-breaking or subsurface planar crack, *Journal of Applied Physics*, Vol. 56, pp 713 — 725, August 1984

- [40] William M. Visscher, Elastic wave scattering by a surface-breaking or subsurface planar crack II. Three dimensional geometry, Journal of Applied Physics, Vol. 57, pp 1538 — 1550, March 1985
- [41] Yih-Hsing Pao and Chao-Chow Mow, Diffraction of Elastic Waves And Dynamic Stress Concentrations, Adam Hilger Ltd, London, 1973
- [42] William M. Visscher, A new way to calculate scattering of acoustic and elastic waves. I. Theory illustrated for scalar waves, Journal of Applied Physics, Vol. 51, pp 825 — 834, February 1980
- [43] William M. Visscher, A new way to calculate scattering of acoustic and elastic waves. II. Application to elastic waves scattered from voids and fixed rigid obstacles, Journal of Applied Physics, Vol. 51, pp 835 — 845, February 1980
- [44] William Visscher, Calculation of the scattering of elastic waves from a penny-shaped crack by the method of optimal truncation, Wave Motion, Vol. 3, pp 49 — 69, 1981
- [45] Jon L. Opsal and William M. Visscher, Theory of elastic wave scattering : Applications of the method of optimal truncation, Journal of Applied Physics, Vol. 58, pp 1102 — 1115, August 1985
- [46] P. C. Waterman, Matrix theory of elastic wave scattering, Journal of the Acoustical Society of America, Vol. 60, pp 567 — 580, September 1976

- [47] Vasundara Varatharajulu and Yih-Hsing Pao, Scattering matrix for elastic waves. I. Theory, Journal of the Acoustical Society of America, Vol. 60, pp 556 — 566, September 1976
- [48] Vasundara V. Varadan, Scattering matrix for elastic waves. II. Application to elliptic cylinders, Journal of the Acoustical Society of America, Vol. 63, pp 1014 — 1024, April 1978
- [49] Vasundara V. Varadan and Vijay K. Varadan, Scattering matrix for elastic waves. III. Application to spheroids, Journal of the Acoustical Society of America, Vol. 65, pp 896 — 905, April 1979
- [50] A. Ilan, L. J. Bond and M. Spivack, Interaction of a compressional impulse with a slot normal to the surface of an elastic half-space, Geophysical Journal of the Royal astronomical Society, Vol. 57, pp 463 — 477, 1979
- [51] A. Ilan and L. J. Bond, Interaction of a compressional impulse with a slot normal to the surface of an elastic half-space — II, Geophysical Journal of the Royal astronomical Society, Vol. 65, pp 75 — 90, 1981
- [52] M. Hong and L. J. Bond, Application of the finite difference method in seismic source and wave diffraction simulation, Geophysical Journal of the Royal astronomical Society, Vol. 87, pp 731 — 752, 1986

- [53] N. Saffari and L. J. Bond, Body to Rayleigh Wave Mode-Conversion at Steps and Slots, *Journal of Nondestructive Evaluation*, Vol. 6, pp 1 – 22, 1987
- [54] A. Bayliss, K. E. Jordan, B. J. LeMesurier and E. Turkel, A fourth-order accurate finite-difference scheme for the computation of elastic waves, *Bulletin of the Seismological Society of America*, Vol. 76, pp 1115 – 1132, August 1986
- [55] R. J. Blake and L. J. Bond, A numerical model for pulsed Rayleigh wave scattering from general surface features, in : *Ultrasonics International 87, Conference Proceedings, London, 6 – 9 July 1987*, Butterworth Scientific Ltd, pp 914 – 919
- [56] R. J. Blake and L. J. Bond, A General Model for Rayleigh Wave – Surface Feature Scattering Problems, in : *Review of Progress in Quantitative Nondestructive Evaluation, 1989*, Plenum Press, in print
- [57] J. A. G. Temple, Elastic Wave Propagation and Scattering in Inhomogeneous and Anisotropic Materials, in : *IEE Colloquium on Mathematical Modelling for NDT, The Institution of Electrical Engineers, March 1989*
- [58] J. A. G. Temple and J. A. Ogilvy , Numerical Techniques for Wave Propagation and Scattering, in : *IUTAM Symposium on Elastic Wave Propagation and Ultrasonic Nondestructive Evaluation, 1989*, Elsevier Science Publishers, in print

- [59] Liao Zhenpeng, Yang Baipo and Yuan Yifan, Effect of three-dimensional topography on earthquake ground motion, Proc. World Conf. Earthquake Engineering, 7th, Istanbul, Vol. 2, pp 161 — 168, 1980
- [60] J. T. Fokkema, Reflection and transmission of time-harmonic elastic waves by the periodic interface between two elastic media, Ph.D. thesis, Delft University of Technology, Delft, The Netherlands, 1979
- [61] Chi-Pin Chang and Hang-Sheng Tuan, On the Surface-to-Bulk Mode Conversion of Rayleigh Waves, IEEE Transactions on Microwave Theory and Techniques, Vol. MTT-21, pp 558 — 560, August 1973
- [62] Hang-Sheng Tuan, On bulk waves excited at a groove by Rayleigh waves, Journal of Applied Physics, Vol. 46, pp 36 — 41, January 1975
- [63] J. P. Parekh and H.-S. Tuan, Reflection and bulk-wave conversion of Rayleigh wave at a single shallow groove, Journal of Applied Physics, Vol. 48, pp 994 — 1003, March 1977
- [64] M. de Billy and G. Quentin, Measurement of the periodicity of internal surfaces by ultrasonic testing, Journal of Physics D : Applied Physics, Vol. 15, pp 1835 — 1841, 1982

- [65] Alain Jungman, Laszlo Adler and Gerard Quentin, Ultrasonic anomalies in the spectrum of acoustic waves diffracted by periodic interfaces, *Journal of Applied Physics*, Vol. 53, pp 4673— 4680, July 1982
- [66] Alain Jungman, Laszlo Adler, Jan D. Achenbach and Ronald Roberts, Reflection from a boundary with periodic roughness : Theory and experiment, *Journal of the Acoustical Society of America*, Vol. 74, pp 1025 — 1032, September 1983
- [67] Ronald Roberts, Jan D. Achenbach, Ray-Tse Ko, Laszlo Adler, Alain Jungman and Gerard Quentin, Beam splitting at the reflection of elastic waves by a periodic surface profile, *Journal of the Acoustical Society of America*, Vol. 74, pp 1638 — 1640, November 1983
- [68] R. Roberts, J. D. Achenbach, R. Ko, L. Adler, A. Jungman and G. Quentin, Reflection of a beam of elastic waves by a periodic surface profile, *Wave Motion*, Vol. 7, pp 67 — 77, 1985
- [69] J. M. Claeys, Oswald Leroy, Alain Jungman and Laszlo Adler, Diffraction of ultrasonic waves from periodically rough liquid-solid surface, *Journal of Applied Physics*, Vol. 54, pp 5657 — 5662, October 1983
- [70] K. Mampaert and O. Leroy, Reflection and transmission of normally incident ultrasonic waves on periodic solid-liquid interfaces, *Journal of the Acoustical Society of America*, Vol. 83, pp 1390 — 1398, April 1988

- [71] Freeman Gilbert and Leon Knopoff, Seismic Scattering from Topographic Irregularities, *Journal of Geophysical Research*, Vol. 65, pp 3437 — 3444, October 1960
- [72] J. A. Hudson, Scattered Surface Waves from a Surface Obstacle, *Geophysical Journal of the Royal astronomical Society*, Vol. 13, pp 441 — 458, 1967
- [73] B. L. N. Kennett, Seismic Wave Scattering by Obstacles on Interfaces, *Geophysical Journal of the Royal astronomical Society*, Vol. 28, pp 249 — 266, 1972
- [74] J. A. Hudson, R. F. Humphryes, I. M. Mason and V. K. Kumbhavi, The scattering of longitudinal elastic waves at a rough free surface, *Journal Physics D : Applied Physics*, Vol. 6, pp 2174 — 2186, 1973
- [75] J. A. Hudson and D. M. Boore, Comments on 'Scattered surface waves from a surface obstacle' by J. A. Hudson, *Geophysical Journal of the Royal astronomical Society*, Vol. 60, pp 123 — 127, 1980
- [76] C. A. Brebbia, *The Boundary Element Method for Engineers*, Pentech Press, London, Plymouth, 1980
- [77] I. R. Gonsalves, D. J. Shippy and F. J. Rizzo, Direct Boundary Integral Equations for Elastodynamics in 3-D Half-Spaces, *Journal of Computational Mechanics*, in print (preprint received)

- [78] H. L. Wong, Effect of surface topography on the diffraction of P, SV and Rayleigh waves, Bulletin of the Seismological Society of America, Vol. 72, pp 1167 — 1183, August 1982
- [79] R. D. Gregory and David M. Austin, Scattering of waves by a semi-cylindrical groove in the surface of an elastic half-space, IUTAM Symposium on Elastic Wave Propagation and Ultrasonic Nondestructive Evaluation, 1989, Elsevier Science Publishers, in print
- [80] Francisco J. Sánchez-Sesma, Miguel A Bravo and Ismael Herrera, Surface motion of topographical irregularities for incident P, SV, and Rayleigh waves, Bulletin of the Seismological Society of America, Vol. 75, pp 263 — 269, February 1985
- [81] K. C. Wong, S. K. Datta and A. H. Shah, Three-Dimensional Motion of Buried Pipeline. I : Analysis, Journal of Engineering Mechanics, Vol. 112, pp 1319 — 1337, December 1986
- [82] K. C. Wong, A. H. Shah and S. K. Datta, Three-Dimensional Motion of Buried Pipeline. II : Numerical Results, Journal of Engineering Mechanics, Vol. 112, pp 1338 — 1345, December 1986
- [83] T. K. Mossessian and M. Dravinski, Application of a hybrid method for scattering of P, SV and Rayleigh waves by near-surface irregularities, Bulletin of the Seismological Society of America, Vol. 77, pp 1784 — 1803, October 1987

- [84] Subhendu K. Datta and Nabil El-Akily, Diffraction of Elastic Waves in a Half-space I : Integral Representations and Matched Asymptotic Expansions, in : Modern Problems in Elastic Wave Propagation, Editors Julius Miklowitz and Jan D. Achenbach, John Wiley & Sons, New York, 1978, pp 197 —218
- [85] S. K. Datta and Nabil El-Akily, Diffraction of elastic waves by cylindrical cavity in a half-space, Journal of the Acoustical Society of America, Vol. 64, pp 1692 — 1699, December 1978
- [86] A. H. Shah, K. C. Wong and S. K. Datta, Single and multiple scattering of elastic waves in two dimensions, Journal of the Acoustical Society of America, Vol. 74, pp 1033 — 1043, September 1983
- [87] K. C. Wong, A. H. Shah and S. K. Datta, Diffraction of elastic waves in a half-space. II. Analytical and numerical solutions, Bulletin of the Seismological Society of America, Vol. 75, pp 69 — 92, February 1985
- [88] A. H. Shah, K. C. Wong and S. K. Datta, Surface displacements due to elastic wave scattering by buried planar and non-planar cracks, Wave Motion, Vol. 7, pp 319 — 333, 1985
- [89] Subhendu K. Datta and Arvind H. Shah, Ultrasonic scattering by planar and non-planar cracks, in : Review of Progress in Quantitative Nondestructive Evaluation, Volume 6A, Editors Donald O. Thompson and Dale E. Chimenti, Plenum Press, New York and London, pp 69 — 78, 1987

- [90] K. R. Khair, S. K. Datta and A. H. Shah, Three-Dimensional Scattering of Elastic Waves by Surface Corrosion Pits, in : Review of Progress in Quantitative Nondestructive Evaluation, Volume 8A, Editors Donald O. Thompson and Dale E. Chimenti, Plenum Press, New York and London, pp 63 — 70, 1989
- [91] K. R. Khair, S. K. Datta and A. H. Shah, Amplification of obliquely incident seismic waves by cylindrical alluvial valleys of arbitrary cross-sectional shape. Part I. Incident P and SV waves, Bulletin of the Seismological Society of America, Vol. 79, pp 610 — 630, June 1989
- [92] J. D. Achenbach, Wave propagation in elastic solids, North-Holland Publishing Company, Amsterdam, New York, Oxford, 1973
- [93] J. A. Hudson, The excitation and propagation of elastic waves, Cambridge University Press, Cambridge, 1980
- [94] Philip M. Morse and Herman Feshbach, Methods of Theoretical Physics, Vol. I and II, McGraw-Hill Book Company, New York, Toronto, London, 1953
- [95] A. Cemal Eringen and Erdoğan S. Şuhubi, Elastodynamics, Vol. I and II, Academic Press, New York and London, 1974
- [96] Julius Adams Stratton, Electromagnetic Theory, McGraw-Hill Book Company, New York and London, 1941

- [97] Igor Aleksandrovich Viktorov, Rayleigh and Lamb Waves, Plenum Press, New York, 1967
- [98] Charles L. Lawson and Richard J. Hanson, Solving Least Squares Problems, Prentice-Hall, Inc., New Jersey, 1974
- [99] George E. Forsythe, Michael A. Malcom and Clive B. Moler, Computer Methods for Mathematical Computations, Prentice-Hall, Inc, New Jersey, 1977
- [100] William H. Press, Brian P. Flannery, Saul A. Teukolsky and William T. Vetterling, Numerical Recipes — The Art of Scientific Computing, Cambridge University Press, Cambridge, 1986
- [101] A. M. Goodbody, Cartesian Tensors With Applications to Mechanics, Fluid Mechancis and Elasticity, Ellis Horwood Limited, Chichester, 1982
- [102] R. F. Millar, The Rayleigh hypothesis and a related least-squares solution to scattering problems for periodic surfaces and other scatterers, Radio Science, Vol. 8, pp 785 — 796, August — September 1973
- [103] Peter. M. van den Berg and Jacob T. Fokkema, The Rayleigh Hypothesis in the Theory of Diffraction by a Cylindrical Obstacle, IEEE Transactions on Antennas and Propagation, Vol. AP-27, pp 577 — 583, September 1979

- [104] Vincent W. Lee, A note on the scattering of elastic plane waves by a hemispherical canyon, *Soil Dynamics and Earthquake Engineering*, Vol. 1, pp 122 — 129, 1982
- [105] M. D. Trifunac, Scattering of plane SH waves by a semi-cylindrical canyon, *Earthquake Engineering and Structural Dynamics*, Vol. 1, pp 267 — 281, 1973
- [106] H. L. Wong and M. D. Trifunac, Scattering of plane SH waves by a semi-elliptical canyon, *Earthquake Engineering and Structural Dynamics*, Vol. 3, pp 157 — 169, 1974
- [107] R. England, F. J. Sabina and I. Herrera, Scattering of SH waves by surface cavities of arbitrary shape using boundary methods, *Physics of the Earth and Planetary Interiors*, Vol 21, pp 148 — 157, 1980
- [108] Anders Boström, Gerhard Kristensson and Staffan Ström, Transformation properties of plane, spherical, and cylindrical scalar and vector wave functions, 1981, unpublished
- [109] H. Eshraghi and M. Dravinski, Scattering of plane harmonic SH, SV, P and Rayleigh waves by non-axisymmetric three-dimensional canyons : A wave function expansion approach, *Earthquake Engineering and Structural Dynamics*, Vol 18, pp 983 — 998, October 1989

- [110] M. N. Jones, *Spherical Harmonics and Tensors for Classical Field Theory*, Research Studies Press LTD., Letchworth, Hertfordshire, England, 1985
- [111] M. Danos and L. C. Maximon, *Multipole Matrix Elements of the Translation Operator*, *Journal of Mathematical Physics*, Vol. 6, pp 766 — 778, May 1965
- [112] A. J. Devaney and E. Wolf, *Multipole expansion and plane wave representations of the electromagnetic field*, *Journal of Mathematical Physics*, Vol. 15, pp 234 — 244, February 1974
- [113] Milton Abramowitz and Irene A. Stegun (Editors), *Handbook of Mathematical Functions*, Dover Publications, Inc., 1965
- [114] P. J. Barratt and W. D. Collins, *The scattering cross-section of an obstacle in an elastic solid for plane harmonic waves*, *Proc. Camb. Phil. Soc.*, Vol. 61, pp 969 — 981, 1965
- [115] Robert K. Chapman, *Three-dimensional problems of wave propagation in an elastic half-space*, PhD thesis, University of Manchester, Department of Mathematics, 1976

- [116] Keiiti Aki and Kenneth L. Larner, Surface Motion of a Layered Medium Having an Irregular Interface Due to Incident Plane SH Waves, Journal of Geophysical Research, Vol. 75, pp 933 — 954, February 1970
- [117] Michel Bouchon and Keiiti Aki, Near-field of a seismic source in a layered medium with irregular interfaces, Geophysical Journal of the Royal astronomical Society, Vol. 50, pp 669 — 684, 1977
- [118] Warwick D. Smith, The Application of Finite Element Analysis to Body Wave Propagation Problems, Geophysical Journal of the Royal astronomical Society, Vol. 42, pp 747 — 768, 1975
- [119] J. A. Rial, Seismic wave resonances in 3-D sedimentary basins, Geophysical Journal of the Royal astronomical Society, Vol. 99, pp 81 — 90, 1989
- [120] Francisco J. Sánchez-Sesma, L. Eduardo Pérez-Rocha and Sergio Chávez-Pérez, Diffraction of elastic waves by three-dimensional surface irregularities. Part II, Bulletin of the Seismological Society of America, Vol. 79, pp 101 — 112, February 1989